Deltares

Modelling of Grain Sorting Mechanisms in the Nearshore Area for Natural and Nourished Beaches

Yorick Bryon Broekema

Deltares

Title
Modelling of Grain Sorting Mechanisms in the Nearshore Area for Natural and Nourished Beaches

Pages
126

Keywords
Modelling, nourishments, sorting, morphodynamics, Delft3D

Summary
In this study a modelling approach was investigated that takes into account the effect of short wave grouping on long wave motions, calculating sediment transport and morphology with multiple fractions and a layered bed stratigraphy. After extensive testing and validating this model using data collected in a wave flume in Hannover this model was used to simulate morphological development at nourished beaches. Based on the model results, an assessment on grain sorting effects during the development of nourished beaches was made, showing the models capabilities in functioning as a tool to predict sorting processes for natural and nourished beaches in a schematized environment.

Version	Date	Author	Initials	Review	Initials	Approval	Initials
	Jan. 2015	Yorick Bryon Broekema		Alessio Giardino		Frank Hoozemans	
				Jebbe van der Werf			
				Arnold van Rooijen			

State
final

MODELLING OF GRAIN SORTING MECHANISMS IN THE NEARSHORE AREA FOR NATURAL AND NOURISHED BEACHES

by

Yorick Bryon Broekema

In partial fulfilment of the
requirements for the degree of

Master of Science
In the field of Civil Engineering

At the Delft University of Technology and the
National University of Singapore

January 2015, Delft, The Netherlands

Graduation Committee

Prof. dr. ir. M.J.F. Stive	Delft University of Technology
Dr. ir. A. Giardino	Deltares
Dr. ir. J.J. van der Werf	Deltares
Ir. A.A. van Rooijen	Deltares/Delft University of Technology
Dr. ir. B.C. van Prooijen	Delft University of Technology
Dr. ir. V.P. Chua	National University of Singapore

TU Delft Delft University of Technology

NUS National University of Singapore

Deltares Enabling Delta Life

De rots in zee

De rots is klein, de zee is groot;
De rots staat stil, de golven woelen;
Maar tot hoe hoog en ver zij spoelen,
Bij najaarsbui en watersnood,
De stortvloed drijft weer van den wal,
De rots staat onbewogen pal.

En wierd ook, als de branding ziet,
De rotskruin door den vloed bedolven,
Zij wascht het hoofd zich in de golven,
Maar waggelt of verzet zich niet.
De zee valt in haar kolken neer,
De rots val des te blanker weer.

En teistert ook de noodorkaan.
De spitsen, die naar boven steken,
Schoon de eiken van hun wortel breken,
De rots blijft op haar wortel staan;
De rukwind, die de stammen klooft,
Woei enkel haar stof van 't hoofd.

Dat, dierbaar erf van Batoos teelt!
Waarop zoo gram de vlagen woeden,
Bestormd door zoo veel holle vloeden!
Dat was en blijft uw zinnebeeld:
In 't windgeloei en 't golfgeklots,
Is Neerland weer Europaas rots.

Hendrik Tollens, 1831

Preface

This thesis is the result of a research carried out at Deltares and it concludes the Double Degree Master of Science programme in Hydraulic Engineering and Water Resources Management at the Delft University of Technology and the National University of Singapore.

First, I would greatly thank the people of my graduation committee for the inspiring discussions we had during the course of my thesis. Their guidance and feedback was invaluable in shaping this work. A special thanks to Alessio Giardino and Jebbe van der Werf for their day to day supervision, support and fruitful discussions during my time at Deltares. I would also like to thank Arnold van Rooijen for providing advice and feedback whenever I needed it.

I would like to thank Michalis Vousdoukas for providing me data from his experiments, making it possible to validate the modelling work with natural behaviour, thereby adding great value to this thesis. I would also like to thank him for the discussions we had about the data, and his suggestions for improvement of the work.

Thanks to all my friends for making my studies an unforgettable experience. Thanks for all the great times, both in The Netherlands and in Asia and the unconditional support. Special thanks to fellow students at Deltares, for the highly enjoyable coffee and lunch breaks and the many interesting discussions about our research. Also thanks for the colleagues of Deltares for the warm, open atmosphere and of course the volleyball tournaments.

Finally, a very special thanks to my family for their unconditional support and encouragement during my studies. For everything you've done for me making it possible to pursue my dreams, whether it concerned studying or side activities, and for always believing in me even if I didn't.

Yorick Bryon Broekema – Zaandam, January 2015

Abstract

The nearshore area is a highly complex and dynamic region, confined by the point from where waves start interacting with the bottom until the point of the highest run-up in the swash zone. A good understanding of physical processes in the nearshore area is essential for the development and use of high-end process based hydro-morphodynamic models, like Delft3D. The aim of this study was to set up a modelling approach to understand and assess the effect of grain sorting on the nearshore morphodynamics. This was done for both natural and nourished beaches.

The literature review carried out for this thesis showed that sediment sorting is dependent on sediment characteristics as well as hydrodynamic conditions and that it is a combination of both that determines transport and sorting in the profile. Although the information found in literature is diverse, some general trends are found by several researchers: finer sediments are found more offshore and coarser sediments are found more onshore. Besides these general trends also a strong seasonal character is observed for grain size patterns.

Physical experiments were performed in Hannover in 2013, investigating not only hydro-morphodynamics but also sorting processes for a beach-profile. The data showed that the sorting processes were highly dependent on the hydrodynamics. Sorting processes were observed in the experiment very clearly. For erosive wave conditions a strong offshore fining was found explained by different transport and settling velocities of the finer sand grains, leading to settling of the finer grains further offshore than the coarser grains. Furthermore, coarsening around the bar area was observed. Milder wave conditions show a slight coarsening higher in the profile, around the part where erosion is observed, explained by different entrainment thresholds of the finer and coarser sand.

To obtain insight in the sorting processes observed in the flume experiment, a modelling study was carried out with the Delft3D modelling suite. Four different modelling approaches were set up and tested. Approach one used a single sediment fraction and did not incorporate the effect of short-wave grouping on bound long waves. Approach number two used a single sediment fraction and did incorporate the effect of short-wave grouping on bound long waves. Approaches three and four were the same as approach one and two, but now instead of a single sediment fraction, multiple fractions were used to model the sediment. Besides including multiple fractions, also a layered bed stratigraphy was used to keep track of the sediment sorting.
It was shown that a modelling approach that takes into account the (bound) long waves yields significantly better results than a modelling approach that does not take this into account. Including long waves into the computation leads to a better prediction of the bar position and height. Simulating with multiple fractions does not lead to significantly better results, although some improvement is observed: there is slightly less upper-shoreface erosion, but the bar is smoothed out a little. The model was able to simulate sorting processes as found by the experiment, predicting the correct patterns. Again significant improvement was found when long waves were taken into account by the model.

After confirming the models capabilities in simulating the correct hydro-morphodynamics and sorting processes in the flume, one model approach was applied to a case study involving nourishments. Based on the results of simulating the morphodynamic evolution as found in the wave flume in Hannover, the modelling approach including long waves and multiple sediment fractions was chosen. Three different nourishment designs were investigated: a beach nourishment and two shoreface nourishments. For the shoreface nourishments two designs were investigated: one located high in the profile (on top of the breaker bar) and one

located low in the profile (seaward of the breaker bar). The morphodynamic evolution of the nearshore area for all nourishment designs was compared to available data. A direct comparison was made for the beach nourishment with data from Vousdoukas et al. (2014) and a qualitative comparison was made for the shoreface nourishments with data from Walstra et al. (2010).

For the beach nourishment, the model was reasonably able to simulate the development of the profile under different wave conditions. However, the erosion rate of the nourishment itself was underestimated for accretive waves and overestimated for erosive waves. The shoreface nourishments qualitatively showed a similar behaviour to observations of Walstra et al. (2010). Even though accretive processes were not found by the model computations, a clear difference in behaviour was found for high energetic wave conditions and milder waves.
The functioning of the nourishments was assessed using the model computations. The beach nourishment was redistributed in the upper part of the profile, not influencing the bar dynamics lower in the profile. A coarsening just offshore of the nourishment was observed. This trend was stronger when the nourishment consisted of coarser grains than the native beach, and a coarse upper layer was formed in the upper part of the profile.
Both shoreface nourishment designs reduced erosion by reducing the wave height. No onshore movement of nourished sand was observed for both nourishment designs. The high nourishment design was more effective in reducing erosion than the low design. The high design reduced wave height throughout the entire surfzone, while the low design showed a more localized reduction of wave height. For both shoreface nourishment designs a coarsening around the nourished area was observed. Due to the reduced wave action compared to a situation where there is no nourishment in the profile, the coarser fractions settle around the nourishment.
For all nourishment designs it was found that nourishing with a coarser grain than the native beach does not yield significant differences. This was attributed to the fact that the sediment size used for the nourishment (400 μm) was rather similar to the native sand (300 μm).

Based on the results found in this thesis, the best simulation results are obtained by using a modelling approach that takes into account long waves and multiple sediment fractions. However, it is not strictly necessary to use multiple sediment fractions in the computation to get a correct representation of the morphodynamic evolution of a beach profile. It was shown that Delft3D is capable of simulating the correct sorting processes for both natural and nourished beaches, so if it is desired to get information on the sorting of the sediment, then multiple fractions can be incorporated into the model computations.

Contents

Part I – Background

1 Introduction

On the shoreface and beach of natural coastal systems, the grain size is generally far from uniform. The spatial variation in grain size is defined as sediment sorting. Highly variable hydrodynamic conditions in the nearshore area contribute to the sorting of sediments, which may impact the morphological development of the area.
Besides the natural sediment sorting phenomena taking place in the coastal system, sediment sorting can also take place when anthropogenic changes are induced in the coastal system. An example of this would be the construction of nourishments with a different grain size than the natural beach.

In this section a problem definition is given, resulting in a research objective. The research objective is divided in three research questions that form the backbone of this thesis.

1.1 Problem definition

To counteract structural erosion and thus recession of the coastline the national policy of Dynamic Preservation has been adopted by the Dutch Government since 1990. This policy aims at a sustainable preservation of safety against flooding and of values and functions in the dune area. In practice this objective is translated into maintaining the coastline at its 1990 position by using sand nourishments along the Dutch coast. This strategy makes use of natural dynamics while on the other hand it creates a lot of space for nature and recreation. One of the best known results of this sand nourishing policy is the Sand Engine (‘Zandmotor’) between Kijkduin and Hoek van Holland.
Accurate predictions of the morphological development of nourished beaches are of great importance, since this will allow the design of the most efficient nourishment solution. This in turn will save money, and will allow for better planning of coastal maintenance and improved beach safety.
As of now, morphological models are capable of correctly predicting the correct erosion and sedimentation patterns (e.g. van Duin et al., 2004), but predictions are not always accurate. To improve the morphological modelling of nourishments, a better understanding of sediment transport processes around nourishments is desired. This could be obtained by investigating sorting processes at both natural and nourished beaches.
The sorting of sediment grains at natural and nourished beaches is a direct representation of the sediment transport patterns. Therefore, in this study sediment sorting processes are investigated for both natural and nourished beaches.

1.2 Research objectives

The main purpose of this study is to gain insight in the grain sorting mechanisms, to contribute to a better understanding of the sediment transport processes and the morphological development of the nearshore area. To achieve this, an innovative modelling approach is set up and tested extensively. The objective of this thesis is defined as:

Setting-up and validation of a modelling approach to understand and assess the effect of grain sorting on the nearshore morphodynamics for both natural and nourished beaches.

The main objective is broken down in several research questions that will be answered during the course of this report. This research will focus on horizontal sorting processes in the cross-shore direction, for natural and nourished beaches forced by wind waves. The research questions are given by:

I. What is the role of grain size sorting on nearshore morphodynamics in cross-shore direction, and what physical processes are important in determining grain size sorting?
II. How can we model with Delft3D the hydro-morphodynamics and sorting processes in cross-shore direction in the nearshore area for both natural and nourished beaches?
III. What is the role of grain size sorting in the morphological development of sand nourishments in the cross-shore direction?

1.3 Methodology

An extensive literature is study is performed to explain the relevant information describing sediment sorting processes. By gathering information on sediment sorting it is already attempted to give a partial answer to question I. Also, this information will be used to qualitatively validate model results.
Experiments were performed in a wave flume in Hannover (section 0), gathering data on not only hydrodynamics and morphology but also on sediment sorting. The data gathered with these experiments was made available to use for this thesis, and will be used to calibrate and validate several Delft3D modelling approaches. By comparing model results to experimental data and knowledge from literature an answer to question II can be found.
Once the modelling approaches have been tested extensively, a choice is made for the model approach that shows the best performance in simulating the experiments. This model is used in a case study investigating the morphological development of several nourishment designs. An assessment on grain size sorting processes during the development of nourishments is made using the outcome of the model simulations.

1.4 Thesis outline

This thesis is divided into four distinct parts. Part I provides a general background, discussing basic physical processes taking place in the nearshore region in chapter 2.
In Part II, the Hannover Flume Model is discussed. Chapter 3 presents the experimental data. The set-up of the experiments is shown and an analysis on the processes is made. In chapter 4 the modelling set-up is discussed. Besides the basic structure of the Delft3D model, four different model approaches are introduced. Chapter 5 discusses the results of the different models. The calibration procedure is highlighted, and an in-depth evaluation of the physical processes computed by the modelling approaches is shown. The performance of the models is rated and also sensitivity on several free parameters of the model is presented.
In Part III hydro-morphodynamics and sorting processes are investigated for nourished beaches. Using the results of Part II of the thesis, one of the four modelling approaches is used to simulate the development of three different nourishment designs. The set-up of the case study is discussed in chapter 6 and the outcome is shown in chapter 7.
Part IV concludes this thesis. In chapter 8 the conclusions are presented. The conclusions are separated and presented for the physical experiment, the modelling approach and the nourishment case study. Chapter 9 discusses some recommendations based on this research. Limitations encountered during this research are listed, and recommendations on improvement on or overcoming these limitations are presented. This is done for the experiments and the numerical modelling. Furthermore, some recommendations for future research are made. Finally, some practical implications based on the outcome of this thesis are presented.

2 Physical processes in the nearshore region

The nearshore coastal region is a highly dynamic and complex region where many hydro- and morpho-dynamic processes occur. A good understanding of the physics in the nearshore region is essential for the development and use of high-end process based morphodynamic models (e.g. Delft3D, XBeach, MIKE). The aim of this section is to provide a concise review of the nearshore physical processes. It is assumed the reader is familiar with the basic concepts of coastal engineering; therefore only concepts relevant for this study are discussed here. For further background in the basics on coastal engineering the reader is referred to various literature concerning coastal processes (e.g. Bosboom & Stive, 2013; Van Rijn, 2013);

In section 2.1 some basic coastal terminology and definitions will be given. The extent of the nearshore region is defined, and some basic parameters used to describe sorting are discussed. In section 2.2 background theory about waves and wave transformation in the nearshore region is discussed, while section 2.3 discusses the resulting hydrodynamics. In section 2.4 sediment transport processes are described and in section 2.5 the morphological response in the nearshore region is treated. Section 2.6 outlines the basics of sediment sorting processes and how they affect morphological response, while section 2.7 discusses sorting patterns found in nature. Finally, in section 2.8 a basic processes concerning the morphological evolution of nourishments are discussed.

2.1 Terminology and definitions

2.1.1 The nearshore region

The coastal engineering discipline focuses on many different types of environments and physical processes. For example, consider the coastline (defined as the area where land meets the sea or ocean). Many different types of coastline can be found in nature, ranging from spectacular cliffs to sandy shores and from uninterrupted coastal stretches to complex delta systems.

This study focuses on sandy coasts that are subject to water level variations induced by waves that propagate, transform and eventually reach the coast. The domain of interest in this study is the nearshore region, which is divided into several zones based on the wave transformation and local beach geometry.

As long as wind or swell waves are propagating in water where the depth is large enough, they will not interact with the bottom. Approaching the coast, there will be a point where the water depth has reduced to such an extent that the waves start to interact with the bottom. At this point, the wave celerity starts decreasing. Before breaking, wave energy flux is conserved within propagating waves (Holthuijsen, 2007):

$$P = Ec_g = Enc = \text{constant} \tag{2.1}$$

where E is the wave energy, c_g is the wave group velocity, c is the wave celerity and n is defined as the ratio of c_g to c. Since the wave celerity decreases, from energy conservation it follows that the wave height increases as a consequence of the decrease in water depth. This process is known as shoaling, and the zone in which this occurs is known as the shoaling zone. If the water depth becomes too shallow the waves will become unstable and start breaking. The zone where wave breaking occurs is defined as the breaker zone. Broken waves propagate further onshore as a bore. The region between the seaward point of the

breaker zone and the water line is called the ‘surfzone’. Finally, the bore will collapse around the waterline and travel up (run-up) and back down on the beach (run-down) in an area known as the swash zone. The swash zone is the zone characterized by continuous flooding and drying by broken waves running up and down the beach. In Figure 2.1 a schematization of the nearshore region is given. The ‘nearshore region’ is confined by the point where waves start interacting with the bottom until the point of the highest run-up in the swash zone. In this definition tide and surge levels are neglected.

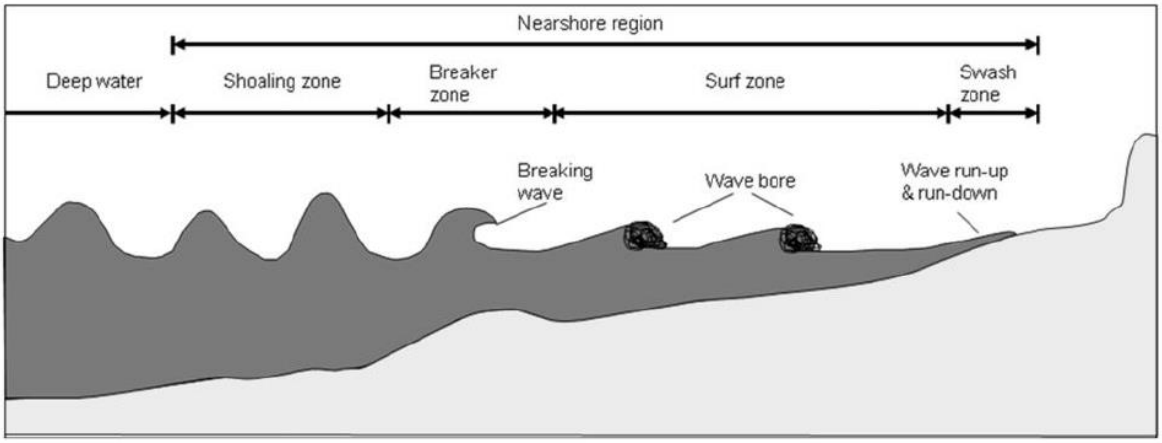

Figure 2.1 – Definition sketch of the nearshore region. Taken from van Rooijen (2011)

2.1.2 Statistical sediment parameters

2.1.2.1 Grain size

Grain size characteristics can be expressed with D_X, the sediment particle for which x% is finer by size (Bosboom & Stive, 2013). Knowing several D_X values for different passing percentages enhances the knowledge of the sediment composition. The D_X values can be constructed through the sieve curve of the sediment sample. The median diameter, D_{50} is a widely used measure for the grain size and allows for a quick (but shallow) comparison between two sediment samples. In Table 2.1 an overview of sediment classification based on size is given according to ISO 14688-1.

Table 2.1 – Classification of sediments according to size

Name				**Size range [mm]**
Very coarse soil		Large boulder	LBo	> 630
		Boulder	Bo	200 – 630
		Cobble	Co	63 – 200
Coarse soil	Gravel	Coarse gravel	CGr	20 – 63
		Medium gravel	MGr	6.3 – 20
		Fine gravel	FGr	2.0 – 6.3
	Sand	Coarse sand	CSa	0.63 – 2.0
		Medium sand	MSa	0.2 – 0.63
		Fine sand	FSa	0.063 – 0.2
Fine soil	Silt	Coarse silt	CSi	0.02 – 0.063
		Medium silt	Msi	0.0063 – 0.02
		Fine silt	FSi	0.002 – 0.0063
	Clay		Cl	≤ 0.002

2.1.2.2 Gradation/sorting

Using the D_{50} is a quick and easy way to compare the size of two different sediment samples. However, it provides no information on uniformity or gradation of the sample. Gradation means the spread in particle sizes in the sediment mixture. Gradation can be computed by the modified geometric standard deviation as described by Folk & Ward (1957) and modified by Blott & Pye (2001). This formulation (2.2) covers 90% of the total range of the sediment sample, since it uses not only D_{84} and D_{16} but also D_{95} and D_5.

$$\sigma_G = \exp\left(\frac{\ln(D_{84}) - \ln(D_{16})}{4} + \frac{\ln(D_{95}) - \ln(D_5)}{6.6}\right) \quad (2.2)$$

σ_G = Sorting parameter [-]

D_i = Grain diameter at i% passing percentage [mm], with i $\in [0,100]$

A classification based on different levels of sorting is given in Table 2.2.

Table 2.2 – Classification of sorting, after Blott and Pye (2001)

σ_G	**Classification**
< 1.27	Very well sorted
1.27 – 1.41	Well sorted
1.41 – 1.62	Moderately well sorted
1.62 – 2.00	Moderately sorted
2.00 – 4.00	Poorly sorted
4.00 – 16.00	Very poorly sorted
> 16.00	Extremely poorly sorted

If a sample is well sorted, the standard deviation is small, and thus the sample is narrow; in other words, the sample is poorly graded. Similarly, a poorly sorted sample has a large standard deviation and thus a wide distribution making it well graded.

2.1.2.3 Skewness

Sieve curves may be similar in average size and in sorting, but one may be symmetrical, the other asymmetrical. Skewness measures the degree of asymmetry as well as the 'sign', so whether a curve has an asymmetrical tail on the left (fine sediments) or on the right (coarse sediments). The skewness is based on the Inclusive Graphic Skewness (IGS) as defined by (Folk & Ward, 1957). This way of computing the skewness covers 90% of the distribution of sediments, but it is originally designed for a log-normal distribution with φ-size values. To use it with metric values, the adapted version of the formula as described by (Blott & Pye, 2001) is used:

$$Sk_I = \frac{\ln(D_{16}) + \ln(D_{84}) - 2\cdot\ln(D_{50})}{2\cdot(\ln(D_{84}) - \ln(D_{16}))} + \frac{\ln(D_5) + \ln(D_{95}) - 2\cdot\ln(D_{50})}{2\cdot(\ln(D_{95}) - \ln(D_5))} \quad (2.3)$$

Sk_I = Inclusive graphic skewness [-]

D_i = Grain diameter at i % passing percentage, with i $\in$ [0, 100]

Symmetrical curves have a skewness of 0, curves with an excess of fine material have negative skewness and those with excess coarse material have positive skewness. A classification based on skewness is given in Table 2.3, as described by (Folk, 1980).

Table 2.3 – Classification of skewness, after Folk (1980).

Sk_I	**Classification**
- 1.00 to - 0.30	Strongly coarse-skewed
- 0.30 to - 0.10	Coarse-skewed
- 0.10 to + 0.10	Near-symmetrical
+ 0.10 to + 0.30	Fine-skewed
+ 0.30 to + 1.00	Strongly fine-skewed

2.2 Waves

Free surface waves can be characterized by several criteria, for example, wave height or frequency. In this thesis a distinction is made between high frequency waves (e.g. wind or swell waves) and low frequency waves (infragravity waves) induced by high frequency waves (bound long waves or free long waves).

Wind waves are waves generated by wind and occur in the area of generation. Wind waves are relatively short, and consist of random and irregular motions; they are often referred to as short waves.

Waves generated by grouping of high frequency waves are known as low frequency waves. These waves are relatively long and often referred to as (bound) long waves or infragravity waves. The generation of low frequency waves by high frequency waves is discussed in section 2.2.2.

2.2.1 Wave transformation

2.2.1.1 Skewness and asymmetry

When waves propagate from deep water into the nearshore region, they start interacting with the bottom, leading to transformation of the waves through shoaling and breaking processes.

Besides an increase in wave height, the shoaling process is typically characterized by a change in the shape of the wave; a gradual peakening of the wave crest and flattening of the trough and relative steepening of the face until breaking occurs (Doering & Bowen, 1995). The asymmetry around the horizontal axis is usually referred to as skewness and the asymmetry around the vertical axis is often simply called asymmetry. These non-linear effects are crucial in correctly determining the cross-shore suspended sediment transport magnitudes and bar formation processes (e.g. Walstra et al., 2007; Grasso et al., 2011.

The effect of wave skewness is that the onshore velocity (velocity under the crest) is higher but of shorter duration and that the offshore velocity (velocity under the trough) is lower but of longer duration. Asymmetry leads to a more abrupt acceleration under the steep front. More abrupt accelerations are associated with thinner boundary layers and thus higher bed shear stresses for a given velocity magnitude (Van Rijn, 2007b).

The Ursell parameter (2.4) can be used as an indicator for wave skewness and asymmetry (Doering & Bowen, 1995). This parameterisation is given in (2.5) and (2.6).

$$Ur = \frac{3}{4}\frac{ak}{(kh)^3} \tag{2.4}$$

$$S_{ww} = \left[0.8 + 0.62\log(Ur)\right]\cos\left\{\left[-90^\circ + 90^\circ \tanh\left(0.73/Ur\right)\right]\pi/180\right\} \tag{2.5}$$

$$A_{ww} = \left[0.8 + 0.62\log(Ur)\right]\sin\left\{\left[-90^\circ + 90^\circ \tanh\left(0.73/Ur\right)\right]\pi/180\right\} \tag{2.6}$$

Ur = Ursell parameter [-]
a = Amplitude of the wave (H/2) [m]
k = Wavenumber [m^{-1}]
h = Local waterdepth [m]

Propagating from offshore towards the coast, waves first become gradually more skewed in the shoaling zone while remaining reasonably symmetric around the vertical axis. Closer to the surfzone phase-shifting of the harmonics leads to an increase in wave asymmetry and eventually to a decrease in wave skewness as well. Ultimately the pitching forward will lead to wave breaking.

2.2.1.2 Wave breaking

Since shoaling causes an increase in wave height, the vertical motion of the water particles also increases. On top of this, the horizontal movements become larger in relation to the vertical motion. This leads to a significant increase in particle velocity near the surface, until the horizontal particle velocity exceeds the wave celerity; the wave becomes unstable and starts breaking. This breaking condition corresponds roughly to an angle of about 120º. In the nearshore this translates into depth-dependent breaking: when the wave height becomes larger than a fraction of the depth, the wave break starts breaking.
An important aspect of the wave breaking is the amount of water carried shoreward by a breaker in the surface roller. Breaking waves generate a layer of air-water mixture, which moves in a landward direction in the upper parts of the water column. This highly turbulent region of recirculation is thought to act as a temporary storage of energy and momentum. It has an effect corresponding to an amount of water (equal to the vertical area of the roller) carried shoreward with the speed of the wave (Svendsen, 1984). To take this effect into account sometimes an additional equation is used: the roller energy balance equation (section 4.3).

2.2.2 Bound long waves

Bound long waves are low frequency motions induced by high frequency waves. Longuet-Higgins & Stewart (1964) found that low frequency waves travel with the short wave groups, and thus with the group velocity, therefore considering these waves bound (to the short wave groups).
Waves carry energy and momentum. Newton's second law states that the net force on an object (or in this case, a fluid element) is equal to the rate of change of its momentum. For waves, the mechanisms to change momentum is by 'inflow' or 'outflow' of momentum, either by a change of particle velocity or a (net) wave induced pressure force. This flux of momentum is called radiation stress (Longuet-Higgins & Stewart, 1964). If there is a change in wave induced momentum flux (thus, radiation stress) wave forces act on the fluid, changing mean water motion and water levels, for instance:

- Lowering the mean water level in the shoaling zone
- Raising the mean water level in the surf zone

Radiation stress consists of an advection component, which is the advection of momentum by horizontal particle velocity, and a wave-induced pressure component. Since this study focuses on cross-shore processes, for simplicity only the transport of x-momentum in x-direction is considered here. Now x is the direction of wave propagation, perpendicular to the coastline where the coastline is assumed alongshore uniform. The radiation stress is given by:

$$S_{xx} = \left\langle \int_{-h}^{\eta} (\rho_w u_x) u_x dz \right\rangle + \left\langle \int_{-h}^{\eta} p_{wave} dz \right\rangle \quad (2.7)$$

$u_x =$ velocity in x-direction

$p_{wave} =$ wave-induced pressure

$\rho_w =$ density of the water

where the brackets denote averaging over one wave period. The first term represents wave induced momentum flux and the second term represents wave induced pressure. Using linear wave theory the radiation stress can be simplified by:

$$S_{xx} = \left(n - \frac{1}{2} + n\cos^2\theta \right) E = \left(2n - \frac{1}{2} \right) E \quad (2.8)$$

In this formulation E is the wave energy, and n is the ratio between wave group velocity and individual wave celerity, given by:

$$n = \frac{1}{2}\left(1 + \frac{2kh}{\sinh(2kh)} \right) \quad (2.9)$$

$k =$ wavenumber $2\pi/L$

$h =$ Local water depth (m)

For an alongshore uniform coast and normal incident waves, the wave-induced force on the water level in cross-shore direction is given by the spatial derivative of the radiation stress:

$$F_x = -\frac{dS_{xx}}{dx} \quad (2.10)$$

The radiations stress gradient is compensated by a water level slope. This equilibrium is given by:

$$F_x = -\frac{dS_{xx}}{dx} = \rho g h \frac{d\bar{\eta}}{dx} = \rho g (h_0 - \bar{\eta}) \frac{d\bar{\eta}}{dx} \quad (2.11)$$

$h_0 =$ Still water depth [m]

$\bar{\eta} =$ wave-induced water level set-up at point x

Combining (2.10) and (2.11) yields a simple model for the variation of the water level as a function of the spatial variation of wave energy:

$$\frac{d\bar{\eta}}{dx} = -\frac{3}{2}\frac{1}{\rho g h}\frac{dE}{dx} \quad (2.12)$$

From this model it can be reasoned that a spatial gradient in wave energy is associated with a spatial gradient in water level of opposite sign. High frequency waves tend to travel in wave groups of higher and lower waves, thus showing a spatial energy variation. This leads to areas with higher and lower average water levels, forming a bound long wave. This long wave

is forced: it has the length and frequency of the wave group and it propagates with the wave group at the wave group speed.
For a perfect bound long wave, the phase shift between the long wave and the short wave envelope equals 180 degrees. In reality, when the short waves show a more irregular pattern the correlation between the long wave motion and the wave group is smaller, but still negative offshore from the surfzone. Upon entering the surfzone the short waves start breaking, leading to the release of the long wave. The long waves are no longer moving with the speed of the wave group, and the correlation changes sign (from negative to positive).
If the effect of the surface roller in breaking waves is taken into account, it will lead to a delay of momentum release in the wave. This means that there will be an extra term in the radiation stress equations containing the roller contribution. This will be elaborated in section 4.3.

2.3 Cross-shore hydrodynamics

Suspended sediment transport is highly dependent on the (mean) vertical structure of the flow while bed load sediment transport is a function of the bed shear stress, or more specific, near bed velocity. The mean wave induced vertical flow profile generally consists of three parts:

- Onshore directed flow above wave trough level (Stokes drift)
- Offshore directed return flow (or undertow) below wave trough.
- Onshore directed near bed streaming (or Longuet-Higgins streaming)

Wave induced mass-flux can be computed by integrating the wave orbital velocity according to linear wave theory (2.13) from the bottom to the instantaneous surface elevation, and averaging over one wave-cycle (2.14).

$$u_x = \frac{a\omega}{\tanh(kh)}\cos\omega t \tag{2.13}$$

$$q_{non-breaking} = \left\langle \int_0^{\eta} \rho u_x dz \right\rangle = \frac{\rho a^2 \omega}{2\tanh(kh)} = \frac{\rho g a^2}{2c} = \frac{E}{c} \tag{2.14}$$

$\omega =$ angular frequency [s^{-1}]
$c =$ Wave celerity [ms^{-1}]
$q =$ Mass-flux

In the surf zone, where waves are breaking, a considerable amount of additional mass flux occurs. The additional mass flux is related to the surface roller (Svendsen, 1984) and is estimated by (2.15):

$$q_{drift} = q_{non-breaking} + q_{roller} = \frac{E}{c} + \frac{\alpha E_r}{c} \tag{2.15}$$

$\alpha =$ Proportionality constant of order 1 [-]
$E_r =$ Roller energy [Jm^{-2}]

Due to a closed boundary in the form of the coastline, there is a net zero transport through the vertical or otherwise water would pile up increasingly at the shoreline. This is obviously not happening, so the onshore directed mass-flux (Stokes drift + roller) is compensated by an offshore directed mass-flux: the return flow. The cross-shore depth mean velocity below the trough level must compensate for the mean velocity above through level (2.16):

$$U_{return} = -\frac{q_{drift}}{\rho_w h} \tag{2.16}$$

Near the bed the flow is affected by the bottom, and most wave theories do not apply anymore. For near bed flow, boundary layer theory can be used to describe the flow. The flow in this boundary layer is generally highly turbulent due to the presence of roughness elements (grains) on the bed. The boundary layer is generally limited in thickness (order of 1-10 cm) since it can not fully develop to a stationary logarithmic flow profile with the continuously changing flow. Besides a purely oscillatory flow, also a non-zero wave averaged horizontal flow is present. This is explained by the additional stresses arising from the disturbance the wave boundary layer causes on the regular wave motion. The (mean) flow is pushed forward by these stresses. Longuet-Higgins found an expression for the magnitude of this streaming at the top of the boundary layer, which is referred to as Longuet-Higgins streaming (2.17):

$$U_0 = \frac{3}{4}\frac{\hat{u}_0^2}{c} \tag{2.17}$$

$U_0 =$ Streaming velocity [ms^{-1}]

$\hat{u}_0 =$ Magnitude of the near bed orbital velocity [ms^{-1}]

2.4 Cross-shore sediment transport

Roelvink & Stive (1989) made a quantitative comparison of the magnitude of the contribution of several components to the total cross-shore sediment transport along the Holland Coast. For their analysis, they assumed that the total velocity signal consists of an average part and an oscillating part. The oscillating part is then further divided in low-frequency and high-frequency oscillations:

$$u = \underbrace{\bar{u}}_{\text{time mean component}} + \underbrace{u_{lo}}_{\substack{\text{low-frequency motion}\\ \text{at wave-group scale}}} + \underbrace{u_{hi}}_{\substack{\text{oscillatory motion at}\\ \text{short wave scale}}} \tag{2.18}$$

To determine the most important contributing mechanisms to the total cross-shore sediment transport they used the third-odd moment as an indicator for transport. By assuming that $\bar{u} << u_{lo} << u_{hi}$ and using a Taylor expansion (Roelvink & Stive, 1989):

$$\left\langle u|u|^2 \right\rangle = 3\left\langle \bar{u}|u_{hi}|^2 \right\rangle + \left\langle u_{hi}|u_{hi}|^2 \right\rangle + 3\left\langle u_{lo}|u_{hi}|^2 \right\rangle \tag{2.19}$$

The term $|u_{hi}|^2$ in all three terms indicates that the sediment is stirred up by short waves. The first term in the RHS of (2.19) is related to transport by the mean current. Sediments are stirred up by the short waves and transported in the direction of the mean current: offshore directed due to the undertow in the surf zone or onshore directed due to near bed streaming in non-breaking waves.

The second term is related to shoaling of waves, causing asymmetry around the horizontal axis. The signal is positively skewed, meaning $<u^3>$ is larger than zero, causing an onshore directed transport.

The third term is non-zero if there is a correlation between short wave variance and the long wave forced on group scale. Outside the surf zone, this correlation is negative (the 'through'

of the long waves is found under the highest short waves), so most sediment is stirred up while the long wave velocities are offshore directed, thus causing offshore directed transport. Once this phase-relationship is changed, net transport direction will also change.
In a study by Deigaard et al. (1999) the net sediment transport under wave groups and bound long waves is investigated. In line with Roelvink & Stive (1989) they found that although bound long waves cause an additional forward motion of the water near the bed, they give a negative contribution to the sediment transport because the backward motion in the long waves is coupled with the high waves and high sediment concentrations. They further concluded that the combined net transport depends on the grain size and transport intensity. For very fine sand the mean water motion and forward drift of the sediment dominate, giving a positive net transport. For coarser sand the coupling between the backward motion and high sediment concentration dominates, giving a negative contribution.
An experimental study of Baldock et al. (2010) shows that the presence of wave groups and the accompanying bound long waves generally reduces onshore transport during accretive conditions and increases offshore transport under erosive conditions.

2.5 Cross-shore morphodynamics

2.5.1 Equilibrium profile

It is often assumed that under controlled (e.g. laboratory) conditions, a beach profile exposed to a constant wave forcing will eventually reach a stable equilibrium profile. In nature the forcing (waves, water level) is far from constant and varies so rapidly (in the order of days) that a stable equilibrium profile is never reached. However, observations indicated that profile variations remain in an envelope that seems stable in time. This has introduced the idea of a dynamic equilibrium profile. One of the first coastal engineers to describe this equilibrium profile was Bruun (1954). He proposed an empirical equation (2.20) for the dynamic equilibrium profile that consists of a power law relating the water depth to the offshore distance:

$$h = A\left(x'\right)^{m} \tag{2.20}$$

$A =$ shape factor [$m^{1/3}$]
$x' =$ offshore distance [m]
$m =$ exponent equal to $2/3$
$h =$ water depth [m]

Dean (1977) supported the Bruun equation (2.20) on semi-empirical grounds. He reasoned that for a certain grain size, nature strives towards a uniform energy dissipation (2.21) per unit volume of water across the surf zone.

$$D = h\varepsilon\left(D_{50}\right) \tag{2.21}$$

$D =$ Dissipation [$Jm^{-2}s^{-1}$]
$\varepsilon\left(D_{50}\right) =$ Loss in wave power

Based on monochromatic waves and a constant breaker index across the surf zone, Dean derived the magnitude of the exponent m as 2/3 in agreement with Bruun's suggestion. Furthermore, he also found an expression for the dimensional shape factor:

$$A = \left(\frac{24\varepsilon(D_{50})}{5\rho_w g^{3/2}\gamma^2} \right)^{2/3} \tag{2.22}$$

$\gamma =$ Wave breaking parameter [-]

In this expression the dissipation rate depends on the particle diameter, and therefore in this approach the shape factor is some function of the particle size. The shape parameter A can be empirically related to the median grain size, showing that a coarser grain size implies a larger value of A and thus a steeper cross-shore profile. This relation can be transformed to a relation that uses the fall velocity as a parameter (Dean, 1987):

$$A = 0.5 w_s^{0.44} \tag{2.23}$$

$w_s =$ fall velocity [ms^{-1}]

If this result is accurate and applicable for all natural beaches, predictions on the equilibrium profile after for instance nourishing with sediment with a different grain size than the native sediment can be made.

2.5.2 Beach states

On the timescale of wave events, highly dynamic variations of the upper shoreface profile and plan form may be observed. Several classifications on the various morphodynamic regimes are found in literature. Wright & Short (1984) distinguished a series of six beach states ranked from the highest (dissipative) to the lowest (reflective) energetic state. In between the ends there are four intermediate beach states. These beach states are based on the dimensionless fall velocity Ω (eq):

$$\Omega = \frac{H_b}{w_s T} \tag{2.24}$$

Intermediate beach states show strong three-dimensional behaviour, showing longshore variation in the bar pattern, while the reflective and dissipative states are relatively two-dimensional. Because they are approximately two-dimensional, these beach states can be described by their cross-shore profile, often referred to as ‘summer’ and ‘winter’ beaches.

Reflective beaches are characterized by a relatively steep and narrow beach face with a berm and surf zone without bars. Typically a value smaller of $\Omega < 1$ is found for reflective beaches. Surging breakers and small wave heights are common, and the sandy material is relatively coarse. Reflective beaches are a result of a period of mild wave conditions that transport sediment onshore. The morphodynamic behaviour of this type of beach is less dynamic than beaches exposed to a storm wave climate.

Dissipative beaches are characterized by a wide and flat sandy coastal zone with one or more linear bars and dunes backing a wide beach. Typically a value of $\Omega > 6$ is found for dissipative beaches. Spilling breakers are common for this type of beach; this beach type is the result of high energy waves that start breaking far offshore. The high energy and short waves are typical for a storm wave climate, and result in a very dynamic coastal profile.

The beach state at a location is not invariable: under different forcings, beaches can move through a series of beach states. Mild wave conditions slowly force a beach towards a reflective state through onshore sediment transport, while storm waves are responsible for fast offshore movement of sediment resulting in a dissipative state.

2.5.3 Bar behaviour

In section 2.5.2 beach states have been classified, ranked form reflective to dissipative. A feature of dissipative beaches is that they often have one or more linear bars. Smit et al. (2010) concluded that sand bar response is mainly determined by hydrodynamic conditions.

Under high energetic wave conditions there is a strong undertow in the surf zone, capable of transporting large amounts of sand offshore. The transport capacity reduces further offshore, and the sediment settles approximately at the end of the surf zone, where the offshore transport changes to onshore transport (Fredsøe & Deigaard, 1992). This profile is more efficient in dissipating energy associated with the incoming waves, reducing the offshore transport rates.

Under lower energetic wave conditions, bars may move a little back onshore. This onshore movement can be related to wave-asymmetry (section 2.3 & 2.4). Smaller waves do not break on the bar, but develop pitched-forward shapes. Under the steep front face of the waves, water is accelerated rapidly while under the gently sloping rear faces it is decelerated slowly. This leads to erosion offshore of the bar crest and deposition onshore of the bar crest and thus onshore bar migration.

Short term observations (2 months) of Gallagher et al. (1998) at Duck, North Carolina, show an offshore moving bar, primarily under high energy wave conditions. Relatively slow onshore bar migration is observed under small waves.

Longer term observations (2 years) of Lippmann & Holman (1990) at Duck, North Carolina show continuous transitions up- or down-state when considering beach states as described by Wright and Short (1984) or the adapted system as proposed by Lippman and Holman (1990). Depending on the wave conditions bars migrate onshore or offshore, further supporting the statement of Smit et al. 2010 that bar formation and migration is a direct result of the wave forcing.

Simulations of Gallagher et al. (1998) show that integrated over a long time, onshore and offshore migration balance each other on a beach that is not losing or gaining sand.

2.6 Sorting processes

Sediment sorting is dependent on sediment characteristics like size, shape and density as well as the hydrodynamic conditions. It is a combination of both that determines the transport and sorting in the profile. Slingerland & Smith (1986) described four hydraulic sorting mechanisms: suspension sorting, entrainment sorting, transport sorting and shear sorting. The first mechanism operates during deposition, the second during erosion and the other two during transportation.

Suspension sorting involves the separation of heavy from light minerals according to their settling velocities. Settling velocity depends on grain size, density, and shape of the grain and the nature of the fluid turbulence. When sediments are in suspension, particles with the largest settling velocity are deposited first and particles with smallest settling velocity are deposited last. In this thesis density and shape variations of grains are taken out of consideration, making the suspension sorting a function of sediment size only.

Entrainment sorting involves separation of light and heavy minerals according to their relative grain entrainment thresholds, usually expressed in terms of a critical bed shear stress (Komar & Wang, 1984). The critical stress is usually a function of size, density and shape of the sediment. Assuming a heterogeneous bed, particles with a critical entrainment stress lower than the flow induced shear stress are transported away, leaving behind particles that have a critical entrainment stress higher than the flow stress.

Transport sorting involves the separation of light and heavy minerals according to their relative grain transport velocities. In this mechanism, implicitly the effect of entrainment is incorporated, since particles that are quickly entrained are transported in a shorter time than

particles that are not so easily entrained. The transport velocity of a grain depends on size, density and shape, bed configuration and flow velocity (Steidtmann, 1982). Again, taking density and shape variations out of the equation, this implies that smaller sediments are transported further by the flow, making this process mainly a horizontal sorting mechanism.
Shear sorting involves the separation of light and heavy mineral grains according to their relative response to dispersive pressure. Coarser grains tend to move upwards in the vertical direction to regions of lower shear while finer grains sink to the base of the layer (Bagnold, 1954).

2.7 Observations of sediment sorting in nature

2.7.1 Spatial variability

On natural beaches, grain sizes are far from uniform. For example, a monitoring campaign carried out by Rijkswaterstaat in 1988 mapping the sediment grain size along the Dutch coast, showed that at the southern part of the coast median grain size is larger at the mean high water line than at the mean low water line (Van Bemmelen, 1988).
In the most general form, an inverse depth dependency applies to the cross-shore grain size distribution. A fining trend is observed by several researchers; coarser grains are found at the shore break with finer material both offshore and onshore of the shore break (e.g. Reniers et al., 2013; Stauble, 2005; Van Rijn, 1998). Although not present at every beach, the shore break is characterized by a sudden increase in steepness of the bottom profile at the offshore edge of the swash zone. Violent wave action leads to an accumulation of coarse material at the shore break. Offshore fining can be explained by different suspension time of coarse and fine material. Coarser material is shorter in suspension due to higher fall velocity and is thus transported over a shorter distance offshore. Finer material is moved further offshore as it lingers in the water column. Experiments conducted by Wang et al. (1998) showed that in general the finest material can be found just landward of the crest of the breaker bar, where the wave energy is lowest.
Observations from Antia (1993) at the Shoreface of Spiekeroog (one of the southern North Sea barrier islands along the Dutch and German coast) showed that the coarsest sands tend to occur in the throughs of bars, especially in the case of the outer ridge. Finer sediments are found at the top of the bar.

2.7.2 Temporal variability

Sorting of sediments occurs on time scales as small as half a wave cycle in the swash zone, where every wave stirs the top layer and changes the composition (Clifton, 1969). At larger time scales one can think of seasonal variation of the grain size pattern (summer-winter behaviour). Storms can influence the shape and location of the beach profile and redistribute the sediments in cross-shore direction.
Observations at ‘El Puntal’ Spit (Medina et al., 1994) showed a strong temporal variation, as important as the spatial variations. In particular the berm recovery is achieved firstly with the fine material from the bar, thus supporting the notion that each sediment size responds to the same hydrodynamics differently.
Medina et al. (1994) also showed that the variability of sediment sorting in time is dependent on the variation of the morphology. Where the morphological changes are highest in the profile, so is the variability of sediment characteristics.

2.8 Nourishments

A nourishment is an artificial supply of sediment on a beach or shoreface to compensate for erosion. Nourishments are often called 'soft' solutions, since the supplied sediment replaces the eroded sediment temporarily; it is no structural solution that stops the erosion process as opposed to 'hard' measures (e.g. groins, breakwaters).

The sediment used to construct nourishments is usually dredged offshore, at such a distance from the coastline that the water depth is larger than 20 meter. Taking away sand from these locations does not influence the protection of the coast since they lie outside of the active part of the profile. The sediment size and grading of the material used for nourishing depends on the offshore conditions at the dredging location. The grain size of the sediment is ideally the same size or slightly coarser than the native material, since it is more likely that use of this material will lead to a more stable situation (Dean, 2002).

2.8.1 Development of nourishments

Nourishments can be applied at several locations in the cross-shore profile, viz. at the beach or at the shoreface. In case of beach nourishments, sand is placed between the low water line and dune-foot level. After a certain amount of time, the sediment will be evenly distributed in the cross-shore profile following the equilibrium rules dictated by wave height and sediment grain size. This means that immediately after constructing a beach nourishment, large quantities of sediment will disappear under the water line; this is not erosion but merely a re-distribution of the nourished sediment.

Observations of Vousdoukas et al. (2014) show the development of a beach nourishment in a wave flume when it is subjected to two different wave heights. They found that for lower waves changes were minimal in the surfzone and mainly taking place along the beach-face, with most of the artificial berm material being distributed in the swash zone of the profile. Higher waves show a continuation of beach-face straightening until the artificial berm was very small. However, for the higher waves a significant amount of the material was transported from the beach-face to the nearshore bars. Several field studies show the same trend in the development of beach nourishments and their effect on mitigating erosion (e.g. Benedet et al., 2004; Dette et al., 2002; Eitner & Ragutzki, 1994).

A study by van Rijn et al. (2011) shows that the lifetime of a nourishment is dependent on the grain size of the fill material. Relatively coarse material shows a significantly longer lifetime than fill material of a finer grain size.

Shoreface nourishments are generally located around the breaker bar. They have proven to be an effective measure to mitigate erosion in the upper shoreface (e.g. Hamm et al., 2002), although relatively large volumes are required since only part of the nourishment volume reaches the upper shoreface. However, since the construction cost of shoreface nourishments per m^3 is much smaller than the construction cost of beach nourishments, generally much larger volumes are added to the system with shoreface nourishments. Located around the breaker bar, shoreface nourishments of large volume often behave as a submerged breakwater, reducing the wave climate in the lee side of the nourishment. This reduced wave action is also contributing to the mitigation of upper shoreface erosion. This effect diminishes over time as the sand used for the nourishment is distributed through the profile.

Experiments performed by Walstra et al. (2011) show the development of two different shoreface nourishment designs: a design located seawards of the breaker bar and a design higher in the profile. For lower waves nourished sand is transported landward and a bar developed for the low nourishment design, the high nourishment design was more or less stable. The upper part of the profile was still eroding for both nourishment designs. For higher

waves the low nourishment design showed a similar response as for the lower waves, while the high nourishment showed a clear offshore migration. The nourishment designs reduced erosion mainly by acting as a submerged breakwater.
The mitigation of erosion processes by shoreface nourishments through acting as a submerged breakwater is also observed in the field. Hoekstra et al. (1996) studied the Terschelling shoreface nourishment for a period of about 2.5 years and concluded that the nourishment only partly acts as a feeder berm and the actual success of the nourishment is also based on its breaker berm function.
Van Duin et al. (2004) found that the shoreface nourishment in Egmond positively contributed to the development of bars, leading to an increase in bar height and moving them onshore. This increased bar height then partly acted as a submerged breakwater. In this case, the shoreface nourishment acted as a feeder for the bars, and very little sand actually reached the beach area.

2.8.2 Observations of sediment sorting at the development of nourishments

Eitner & Ragutzki (1994) investigated the development of a beach nourishment at the Island of Norderney in the southern North Sea, where the beach was partly refilled with well sorted fine sands. The fill material used for this nourishment was finer than the native sands. Despite a selective erosion of finer sediment particles and the relative enrichment of coarser grains, the grain size spectrum as it was before the replenishment was observed after two years. In time, the natural grain size distribution which is in equilibrium with the hydrodynamic forces is reproduced by erosion of the beach material.
Observations at Delray Beach, Florida East Coast and at Longboat Key, Florida West Coast by Benedet et al. (2004) show the cross-shore grain size variability during and after nourishing the beachface. They found coarser sediments on the beach face and finer sands in the submerged section of the active profile. This trend is maintained through several years, and at Longboat Key a coarsening of beach sediments is observed over time.
At Hoek van Holland, the Netherlands a mega nourishment (the Sand Motor) was built in 2011 with an average grain size that is significantly coarser than the native sands. Results from a measurement campaign show that the sediment composition has become more sorted in time and a coarsening of the sediment occurs in the cross-shore direction (Sirks, 2013).

Guillén & Hoekstra (1996) investigated sediment sorting at the shoreface nourishment at Terschelling. They found that shortly after construction, the nourishment caused a significant coarsening of the sediment in the nourished area. On a longer time scale, the new sediments have dispersed over and mixed with the original sediments and the effects of the discharged sands are no longer recognizable.
In the experimental study performed by Walstra et al. (2011) analysis of the bed samples taken at different positions along the flume showed that on top of the breaker bar a slightly more coarse grain size is present compared to the grain size adjacent to the breaker bar. Long term effect is not investigated in this study, although it is hypothesized that over a longer time the sediments will have restored to the original distribution.

Part II – Hannover Flume Model

3 Physical model

In 2014 physical experiments were carried out by Michalis Vousdoukas (Joint Research Centre, European Union) to assess nearshore and beach hydro-morphodynamics and the effects of sorting. This data-set is used to analyse sorting phenomena in the nearshore area and to calibrate a numerical model (section 5.1).
The dataset was acquired in the framework of the WISE-project. The aim of WISE (Water Interface Sediment Experiment) was to observe water and sediment flow and the associated bed-dynamics and particle features as well as scaling effects. To accomplish this experiments have been carried out in Hannover and Barcelona. The data used in this thesis was collected at the wave flume in Hannover, the Großer WellenKanal (GWK).
The data-set used in this thesis is unique, since it contains information not only on hydrodynamics and bed level change but also on grain size parameters along the flume. In this way sorting processes in the nearshore area can be studied in great detail.
In this chapter the physical experiments are described and analysed. First the experimental set-up is discussed in Section 3.1. A description of the experiments used to investigate sorting processes is given in Section 3.1.3. Finally, the results of these experiments are discussed in Section 3.2.

3.1 Experimental set-up

3.1.1 Facility

The Large Wave Channel GWK of the Coastal Research Centre FZK has a total length of 307 m, a width of 5 m and a depth of 7 m, with a maximal water depth of 5 m to still allow wave generation (Figure 3.1). Waves are generated by an hydraulically driven wave generator, which is computer controlled and enables absorption of reflected waves at the wave paddle to provide same wave conditions during long tests.

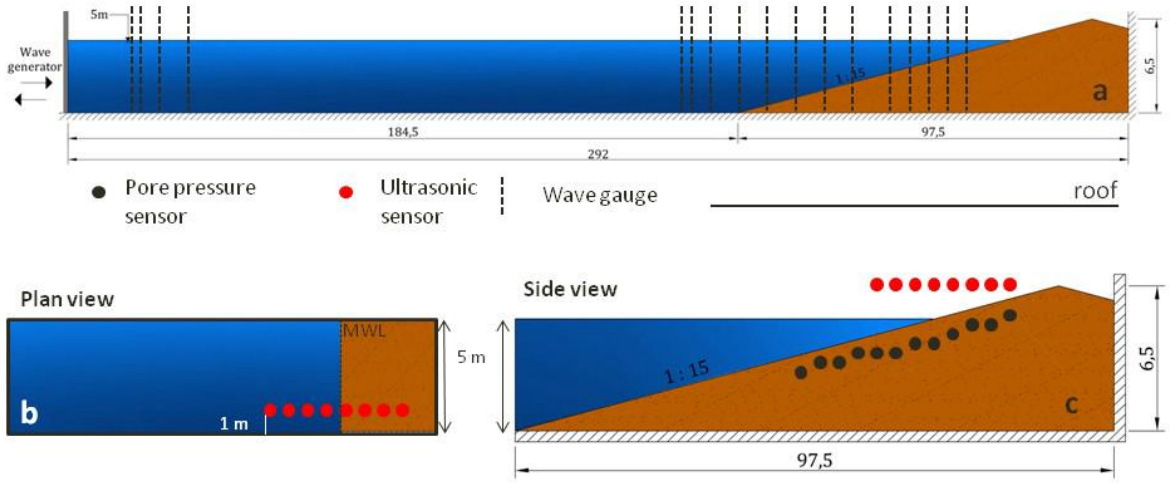

Figure 3.1 – Schematic overview of the GWK in Hannover. Taken from Deliverable D8.3, WISE Data set, by Ivan Caceres

All wave time series have been generated using 1st order approximation and follow the JONSWAP spectrum with gamma 3.3. As mentioned, one of the aims of WISE was to

investigate scaling processes. Therefore experiments were conducted in Barcelona and Hannover. Due to different wave paddles in Barcelona and Hannover, and different generation software driving the wave paddle it was decided to avoid second order generation and active absorption. After the generation of each time series the wave paddle stops for a lapse of 10 minutes, after which the next wave time series is started.
The experiments started with a constant bed slope of 1:15 (Figure 3.2). The sand used to create the beach profile in the GWK is non-sieved natural sand. The properties of the sediment are determined at the initiation of the experiment. To obtain an average measure of the grain size and sorting parameters, initially 12 samples were taken at different locations along the flume (Figure 3.2) to determine the sediment characteristics.
Measurements on bed level and sediment sampling were performed before and after the tests. At each location one sample is taken from the surface (2-3 cm depth) with a size of a tennis ball. Under the assumption of transversal uniformity one sample per cross-shore direction is taken and seen as representative for that longitudinal location.
The sand is classified as fine sand that is moderately sorted with d_{50} = 300 µm, a sorting parameter of approximately 1.8 (moderately sorted) and an initial skewness of -0.05 (near-symmetrical). Sorting and skewness are defined according to equations 2.2 and 2.3 respectively (section 2.1.2).

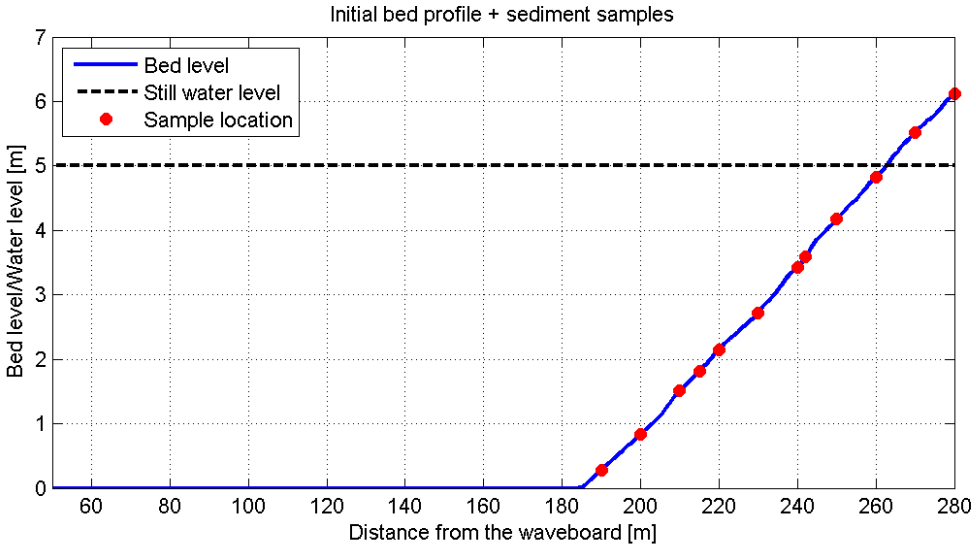

Figure 3.2 - Sample locations for determining the initial sediment distribution along the flume.

3.1.2 Measuring equipment

The bed profiling was performed with a mechanical bed profiler attached at a measuring carriage. The profiler is computer controlled and the accuracy of the system is approximately 10 mm, caused by compression of sand due to the dead weight of the sensor arm.
Surface elevations were measured electronically by wire type gauges located at different cross-shore position (Table 3.1). The wire type wave gauge is based on the 'resistance-capacity measurement' principle. The voltage in the wire changes proportional to the immersed depth of measuring wire in the water column. The accuracy of the wave gauge measurements is approximately 5 mm.
In the swash zone several ultrasonic sensors and pore pressure sensors are deployed to continuously monitor swash zone water surface elevation, swash flow velocity and morphological changes after each wave. The wave height data gathered by the ultrasonic

sensors is not used for calibrating or validating the model since the reliability of these measurements turned out to be questionable after close examination.

Table 3.1 – Positioning of wave gauges along the flume. (Deliverable D8.3, WISE Data set, by Ivan Caceres)

Device	Distance from the waveboard [m]
WG01	50.00
WG02	51.90
WG03	55.20
WG04	60.00
WG05	160.00
WG06	161.90
WG07	165.20
WG08	170.00
WG09	190.00
WG10	200.00
WG11	210.00
WG12	219.60
WG13	230.00
WG14	235.00
WG15	240.00
WG16	245.00
WG17	250.00

3.1.3 Experiments

A total number of 15 tests using different wave conditions were performed in the GWK (Appendix 0). In this thesis three test cases are used, which are described in Table 3.2. These three cases are chosen because they represent a large range of wave conditions as well as an initially uniform and non-uniform bed. The classification of the test cases in this table will be used throughout the rest of this thesis. These cases are seen as representative and suitable for calibrating and validating the model. With the chosen cases three different wave conditions are chosen: an erosive condition (case 1), a mildly accretive condition (case 2) and an accretive condition (case 3).

Table 3.2 – Summary of the experiments used is this thesis.

Test case	Test nature	H_s [m]	T_p [s]	Duration [hrs]	Dean number [-]
1	Erosive	0.9	5.1	4.25	4.83
2	Mildly accretive	0.6	6.3	9.00	3.00
3	Accretive	0.4	10.0	7.50	1.16

In each test data is collected on wave heights, bed level, and sediment statistics along the flume. The wave heights (H_s) and peak periods (T_p) mentioned in Table 3.2 are the desired wave heights to be generated by the wave board; the measured wave heights are slightly different than the desired wave heights.
The duration mentioned in the last column is the total effective time waves are active in the flume; for each test several wave sequences are run. Measurements on bed level and sediment sorting were performed before the start of the wave sequences and after all wave

sequences were completed. All initial and final bed levels and bed compositions are treated in section 3.2.

3.2 Data analysis

In this section the data obtained in the chosen test cases is analysed. An assessment on sorting processes and their influence on the morphological development is made by analysing the data on waves, bed level change and sediment statistics. This analysis is performed for case 1 (section 3.2.1), case 2 (section 3.2.2) and case 3 (section 3.2.3).

3.2.1 Case 1 – Erosive conditions (H_s = 0.82 m & T_p = 5.1 s)

3.2.1.1 Wave data analysis

The water level data from the wave gauges is converted from a time series to a wave-spectrum. The swash-zone measurements were recorded using ultrasonic sensors. For case 1 and 2 this data is displayed, however, it was found that for lower wave heights the observed values were extremely noisy and did not correspond to theory. The waves are split into their long-wave and short-wave components to check if long waves play a significant role in the wave flume since this will have a large impact on the modelling methodology (section 4.3).

The splitting of waves into their long-wave and short-wave components is performed by assuming that above a certain frequency the waves are seen as short waves, and below that frequency the waves are interpreted as long waves. This split-frequency is half the peak frequency; the peak frequency is defined as the frequency at which the wave energy is largest. For case 1 this means a peak frequency of 0.2 Hz and thus a split frequency of 0.1 Hz.

In Figure 3.3 the propagation of the spectrum along the wave flume is depicted. In the upper panel the spectra through the flume are plotted along with the short wave peak energy propagation and the split frequency. There is a little contribution from long waves visible in the spectra, and this contribution increases in the surfzone. This is also visible in the second panel of the figure, where the relative energy through the flume is plotted (E/E_{max}). In this formulation E_{max} is the local maximum, thus the highest energy found at a location in the flume. In this way, a shift from short wave energy dominance to long wave energy dominance is made visible in the figure. In the third panel the energy is translated to wave heights through (3.1):

$$H_{m0} = 4 \cdot \sqrt{m_0} \tag{3.1}$$

$$m_0 = \int_0^\infty E(f)\,df \tag{3.2}$$

H_{m0} = Significant wave height computed from the zero-moment of the spectrum

m_0 = Zero-moment of the wave spectrum

$E(f)$ = Energy-density spectrum

This method applies to both long and short waves, but instead of taking the complete energy function only the part below or above the split frequency is taken into account to compute the wave height. It is observed that the long wave influence is seen throughout the entire flume; in the deeper part the wave height of the long waves is approximately 10% of the wave height of the short waves. In the shoaling zone this increases to about 30-40%.

From this figure it becomes apparent that short wave contribution is the most important in the flume, but long waves are also relevant. This suggests it is important to consider the effect of bound long waves on group scale in the sediment transport computation in the numerical modelling work.

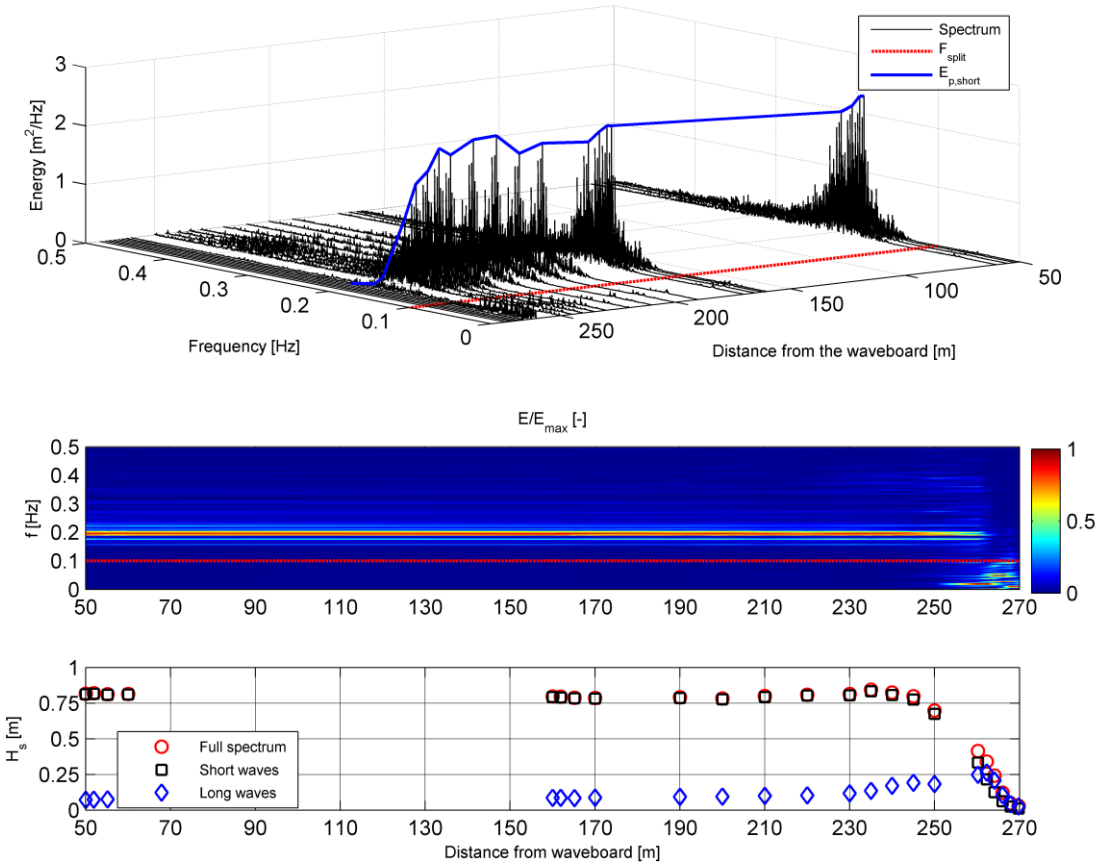

Figure 3.3 – Wave transformation through the flume. Upper panel shows the transformation of wave spectra through the flume. Note that the x-axis is reversed to emphasize the nearshore spectra. The middle panel depicts the relative energy through the flume and the lower panel translates the spectra to wave heights (long and short).

3.2.1.2 *Morphology and sorting phenomena*

In Figure 3.4 the initial and final bed profile are depicted, along with the initial and final D_{50}, standard deviation (σ_G) and skewness (Sk) calculated from the sieve distributions. Samples for sieving are taken at the beginning and at the end of each case (after all wave sequences).
A clear response of the bed to the wave conditions is visible. Erosion is observed in the upper-shoreface (x = 255-270 m) and this sand is deposited further offshore forming a bar. Besides the very clear primary bar (x = 245 m) also a trough (x = 248 m) and a smaller secondary bar (x = 250 m) can be observed in the newly formed profile.
Looking at the upper-shoreface (x = 255 to x = 270 m) no change in D_{50} is observed in the profile. The standard deviation also does not change in that area indicating that there is erosion of all the grain sizes in this part, so the erosion is not limited to only finer sediments. The wave action is strong enough in this area to transport the full range of grain sizes. A coarsening of the D50 is observed in the area from the bar crest until the onshore boundary

of the secondary bar (x = 245-252 m). No change in standard deviation is observed in this location, thus indicating that coarse sediments settle in this area while finer sediments are still eroded away leading to a shift of the sediment curve. Offshore from the bar crest fining of the sediments is observed indicating that finer sediments are settling due to loss of transport capacity of the undertow. The drop in D_{50} is paired with an increase in standard deviation which implies a less sorted sediment sample. The sediment distribution gets wider, and thus the sand gets more graded. Also an increase in skewness is observed offshore of the breaker bar. The increase in skewness can be interpreted as a shift from a nearly symmetrical sample to a fine-skewed sample due to the large amounts of fine sediment settling.
Thus, in the upper shoreface sediments are eroded uniformly; the full range of grain sizes is transported by the flow. Coarser sediments settle first when the flow loses transporting capacity leading to a coarsening of the profile in the inner bar area. Finer sediments do not settle in the inner bar area and are still being eroded away; they are transported more offshore and settle later leading to a strong fining of the sand offshore of the bar crest.

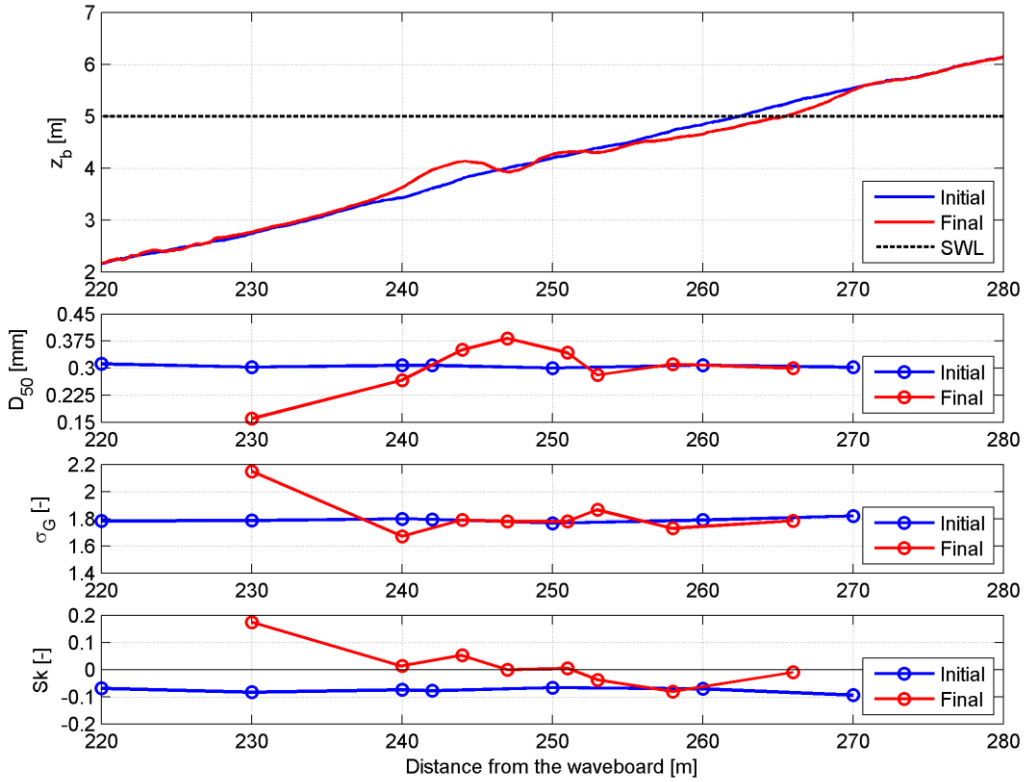

Figure 3.4 – Morphology and sediment statistics measured at the first case of the experiment. Upper panel shows morphology, second panel median grain size (D_{50}), third panel the standard deviation (σ_G) and the fourth panel shows the skewness (Sk).

3.2.2 Case 2 – Mildly accretive conditions (H_s = 0.62 m & T_p = 6.3 s)

3.2.2.1 Wave data analysis

The wave data analysis is performed using the methodology explained in section 3.2.1.1. In Figure 3.5 the propagation of the spectrum through the flume is depicted. For the experiments in case 2 the peak frequency is 0.16 Hz and the split frequency is 0.08 Hz.
Again, a small long wave contribution is visible in the flume, increasing in the surfzone. This is also seen in the second and third panel of the figure, so for the milder wave conditions again long waves prove to be significant making it indispensable to include long waves in the modelling approach.

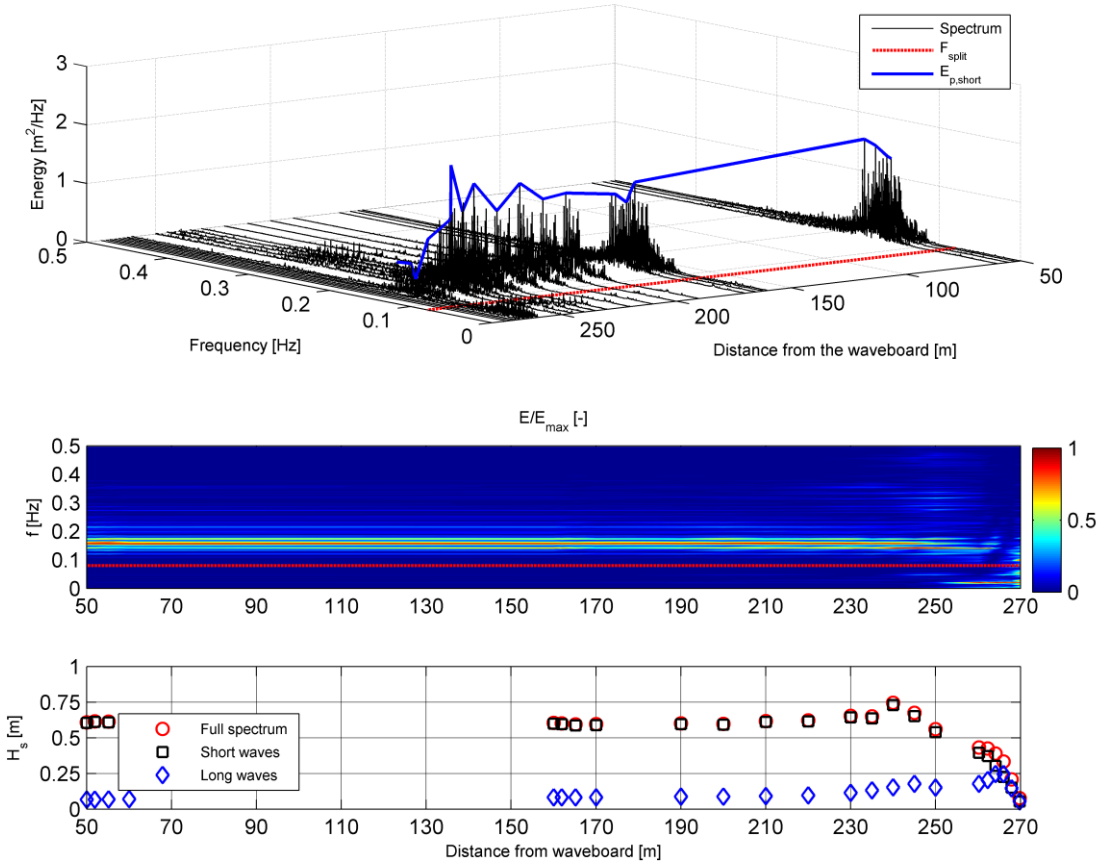

Figure 3.5 - Wave transformation through the flume. Upper panel shows the transformation of wave spectra through the flume. Note that the x-axis is reversed to emphasize the nearshore spectra. The middle panel depicts the relative energy through the flume and the lower panel translates the spectra to wave heights (long and short).

3.2.2.2 Morphology and sorting phenomena

Figure 3.6 shows initial and final bed profile, as well as the initial and final D_{50}, standard deviation (σ_G) and skewness (Sk) for the second case of the experiment. This experiment was performed right after the first case of the experiment, making the initial bottom configuration of case 2 the final bottom configuration of case 1. A continuation of upper shoreface erosion is observed under the lower wave conditions. The eroded sands are deposited around the bar area, where specifically a growth and offshore movement of the

secondary bar is found; the crest of the primary bar stays in approximately the same place and at the offshore side of the bar deposition of sand is found. Under less energetic wave conditions not the full range of grain sizes are eroded away since a coarsening of the sand is observed between x = 250 m and x = 265 m. Besides the reduced entrainment of the coarsest particles, also earlier settling of the coarsest particles that are eroded away plays a role at the observed coarsening.

In the bar trough area the standard deviation increases (indicating a wider distribution) which can be explained by earlier settling of finer sediments in this area compared to case 1. In case 1 it was deduced that a settling of coarse sediments in combination with a continued erosion of finer sediments led to the coarsening in this area. With lower wave heights the flow loses its transport capacity earlier leading to settling of finer sediments in this area compared to case 1 thus leading to the slight fining around x = 248 m and the wider distribution. The decrease in standard deviation more offshore is explained in the same way: the sorting increases due to more fine sediments settling in this area, leaving a top layer of fine sediment above the original sand. In case 1, this layer was not yet large enough to completely cover the original sand, leading to the poorly sorted sample. More fines settle in case 2, leading to a better sorted fine sediment distribution at the offshore location. This is supported by the skewness restoring to a more or less symmetrical value.

At the upper most part of the upper-shoreface a slight fining is observed. This is possibly explained by swash motions; a small berm is found around x = 272 m. Although no sediment sample is taken at this location, according to literature a shore-break like this consists of coarse sand, while directly offshore of the berm fine sands are found, which is the case at x = 270 m.

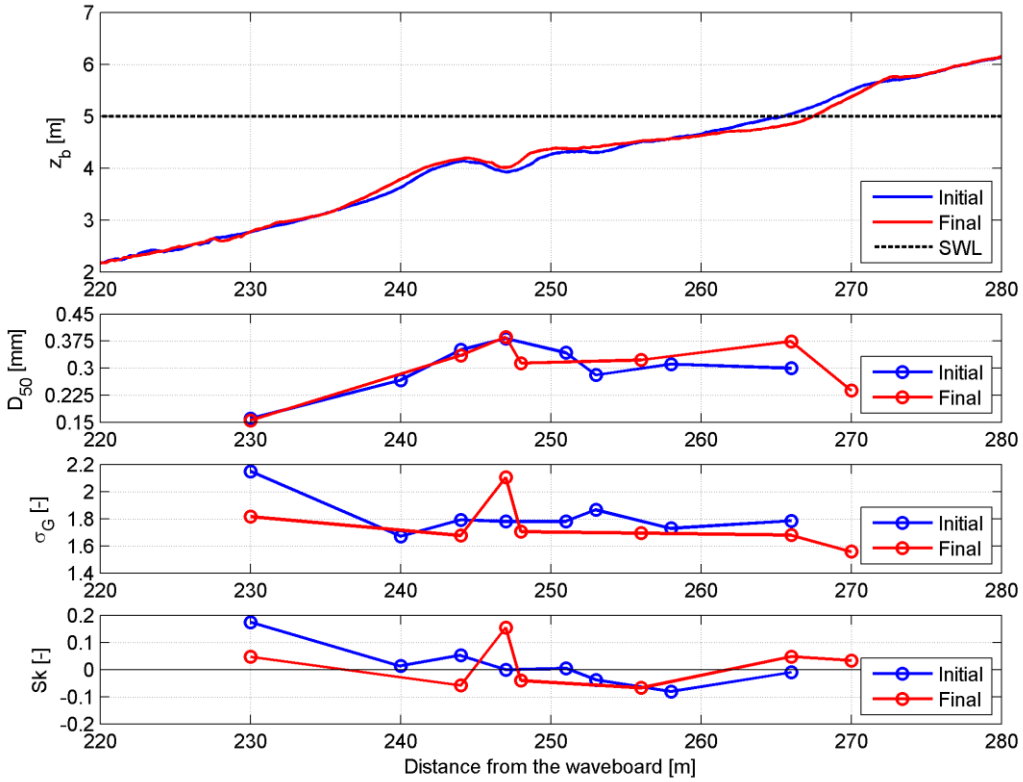

Figure 3.6 - Morphology and sediment statistics measured at the second case of the experiment. Upper panel shows morphology, second panel median grain size (D_{50}), third panel the standard deviation (σ_G) and the fourth panel shows the skewness (Sk).

3.2.3 Case 3 – Accretive conditions (H_s = 0.4 m & T_p = 10 s)

3.2.3.1 Wave data analysis

As mentioned before, the swash zone measurements are not displayed in this figure. For lower wave conditions, the location were long waves become important is located further inside the surfzone at shallower water, where no wave gauges were available. Therefore long wave contribution may not be as evident as in cases 1 and 2, as can be seen in Figure 3.7. For case 3 the peak frequency is 0.1 Hz and the split frequency is 0.05 Hz. Long waves throughout the flume are approximately 5% of the short-wave wave height. Although not as obvious as the previous case, long waves are still important in the flume.

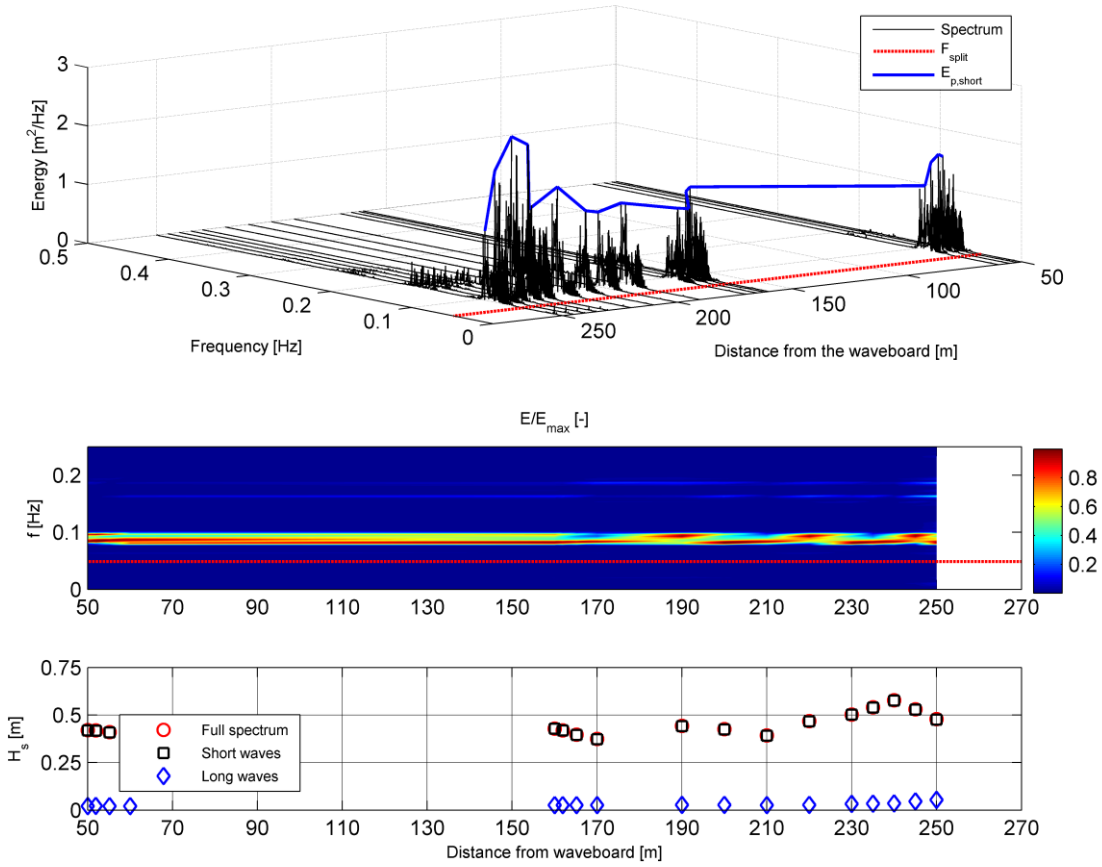

Figure 3.7 - Wave transformation through the flume. Upper panel shows the transformation of wave spectra through the flume. Note that the x-axis is reversed to emphasize the nearshore spectra. The middle panel depicts the relative energy through the flume and the lower panel translates the spectra to wave heights (long and short).

3.2.3.2 *Morphology and sorting phenomena*

Figure 3.8 shows initial and final bed profile, as well as the initial and final D_{50}, standard deviation (σ_G) and skewness (Sk) for the third case of the experiment. The wave conditions of this experiment are classified as accretive; sediment is eroded from the secondary bar and deposited higher in the profile. Between x = 260 and x = 265 m also erosion is observed, and accretion is found from x = 265 m to x = 275 m. A coarsening is found at the still-water line, onshore and offshore from this location a fining is observed. The coarsening around the still-water line is a result of swash motions; the onshore fining is caused by incidental high run-up that possesses enough power to transport finer sediments onshore. The fining offshore of the still water-line is a related to transport of finer sediments by less energetic offshore movement of the water, entraining only finer sediment around x = 267 m. The fining further offshore is caused by onshore movement of sediments that are eroded from the secondary breaker bar that settle between x = 248 m and x = 258 m. The fining offshore of the breaker bar shows that there are still fine sediments transported offshore by the undertow.

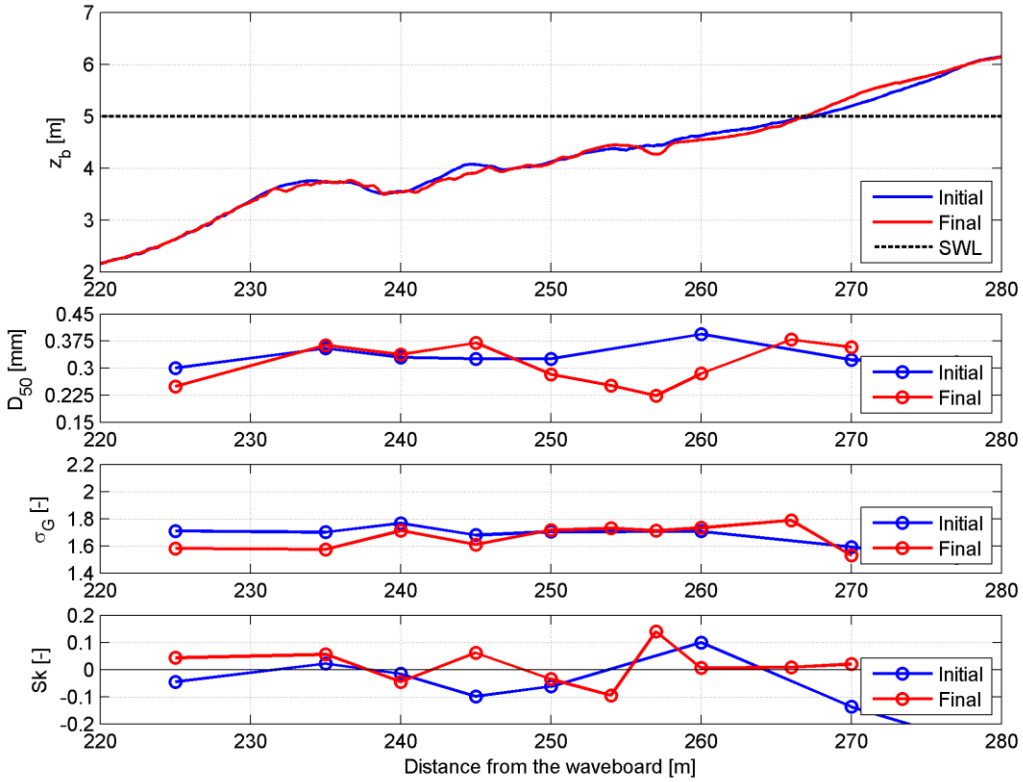

Figure 3.8 - Morphology and sediment statistics measured at the third case of the experiment. Upper panel shows morphology, second panel median grain size (D_{50}), third panel the standard deviation (σ_G) and the fourth panel shows the skewness (Sk).

3.3 Summary

Experiments were performed in the GWK at Hannover. Three cases are chosen as representative: one with erosive conditions, one with mildly-accretive conditions and one with accretive conditions.

Analysis of the wave gauge data shows that there is a significant contribution of long waves in the flume. This has large consequences for the modelling choice, as will be discussed in chapter 4.

By investigating the morphology and sediment samples, sorting processes could be described during the morphological change of the profile. Based on these experiments it can not be concluded that sorting is crucial for the morphological development of the profile, but it can be stated that sorting is clearly observed during the experiments.

The sorting processes are highly dependent on the hydrodynamics. Under high energetic waves (case 1), no entrainment sorting is observed during the erosion of the sand of the upper part of the profile. A clear suspension and transport sorting is observed lower in the profile, since a coarsening is found around the bar area and a fining is found offshore of the breaker bar. Around the bar area, where the undertow is less strong it is hypothesized that the coarsening is due to a combination of suspension sorting (coarse grains settling) and entrainment sorting (finer sand is still entrained by the less energetic flow).

Under less energetic waves, entrainment sorting plays a larger role in the upper part of the profile, since now not all sands are uniformly eroded away leading to a coarsening of the sediment. Suspension and transport sorting again are observed in the lower part of the profile.

To conclude this section, it is stated that the results of these experiments are in agreement with the sorting processes (section 2.6) and observations (section 2.7) found in literature.

4 Numerical model

In this section the set-up of the numerical model is presented. The numerical model used in this research is Delft3D. Delft3D is a process based modelling suite that is designed to simulate 2D or 3D flow, sediment transport and morphology, waves, water quality and ecology and is capable of handling interactions between these processes, either with online or offline coupling. The Delft3D model is designed for situations where the horizontal length and time scales are significantly larger than the vertical length and time scales; e.g. shallow water areas like estuaries, coastal seas, lagoons, rivers and lakes. For a more detailed description of Delft3D see e.g. Lesser et al. (2004).

Before the different model methodologies are discussed, the general set-up of the model will be presented; this model will be referred to as the Hannover Flume Model (HFM). Then, the four different modelling methodologies are shown in section 4.2. A distinction is made on the wave model used (section 4.3), the number of sediment fractions used (section 4.4) and the bed model used (section 4.5).

4.1 Set-up of the Hannover Flume Model

A Delft3D model of the GWK-flume in Hannover has been set up. In line with the experiments, the interest is in the cross-shore direction. It is assumed that there is no variation perpendicular to the main direction of the flow, which is a valid assumption for the wave flume experiment. Further it is assumed that the vertical structure of the flow is highly important for correct predictions of sediment transport and sorting processes; therefore it is chosen to use a 2D-vertical model, with one dimension in the x-direction and one dimension in the z-direction.

The dimensions of the model reflect the dimensions of the GWK. The model has a width of 5 meter (one grid cell), and the total length of the model equals 280 meter. The size of the grid cells is variable along the x-direction since a high resolution is not necessary everywhere. Coarser grid cells are found at the offshore boundary of the model, while very fine grid cells are applied in the nearshore area. The size of the largest grid cell is 2.00 m and the size of smallest grid cell is 0.7344 m.

The vertical direction is described by twelve σ-layers, each representing a constant percentage of the total water depth. The layer distribution in the z-direction is such that there is a high resolution near the bottom as well as at the surface. Going from bottom to surface, the layer distribution is [2, 3.2, 5, 7.9, 12.4, 19.6, 19.6, 12.4, 7.9, 5, 3.2, 1.8] % of the depth.

The bathymetry used at the start of the simulation is taken from the measurements. Depending on which case of the experiment is simulated, the corresponding bathymetry that is measured at the start of that experiment is used. In the GWK the beach is situated at end of the flume. This means that there is no sand available in most of the flume, and only a beach profile at the end should be modelled. This is taken into account when setting up the bathymetry and the sediment availability of the HFM.

There is one open boundary used in the Delft3D model of the GWK. The open boundary is situated at the far left of the model domain (x = 0). The open boundary represents the wave board of the GWK; this means that at the boundary a wave condition is prescribed as explained in section 3.1.

In the HFM the k-ε turbulence closure model is used and for the roughness of the model domain the Van Rijn (2007a) roughness predictor is used, including ripple and mega-ripple contribution and ignoring dune roughness. For computing sediment transport the Van Rijn (2007a,b,c) formulations are used, with the vertical sediment mixing according to Van Rijn which overrules the k-ε model. A horizontal background eddy viscosity of 0.1 m^2/s is used and

a horizontal sediment diffusivity of 0.01 m^2/s is used. For the vertical background eddy viscosity a value of 1e-6 is used. An upwind approach is used to compute bedload transport at the velocity points instead of a central approach. Morphological updating is switched on after a simulation time of 12 minutes, to allow for spin-up of the waves. To reduce the overestimation of upper-shoreface erosion, not all erosion of a wet cell is assigned to the adjacent dry cell but an amount of 75%. The threshold depth for drying/flooding as well as the threshold depth of sediment transport computation is taken as 2.5 cm.

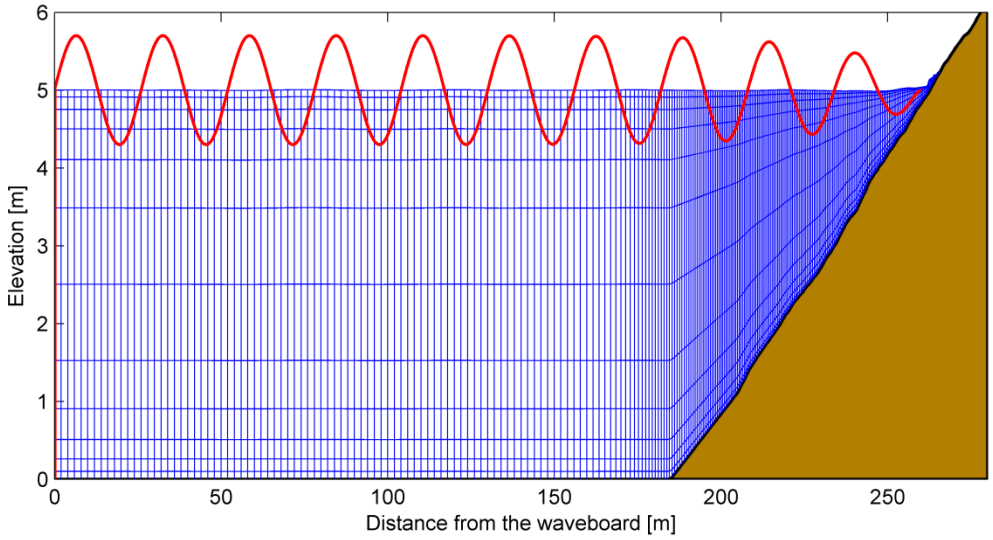

Figure 4.1 – Schematization of the Hannover flume model. In red, the left open boundary is denoted (x = 0 m), representing the wave board. The sand bottom starts at x = 180 meters.

4.2 Modelling methodologies

In this study several different models are used, leading to four different model methodologies (Table 4.1). The models are differentiated on three key-points:

1. Wave model
2. Number of sediment fractions
3. Bed model

For each key-point there are two options. For key-point 1, the wave model, the available options are the standard roller model with quasi-steady boundary (SRM, Stationary Roller Model) or the standard roller model with instationary boundary (ISRM, InStationary Roller Model). Both models will be elaborated on in section 4.3, the main difference is that the SRM does not model the effect of short wave groups on long waves while the ISRM does explicitly solve for this.
For key-point 2, the number of sediment fractions, the model can perform simulations using one sediment fraction or using multiple sediment fractions. This is elaborated in section 4.4.
For key-point 3, the bed model, the available options in Delft3D are a uniform, well-mixed bed (consisting of one single layer of sediment) or a layered bed stratigraphy. The layered-bed stratigraphy has two functions: on one hand it is a bookkeeping system, keeping track of eroded and deposited sediments and the change of sediment composition, while on the other

hand the change in sediment composition also affects the eroded volumes. This principle will be explained in more detail in section 4.5.
In this study, four combinations are considered. The first combination is a standard approach, as applied in present studies. In this combination the model uses the stationary roller model, with a single fraction and a uniform well-mixed bed. The second combination uses the instationary roller model, with a single fraction and a uniform well-mixed bed. The first two combinations are used to verify the performance of the wave models in simulating the morphology (e.g. bar dynamics).
The third combination uses the stationary roller model, with multiple sediment fractions and a layered-bed stratigraphy. The fourth combination uses the instationary roller model, with multiple sediment fractions and a layered-bed stratigraphy. The third and fourth combinations are used to investigate the consequences of using multiple fractions and a layered-bed stratigraphy on the morphology and to investigate the models capability of simulating sorting processes.

Table 4.1 – Summary of different models used in this study

Model combination	Abbreviation	Features
1 (Standard)	SRM	Stationary Roller 1 Sediment fraction Uniform well-mixed bed
2	ISRM	Instationary Roller 1 Sediment fraction Uniform well-mixed bed
3	SRMn	Stationary Roller n Sediment fractions Layered-bed stratigraphy
4	ISRMn	Instationary Roller n Sediment fractions Layered-bed stratigraphy

4.3 Wave model

As mentioned two different wave propagation models are used for calculating the wave hydrodynamics in the flume: the Stationary Roller Model (SRM) and the InStationary Roller Model (ISRM). This extension of Delft3D-FLOW does not model the individual waves but the forcing caused by short waves. In this section both the SRM and ISRM are described.

4.3.1 Stationary Roller Model

4.3.1.1 Equations

The equations provided in this section are given with one horizontal dimension. The stationary short wave energy balance now reads:

$$\frac{\partial}{\partial x}\left(Ec_g\right) = -D_w - D_f \tag{4.1}$$

E = short wave energy
c_g = group velocity
D_w = Wave energy dissipation due to breaking
D_f = Wave energy dissipation due to bottom friction

The wave energy dissipation by breaking is calculated with the expression of Baldock et al. (1998):

$$D_w = \frac{1}{4}\alpha_{rol}\rho_w g f_p \exp\left(-\frac{H_{\max}^2}{H_{rms}^2}\right)\left(H_{\max}^2 + H_{rms}^2\right) \quad (4.2)$$

α_{rol} = User defined constant
f_p = Peak frequency
$H_{\max}$ = Maximum wave height
H_{rms} = Root-mean-squared wave height

In this equation, α_{rol} is a user-defined constant of order 1. This constant influences the wave energy dissipation by breaking over the complete cross-shore profile, leading to lower waves for higher α_{rol}. This parameter is not used as a calibration parameter in this study.
In (4.2) the maximum wave height H_{max} is given by:

$$H_{\max} = \frac{0.88}{k}\tanh\left(\frac{\gamma_w}{0.88}kh_{ref}\right) \quad (4.3)$$

k = Wave number
γ_w = Wave breaking index
h_{ref} = Reference water depth

The wave breaking index γ_w is a user-defined parameter. For the SRM, this parameter can be set at a constant value, or a spatially varying value as defined by Roelvink (1993). The wave breaking index is an important parameter in the wave height prediction in the surfzone, because it imposes an upper limit on the wave height as a fraction of the local water depth.
In the right-hand side of (4.1) a second dissipation term is present: the wave dissipation due to bottom friction, D_f. This is defined as:

$$D_f = f_w \frac{\rho_w}{\sqrt{\pi}} u_{orb}^3 \quad (4.4)$$

f_w = Bottom friction factor
u_{orb} = Orbital velocity

The bottom friction factor f_w is a user defined constant. Wave energy dissipation by bottom friction is a second order effect in the surf zone; therefore this parameter mainly affects the wave dissipation more offshore.
The short wave energy dissipation is a source term in the stationary balance equation for the short wave roller energy E_r:

$$\frac{\partial}{\partial x}\left(2E_r c\right) = D_w - D_r \tag{4.5}$$

$$D_r = 2\beta_{rol} g \frac{E_r}{c} \tag{4.6}$$

$E_r =$ Wave roller energy

$c =$ Wave celerity

$D_r =$ Wave roller dissipation

$\beta_{rol} =$ Roller slope

The factor 2 in (4.5) results from additional dissipation of roller energy due to a net transfer of water from the wave to the roller (Svendsen, 1984). The slope of the wave front (β_{rol}) determines largely the rate of wave energy transferred to the roller and from the roller to the underlying water. It is a user-defined constant of order 0.1 determining the cross-shore distribution of the surface shear stress due to wave breaking. Therefore it is a significant parameter for calibrating water levels and currents (Giardino et al., 2011).
From the energy balance equations the energy distribution in the model is calculated. Subsequently, from the energy the vertically averaged radiation stresses are calculated:

$$S_{xx} = \left(2\frac{c_g}{c} - \frac{1}{2}\right)E + 2E_r \tag{4.7}$$

$$S_{xx} = S_{yx} = 0 \tag{4.8}$$

$S_{xx} =$ Radiation stress in the x-direction

Wave forcing is calculated from the radiation stress gradient minus the surface stress. The surface stress applied is the shear stress related to the roller motion. The roller motion delays the transfer of wave energy to the current in regions where dissipation takes place.

$$F_{w,x} = -\frac{\partial S_{xx}}{\partial x} - F_{x,r} = \frac{\partial S_{xx}}{\partial x} - \frac{D_r}{c} \tag{4.9}$$

In the SRM the breaker delay effect can be taken into account by the free parameter F_lam. Observations show that waves need a certain distance to actually start or stop breaking (Roelvink et al., 1995). When a wave reaches a water depth equal to the theoretical breaker depth, it takes a certain distance for the wave to complete the breaking process. This is accounted for by replacing the local water depth with a water depth weighted over a certain distance seaward of the breaking point. This distance is user-specified with F_lam, where F_lam is the amount of wave lengths it takes for the wave to break since reaching the theoretical breaking point.

4.3.1.2 *Model input*

To apply the roller model in stationary mode, the boundary conditions are generally taken over from the wave information or communications file since the main purpose of the surfbeat/roller extension is to include the roller equations that lead a shoreward shift of the wave set-up and the longshore and cross-shore flow. Very little extra information is needed, except some coefficients specified by the user.
In this model, the wave information is taken from a wavecon-file. This is either output from Delft3D-WAVE (SWAN) or a user-defined file. In this study, the Delft3D-WAVE module is not used; instead a user-defined wave boundary condition file is used. To have the FLOW-

module calculate the wave action with the surfbeat/roller extension, the roller model has to be switched on. For further details on implementing the roller extension in the FLOW-module the reader is referred to appendix B.1.

4.3.2 InStationary Roller Model

4.3.2.1 Equations

For the ISRM the short wave energy balance reads:

$$\frac{\partial E}{\partial t} + \frac{\partial}{\partial x}\left(E c_g\right) = -D_w \tag{4.10}$$

Note that there is no loss due to bottom friction in this equation; this option was not implemented in Delft3D for the ISRM at the time of this study. The wave roller energy balance equation now reads:

$$\frac{\partial E_r}{\partial t} - \frac{\partial}{\partial x}\left(2E_r c\right) = D_w - D_r \tag{4.11}$$

This leads to time varying radiation stresses and subsequently to a time varying wave force. This time varying wave force is the driving force behind the bound long wave, which is essentially a time varying set-up and set-down.

The ISRM differs from the SRM in the way the wave energy dissipation is calculated. Besides the absence of the bottom friction dissipation on the right-hand side of (4.10), the wave energy dissipation is calculated differently for the ISRM. Instead of the Baldock-formulation, the wave energy dissipation is computed according to the formulation of Roelvink (1993):

$$D_w = 2\alpha_{rol} f_p \left(1 - \exp\left(-\left(\frac{\sqrt{8E / \rho g}}{\gamma_w h_{ref}}\right)^n\right)\right) E \tag{4.12}$$

$n =$ Similarity constant [-]

4.3.2.2 Model input

To apply the roller model in instationary mode, a wave spectrum has to be prescribed on the boundary. For the model to work properly the open boundary must be of the Riemann-type, where the input for the boundary is calculated from the wave spectrum; a dummy boundary condition file must be present in the work directory. Besides this dummy-file, also a wave boundary condition file for the Delft3D roller model must be present in the working directory. The wave spectrum that is used to calculate the instationary boundary conditions has to be given in a file specified in the mdf-file. For further details on the boundary conditions, the reader is referred to the Delft3D manual, section B15.3 (Deltares, 2012).

To reduce the size of the file specifying the wave spectrum as wave components, the energy spectrum that is obtained from the wave gauge data is reduced. In reducing the spectrum special attention is paid to represent the high energetic frequencies. A higher frequency component resolution is chosen in the peak area, as noted in Table 4.2. The frequencies lower than the splitting frequency are not taken into account in the reduction of the spectrum; the model generates these low frequencies based on the short wave input.

Table 4.2 – Resolution of bins used for dividing the original wave spectrum into wave components.

Frequency (Hz)	Number of bins (%)
0 - f_{split}	0
f_{split} - 0.5	80
0.5 - 1.0	10
1.0 - f_{end}	10

In Figure 4.2 the reduction of the spectrum is shown for case 1. The original spectrum is depicted, together with several reduced spectra consisting of a different number of wave components. The original spectrum provides a significant wave height of 0.82 meter at the boundary. For the reduced spectra a significant wave height is also computed. The spectrum with 100 components and the spectrum with 1000 components deliver the same wave height as the original spectrum, while the spectrum with 200 components delivers a higher wave height. The spectrum with 1000 components captures most of the information in the high energy region; therefore this one is chosen to prescribe at the boundary. For further details on implementing the instationary roller extension in the FLOW-module the reader is referred to appendix B.2.

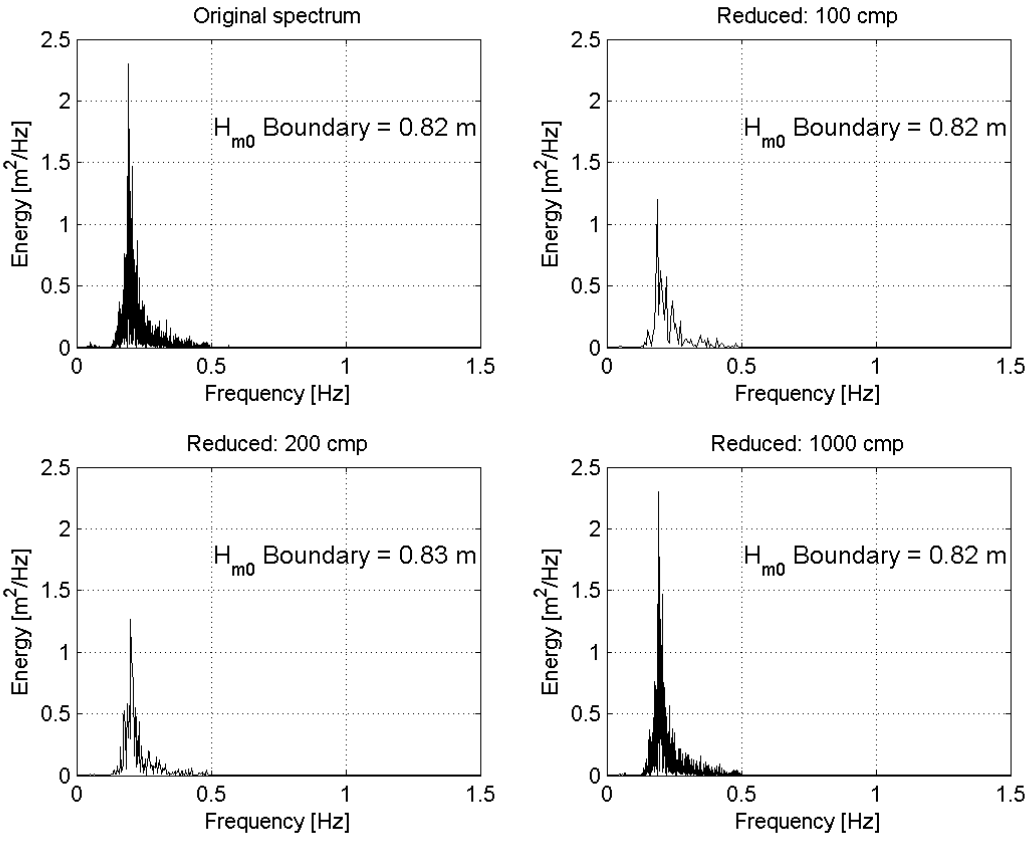

Figure 4.2 – Visualization of reduced spectra. Original spectrum is depicted in the upper left panel. For all spectra, the resulting significant wave height at the boundary is given.

4.4 Number of sediment fractions

Two modelling methodologies are chosen for the sediment transport model: one is using a single sediment fraction and one is using multiple sediment fractions. In this section both methodologies are discussed. It is noted that for both the single and multiple fraction model the transport formulations are the same, with the difference that for the multiple fraction model that the computations are performed for each fraction separately, simply added up in the final step of the computation process. No interaction between sediment fractions is taken into account.

4.4.1 Single sediment fraction

For the single fraction model the sediment used in the experiment is represented by one fraction in the model, capturing the sample information in three parameters. These parameters are the median grain diameter D_{50}, the 10% passing percentage D_{10} and the 90% passing percentage D_{90}. With these parameters a piecewise log-uniform distribution is created by Delft3D that describes the sediment. It is chosen to prescribe the D_{10} and D_{90} in the sediment input file, to avoid inaccuracies due to Delft3D estimating these quantities by itself.

The sediment availability is prescribed by a thickness file. For each grid cell, the thickness of the sediment layer is given. In this way, a distinction can be made between the beach part of the flume and the part where there is no sediment. The input block for the single sediment fraction model is given in appendix B.3.

4.4.2 Multiple sediment fractions

For the multiple fraction model the sediment used in the experiment is represented by multiple fractions in the model. The original sample is divided in multiple fractions consisting of a certain part of the original profile. Each sample is defined with a median grain diameter, and a maximum and minimum value indicating the borders. Delft3D then interpolates a piecewise log-uniform distribution between these values. By prescribing minimum and maximum values, overlap between samples is prevented. An example of the construction of multiple samples from the original sample is depicted in Figure 4.3.

A higher resolution in the fine tail of the sample is chosen, since it is expected that the finer sediments play a larger role in the morphodynamics. A correct representation of the sediment variability in the fine segment is therefore thought to be indispensable. A sensitivity analysis on the distribution of fractions is presented in section 5.5.

A representation of the sediment input file is given in appendix B.4. The input is almost the same as for the single fraction, but now the sediment variability is not given by SedD10 and SedD90, but by SedMinDia and SedMaxDia, allowing for no overlap between different sediment fractions. Delft3D construct a piecewise log-uniform distribution between the minimum, median and maximum diameter.

Sediment availability is prescribed by total available mass per fraction. In a way similar to the thickness, for each fraction a (spatially varying) total mass is prescribed. The mass is derived from the original thickness file by multiplying it with the size of the fraction and the dry-bed density. This way of specifying the sediment availability is more transparent since a conservative entity is prescribed, it is also more convenient to specify an initially layered bed stratigraphy using this method.

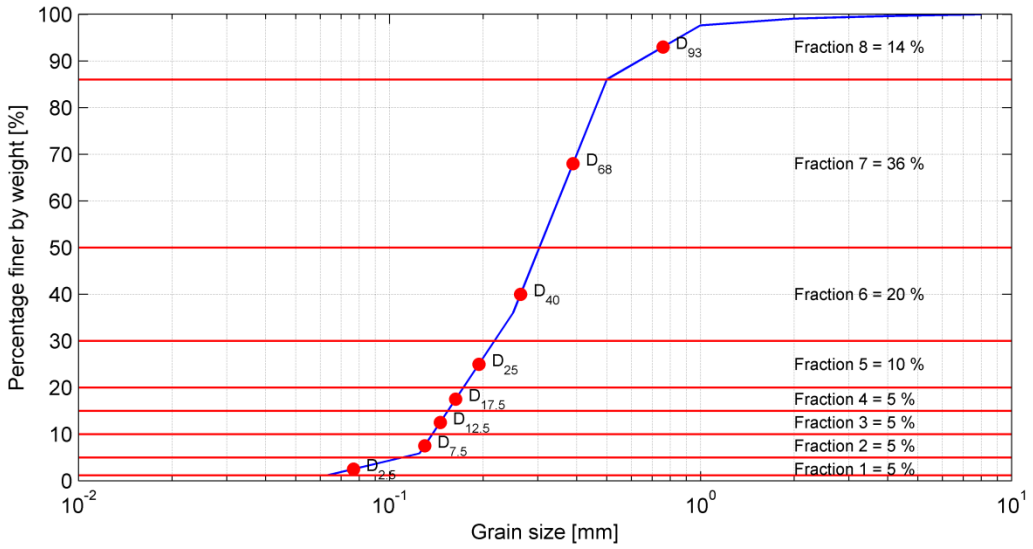

Figure 4.3 – Division of original sample in several fractions.

4.5 Bed model

In Delft3D currently two bed composition models exist: a uniformly well-mixed bed and a layered bed stratigraphy. The uniformly mixed bed consists of one single sediment layer, while the layered bed has multiple sediment layers.

4.5.1 Uniformly well-mixed bed

The uniformly well-mixed bed (Figure 4.4) is characterized by:

- There is no bookkeeping of the order in which sediments are deposited
- All sediments are well mixed according to their assigned amount
- All sediments are available for erosion

In the Delft3D, the uniformly well-mixed bed composition is the default bed composition model. Since only a single layer of sediment is used all sediments are directly available for erosion. As input the model requires the available amount of sediment specified either as sediment thickness or total dry mass. This value may be constant for the entire model, or spatially varying. If a spatially varying value is desired, the sediment thickness or total dry mass must be specified in a separate input file.

The uniformly well-mixed bed can be used for one single fraction or for multiple fractions. For a single fraction a single grain size parameter is used to describe the uniformly well-mixed bed, grain size variability is only taken into account by means of secondary grain size parameters in the transport formulation (e.g. D_{84} or D_{90}). To use the uniformly well-mixed bed with multiple fractions, for each fraction the sediment availability at the bed must be prescribed.

The disadvantage of using a well-mixed bed model is that when sediment is deposited it is mixed instantaneously with all the sediment already present in the bed. This means that when sediment is eroded it is removed irrespective of how long ago it was deposited. A more realistic behaviour is that when sediment is deposited it is not mixed (completely) with the sediment in the bed. In this way the most recent deposited sediment is eroded first.

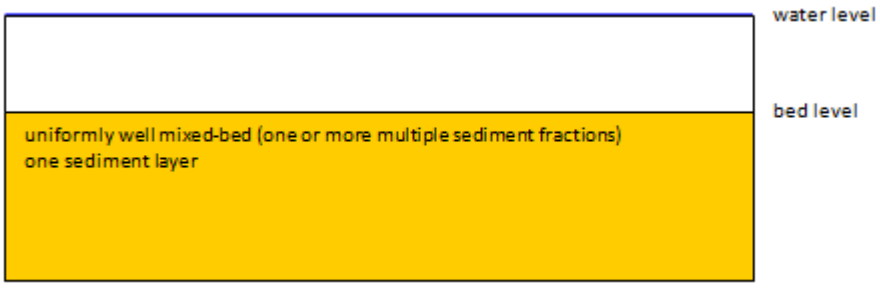

Figure 4.4 – Uniformly well-mixed bed structure

4.5.2 Layered bed stratigraphy

The layered bed stratigraphy (Figure 4.5) is characterized by:

- A user-defined number of underlayers.
- Different initial distributions of sediments can be assigned to each underlayer.
- Only sediments in the top-most layer are available for erosion.
- The top layer is replenished after erosion with sediment from the layer beneath it.
- During deposition, sediment is added to the top-most layer, the transport layer. The transport layer has an assigned maximum thickness and therefore transports the sediment after mixing to the layer below.

The general composition of the bed for a layered bed per grid cell is divided into three main parts: the transport layer, the underlayers and the base layer. The total number of layers therefore exists out of 2+N layers, where the 2 stands for both the transport layer and the base layer, and the N stands for the number of underlayers.
The transport layer has a distribution function as it imports sediment to the grid cell in the case of deposition and it exports sediment in the case of erosion. The thickness of this layer is user-defined, and several options exist to describe the transport layer thickness: constant, proportional to the water depth and proportional to the dune height. Delft3D uses by default a mixed Lagrangian-Eulerian framework to treat aggradation and degradation. In a fully Lagrangian framework, the thickness of the layers is constant and the set of layers moves with the aggradation/degradation by means of an artificial advection velocity. In the Eulerian framework the position of the layers is kept constant. The aggradation/degradation is accounted for by changing the thickness of the top layer. In case the top layer becomes too thick due to deposition it will be split and in case the thickness reduces to zero the layer is merged with the second layer.
In Delft3D by default a partially mixed framework is used: the top layer has a predefined thickness that does not change over time, it is the second layer that changes in size. The thickness of the top layer is a very important parameter for the time-scales of the system, thus it is desirable to have a top layer with a constant thickness. Also, by not moving the grid to account for aggradation/degradation, there is no artificial diffusion introduced between the layers.
The underlayers mainly have a bookkeeping function; in case of erosion, they supply sediment to the transport layer and in case of deposition they store sediment. The number and thickness of the underlayers therefore determines how well sorting processes are captured by the model. The base layer acts as a storage for all the information that does not fit in the underlayers.

The layering system is prescribed in the morphology input file of Delft3D. An extra input block is added to this file, in which the characteristics of the layered bed stratigraphy can be defined, such as the transport layer thickness and the number of underlayers. The structure of this input block is given in appendix B.5.

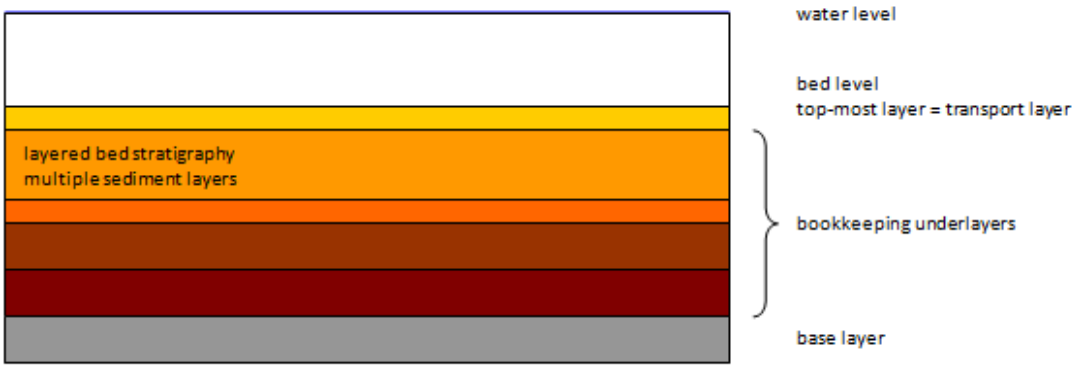

Figure 4.5 – Layered bed stratigraphy structure

In this study the layered bed model is used with two different initial states, influencing the functioning of the model. One way to use the model is with an initially uniform well-mixed bed. In this case the layered bed model functions as a bookkeeping system, keeping track of erosion and deposits. By using the model this way, there is no need in using an initial bed composition file. The initial composition is fully determined by prescribing the total available mass per sediment fraction.
Another way of using the layered bed model is with an initially non-uniform layered bed stratigraphy. To apply an initially non-uniform layered bed, the initial bed is prescribed in an initial bed composition file (<*.*inb*> –file). In this file the user can define multiple layers of varying thickness and prescribe the sediment availability per layer as thickness or total mass. Every layer block adds a sediment layer to the bed in the order specified (first block is found at the top of the column, last block at the bottom). In this study, the initial layering is prescribed by prescribing a total available sediment mass for each fraction per layer. This is done using sediment mass files to include spatial variation. The structure for the initial bed composition file is given in appendix B.5. The thickness of the underlayers in the initial bed composition file overrules the thickness of the underlayers defined in the morphological input file. All new created layers however will be subjected to this assigned thickness if the maximum number of underlayers defined in the morphological input file is not yet reached by the initial bed composition file.

5 Model results

In this chapter the results of the simulations with the different models as described in section 4.2 are shown. First, the calibration process is outlined for case 1 in section 5.1. After calibration, an in depth comparison of the model approaches is made in section 5.2 by looking closely at the physical processes. In section 5.3 the model is validated for the other cases of the experiment. Finally model performance is quantified with the Brier Skill Score in section 5.4 to compare the performance of the different models.

5.1 Calibration

5.1.1 Calibration procedure

The performance of a numerical model is largely determined by the free parameters that reflect uncertainty in modelling certain physical processes. The calibration process for the free parameters of the models is based on the work of Giardino et al. (2011), where the free parameters of the wave-roller, flow and transport module of Delft3D are discussed. In the study of Giardino et al. an attempt is made to find optimal parameter settings for modelling bar dynamics that apply in general, to avoid the need for excessive tuning and input by the user. They found general agreement for the values on several parameters. Starting point for the calibration is that these parameters are set to the agreed upon values as found by Giardino et al. (Table 5.1) to reduce the number of free parameters that must be tuned.

With the calibration procedure it is first attempted to get the hydrodynamics represented correctly. Once this is achieved, the transport parameters are calibrated. This routine is performed on both the single fraction models (SRM & ISRM) for the first experiment. The SRM and ISRM are both calibrated separately.

When the extension is made from one sediment fraction to multiple sediment fractions a number of additional free parameters are introduced. It is assumed that the values of the free parameters obtained for the wave-roller, flow and transport modules also apply to the multiple fractions model. This means that there is only need to calibrate the free parameters that are coupled to the use of the multiple fractions model. In Figure 5.1 the calibration procedure is displayed in a flow-chart.

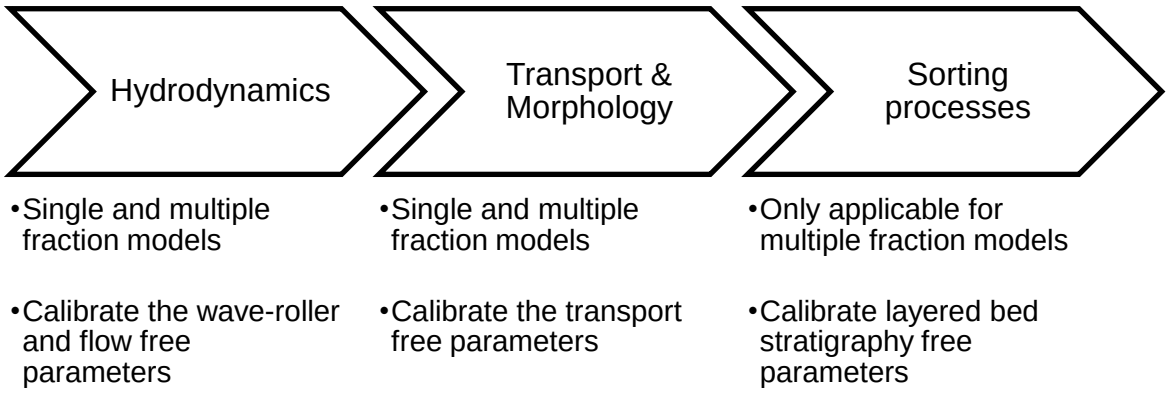

Figure 5.1 – Calibration procedure used in this study

5.1.2 Calibration of the single fraction models

In Table 5.1 an overview is provided of the free parameters with a description and a generally agreed upon value based on the study of Giardino (if applicable). Based on this table, there are three free parameters that can be tuned for the flow and roller modules. The horizontal background viscosity is set to 0.01 and is not calibrated any further during this study. The breaker delay parameter is found to have an optimal value of -2.0 according to several studies (Giardino et al., 2011). These studies were based on field cases where the length scales are such that a breaker delay is indeed found. The present study is based on a wave flume experiment, where the breaker delay effect is not as strong as in the field. The model performed better when the breaker delay effect was not taken into account (F_lam = 0.0). This results into two free parameters that can be used to calibrate the wave height and the hydrodynamics: the roller slope β_{rol} and γ_w.

Table 5.1 – Summary of free parameters for the flow, roller and transport module

Module	Parameter	Keyword	Description	Generally agreed upon value (Giardino et al.)
Flow	$f_{w,fac}$	FWFAC	Streaming factor	0.0
	$v_{h,back}$	Vicouv	Horizontal background viscosity	-
	$v_{v,back}$	Vicoww	Vertical background viscosity	$1.0*10^{-6}$
Roller	f_w [1]	Fwee	Bottom friction factor	0.0
	F_{lam} [1]	F_lam	Breaker delay parameter	-2
	α_{rol}	Alfaro	Roller dissipation coefficient	1.0
	β_{rol}	Betaro	Roller slope	-
	γ_w	Gamdis	Wave breaker parameter	-
Transport	f_{bed}	Bed	Current related bed load scaling factor	1.0
	$f_{bed,w}$	BedW	Wave related bed load scaling factor	1.0
	f_{sus}	Sus	Current related suspended load scaling factor	1.0
	$f_{sus,w}$	SusW	Wave related suspended load scaling factor	-
	$D_{h,back}$	Dicouv	Horizontal background diffusivity	0.1
	$D_{v,back}$	Dicoww	Vertical background diffusivity	1.0*10^-6
	α_{bn}	AlfaBn	Transverse bed slope effect factor	1.5
	α_{bs}	AlfaBs	Longitudinal bed slope effect factor	1.0

Based on the work of Giardino et al. (2011) a choice is made to tune the wave heights using the wave breaker parameter (γ_w) and the roller slope (β_{rol}). Starting point of the calibration routine were the default values for these two parameters, while the other parameters were set at the values based on the study of Giardino et al. For the sediment transport, based on Table 5.1, there is only one free parameter that has to be tuned for the transport module. This has proven to be false; for the instationary roller model significantly better results were found by scaling all four sediment transport factors instead of only the wave related transport scaling factor. For both the stationary and instationary roller model the value for the longitudinal bed

[1] *Only applicable for the Stationary Roller Model*

slope factor was too low, leading to instabilities since the bed slope factor serves as a diffusion term that can damp the instabilities in the system (De Vriend, 1989).
Both wave models show different optimal values for the two free parameters; these are given in Table 5.2. The difference between both models shows strongly in the calibration process of the transport parameters. For the SRM calibration of the wave related suspended load scaling factor and the longitudinal bed slope is sufficient for an accurate solution; varying the values of the other parameters compared to the generally agreed upon values does not influence the solution (section 5.5). The longitudinal bed slope factor is simply taken as small as possible to obtain a stable solution. To obtain a bar profile that is 'sharp' enough, the value of the wave related suspended load scaling factor is lowered significantly.
For the ISRM this is not enough; the ISRM leads to increased transports in the nearshore area (section 5.2) and therefore also the current related suspended load must be scaled accordingly to obtain the correct upper-shoreface erosion and bar formation. The other sediment transport scaling factors are lowered based on the studies of Brière & Walstra (2006) and Giardino et al. (2011). For the calibration process of the SRM and ISRM using a single fraction respectively four and seven free parameters have to be tuned to obtain a correct solution from the model. Both wave models show different optimal values for the two free parameters; these are given in Table 5.2.

Table 5.2 – Final values for the calibrated models.

Parameters	Keyword	Default value	SRM	ISRM
β_{rol}	Betaro	0.1	0.09	0.08
γ_w	Gamdis	0.55	0.55	0.48
f_{bed}	Bed	1.0	1.0	0.25
$f_{bed,w}$	BedW	1.0	1.0	0.25
f_{sus}	Sus	1.0	1.0	0.6
$f_{sus,w}$	SusW	1.0	0.2	0.05
α_{bs}	Alfabs	1.0	5.0	4.0

5.1.3 Calibration of the multiple fraction models

When simulating with multiple fractions and using the layered bed stratigraphy model a number of new free parameters are introduced. In Table 5.3 an overview is provided of the newly introduced options. Since this feature is relatively new in Delft3D, few studies on the general applicability of values for these parameters have been performed.

Table 5.3 – Summary of the free parameters for the underlayer module

Module	Parameter	Keyword	Description	Generally agreed upon value
Underlayer	-	TTLForm	Transport layer thickness formulation	-
	-	ThTrLyr	Thickness of the transport layer	-
	-	MxNULyr	Number of underlayers	-
	-	ThUnLyr	Thickness of each underlayer	-

For the transport layer thickness formulation there are several options to choose from:

1. Constant thickness
2. Proportional to the water depth
3. Proportional to the dune height

In this study the transport layer thickness is taken as constant; the effect of choosing a different formulation is not investigated in this thesis.
The order of magnitude of the thickness of the transport layer may be estimated as 50% of the observed bedform height. A restriction on the thickness of the transport layer is that the erosion per time step should be less than the thickness to guarantee stability and validity of results. The thickness of the transport layer is the most important parameter that can be tuned to obtain correct representation of the sorting processes; it determines the time scale of the response of the transport processes.
The maximum number of underlayers (excluding transport layer and base layer) determines the upper limit of the amount of bookkeeping underlayers active at any point during the simulation. The number of underlayers mainly determines the systems capability of bookkeeping. During erosion, if all the underlayers are eroded away and the base layer is reached, sediments are mixed uniformly into this layer instead of the underlayers. In this study, the number of underlayers is chosen in such a way that the maximum erosion in time is smaller than the total thickness of the bookkeeping underlayers. The maximum thickness of the underlayers determines how well the vertical sorting is accounted for. In Table 5.4 the final values for the calibrated multiple fraction model is shown. Sensitivity of these settings is shown in appendix E.

Table 5.4 – Final values for the calibrated models.

Parameters	**Keyword**	**Default value**	**SRM**	**ISRM**
Additional options multiple fractions / Layered bed stratigraphy				
-	TTLForm	1	1	
-	ThTrLyr	-	0.01 [m]	
-	MxNULyr	-	10	
-	ThUnLyr	-	0.1 [m]	

5.1.4 Calibrated model results

In Figure 5.2 the results of the SRM for case 1 are depicted. The SRM accurately reproduces the wave height, though it over predicts the wave height in the shoaling zone. The highest wave height is computed correctly by the model.
The upper shoreface erosion is computed correctly by the model although a small overprediction can be observed. The bar height and the shape of the bar are computed accurately by the model, but the location of the bar crest is not computed right; the SRM underestimates the offshore migration of the bar. The secondary bar and trough are not found back in the model computations.

In Figure 5.3 the results of the SRM8 for case 1 are depicted. Compared to the SRM, the bar is significantly smoothened when the sediment is represented by 8 fractions. The upper shoreface erosion computed by the SRM8 is comparable to the upper shoreface erosion computed by the SRM, but the eroded sediments are diffused more compared to the SRM.
The sorting parameters computed by the SRM8 are also shown in Figure 5.3. At the onshore edge of the surfzone and the swash zone, the SRM8 computes a coarsening of the sediment that is not measured in the wave flume. The coarsening in the bar area as measured in the wave flume is found back in the model computations. There is offshore fining observed in the model computations but not as strong as the fining observed in the experiments. The standard deviation computed by the model shows resemblance to the measurements in the surfzone, but offshore of the surfzone no resemblance is found. The simulated skewness shows the same tendency as the measured skewness even though the increase is found more offshore. In section 5.2 the results on sorting will be elaborated further.

In Figure 5.4 the results of the ISRM for case 1 are depicted. The ISRM accurately reproduces the wave height along the flume, though it over predicts the wave height in the shoaling zone, just like the SRM. The highest wave height is computed correctly by the model.
The upper shoreface erosion is computed accurately by the model, with a small overprediction observed similar to the SRM. The bar height and the shape of the bar are computed accurately by the model just like the location of the bar crest. Offshore from the bar crest, the simulated bed level shows strong resemblance to the measured bed level. The secondary bar and the trough are not found back in the model computations.

In Figure 5.5 the results of ISRM8 for case 1 are depicted. Compared to the ISRM, the simulated morphology shows some small differences. The upper shoreface erosion is less, and the bar is smoothed out a little.
The sorting parameters computed by the ISRM8 are also shown in Figure 5.5. In the upper shoreface, the median grain diameter is computed correctly. The coarsening in the bar area is not represented by the model computations, but the offshore fining is computed accurately. The standard deviation computed by the model shows resemblance to the measured standard deviation, although the increase of the standard deviation seems to occur more offshore in the model. The simulated skewness resembles the measured skewness well; the increase of the skewness offshore of the bar area is predicted accurately by the model.

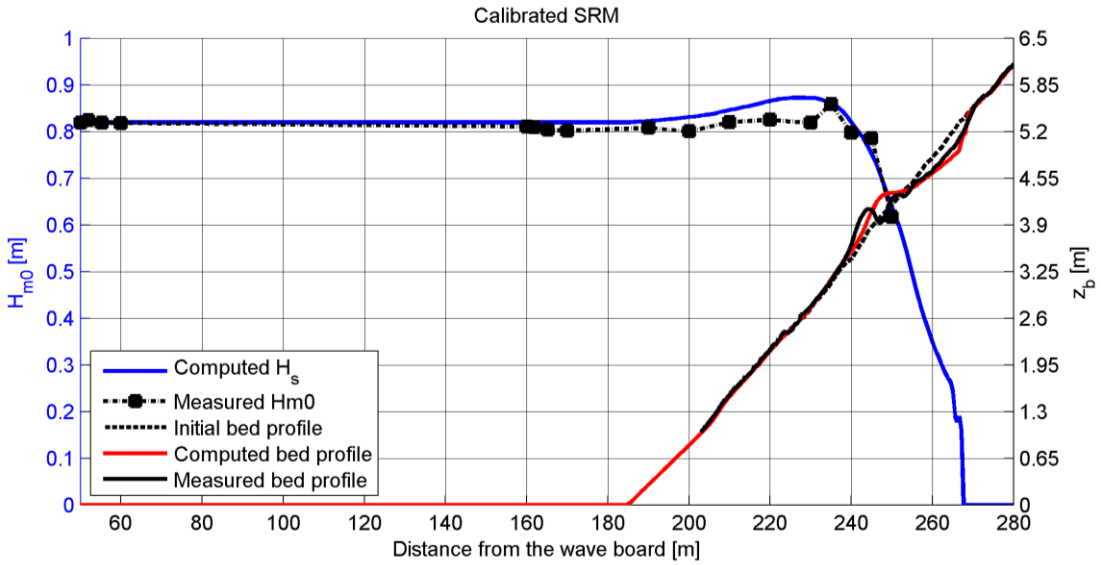

Figure 5.2 – Simulation results for the calibrated SRM (1 sediment fraction)

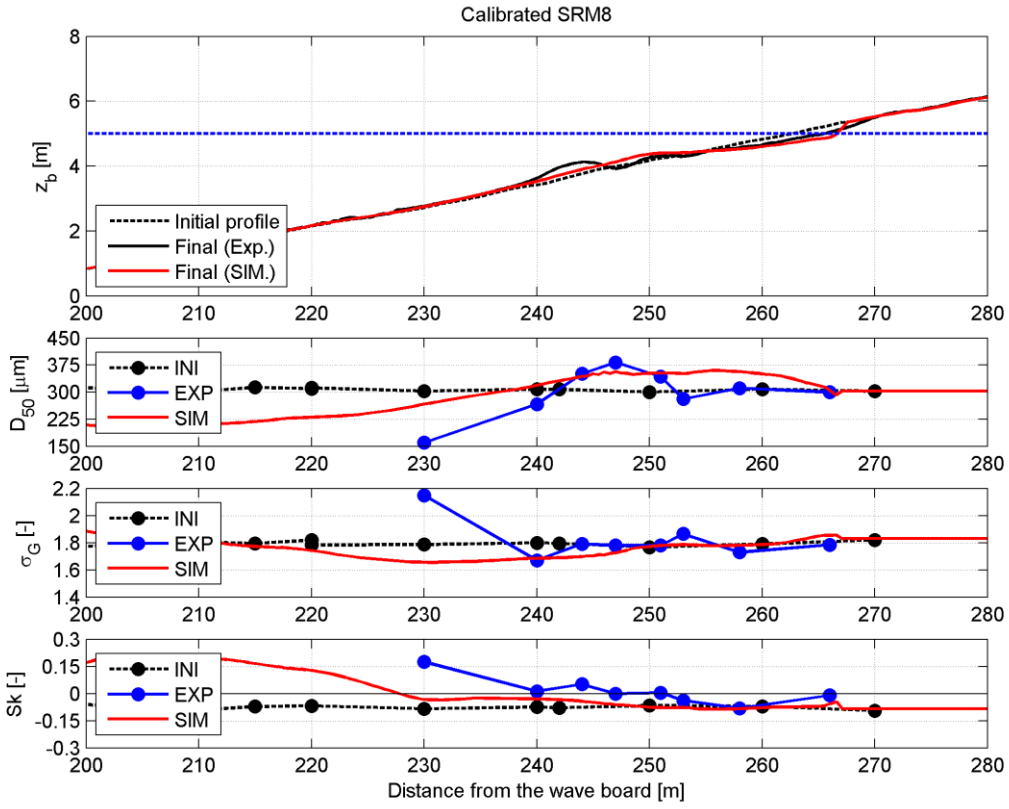

Figure 5.3 – Simulation results for the calibrated SRM8 (8 sediment fractions). The bed level is shown in the upper panel, the D_{50} is shown in the second panel, the sorting σ, is shown in the third panel and the skewness is shown in the fourth panel.

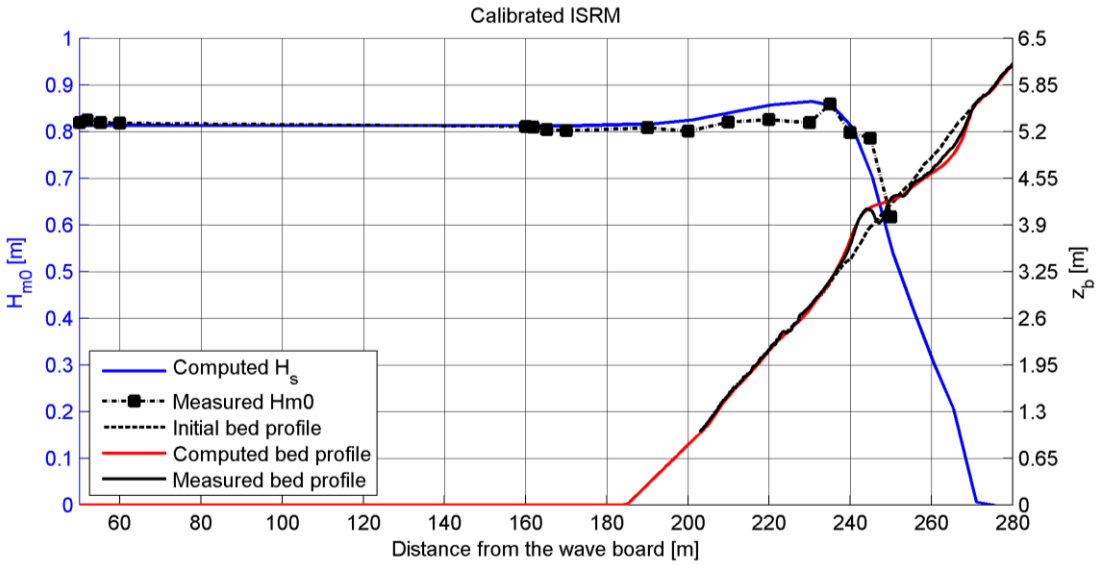

Figure 5.4 – Simulation results for the calibrated ISRM (1 fraction)

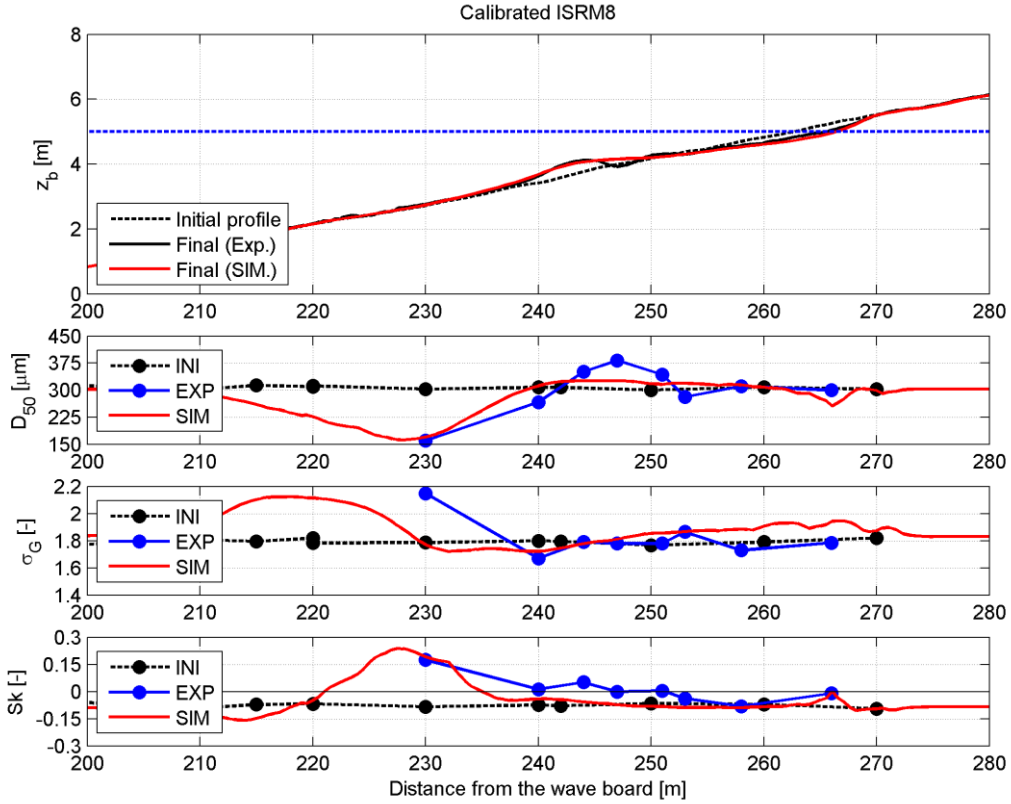

Figure 5.5 – Simulation results for the calibrated ISRM8 (8 fractions). The bed level is shown in the upper panel, the D_{50} is shown in the second panel, the sorting σ, is shown in the third panel and the skewness is shown in the fourth panel.

5.2 Evaluation of physical processes

In this section the model physics are analysed in more detail. Results of the model computations are compared with one another. The first part of this section is devoted to highlighting the differences between the use of the stationary roller model and the instationary roller model. The inclusion of long waves turned out to be crucial for predicting the morphodynamics in the GWK (section 5.1.4). Therefore, much attention is paid in comparing the physical processes of both the SRM and ISRM. By comparing the physical processes of both the SRM and ISRM with the data, a qualitative assessment on the performance of both models is made.
Further on in this section a detailed look is taken at the sorting processes in the model. Again, the results of the model are compared to the data and to literature to perform a qualitative assessment on the model capabilities.

The analysis of the physical processes in section 5.2.1 computed by the model is performed for a fixed bottom profile without morphological updating. This is done to be able to compare velocity profiles, concentration profiles and transport rates while having the same bathymetry. The bottom profile used for this analysis is the initial, uniform bathymetry with 1/15 slope.

5.2.1 Wave action

As shown in Figure 5.2 & Figure 5.4 both models accurately compute the wave height along the flume. In this section several wave related phenomena are investigated: the groupiness of the short waves, the long wave factor, the correlation between long and short waves and the asymmetry and skewness (Figure 5.6). These parameters are chosen since they provide insight in the effect of the presence of long waves. Wherever possible these parameters are compared to the measured data. Since most of these parameters are related to the presence of long waves, most of the plotted results are taken from the ISRM. If a comparison is made between models, this will be indicated in the text.

The upper panel of Figure 5.6 depicts the wave height of the short waves (blue line) and the wave height of the long waves (red line) as computed by the ISRM, and the measured values (blue and red circles). Besides accurately predicting the wave height of the short waves, the model is also capable of accurately computing the wave height of the long waves. The computed values slightly deviate from the measurements: the simulated values are lower than the measured values. A possible explanation for this is the wave-board boundary. In the model a Riemann-type boundary must be used for the model to work properly (Deltares, 2012). The Riemann boundary is weakly reflective; this boundary-type is generally applied to reduce (numerical) reflection. In reality, the wave-board is situated here causing reflection of the long waves, eventually leading to a standing wave pattern. To prevent this, the wave-board is turned off after a certain time (section 3.1). Therefore more reflection is expected in the experiments in the GWK leading to slightly higher values of the measured wave height of the long waves in the flume.
The second panel of Figure 5.6 depicts the groupiness factor (GF) of the short waves and the long wave factor. The groupiness factor is defined by List (1991) in the following manner:

$$GF = \frac{\sqrt{2\sigma_A}}{\mu_A} \tag{5.1}$$

$\sigma_A =$ Standard deviation of the mean wave envelope signal [m]

$\mu_A =$ Mean of the wave envelope signal [m]

The groupiness factor is an indication of how well the high frequency waves are grouped. For perfectly grouped waves GF equals 1, for fully non-grouped waves GF equals zero. In reality, the value of GF is somewhere between one and zero, with higher values indicating a stronger grouping of the short waves.
By looking at the computed GF it becomes apparent that the GF is approximately 0.65 throughout the entire flume indicating a clear grouping of the high frequency waves. The GF decreases from the moment the first waves start breaking (around x = 230 m) and increases again at the edge of the swash zone. The decreasing GF can be explained by the breaking of higher waves in the group thus reducing the short wave grouping. A possible explanation for the increase of the GF in the swash-zone is the influence of local water depth on the high frequency wave heights (van Rooijen, 2011). The water depth decreases and will be dominated by low frequency motions which now control the short wave height. This is further illustrated by the long wave factor, LF:

$$LF = \frac{\sigma_h}{\mu_h} \tag{5.2}$$

$\sigma_h =$ Standard deviation of the water surface level signal [m]

$\mu_h =$ Mean of the water surface level signal [m]

In the inner surfzone and the swash zone, the low frequency water level motions are more dominant than the high frequency motions; the LF increases as the GF decreases indicating a shift from short wave dominance to long wave dominance.
The third panel of Figure 5.6 depicts the correlation R between wave groups and the long wave motion. According to theory (section 2.2) the bound long wave is negatively correlated with the short wave groups when there is no influence of the bottom. This can be seen in the figure, where a strong negative correlation of -0.75 is computed by the model. More onshore the wave groups and bound long waves lose their negative correlation when the first waves start breaking and the wave groups fall apart, thus releasing the bound long wave (free long waves). This is supported by the second panel of the figure, showing that indeed the GF decreases from the breaking point and the correlation increases from the breaking point, as well as the long wave influence seen from the LF.
The fourth panel of Figure 5.6 shows the computed wave skewness and asymmetry as defined by Doering & Bowen (1995) (section 2.2.1.1) compared with the measured values of these quantities. Wave asymmetry values are approximately zero troughout the flume and decrease when the waves start breaking. Wave skewness value increases from the edge of the shoaling zone, where the waves start to feel the bottom, and decrease again shoreward from the breaking point. In the limit, a skewness value of 0 and an asymmetry value of -2.86 correspond to a sawtooth-like wave with a steep vertical front. Even though these values are not reached in the flume, from the figure it can be concluded that the waves show a strong asymmetric character in the nearshore area. The computed values are accurately representing the values measured during the experiments. The measured skewness and asymmetry are calculated using the Ursell number parameterization of Doering and Bowen the same way as for the model computations.
The sudden cut-offs in the computed lines are related to a numerical drying/flooding threshold, setting a cell to ‘dry’ when the water-depth is lower than a user-defined threshold. This means that the very shallow parts are not taken into account in the computation.

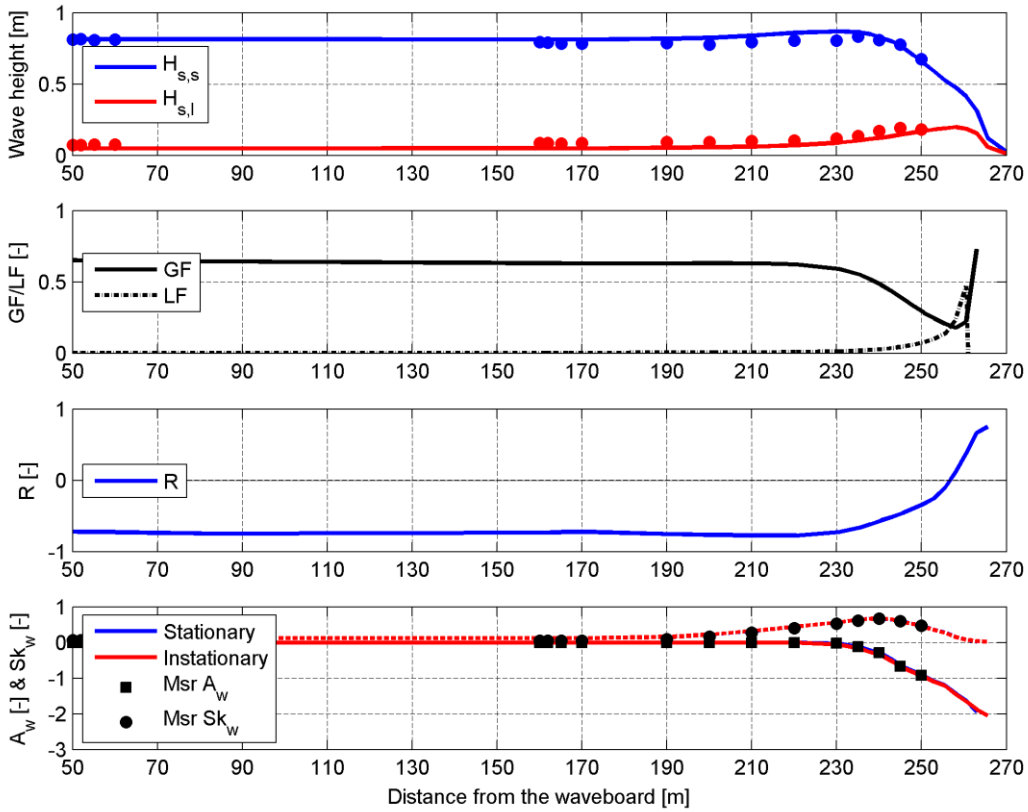

Figure 5.6 – Parameters describing the wave action in the GWK. In the upper panel short wave height ($H_{s,s}$) and long wave height ($H_{s,l}$) as computed by the ISRM are compared to measured short and long wave height (colored dots). In panel two the Groupiness Factor (GF) and Long wave factor (LF) as computed by the ISRM are depicted. In panel three the correlation between long and short waves (R) as computed by the ISRM is depicted. In panel four skewness (Sk_w, dotted lines) and asymmetry (A_w, solid lines) is plotted for the SRM (blue) and ISRM (red). Measured skewness and asymmetry is plotted as solid black circles and solid black squares respectively.

5.2.2 Velocity

In Figure 5.7 computed velocity profiles are depicted for the SRM and the ISRM. The plotted velocities are GLM velocities, used for the computation of sediment transport. Small differences are observed between the SRM and the ISRM; in the inner surfzone the onshore directed velocity in the upper part of the profile is higher for the SRM than for the ISRM.

To investigate the sediment transport and the influence of different transport mechanisms, the near-bed time varying flow induced by waves as they propagate towards the shore is investigated. The energetics approach (e.g. Bagnold, 1963) is one of the most robust sediment transport formulations for surf-zone conditions. In this approach, the time averaged bed-load and suspended-load are proportional to four velocity moments (Roelvink & Stive, 1989). The most important terms in the cross-shore transport equation are those included in the third and fourth velocity moments. For the analysis on the relative contributions of incident waves, long period motions and interactions between the three the third velocity moment is used. This moment is chosen for having a clearer cross-shore structure, being statistically more robust, and its expansion into individual terms being easily coupled with well-known sediment transport mechanisms (Rocha et al., 2013).

In the analysis of moments, the velocity is decoupled into a mean part and an oscillating part. The oscillating part can then later be decoupled again into high frequency oscillations and low frequency oscillations. Since the analysis is performed on Delft3D output, there are some limitations on the computations of the velocity moments. In Delft3D output, the oscillating part of the velocity signal is due to long waves, thus leading to the following computation of the velocity moments:

$$u = \bar{u} + \tilde{u}_l \tag{5.3}$$

$$\left\langle u^3 \right\rangle = \bar{u}^3 + \left\langle \tilde{u}_l^3 \right\rangle + 3\left\langle \tilde{u}_l^2 \right\rangle \bar{u} \tag{5.4}$$

Using linear wave theory, two transport components related to short wave effects can be computed using Delft3D output. Short wave velocities calculated in this sense are peak orbital velocities, therefore only terms from the third odd moment that contain the short wave velocity squared can be computed this way. The total number of terms that can be analysed and their physical meaning is summarized in Table 5.5.

Table 5.5 – Velocity moments used for analysing the relative contribution of several different sediment transport mechanisms to the total transport.

Name	Formulation	Physical meaning
Sk_1	$\bar{u}^3$	Mean velocity cubed
Sk_2	$\left\langle \tilde{u}_l^3 \right\rangle$	Long wave skewness
Sk_3	$3\left\langle \tilde{u}_l^2 \right\rangle \bar{u}$	Stirring by long waves and transport by mean flow
Sk_4	$3\left\langle \tilde{u}_s^2 \tilde{u}_l \right\rangle$	Correlation of short wave variance and long wave velocity
Sk_5	$3\left\langle \tilde{u}_s^2 \right\rangle \bar{u}$	Stirring by short wave velocity and transport by mean flow

The result of this analysis is plotted in Figure 5.8. As a reference, in the upper panel the bed profile and wave heights are depicted. The lower six panels show the computed near-bed mean velocity profile in cross-shore direction and the corresponding third velocity moments as defined in Table 5.5.

The structure of the mean near-bed velocity along the flume is as expected; onshore directed throughout the entire flume until the breakpoint. From the breakpoint until the beach the velocity is offshore directed. For the SRM the velocity is negative throughout the entire surfzone, while for the ISRM the velocity signal turns positive at the edge of the swash zone, where the long wave motion is dominant. The mean velocity cubed (Sk1) follows the mean velocity profile leading to a slightly larger difference between the SRM and ISRM.
The long wave skewness (Sk2) is onshore directed at approximately x = 260 m; this location is corresponding to the breakpoint of the long waves. The long waves show a larger skewness value here due to their deformation: they form a bore and propagate towards the upper-swash zone. The skewness value decreases again until the waves reach the edge of the swash zone.
The long wave stirring and mean flow transport (Sk3) shows that from the moment short waves start breaking, offshore transport increases. Close to the shoreline, the moment changes sign, corresponding to onshore transport. The long waves cause an extra transport term that follows the mean flow direction.
An important contributor to transports is the interaction between short waves and long waves (Sk4). Short waves stir up sediment that is transported by the long wave motion. Because of the negative correlation between long and short waves (Figure 5.6) the long waves cause sediment to be transported offshore when it is stirred up by the short waves. At the edge of the swash zone this transport is onshore directed due to the positive correlation.
For both the SRM and the ISRM, the largest contributor to the total transport is the short wave stirring and transport by mean flow (Sk5). In this component there is a contribution from the mean flow and a contribution from the short waves. Comparing the SRM and the ISRM, it is seen that the magnitude of Sk_5 is larger for the SRM than for the ISRM. Part of this can be attributed to the contribution of the mean flow; the mean flow is higher for the SRM around x = 250-260 m. It is plausible that the stirring by short waves is approximately equal for both the SRM and ISRM, but that the transport capacity of the mean flow is higher for the SRM.

Based on the computed velocity moments, it can be concluded that the presence of long waves leads to additional transports. These are onshore directed in the inner swash zone, and offshore directed in the surfzone.

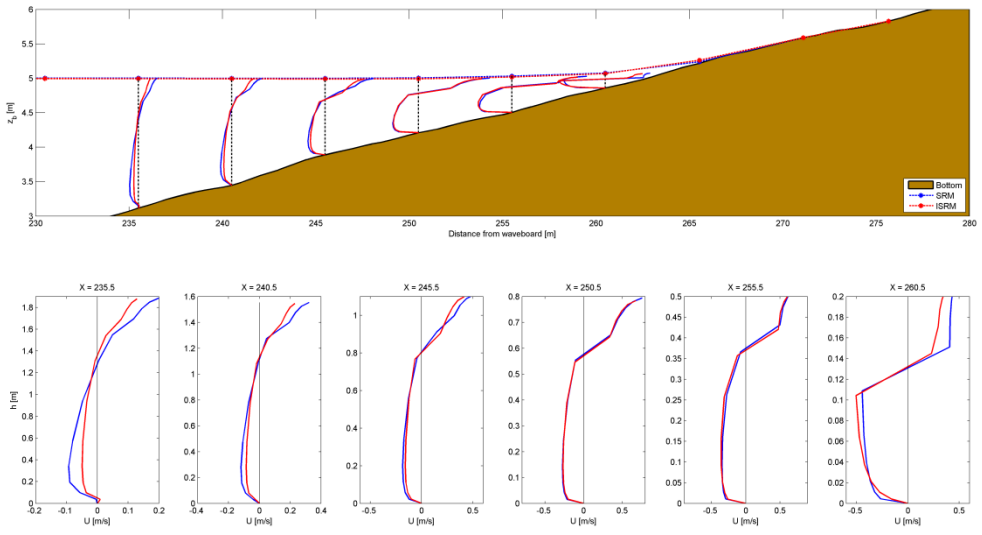

Figure 5.7 – Velocity profiles along the flume for the SRM (blue) and the ISRM (red).

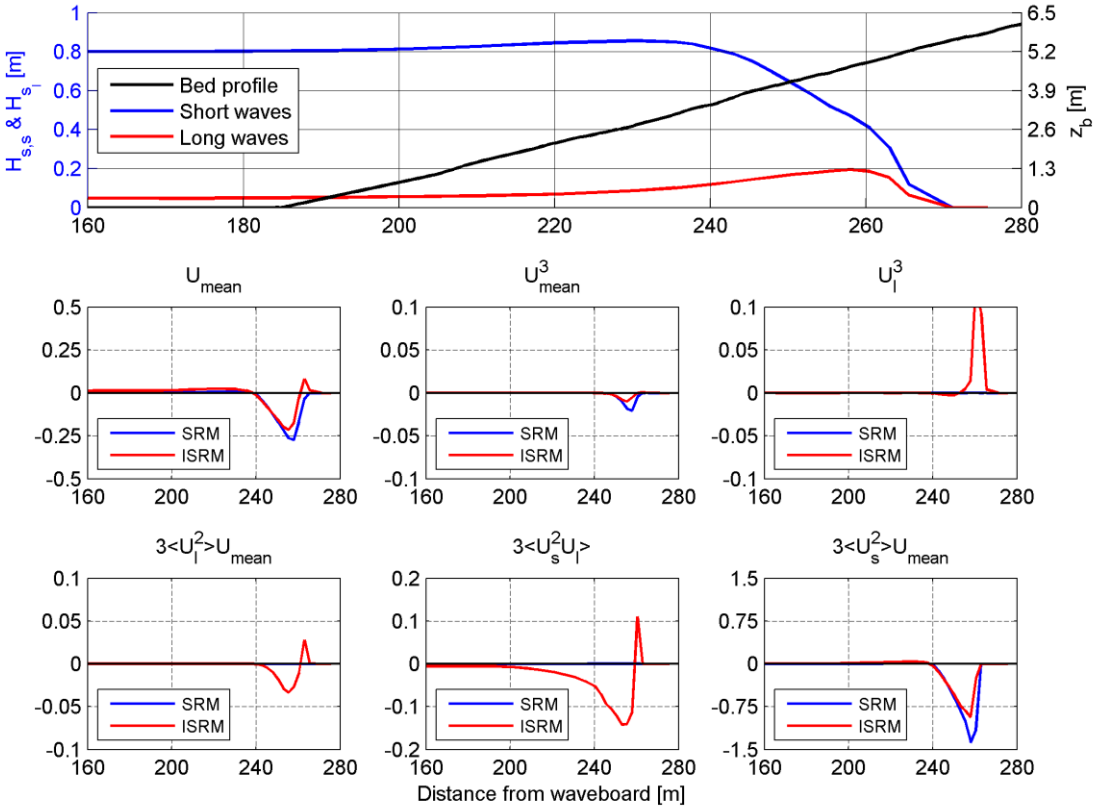

Figure 5.8 – Upper panel: computed wave height for short waves (blue) and long waves (red). The six lower panels show computed velocity moments along the wave flume for the SRM (blue) and the ISRM (red). Positive values are onshore directed and negative values are offshore directed.

5.2.3 Sediment transport

In Figure 5.9 the computed sediment transport rates are plotted. In the figure a distinction is made between total transport, near-bed transport and suspended transport rates. In Table 5.6 the transport rates for the total, bed load and suspended load transports are summarized.

First the total transport is considered. The maximum transport rates of the SRM and ISRM do not show a very large difference; the total transport rate for the SRM is approximately 15 % smaller than the total transport rate of the ISRM. More offshore from the position of the peak sediment transport rate, the difference between the SRM and ISRM is larger. This larger transport rate further contributes to the stronger offshore bar migration.

Comparing the bed load transport and suspended load transport rates shows a larger difference. Looking at the figure and the table, we can see that the bed load transport rate (q_b) computed by the SRM is larger than q_b computed by the ISRM. For the suspended load transport rate (q_s) this is the other way around; the SRM predicts a smaller q_s than the ISRM.

Thus, including long waves in the computation has a large effect on the way the sediment is transported: there is a shift from bed load transport to suspended load transport. A possible explanation for this is that there is increased entrainment of sediments due to long wave skewness, leading to higher sediment concentrations in the inner surfzone; with increased suspended sediment concentrations there is an increased offshore transport by the mean flow. In Figure 5.10 the sediment concentration profiles along the flume are plotted to support this explanation.

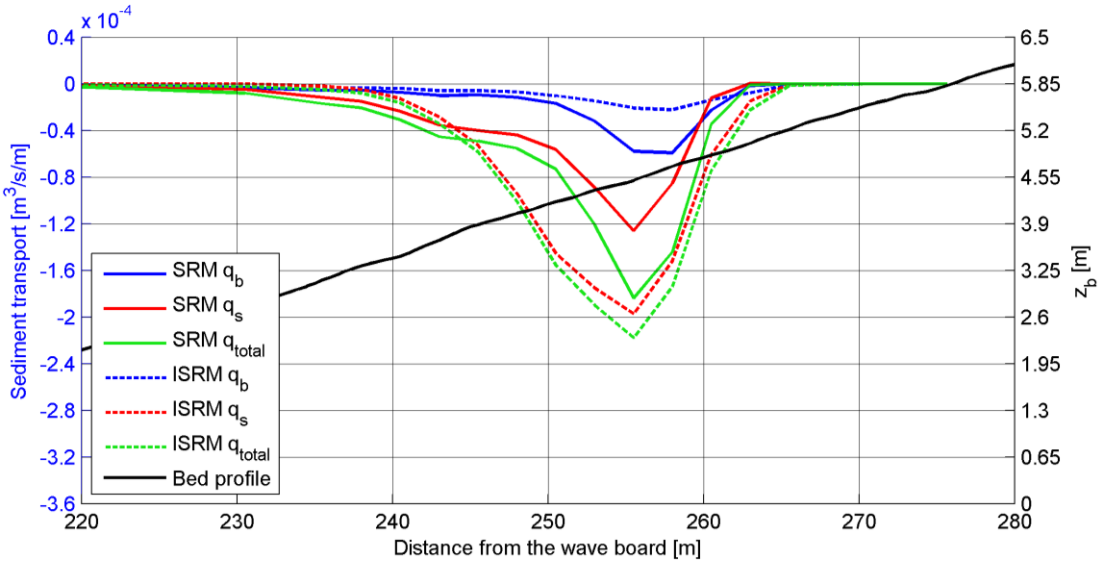

Figure 5.9 – Sediment transport rates along the flume, decomposed in bed-load transport (blue), suspended load transport (red) and total transport (green) for both the SRM (solid line) and the ISRM (dashed line).

Table 5.6 – Transport quantities and relative contributions

Transport type	Transport (x 10^{-4} m^3/s/m)		Percentage of total load transport (%)	
	SRM	ISRM	SRM	ISRM
q_b	0.60	0.22	33	10
q_s	1.26	1.97	67	90
q_{total}	1.84	2.18	100	100

In this figure a large difference between the concentration profiles from the SRM and the ISRM is observed. The suspended sediment concentrations start growing in the surfzone and are largest in the swash zone for the SRM. Comparing the location from where the suspended sediment concentrations increase with Figure 5.6 it is apparent that the concentration starts growing when the GF decreases. As the long wave influence grows, so does the sediment concentration. In Figure 5.9 it was also observed that offshore of x = 245.5 m the total transport for the SRM is higher than the total transport for the ISRM. This can be related to the observed sediment concentration profiles; for the SRM the concentration is (significantly) higher than the concentration computed with the ISRM.

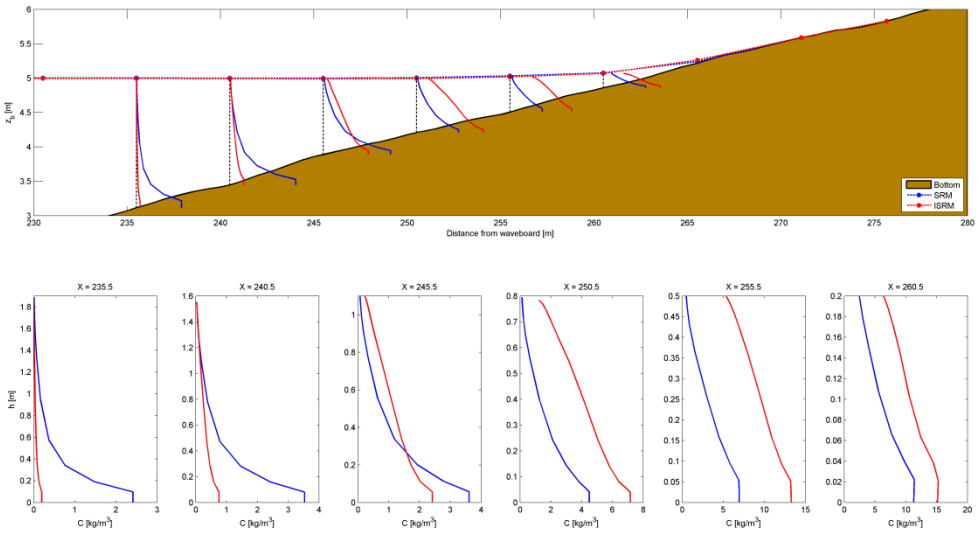

Figure 5.10 – Suspended sediment concentration profiles along the flume for the SRM (blue) and ISRM (red)

So far we have concluded that the ISRM is able to correctly simulate the bar position as opposed to the SRM. By analysing the transport mechanisms and the total transport it was observed that for the ISRM the contribution by suspended load transport is significantly higher than for the SRM. This is further explained by looking at the concentration profiles: the inclusion of long waves leads to higher sediment concentrations in the inner surfzone and thus an increased transport and accompanying offshore sandbar migration.
The increased sediment concentrations can be explained by looking at the way the concentration profile is computed. The concentration profile follows from solving the advection-diffusion equation with some reference concentration at the top of the bed load layer acting as a boundary condition. The reference concentration is calculated according to Van Rijn et al. (2000):

$$c_a = 0.015 \rho_s \frac{D_{50} T_a^{1.5}}{a D_*^{0.3}} \tag{5.5}$$

c_a = reference concentration
ρ_s = Density of the sediment
T_a = Non-dimensional bed shear stress
a = Reference height a (usually taken as the top of the bed load layer)
D_* = Non-dimensional grain diameter

For both the SRM and ISRM most parameters of this formula are equal; they are not dependent on whether or not long waves are included in the computation. This does not yield for the non-dimensional bed shear stress T_a. This parameter is calculated by:

$$T_a = \frac{\tau_{b,cw} - \tau_{cr}}{\tau_{cr}} = \frac{\left(\mu_c \tau_{b,c} + \mu_w \tau_{b,w}\right) - \tau_{cr}}{\tau_{cr}} \tag{5.6}$$

$\tau_{b,cw}$ = Bed shear stress due to combined current-wave motion

μ_c = Current related efficiency factor

$\tau_{b,c}$ = Bed shear stress due to current

μ_w = Wave related efficiency factor

$\tau_{b,w}$ = Bed shear stress due to waves

In appendix G a full description is given for calculating all different components in this formulation; in this section the focus is on the end result of this formulation and what it implies for the sediment transport. In Figure 5.11 the results of this computation are depicted. There is barely any difference between the current related efficiency factor μ_c for the SRM and the ISRM and no difference between the wave related efficiency factor μ_w. The latter is because μ_w is only dependent on grain size and not on flow characteristics.
The difference is found in the bed shear stresses τ_w due to waves and τ_c due to currents. There is not one more responsible for the increased non-dimensional bed shear stress; an increase is observed in both, leading to an equivalently higher bed shear stress due to the combined wave current motion. Including long waves into the computation causes additional bed shear stresses that are extremely important in entraining sediment into the water column. These additional bed shear stresses are due to the extra velocity induced by the long waves. More sediments are entrained in the water column leading to higher suspended load transports and an enhanced offshore migration of the bar corresponding better to reality.

In line with Deigaard et al. (1999) the presence of long waves causes additional offshore net transport, due to the coupling of high sediment concentrations with high offshore velocities. The higher concentrations induced by the long waves are caused by higher shear stresses due to the higher (momentarily) velocity.

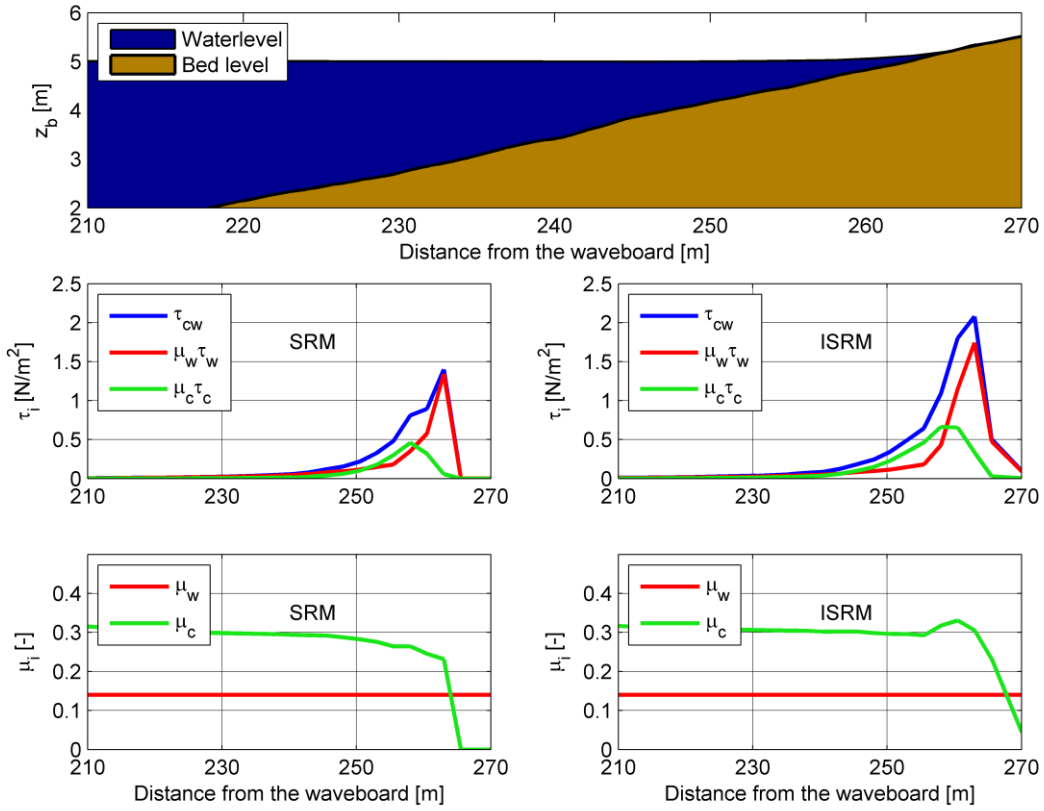

Figure 5.11 – Computed efficiency factors and bed shear stresses for the SRM and the ISRM. As a reference, the bed profile and water level are depicted in the upper most panel.

5.2.4 Morphological development

In Figure 5.2 - Figure 5.5 it was already seen that the models show different results in terms of morphological behaviour (e.g. bar movement). In Figure 5.12 the development of bar position and bar height are shown for the single fraction models SRM and ISRM as well as for the multiple fraction models SRM8 and ISRM8.

In the upper left panel the position of the bar is shown for the single fraction models (SRM & ISRM) as well as the measured position of the bar at the end of the experiment, x_{exp}. In the upper right panel this is shown for both multiple fraction models (SRM8 & ISRM8). Considering the single fraction models, it is seen that the bar position of the SRM is predicted more onshore than the ISRM. Comparing it to the measured value, the ISRM predicts the bar position better than the SRM. This is also observed for the multiple fraction models. Comparing the results of the SRM and SRM8, including multiple fractions leads to a reduced offshore migration of the bar. This is also related to the reduced erosion of the upper shoreface by using the SRM8. For the models where long waves are included in the computation, no differences are observed in the computed bar position. A slight reduction in erosion of the upper shoreface can be observed, but this reduction is significantly smaller than the reduction found by using the SRM. This is likely related to the lower shear stresses in the inner surfzone computed by the SRM; the coarser sediment fractions are not easily entrained by the lower shear stress, leading to a coarse armouring layer in the upper shoreface for the SRM reducing erosion. For the ISRM, shear stresses are still large enough to bring the sediment into motion.

In the lower left panel the height of the bar is shown for the single fraction models (SRM & ISRM) as well as the measured bar height at the end of the experiment, z_{exp}. In the lower right panel this is shown for both multiple fraction models (SRM8 & ISRM8). The SRM underestimates the bar height, while the ISRM slightly overestimates the bar height. The influence of including multiple fractions is seen in the right panel. In section 5.1.4 it was mentioned that including multiple fractions seems to smoothen out the bar. This is supported by Figure 5.12; although the position of the bar crest does not change the bar height decreases, indicating a smoothening of the bar profile. This is likely related to the finer sediment fractions being transported more offshore by the flow and the coarser fractions being deposited earlier. The decrease in bar height for the SRM is significantly larger than the decrease in bar height for the ISRM. An explanation is that this difference is because of the reduced erosion for the SRM8; less sediment is available for bar formation and thus the bar is lower.

In Figure 5.13 the change in bed level as computed by the models and measured is shown. This further supports the findings of Figure 5.12. Including multiple fractions in the model leads to a smoothened bar that is lower compared to the single fraction simulations. Simulating with multiple fractions shows a slightly reduced erosion of the upper part of the profile.

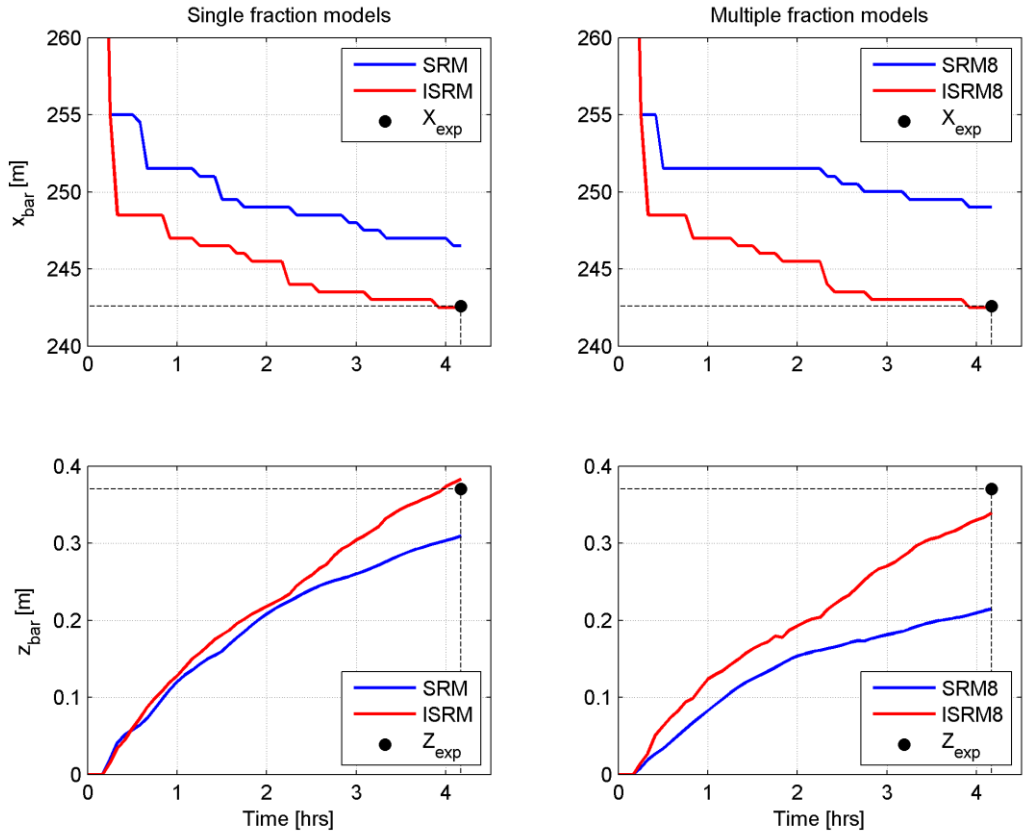

Figure 5.12 – Bar position (upper panels) and bar height (lower panels) for the SRM (blue) and ISRM (red). Single fraction models are depicted in the left panels, multiple fraction models (SRM8 and ISRM8) are depicted in the right panels. The final measured values of bar position and bar height is denoted in the figure using a black dot.

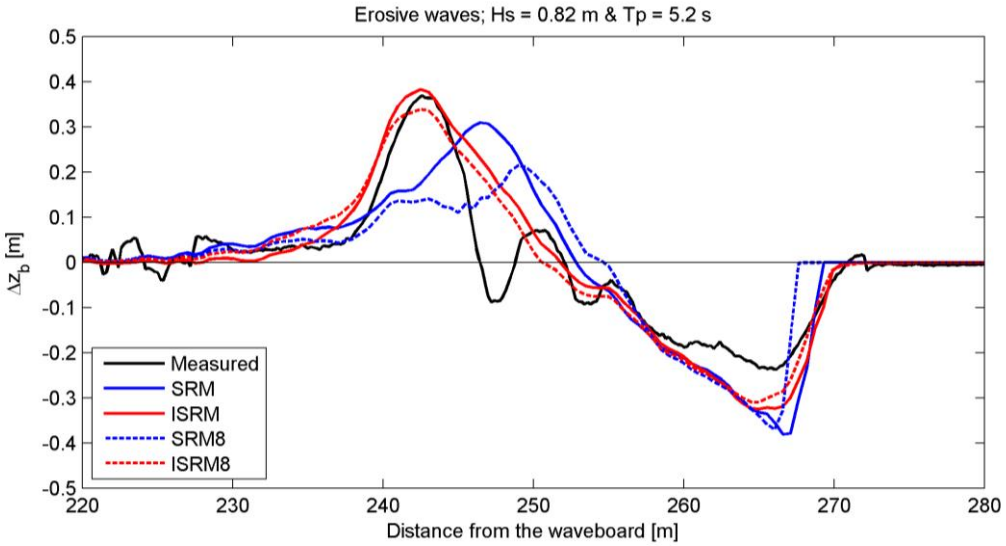

Figure 5.13 – Change in bottom depth as measured (black line), and computed for the SRM (blue, solid), the ISRM (red, solid), the SRM8 (blue, dashed) and the ISRM8 (red, dashed).

5.2.5 Sediment sorting processes

This section will focus on sorting processes: an assessment of how these are represented by the model compared with the experiments is made, as well as an analysis of how including sorting phenomena in the model computations influences model results.

First the SRM is analysed. In Figure 5.3 the results of the calibrated SRM8 are plotted. It was already mentioned that the SRM8 model run results in a coarsening of the sediment that is not found in the measurements (section 5.1.4). In Figure 5.14 the median grain diameter distributed over the vertical for the final situation is depicted. Around the swash zone (x = 265-270 m) no change in D50 is observed. The erosion at that location occurs for all fractions; the shear stress is large enough in that area to erode all sediments. From x = 250-265 m a coarsening in sediments is observed. The standard deviation and skewness are unchanged in that area, indicating a deposition of the coarser sediments due to declining shear stress and flow velocity, but an ongoing erosion of finer sediments. The deposition of the coarser sediments seems to have a mitigating effect on the erosion compared to the SRM (Figure 5.13).
From x = 240-250 m the bar is formed. A coarsening is observed in this area, just like a slight increase in standard deviation. Looking at Figure 5.14, coarse sediments are deposited at the bar location; the same trend as observed more onshore. The change in standard deviation (Figure 5.3) indicates a narrower sediment distribution. The skewness increases slightly (Figure 5.3), indicating a shift from a more coarse tail to a more fine tail. The increase in median diameter is related to settling of the coarser sediments and the further transport offshore of finer sediments. Although there is settling of finer sediments, more coarse sediments are deposited decreasing the standard deviation and also the median diameter.
Further offshore, fining is observed. The finer sediments are transported far offshore by the flow; this is related to the slowly declining sediment concentration along the profile (Figure 5.10). Once the flow loses transport capacity the finer sediments settle; the increase in skewness to fine skewed shows the distribution obtains a finer tail.
The SRM8 shows the influence of sorting processes on the simulation. Compared to the data however, it does not always show the right processes. The armouring of the upper shoreface and the accompanying reduction of upper shoreface erosion is not found in the experiment. In the experiment it was found that for high energetic waves, there is no entrainment sorting around the beach area while the model computations of the SRM8 clearly show there is. Only in the highest part of the profile sediments are eroded away uniformly. The suspension and transport sorting are spread out more than found in the experiment.

For the ISRM some different trends are observed. In Figure 5.3 it was seen that the ISRM8 is capable of accurately representing the change in D50. The coarsening in the bar trough and secondary bar area is not computed correctly by the model. This is due to the fact that the trough and secondary bar are not correctly calculated by the model. This will also translate into the sediment sorting, with coarser grains found around the trough area since the flow is calmer at that location. This is not found in the model, only a slight coarsening is observed around the bar area (Figure 5.5). The fining is represented accurately by the model computations.
Compared to the SRM8 there is no coarsening in the inner-surfzone and consequently there is also no large reduction of erosion. Coarsening of the sand is found from x = 255-240 m, where the flow loses transport capacity (Figure 5.5). Around this area no significant changes are found in the standard deviation and skewness, indicating that fine sediments are transported further. They settle further offshore, leading to a fine-skewed sediment distribution. No change is observed in the standard deviation from x = 230-240 m as opposed

to the observations. So, the fining is represented by the model simply through settling of the fine sediments as indicated by the skewness.
Compared to the observations made in section 3.2.1, the ISRM correctly shows no entrainment sorting in the upper part of the profile, and a clear suspension and transport sorting further offshore of this location.

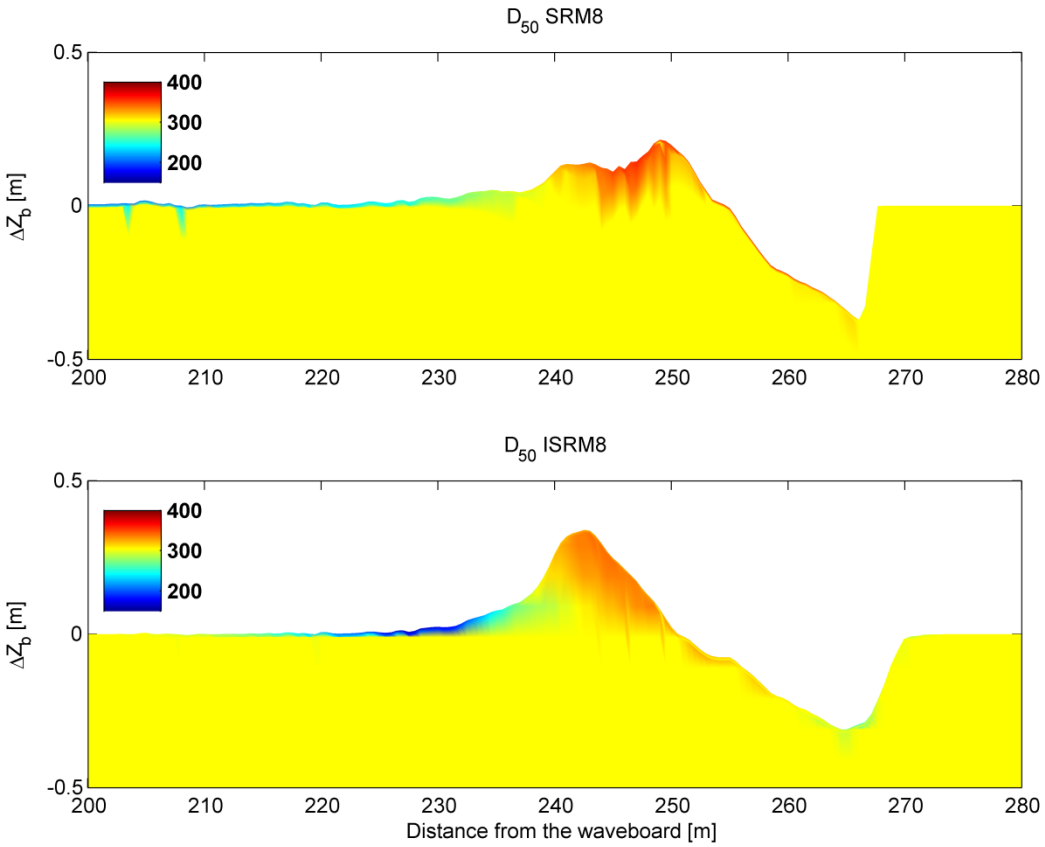

Figure 5.14 – Vertical distribution of the median grain diameter for the SRM8 (upper panel) and ISRM8 (lower panel) along the flume. Instead of the bed level, the change in bed level compared to the initially uniform bed Δz_b is taken on the y-axis.

5.3 Validation

Validation of the models is performed for the mildly accretive case and the accretive case of the experiments. No changes to the model settings are made; the model as calibrated for the erosive wave conditions is used. For both case 2 and 3 of the experiments figures showing the morphological development are shown in terms of change in bed level (Δz_b). Figures similar to Figure 5.2-Figure 5.5 and figures on bar behaviour are shown in appendix C.

5.3.1 Case 2 – Mildly accretive waves

Figure 5.15 shows the computed change in bed level for all models and the measured value. Both the ISRM and ISRM8 show more accurate upper shoreface erosion around the swash zone than the SRM and SRM8, which both show a large deviation of the measured value. Further offshore (x = 250 m to x = 265 m) all models show good agreement with the measurements. Around x = 248 m large deviation from the measured change in bed level are observed, related to the disappearance of the trough by the model. Around x = 240 m the ISRM and ISRM8 show better results than the SRM and SRM8, with the ISRM8 computing the most accurate bar height.

Figure C.1 visualizes the results of the SRM in a way similar to Figure 5.2. The SRM accurately reproduces the wave height along the flume and the highest wave height is computed correctly by the model.

Similar to Figure 5.3, sorting phenomena are depicted in Figure C.2. Clear entrainment sorting is found high in the profile and similar to case 1 coarser sediments settle earlier in the profile due to loss of transport capacity by the flow. Offshore fining is observed far from the bar crest, leading to an increase of skewness.

Bar height is growing, though not enough compared to the measurements. The bar is moving further offshore, this offshore movement is overestimated by the model; this is partly related to the definition of the bar crest position (Figure C.5).

Figure C.3 visualizes the results of the ISRM in the same way as Figure 5.4. The ISRM is able to reproduce the wave height trough the flume, but in the nearshore area the shoaling is underpredicted. The largest wave height is not computed correctly by the model. This does not seem to influence the prediction of the morphological development; continuation of erosion is predicted correctly, as well as the bar growth. The secondary bar disappears in the computation.

Sorting phenomena are shown in Figure C.4. It is observed that using multiple fractions has a mitigating effect on the upper shoreface erosion, yielding better results in this part of the profile. The predicted D_{50} shows resemblance to the measured D_{50}; a coarsening in the upper part of the profile is observed and offshore of the bar crest little change is found in the median grain size. The increase in standard deviation is modelled around the bar trough area, though much less than the measured value. Qualitatively, the same sorting processes as found in the experiments are observed with the model. The skewness[2] increases according to the model computations, indicating more fine sediments in the tail of the distribution. This is not found in the observations; as mentioned in section 3.2 the deposition of different sediments due to decreased wave power should restore the fine tail more to a symmetrical distribution.

All combined the model calibrated for storm conditions shows good results for a slightly lower wave condition. The ISRM seems to have more trouble than the SRM to accurately compute wave heights, but the morphology and sorting processes are computed more accurate for the ISRM8 than the SRM8, supporting what was seen for case 1: including long waves in the computation leads to the model predicting more realistic sorting phenomena. Re-calibration is possible to obtain a better prediction of the wave heights for the ISRM. This does not significantly influence the modelled morphology. The results of re-calibrating the model are shown in appendix F.

[2] *Note that although skewness is included in the images, extra analysis showed high sensitivity of this parameter questioning the reliability of this parameter to describe sorting processes.*

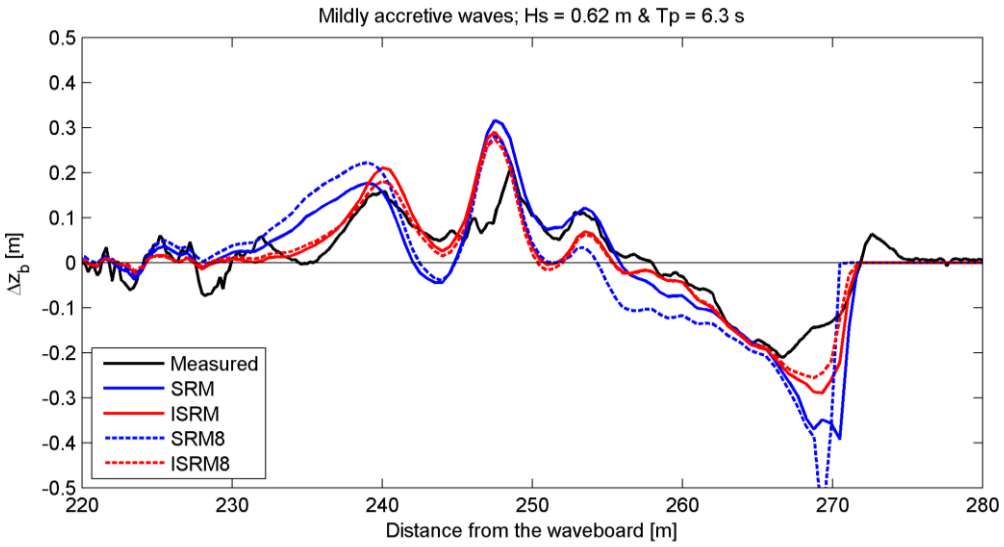

Figure 5.15 - Change in bottom depth as measured (black line), and computed for the SRM (blue, solid), the ISRM (red, solid), the SRM8 (blue, dashed) and the ISRM8 (red, dashed).

5.3.2 Case 3 – Accretive waves

In this section the models capability to simulate hydro-morphodynamics under accretive wave conditions is tested. It is well known that Delft3D has trouble simulating under accretive wave conditions, since upper shoreface and swash computations still lack accurate implementation (e.g. Tonnon et al., 2009; van Rijn et al., 2011).

Figure 5.16 shows the computed and measured change in bed level for the different modelling methodologies for the accretive wave conditions. All models show a continuation of erosion instead of accretion high in the profile. Lower in the profile all models, except the ISRM, qualitatively show the correct behaviour. Erosion is observed around x = 230 and accretion is observed around x = 240. Erosion is observed around x = 245 m and accretion is again observed around x = 250 m. The modelled accretion with the ISRM is likely related to sediment deposits that are eroded away from the upper shoreface. For the other models, the accretion around x= 258 m is most likely related to sediment deposits eroded away from the upper part of the profile. This means that beside the ISRM, all other modelling methodologies show the correct behaviour lower in the profile, and not in the swash zone. The ISRM8 and SRM8 show qualitatively the correct behaviour, but the magnitude of the changes is too small. The ISRM does show accretion at the right places, but not erosion at the right places, thus relating the erosion to deposits from sand eroded away from the upper shoreface.

Figure C.7 shows results of the SRM in a way similar to Figure 5.2. The SRM manages to reproduce the wave heights along the flume, with an accurate prediction of the highest wave height. The decline of the wave heights after the breaking point is not computed accurately by the model. Including multiple fractions in the computation leads to instabilities in the upper shoreface (Figure C.8); this is likely resolved by introducing extra diffusion through increasing the longitudinal bed slope parameter. Besides the instabilities little to no change in D_{50} is observed; the same goes for the morphology. Apparently, simulating with multiple fractions shows little to no change in the morphology of the upper part of the profile.

Figure C.9 shows results of the ISRM in a way similar to Figure 5.4. The computed wave height is underestimated in the shoaling zone and the highest wave height is predicted

significantly lower than measured. Adding multiple fractions into the computation does not yield significant improvement (Figure C.10); very small changes are observed in the computed D_{50}. The large fining is not computed by the model, since the accretion is also not modelled.

As expected, Delft3D shows difficulties in computing the hydro-morphodynamics under accretive wave conditions. Onshore transports are, however, modelled lower in the profile as can be seen in Figure 5.17. So, high in the profile, for shallower depths, Delft3D is not able to compute onshore transports and accretion, but lower in the profile the model seems capable of doing so. This will have some consequences for the case study performed in the second main part of this thesis; in section 6.1 this will be treated in more detail.

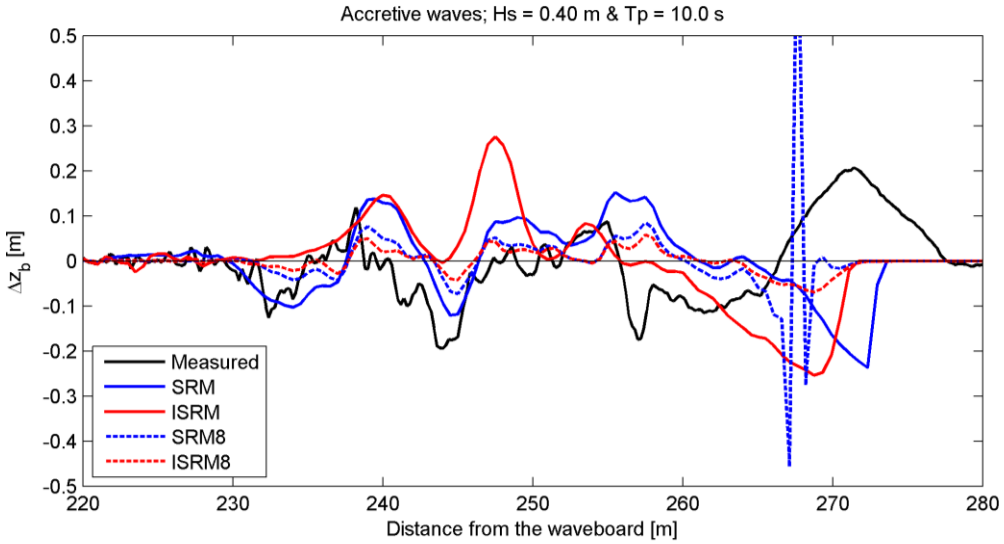

Figure 5.16 - Change in bottom depth as measured (black line), and computed for the SRM (blue, solid), the ISRM (red, solid), the SRM8 (blue, dashed) and the ISRM8 (red, dashed).

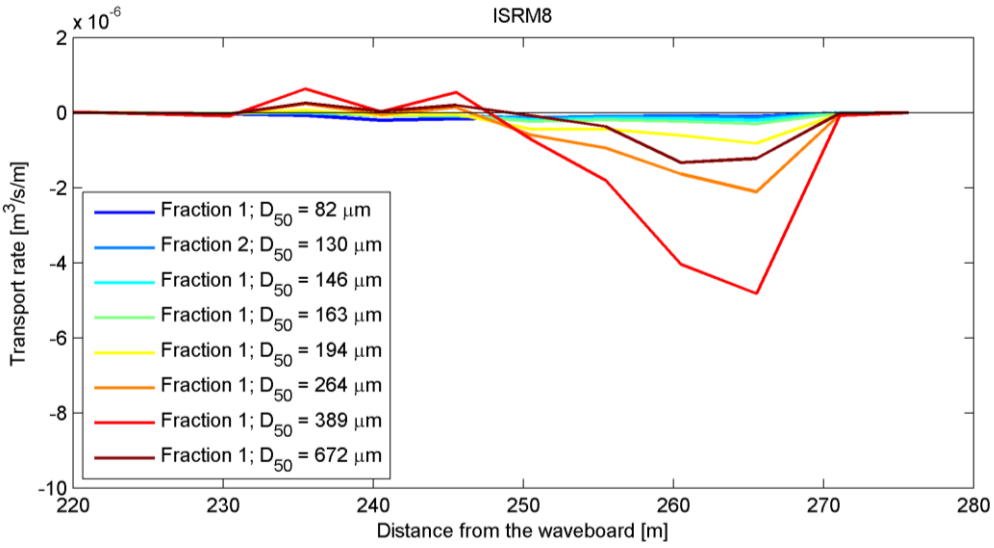

Figure 5.17 - Modelled sediment transport per fraction for the ISRM8. The SRM8 shows the same trends.

5.4 Model performance statistics

In this section the models performance is rated using the Brier Skill Score (BSS) for morphology and the Root Mean Absolute Error (RMAE) for wave heights based on van Rijn et al. (2003):

$$BSS = 1 - \frac{\left\langle \left(| z_{b,c} - z_{b,m} | - \Delta z_{b,m} \right)^2 \right\rangle}{\left\langle \left(z_{b,0} - z_{b,m} \right)^2 \right\rangle} \tag{5.7}$$

$$RMAE = \frac{\left\langle \left(| H_c - H_m | - \Delta H_m \right) \right\rangle}{\left\langle | H_m | \right\rangle} \tag{5.8}$$

H_c = Computed wave height
H_m = Measured wave height
ΔH_m = Error of measured wave height
$z_{b,c}$ = Computed bed level
$z_{b,m}$ = Measured bed level
$\Delta z_{b,m}$ = Error in measured bed level
$z_{b,0}$ = Initial bed level
$\langle .. \rangle$ = Averaging over timeseries

The error of measured wave height and the error of measured bed level are taken as the accuracy of the measurement equipment. This is 5 mm for the wave gauges and 10 mm for the bed profiler (section 3.1.2). A classification of the BSS and the RMAE is given in Table 5.7 as given by van Rijn et al. (2003):

Table 5.7 – Qualification of Brier Skill Score and Root Mean Absolute Error.

Qualification	Brier Skill Score	Root Mean Absolute Error
Bad	< 0	> 0.3
Poor	0.0 – 0.3	0.2 – 0.3
Fair	0.3 – 0.6	0.1 – 0.2
Good	0.6 – 0.8	0.05 – 0.1
Excellent	0.8 – 1.0	< 0.05

5.4.1 Hydrodynamics

The Root Mean Absolute Errors for the wave heights are summarized in Table 5.8 for the three different modelling methodologies. For the computation of the RMAE the nearshore wave heights are taken used (From x = 200 m until the beach).

Table 5.8 – Root Mean Absolute Errors for the wave heights for all simulations performed in this section

Model type	Case 1 Erosive	Case 2 Mildly Accretive	Case 3 Accretive
SRM	0.03 m	0.02 m	0.05 m
ISRM	0.04 m	0.05 m	0.09 m
SRM8	0.02 m	0.03 m	0.05 m
ISRM8	0.03 m	0.05 m	0.09 m

Predicted wave heights for the erosive case are classified as excellent predictions. This was already concluded from the figures at section 5.1.4. For the mildly accretive case it was shown that for the ISRM the computed wave heights were too low in the shoaling zone; the highest wave height was significantly lower than the measured value. Overall, the prediction of wave heights still classifies as good. The same goes for the accretive case. For the SRM especially lowering of the wave heights after breaking is not computed correctly, leading to the higher RMAE. For the ISRM the wave heights in the shoaling zone are underestimated leading to a higher RMAE, though the predictions still classify as good.

5.4.2 Morphology

The Brier Skill scores for morphology are given in Table 5.9 for the three test cases and four different modelling methodologies.

Table 5.9 – Brier Skill Scores for all simulations performed in this section

Model type	Case 1 Erosive	Case 2 Mildly Accretive	Case 3 Accretive
SRM	0.50	0.32	-0.98
ISRM	0.78	0.64	0.11
SRM8	0.56	0.05	-0.24
ISRM8	0.83	0.69	0.09

Simulations for the erosive case show that Delft3D is capable of accurately simulating morphological development with skill ranging from fair (SRM) to excellent (ISRM8). The biggest increase in performance is observed when long waves are included in the computation. This was already concluded from simply looking at the figures, but it also shows in the BSS. Adding multiple fractions in the computation also shows an improved performance; including sorting phenomena leads to better morphodynamic predictions of the model.

Delft3D performs slightly less for the mildly accretive waves, showing even poor skill for the SRM8. This is mainly caused by the extremely large upper shoreface erosion computed with the SRM8. Also for this case it seems that including long waves in the computation enhances performance. Including multiple fractions improves performance for the simulation where long waves are included in the computation, but it reduces performance dramatically for the standard roller model. This raises the thought that for the Delft3D model to work optimally with multiple fractions, excellent prediction of the bed shear stresses due to waves and undertow is needed; it was indicated in section 5.2.3 that this is the case for the model including long waves. The low BSS for the SRM8 model raises suspicions that the long wave model indeed leads to more realistic predictions of bed shear stresses and corresponding sediment transports.

For the accretive case, Delft3D performs in the range of bad to poor. It is a known problem that Delft3D is not able to accurately compute morphodynamics under accretive wave conditions and the BSS for case 3 indeed supports this notion. It is noted that the BSS might not be the best performance indicator for the accretive conditions, as it was shown in section 5.3.2 that although accretion in the swash zone was not modelled correctly, lower in the profile qualitatively the correct trends are modelled and that onshore transports are observed.

5.5 Sensitivity

A sensitivity analysis on the free parameters given in Table 5.2 was performed. This was done for the first case of the experiments (erosive wave conditions) for the SRM and ISRM. For ISRM8, sensitivity is performed on the active layer thickness and the distribution of the sediment fractions. The findings of the analysis are summarized in this section; background is presented in appendix E. Sensitivity is valued on morphology.

5.5.1 Set-up of sensitivity analysis

To calibrate the model, a number of parameters were used, also shown in Table 5.10. The sensitivity analysis for the SRM and ISRM is performed on the parameters used to calibrate both these models. The parameters were deviated from their calibrated value to a lower and an upper boundary that is taken the same for both the SRM and ISRM. This range is also shown in Table 5.10. The sensitivity of the parameters is rated by using the simulated morphology.

For the multiple fractions model, a sensitivity analysis is performed just for the ISRM8. Sensitivity of the active layer thickness and the number of fractions as well as the distribution of the fractions is rated on the sorting processes, e.g. the change in median grain diameter.

5.5.2 Results of the sensitivity analysis

In appendix E.2 the results of the sensitivity analysis on the free parameters of the SRM and ISRM are depicted. Figure 5.18 shows the difference between the models ran with default settings and calibrated settings for the SRM, while Figure 5.19 shows this for the ISRM.

Identifying the most sensitive parameters can be important for rapid assessments; for a first assessment on the model performance it should be enough to just tune the highly sensitive parameters while the rest of the parameters can be left at default value. In Table 5.10 the free parameters and their sensitivity are summarized.

The classification on high and low sensitivity is explained in appendix E.1. Basically, a parameter is defined as highly sensitive if the relative change of this parameter leads to an equal or larger relative change in the model outcome.

A note is made on the parameters belonging to the multiple fractions; the number of underlayers and the thickness of the underlayers do not influence the computations whatsoever; they mainly determine the accuracy of the outcome of the layered bed stratigraphy, thus how fast sediments are stored in the base layer.

Table 5.10 – Sensitivity of the free parameters. Background is found in appendix E.

Parameter	Keyword	Range	Sensitivity
β_{rol}	Betaro	0.05 – 0.15	High
γ_w	Gamdis	0.45 – 0.65	High
f_{bed}	Bed	0.10 – 1.50	Low
$f_{bed,w}$	BedW	0.10 – 1.50	Low
f_{sus}	Sus	0.30 – 1.20	High
$f_{sus,w}$	SusW	0.01 – 0.50	Low
α_{bs}	Alfabs	1.00 – 10.0	High
Additional options multiple fractions/Layered bed stratigraphy			
-	ThTrLyr	0.01 – 0.10 m	High
-	Number of fractions	5 – 12	-
-	Division of fractions	Equal – Fine tail	-

The roller slope coefficient (β_{rol}) shows a high sensitivity for both the SRM (Figure E.1 & Figure E.8). Based on this study, it seems to provide a good handle to control upper-

shoreface erosion and subsequent bar formation. Lower values give a sharper, more pronounced bar but also larger upper-shoreface erosion. In this study it was attempted to find a balance between the overestimation of the upper-shoreface erosion and pronunciation of the bar.

The wave breaker parameter (γ_w) also showed a high sensitivity for both the SRM (Figure E.2) and the ISRM (Figure E.9). This parameter influences the wave height in the shoaling zone and subsequently the morphological changes in the active part of the profile. This parameter is mainly used to get a correct representation of the wave heights. When this is achieved, the parameters concerning the morphology are tuned.

The current related bed load scaling factor (f_{bed}) shows a low sensitivity for both the SRM (Figure E.3) and the ISRM (Figure E.10). The same goes for the wave related bed load scaling factor, $f_{bed,w}$ (Figure E.4 & Figure E.11) and the wave related suspended load scaling factor, $f_{sus,w}$ (Figure E.6 & Figure E.13). However, it turned out that tuning of these low-sensitive parameter can optimize model outcome in terms of upper-shoreface erosion and pronunciation of the bar (see also Brière & Walstra (2006); Brière et al. (2010); Giardino et al. (2011); Ruessink et al. (2003)).

The current related suspended load scaling factor shows a high sensitivity for both the SRM (Figure E.5) and the ISRM (Figure E.12). For the SRM the default value delivers good results, and the parameter does not need calibration, for the ISRM however, the parameter needs calibration to give the correct answer. It shows that suspended load transport by the undertow is the dominant mechanism for erosive wave conditions. With the tuning of this parameter a certain degree of control over the upper-shoreface erosion and the subsequent bar characteristics is obtained.

The longitudinal bed slope factor (α_{bs}) shows a high sensitivity because this parameter is mainly used to eradicate instabilities of the morphology. Taking a too low value of α_{bs} leads to instabilities in the computed bed level, in general it is taken as low as possible too still deliver a stable solution.

The options that were tested for the multiple fractions model were the thickness of the transport layer, the number of fractions and the way the sample was divided into fractions. These options did not significantly influence the morphology (no changes visible), but they do determine the accuracy with which sorting processes are solved. Therefore, results of this sensitivity study are shown for the grain size parameters D_{50}, σ_G, and Sk.

The thickness of the active layer is very important for getting the sorting processes correctly (Figure 5.20). The magnitude of the fining is greatly determined by the active layer thickness, and the tails of the distribution are also predicted more accurately for a lower active layer thickness.

In Figure 5.21 the sensitivity of the model outcome for the fraction division is depicted. The model does not seem very sensitive for the number of fractions, but the way the fractions are divided does seem very important. The fractions that were divided with an emphasis on the fine tail of the sample seem to perform slightly better than the ones that have an equal distribution. In Figure 4.3 the division of the original sample into eight fractions, Figure B.1 to Figure B.3 show other different distributions.

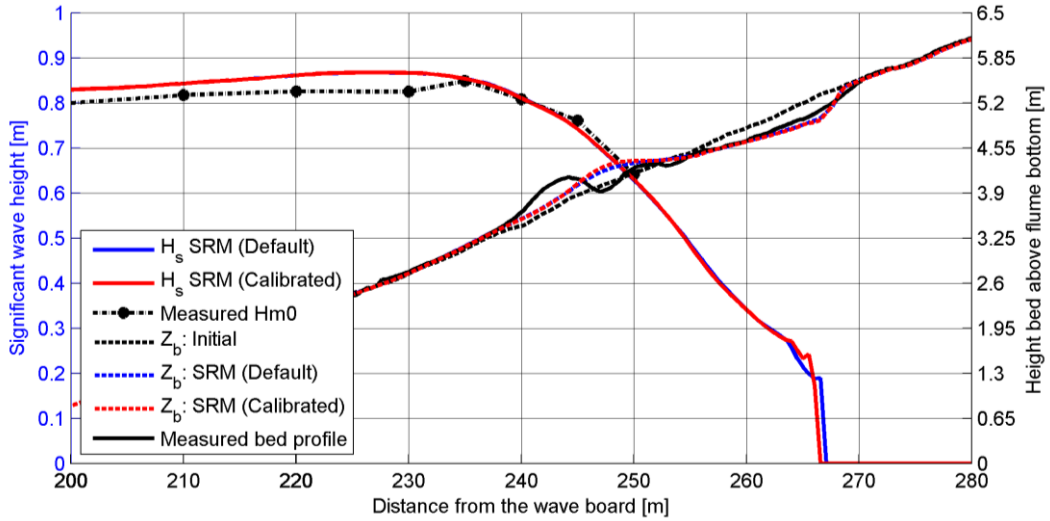

Figure 5.18 - The effect of calibration on the results of the SRM.

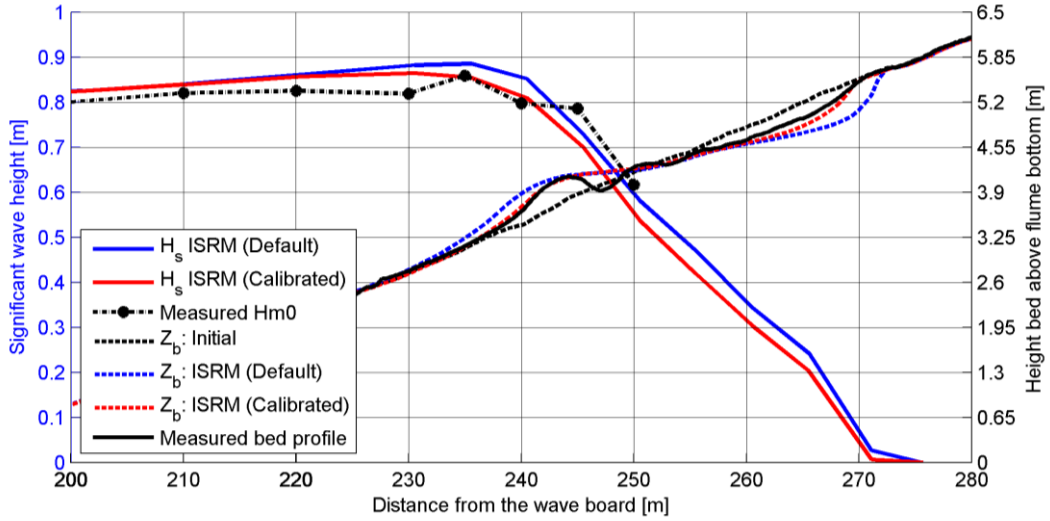

Figure 5.19 - The effect of calibration on the results of the ISRM

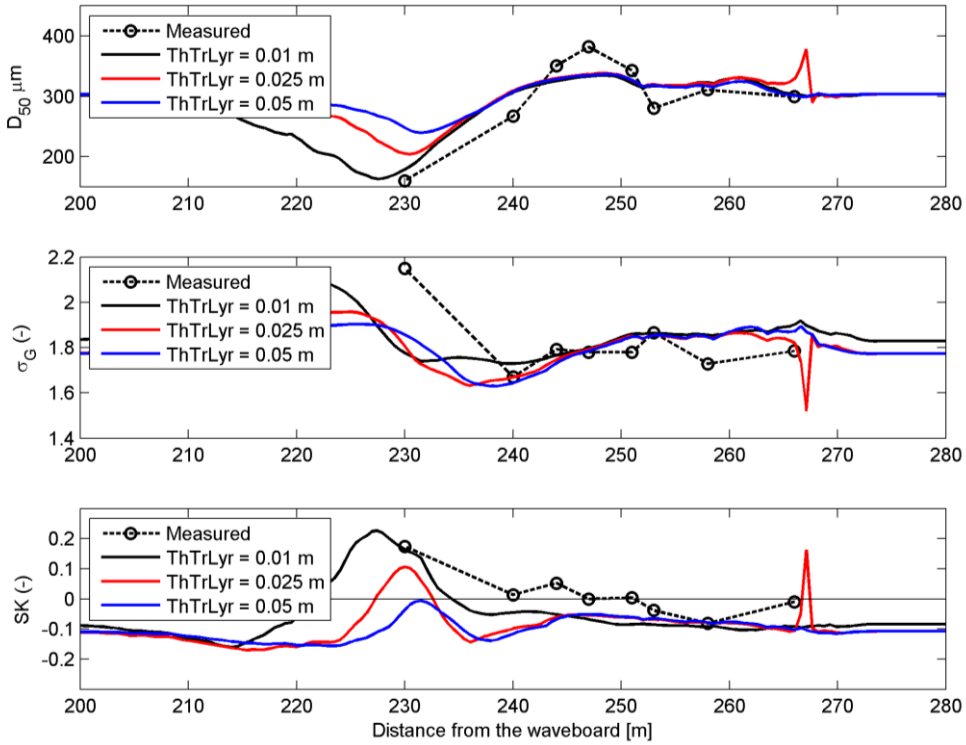

Figure 5.20 - Sensitivity of the active layer thickness (ThTrLyr) for the ISRM8.

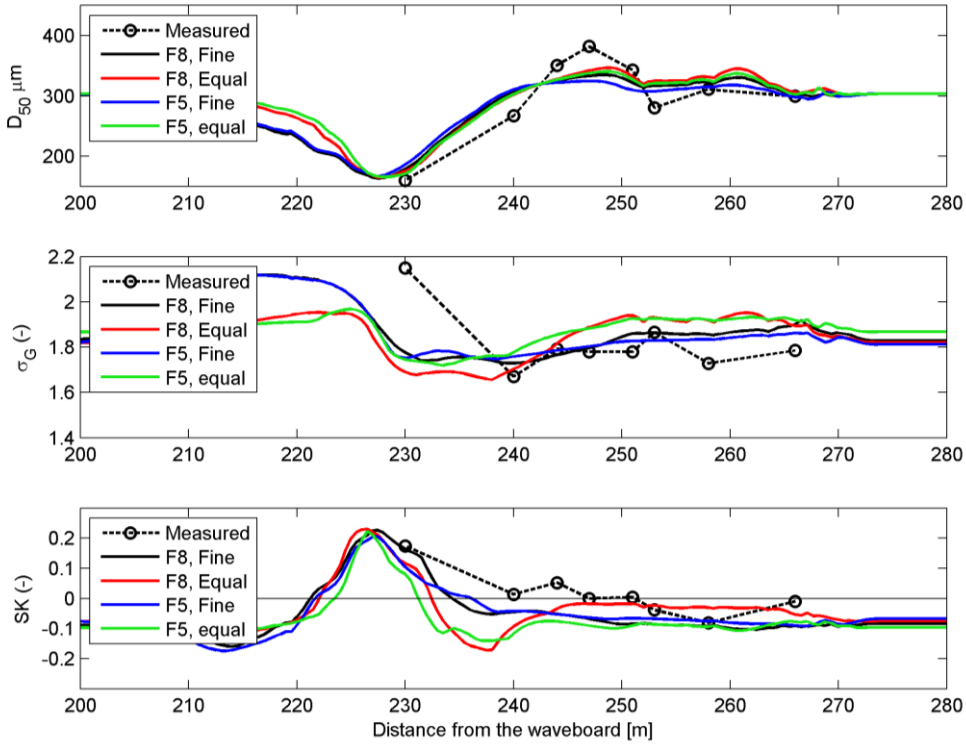

Figure 5.21 - Sensitivity of the division of the sample into fractions. Results are shown for the ISRM8, for a division that emphasizes the fine tail (black) and one that divides the sample into equal fractions (red). The same is shown for the ISRM5, with the fine division in blue and equal division in green.

5.6 Summary

A total number of four modelling approaches were tested (see section 4.2). First the effect of applying different wave models was investigated. This effect was studied for models using only one sediment grain size (SRM & ISRM). During calibration it turned out that the ISRM needs more calibration than the SRM, since scaling of the transports is necessary to optimize the result. However, comparing results of the SRM and ISRM with one another large differences are found in the computed morphology (Figure 5.13). Including long waves into the computation leads to an improvement in simulated bar dynamics; both the location and the magnitude of the breaker bar are computed more accurately with the ISRM compared to the SRM (Figure 5.12). This was related to additional shear stresses induced by the long waves that enhance offshore suspended sediment transport.

After analysing the different wave models the effect of including multiple sediment fractions in the computation was investigated as well as the model's capability of simulating sorting processes. The SRM and ISRM were extended to simulate with eight sediment fractions and sorting processes were investigated by monitoring the development of the median grain size, the standard deviation and skewness of the sediment. Both the SRM8 and ISRM8 are affected by the inclusion of multiple sediment fractions; the bar is smoothened out somewhat caused by the spatial variation in settling of the sediments (suspension sorting). The SRM8 is most influenced by the multiple fractions because of armouring of the upper shoreface caused by entrainment sorting. The wave power of the short wave model does not yield a large enough shear stress to erode all sediment fractions uniformly as observed in the experiments; the coarsest fractions are brought into motion less (transport sorting). The ISRM8 does not show this behaviour (section 5.1.4).

Offshore fining due to suspension sorting is predicted by both models. However, the SRM8 shows a larger offshore movement of the finer sediments; this is supported by the higher offshore suspended sediment concentration profiles. The ISRM8 has a much stronger decline in suspended sediment concentration profiles in offshore direction, leading to faster suspension of the fine sediments (Figure 5.10).

Although both the SRM8 and ISRM8 are capable of representing sorting processes when simulating with multiple fractions, the ISRM8 yields much better results. This is attributed to the more accurately computed shear stresses due to including long wave motions into the simulations (section 5.2.3). Since the response of different sediment classes is dependent on the shear stress, an accurate computation of this quantity is crucial, which is shown by the results.

The model as calibrated for storm conditions was then validated for experimental cases 2 and 3, with lower, thus more accretive, wave conditions. For case 2 again the ISRM8 shows the best model results (section 5.3.1). The shoaling is underestimated by the model, but the morphology and sorting processes are computed accurately. The SRM8 shows accurate prediction of the wave heights and a correct shoaling, but overestimates the erosion in the upper part of the profile. Besides this the SRM8 also shows difficulties predicting bar height and location as well as sorting phenomena.

For case 3 both the SRM8 and ISRM8 show poor results (section 5.3.2). It is that Delft3D has difficulties computing morphodynamics under accretive wave conditions. Although the ISRM8 shows slightly better results than the SRM8, both models are not able to simulate accretion in the upper part of the profile, therefore also not accurately representing the sorting processes. However, in deeper water onshore transports were observed in the model computations.

To independently compare the performance of the four different models the Brier Skill Score was used (section 5.4). The Brier Skill Score shows that for all three cases the model performs best when including long waves into the computation; significant improvements are observed when calculating with long waves, leading to a Brier Skill Score as high as

excellent. To accurately compute the development of the profile, it is not necessary to simulate with multiple sediment fractions. The Brier Skill Score slightly increases for the simulations taking into account multiple sediment fractions, which is mainly related by reduced upper-shoreface erosion. The bar is computed slightly less than the models that only use one sediment fraction.
If the aim of a study is to investigate sorting processes, then the use of multiple sediment fractions is unavoidable, and Delft3D is capable of simulating those. A modelling approach that explicitly calculates the effect of bound long waves shows significantly better results in terms of sorting. Therefore, the model used for the continuation of this thesis, where the role of sediment sorting during the development of nourished beaches is investigated, will be the ISRM8.

Part III – Nourishment case study

6 Set-up of the case study

In this section the set-up of the nourishment case study is discussed. In this part of the thesis the emphasis will be on investigating sorting processes at the development of nourishments. This will be investigated using the Delft3D-modelling approach including long waves and multiple sediment fractions since this modelling approach proved to deliver the best results.
In section 6.1 the set-up of the case study will be discussed. The choices made to get to the structure of the case-study are treated, as well as the available data for validation. In section 6.2 an overview of the simulations is given.

6.1 Structure of the case-study

In the case study sorting processes are investigated for several nourishment designs: two shoreface nourishments and one beach nourishment. The designs are based on studies of Walstra et al. (2011) and Vousdoukas et al. (2014). The study of Vousdoukas was carried out in the GWK at Hannover, with the aim of investigating monitoring equipment for detailed measurement of swash-zone processes by using the development of a beach nourishment.
The study of Walstra was carried out in the Scheldt flume at Deltares in Delft, with the purpose of investigating the effect of the design height of shoreface nourishments on dominant physical processes playing a role in the development of the profile.
In the study of Vousdoukas et al. (2014) a linear 1:15 slope profile was brought into a more 'natural', close-to-equilibrium shape by applying several erosive and accretive wave conditions. They replenished the profile by adding a nourishment at the beach face (Figure 6.1). After nourishing the beach they subjected the profile to a series of accretive waves during 3 separate tests and followed up by an equal number of tests with more erosive conditions monitoring the development between each test.

In this case study three nourishment designs are investigated and evaluated: two shoreface nourishment designs and one beach nourishment designs. The beach nourishment (Figure 6.1) design is based on the study of Vousdoukas et al. (2014) and the shoreface nourishment designs (Figure 6.2) are based on the study of Walstra et al. (2011). The Hannover Flume model is used to simulate the morphological development of the nourishments. The experiment concerning the beach nourishment was performed in the GWK under similar conditions as the experiments from chapter 0; bathymetric data and wave data on those experiments is made available to use in this thesis so a quantitative validation can be performed for the beach nourishment. The shoreface nourishments are evaluated in a more qualitative way since those experiments were performed in the Scheldt flume at Deltares, which is smaller than the GWK. All in all validation can be performed for all different nourishment designs; a direct comparison with data can be made for the beach nourishment design and a more qualitative validation can be made for the shoreface nourishment designs.

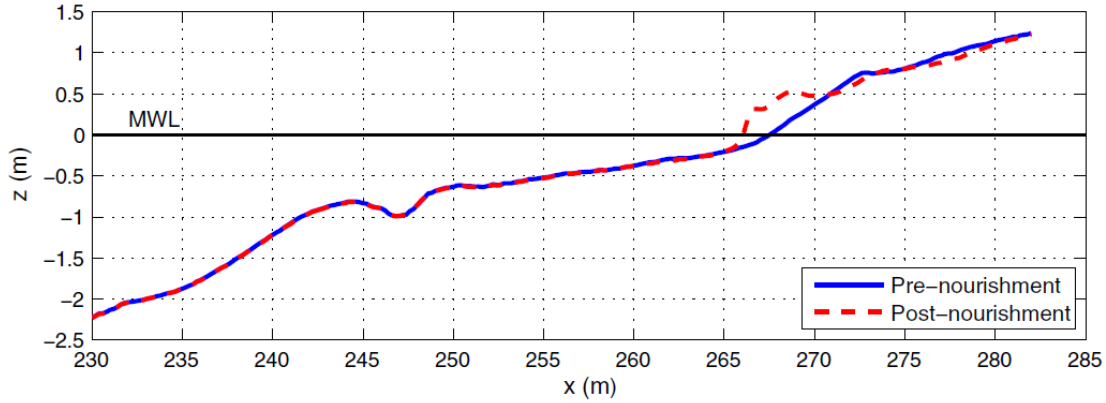

Figure 6.1 – Nourished profile subjected to waves in the study of Vousdoukas et al. (2014)

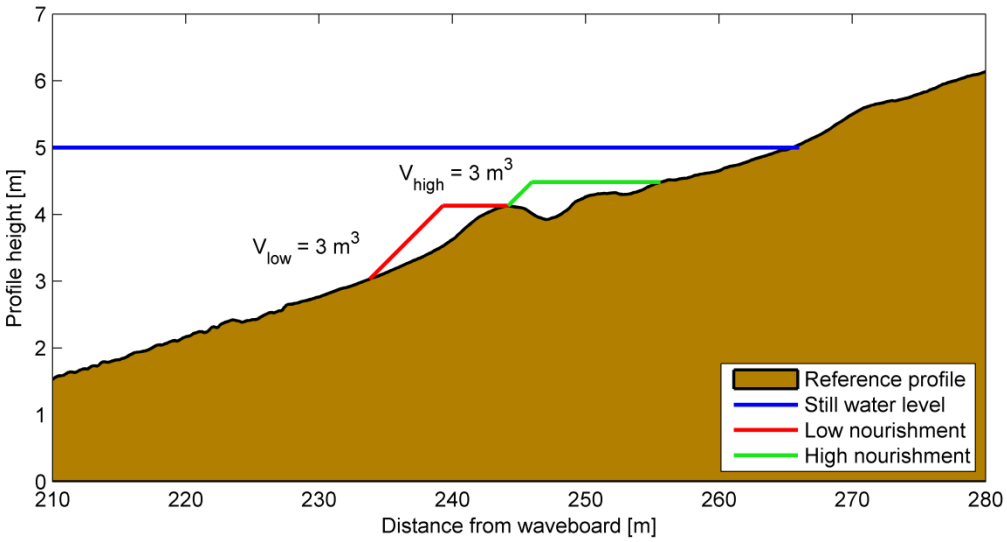

Figure 6.2 – Shoreface nourishment desings in the Hannover Flume model. Reference profile is taken as the bathymetry at the end of case 1 of previous experiments. Both nourishment designs have an equal volume of sand.

6.2 Modelling approach

In Table 6.1 a summary of the simulations is given. The abbreviation SFN stands for shoreface nourishment and BN stands for beach nourishment. For the simulations applying to beach nourishments the accretive and erosive conditions are run directly after each other, without stopping or resetting the model. This is done because the experiments are performed in the same manner; the erosive waves are run directly after the accretive waves, the nourished profile was not reconstructed as opposed to the experiments concerning the shoreface nourishments.

The ISRM8 as described in section 4.2 and calibrated for storm conditions in section 5.1 is used to model sorting phenomena for nourished beaches. The reference simulations that are performed function as a benchmark to quantify the effect of nourishments. They run the same profile as the nourished beaches minus the nourishment. In this case, a direct comparison between physical processes for natural and nourished beaches can be made.

The beach nourishment is subjected to the exact same wave conditions as used in the experiment of Vousdouskas et al. (2014). In this way a direct comparison between the model outcome and the experiments is performed. For the beach nourishment the erosive conditions are H_s = 0.90 m and T_p =5.17 s and the accretive conditions are H_s = 0.51 m and T_p =7.00 s.
The profiles nourished at the shoreface will be subject to an erosive and a mildly accretive wave condition. Erosive wave conditions for the shoreface nourishments are H_s = 0.82 m and T_p = 5.2 s. Mildly accretive wave conditions for the shoreface nourishments are characterized by H_s = 0.62 m and T_p = 6.3 s. It is chosen to only simulate erosive and mildly accretive waves on these profiles, since the model has shown to be able to accurately compute hydro-morphodynamics and sorting processes under these wave conditions. In this way, the model outcome for the nourished profiles is thought to be more reliable.
Besides varying the wave conditions and the design of the nourishments, also the grain size of the fill material is varied. For each wave condition and nourishment design, a simulation is performed using a similar grain size for the nourishment fill material than the native beach (D_{50} = 300 µm) and a simulation is performed using a larger grain size for the nourishment fill material than the native beach (D_{50} = 400 µm). The native sand has the same distribution as described in section 3.1.
Initial sediment composition of the nourished profiles is depicted in Figure 6.3 - Figure 6.5. The coarser sediment of the nourishment is described in a similar way as the native beach, according to the method explained in section 4.4.2: the sand is divided in 8 fractions, with an emphasis on the fine tail of the sediment. Besides being able to construct a different grain distribution for the nourished sand, this distribution also allows for tracing the nourished sand through the entire simulation. However, this also implies that simulations B02, H03, H04, L03 and L04 are now using 16 sediment fractions (8 for the native sand and 8 for the nourished sand) which will increase the computational time.

Table 6.1 – Summary of the simulations performed for the case study

Simulation	Wave condition	Design	Fill material	Duration
R01	Erosive	Reference SFN	-	4 hrs
R02	(Mild) Accretive	Reference SFN	-	8 hrs
R03	1) Accretive 2) Erosive	Reference BN	-	1) 2 hrs 2) 3 hrs
B01	1) Accretive 2) Erosive	Beach Nourishment	$D_{50,nou} = D_{50,na}$	1) 2 hrs 2) 3 hrs
B02	1) Accretive 2) Erosive	Beach Nourishment	$D_{50,nou} > D_{50,na}$	1) 2 hrs 2) 3 hrs
H01	Erosive	High SFN	$D_{50,nou} = D_{50,na}$	4 hrs
H02	(Mild) Accretive	High SFN	$D_{50,nou} = D_{50,na}$	8 hrs
H03	Erosive	High SFN	$D_{50,nou} > D_{50,na}$	4 hrs
H04	(Mild) Accretive	High SFN	$D_{50,nou} > D_{50,na}$	8 hrs
L01	Erosive	Low SFN	$D_{50,nou} = D_{50,na}$	4 hrs
L02	(Mild) Accretive	Low SFN	$D_{50,nou} = D_{50,na}$	8 hrs
L03	Erosive	Low SFN	$D_{50,nou} > D_{50,na}$	4 hrs
L04	(Mild) Accretive	Low SFN	$D_{50,nou} > D_{50,na}$	8 hrs

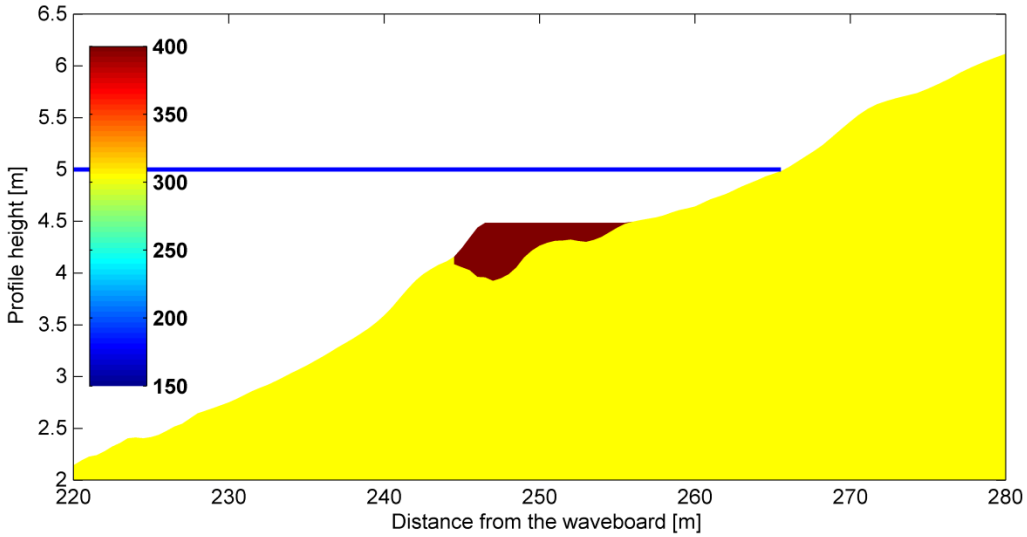

Figure 6.3 – Initial sediment composition using a coarser grain size for the fill material, high design of the shoreface nourishment.

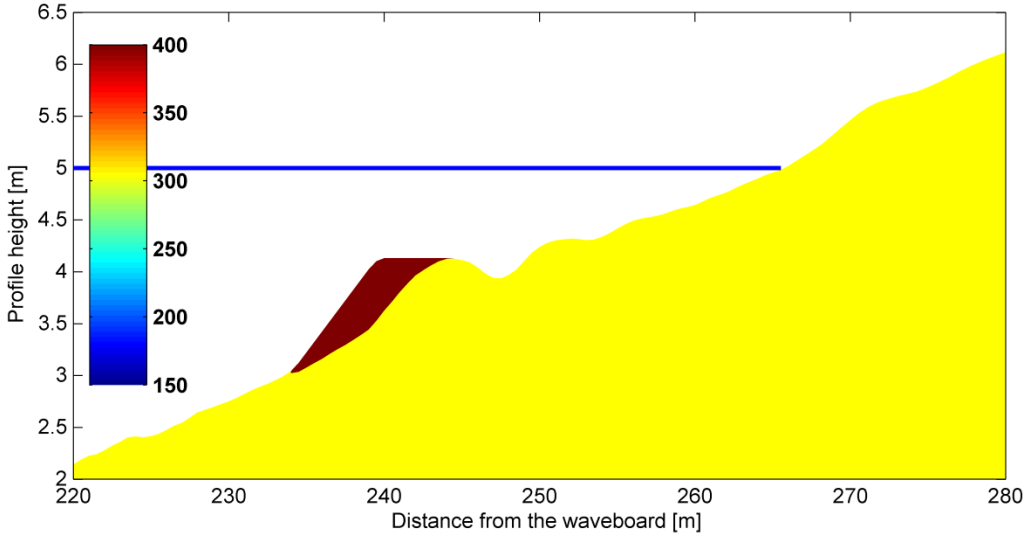

Figure 6.4 – Initial sediment composition using a coarser grain size for the fill material, low design of the shoreface nourishment.

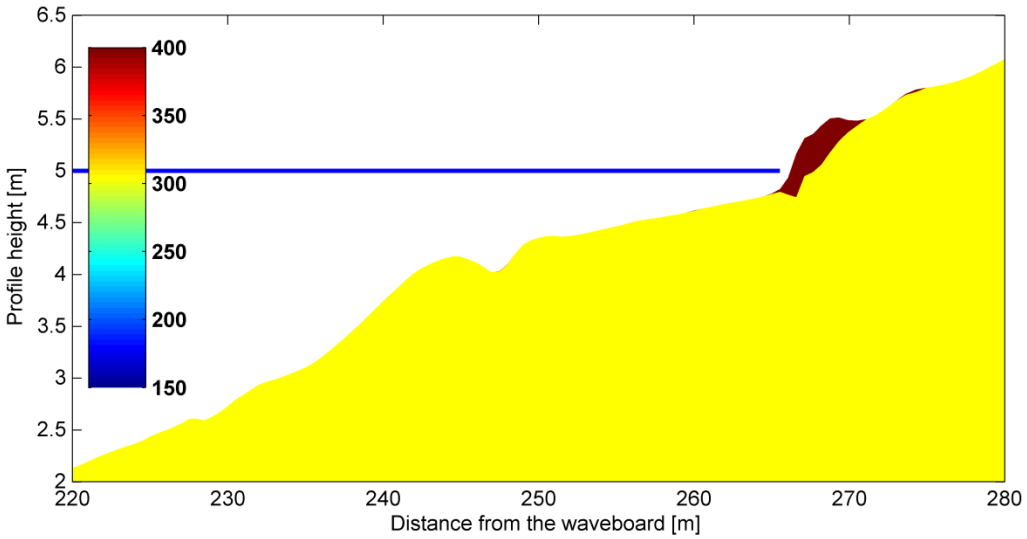

Figure 6.5 - Initial sediment composition using a coarser grain size for the fill material, beach nourishment.

7 Model results

In this section the results of the case study are shown and discussed. First the validity of the model results are checked by comparing them to the available data; for the shoreface nourishment designs this will be a qualitative validation while for the beach nourishment a quantitative validation can be performed.
After showing the model's capabilities in simulating hydro-morphodynamic processes of the nourished beaches, an in-depth evaluation of the processes is made. The effect of the nourishments is investigated by looking at differences in erosion of the upper part of the profile. Next to the effects of the nourishment on the morphological development of the beach also the sorting processes are investigated.

For the case study a large number of simulations are performed resulting in a several figures. The most important figures are shown in this chapter, while additional figures are provided as attachment in appendix D.

7.1 Comparison of the results to the available data

In this section the performance of the model is investigated. First, a direct comparison of the simulated results for the beach nourishments is made based on the data of Vousdoukas et al. (2014). Then, a qualitative comparison for the shoreface nourishments is made with the measured development derived from the experiments of Walstra et al. (2011).

7.1.1 Morphological development of the beach nourishment

For analysing the performance of the model in simulating the morphological development of the beach nourishment the result of simulation B01 is compared to the data of Vousdoukas et al. (2014) where morphological development was measured on regular time intervals. In Figure 7.1 the model computations are plotted next to the measurements for both phases in the modelling. In this figure only the final computed bathymetries of both phase 1 and phase 2 are shown, along with the measured bathymetry.

Phase 1 is characterized by an accretive wave condition (H_s = 0.51 m & T_p = 7 s) and phase 2 is characterized by an erosive wave condition (H_s = 0.9 m & T_p = 5.17 s). During phase 1 barely any change was observed in the surf zone; most changes were found at the beach face. A large part of the nourished sands was distributed along the profile section between -0.5 m < z < 0.5 m MWL. During phase 2 the erosion of the nourishment continued, eventually leaving a very small artificial berm. However, under the higher waves much more activity was observed in the surf zone. At the end of the testing, the nearshore bars migrated offshore for approximately 1-2 m, while overall a large portion of the sand initially added at the beach-face was deposited at the nearshore bars.
The results of phase 1 of simulation B02 show a similar trend to the observations; little to no activity is observed in the surf zone and a redistribution of the nourished sands high in the profile is computed. However, the simulation results show a small deposition between the primary and secondary bar, leading to an increase in bed level. Compared to the observations the model underestimates the erosion of the beach nourishment.
Phase 2 of simulation B02 shows increased activity in the surf zone with an offshore migration and growth of the breaker bar. The erosion of the nourishment continues until completely eroded away. The model overpredicts the erosion in the upper part of the profile, and in the measured trough area secondary bar dynamics are lost in the simulation.

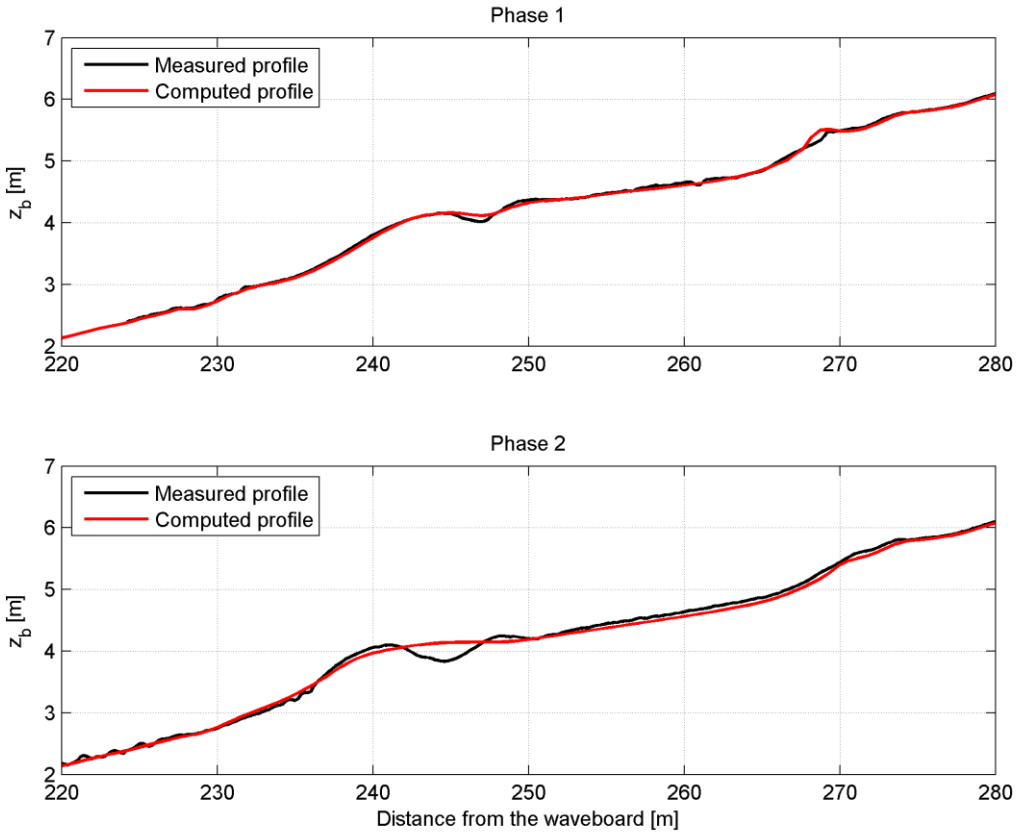

Figure 7.1 – Measured (black) and computed (red) profiles at the end of phase 1 (upper panel) and phase 2 (lower panel).

The Brier Skill Score was used to classify the performance of the model for both phase 1 and 2. For phase 1 a BSS of 0.48 was found, indicating a fair performance of the model. This is a surprisingly high skill score for Delft3D which usually underperforms for accretive wave conditions. For phase 2 a BSS of 0.63 was found, indicating a good performance of the model.

Despite some differences in the computed erosion rates with the measurements (see also section 7.2.1), the model does show the correct trends for both phases (little to no activity in the surfzone in phase 1, and large activity in the surfzone during phase 2).

Therefore, looking at the results of simulation B01, it can be concluded that the model is capable of representing the measured data of the morphological development of a beach nourishment, making the model a suitable tool for investigating sorting processes in combination with of a beach nourishment.

7.1.2 Morphological development of the shoreface nourishments

To analyse the performance of the model in simulating the morphological development of the shoreface nourishments the results of simulations R01, R02, H01, H02, L01 and L02 are investigated. Nourished sand has the same distribution as the native sand, corresponding to the set-up of the experiments of Walstra et al. (2011). A note must be made that in this study, the lower wave conditions used are categorized as ‘mildly accretive’ while in the study of Walstra et al. the lower wave conditions used are classified as ‘accretive’. Looking at the

Dean numbers however, there is not much difference between the two. However, these conditions were classified as mildly accretive in part II of the thesis; this classification will be kept the same for this part of the thesis, hence mildly accretive instead of accretive.
Results of the model computations are compared to observations of Walstra et al. (2011), these observations are provided in appendix D.1.

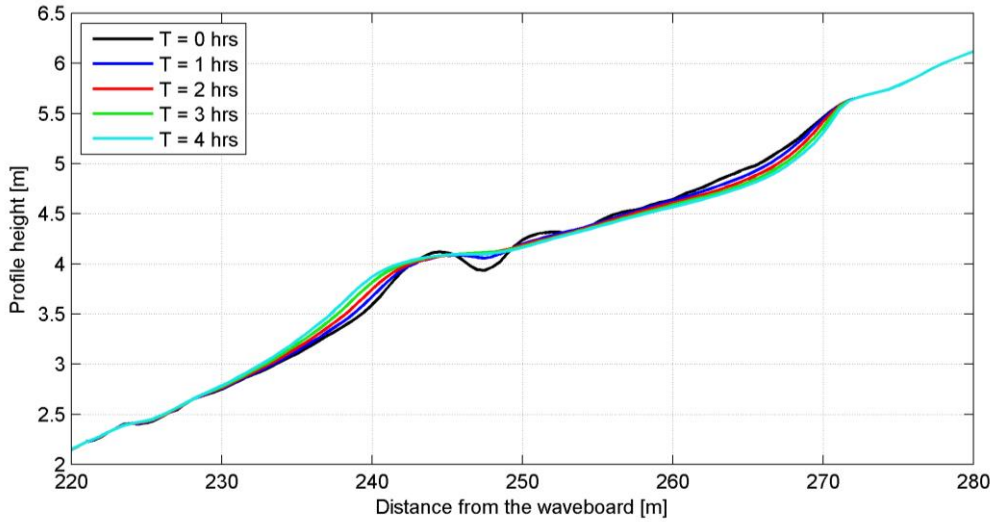

Figure 7.2 – Computed morphological development of simulation R01 (Erosive waves, Hs = 0.82 m & Tp = 5.2 s)

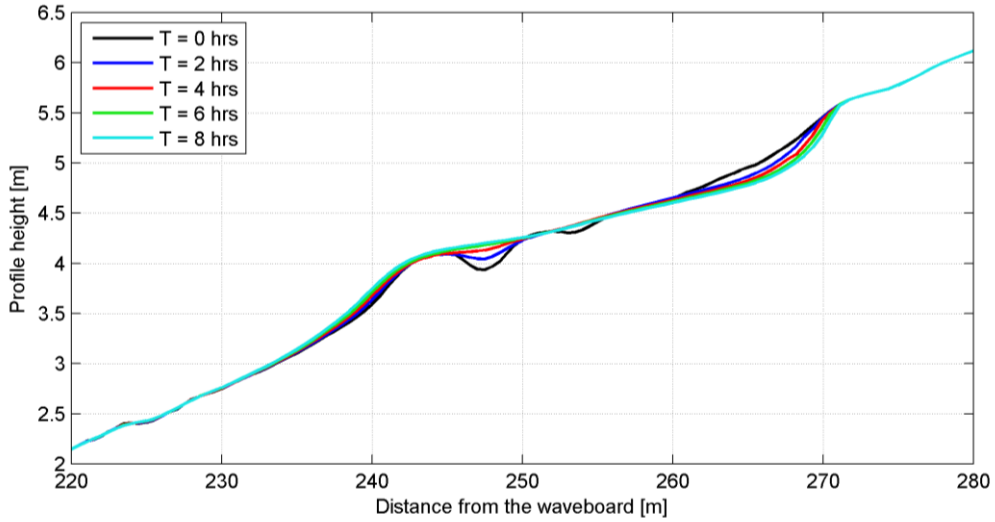

Figure 7.3 – Computed morphological development of simulation R02 (Mildly accretive waves, Hs = 0.62 m & Tp = 6.3 s)

Under erosive conditions, observed profile development for the reference profile clearly shows erosion of the upper part of the profile (Figure D.1). An offshore movement and growth of the breaker bar is observed, thus sand of the upper part of the profile is transported offshore.
The results of simulation R01 show a similar behaviour (Figure 7.2). Sand is eroded in the upper part of the profile and deposited further offshore causing offshore movement and growth of the breaker bar. As also observed in the simulations in part II of the thesis, a clear trough and/or secondary bar are not computed by the model. Qualitatively, there is agreement between the modelled and measured morphological development.
Under accretive conditions, observed profile development for the reference profile still shows erosion of the upper part of the profile (Figure D.2). However, the breaker bar shows a different response than under erosive conditions; now an onshore movement of the bar is observed.
For simulation R02 (Figure 7.3) mildly-accretive waves are used. The wave conditions used correspond to wave conditions used in case 2 of the experiments of Part II (section 3.2.2). It was shown in section 5.4 that the model simulations qualified as good based on the Brier Skill Score. Therefore it is assumed that the model in this state is capable of simulating morphological development of nourishment designs under these wave conditions. Considering the development of the reference profile, compared to the erosive wave conditions no offshore migration of the bar is observed; the bar trough is filled with sand, and a slight bar growth offshore of the bar crest is found. For the milder wave conditions the models computes a more or less stable bar location and height.

The observed development of the nourishment high in the profile under erosive wave conditions (Figure D.3) shows a clear offshore migration with a bar emerging offshore of the nourishment. The upper part of the profile is still eroding.
The results of simulation H01 (Figure 7.4) show a similar behaviour as the experiment. There is still erosion of the upper part of the profile and a clear offshore migration and growth of the bar is observed. Sand of the nourishment is transported offshore and is deposited on the existing bar.
Under accretive waves the observations show that the high nourishment is more or less stable (Figure D.4). There is barely any sand of the nourishment transported and the upper profile erosion is significantly less than under erosive waves.
The results of simulation H02 (Figure 7.5) show a different trend, related to the slightly different wave conditions used in the model. The nourishment is still eroded away by the wave action, but the offshore migration and growth of the breaker bar is significantly less than for simulation H01. Also slight accretion is found at the onshore edge of the nourishment.

The observed development of the nourishment low in the profile under erosive wave conditions (Figure D.5) shows a bar developing at the top of the nourishment. The nourished sand is transported landward and a bar is formed.
The results of simulation L01 (Figure 7.6) show a different development. The nourished sand is not transported landward but seaward, leading to an offshore bar migration. The erosion of the upper part is predicted correctly by the model. Again, Delft3D shows difficulties in computing landward transports and corresponding accretion of the material.
Under accretive waves the observations show a development comparable to the development of the reference profile (Figure D.6); a bar is formed migrating onshore while still erosion in the upper part of the profile is observed.
For simulation L02 (Figure 7.7) the low nourishment is more or less stable. Erosion of the upper part of the shoreface is still observed, but strong offshore movement of the breaker bar is not found with the model simulation.

Even though accretive processes are not represented by the model, qualitatively the simulations show a similar behaviour to the observed morphological development of the different designs of nourishments, making it a suitable tool for investigating sorting processes at the development of shoreface nourishments.

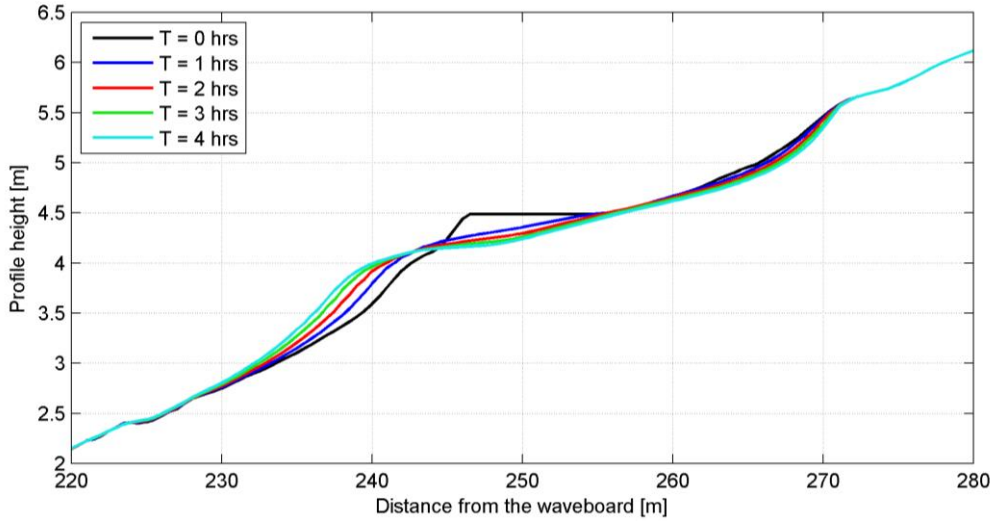

Figure 7.4 - Computed morphological development of simulation H01, high design, erosive wave conditions (Hs = 0.82 m & Tp = 5.2 s).

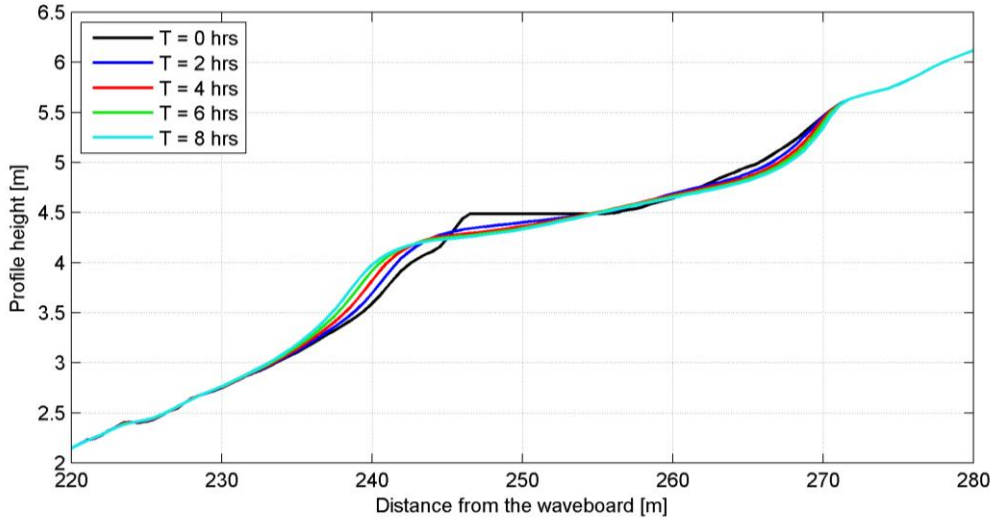

Figure 7.5 - Computed morphological development of simulation H02, high design, mildly accretive wave conditions (Hs = 0.62 m & Tp = 6.3 s)

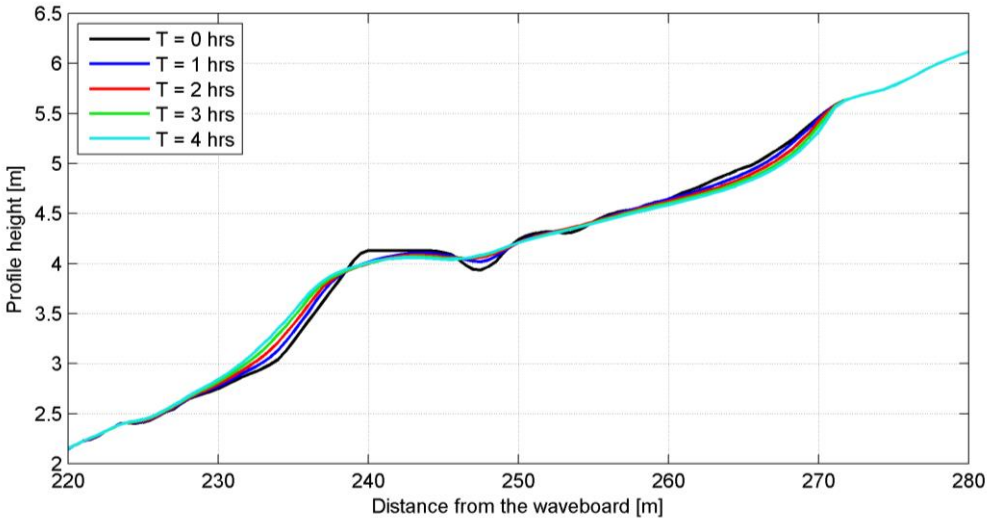

Figure 7.6 - Computed morphological development of simulation L01, low design, erosive wave conditions (Hs = 0.82 m & Tp = 5.2 s).

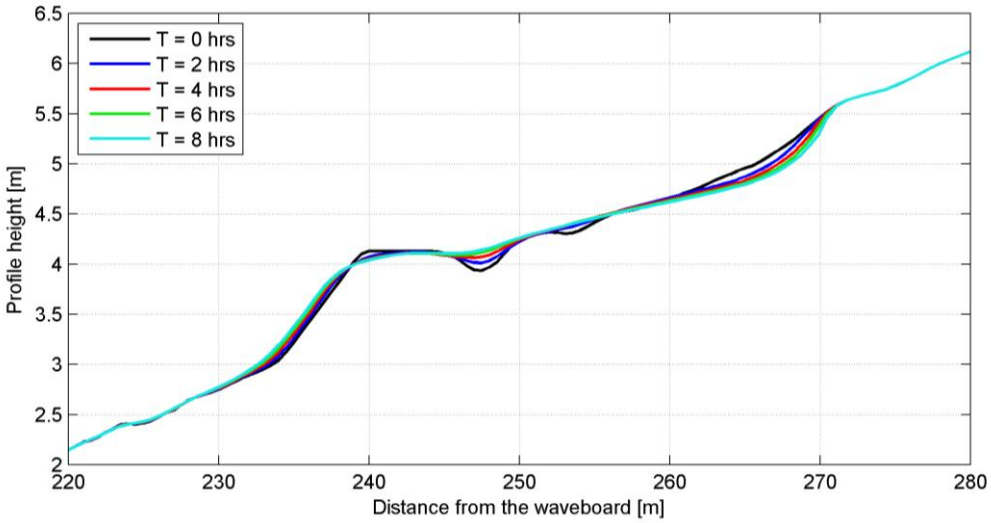

Figure 7.7 - Computed morphological development of simulation L02, low design, mildly accretive wave conditions (Hs = 0.62 m & Tp = 6.3 s).

7.2 Effect of the nourishment

In section 7.1 the model performances were evaluated in terms of morphological prediction of the entire profile. In this section the effects of the nourishment designs on the erosion of the upper part of the profile are assessed. This allows drawing general conclusions on the most optimal nourishment design.

7.2.1 Beach nourishment

To assess the influence of the beach nourishment on the development of the profile, the relative development of the beach nourishment is plotted in Figure 7.8. This figure shows the difference between the development of the profile with and without nourishment, by subtracting the results of the simulation without nourishment from the results of the simulation with nourishment. It can be seen that the beach nourishment mainly affects the upper part of the profile. For the lower waves the nourishment is more or less stable, and there is even an onshore movement of the crest visible. For higher waves the height of the nourishment quickly declines and more sand becomes available in the upper shoreface. The nourishment does not affect the bar position or bar height according to Figure 7.8. This further illustrated by Figure 7.9, which shows bar height and position for the different simulations involving the beach nourishment.

The wiggle on the right of the figure (x = 272-280 m) does not change, and the presence of this wiggle is only related to the way the nourished profile was constructed. In the experiments performed by Vousdoukas et al. (2014) the nourishment was constructed on top of a reference profile, but by constructing also the bottom higher in the profile (x = 270-280 m) was changed. This is what is seen in the figure; profile changes occur until x = 272 m, more onshore of this location there is no wave activity that can change the profile.

Figure 7.10 shows the erosion of the beach nourishment. In this figure the computed erosion between x = 265 m and x = 272 m is depicted and compared to the measured eroded volume. This allows for an estimation of the lifetime of the beach nourishment. The first two hours of the test are performed using an accretive wave condition. As was seen before, the model predicts less erosion than measured in the experiment for accretive waves. It can be seen in the figure that the erosion rate for the accretive waves is underestimated by the model. After 2 hours of accretive waves, the coastal profile is subjected to an erosive wave condition. The measurements show a gradual continuation of the erosion, while the model computations show a strong increase in erosion. For the erosive wave condition the erosion rates are overestimated by the model.

According to the measurements it will take 2 hours and 45 minutes for the nourishment to be completely eroded away. The model computations predict 3 hours and 30 minutes for the nourishment to be eroded away. However, this is strongly dependent on the wave conditions used in the model, since erosion is underestimated for accretive waves and overestimated for erosive waves based on this figure. Measurements show a trend towards an equilibrium situation towards the end of the experiments which is not observed in the model simulations.

In Figure 7.11 the total transports for simulation R03 and B01 are depicted. The largest differences in transport are found at the location of the nourishment, at the beginning of the test sequence. The transports computed by simulation B01 very quickly adapt to the transports as simulated for the reference situation. Also in phase 2 some small differences are observed between R03 and B01, but more offshore those differences are negligible. The nourishment therefore does not influence the transports along the entire profile but only shows a local influence in the upper part of the profile.

Based on Figure 7.8 - Figure 7.11 it can be stated that the beach nourishment is quickly redistributed in the swash area. It reduces erosion simply by adding extra sand in the system; transports are not affected by the nourishment. Sediment transport is only influenced initially,

but after a while the transports of the nourished profile are approximately equal to the transports of the reference profile. The erosion of the nourished beach continues at the same rate as the erosion of the non-nourished beach, but with the latter more sand is present in the system.

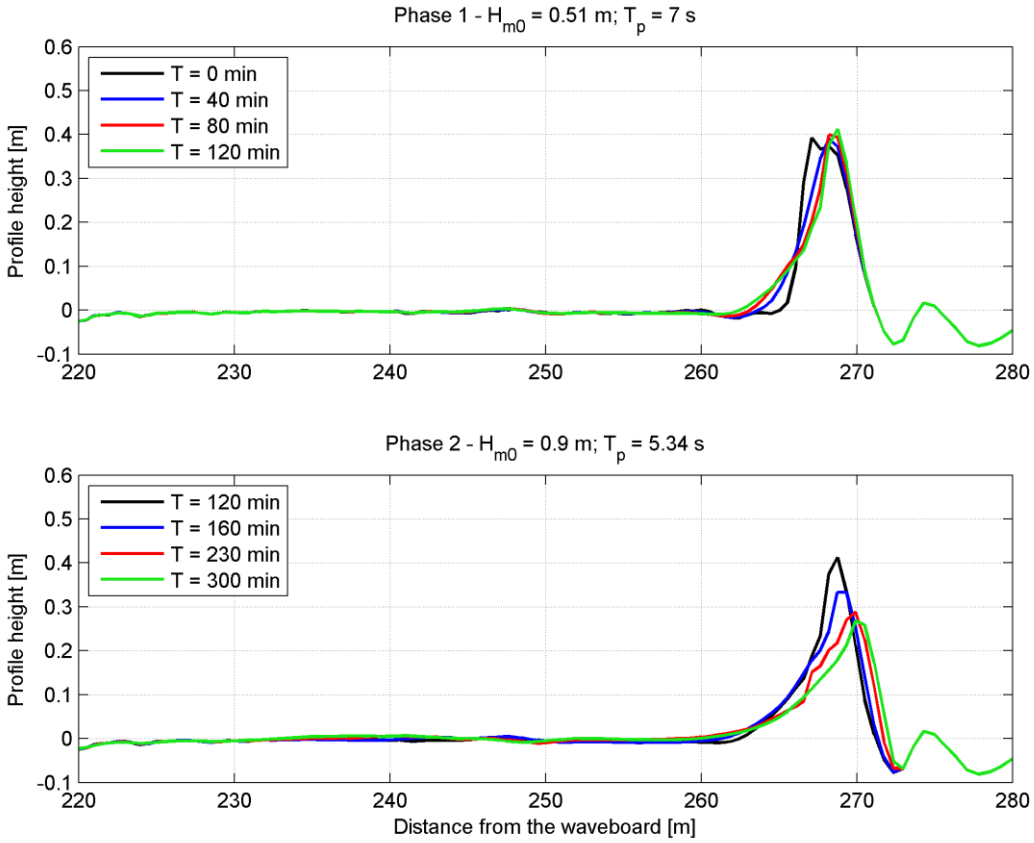

Figure 7.8 – Computed relative morphological development of simulation B01 (Beach nourishment)

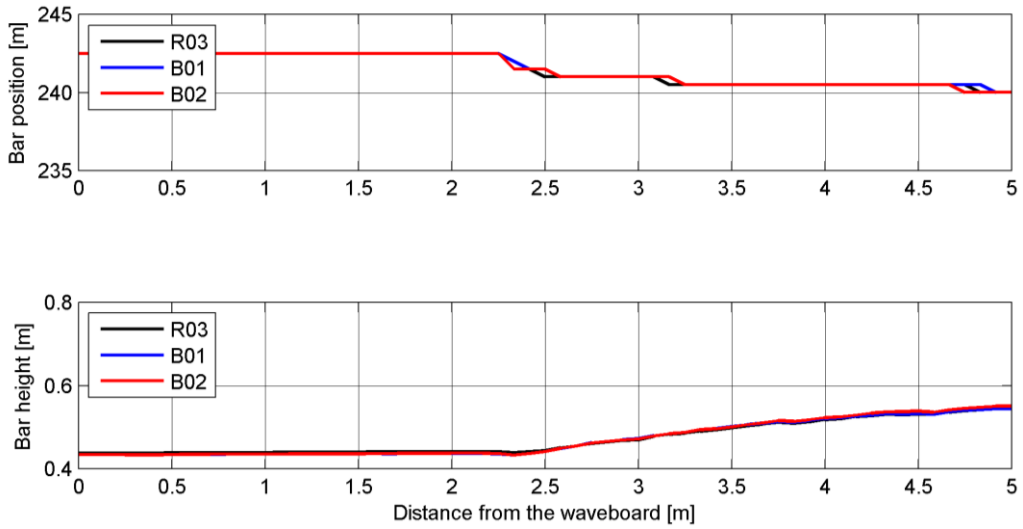

Figure 7.9 – Bar position (upper panel) and bar height (lower panel) for simulation R01 (black), B01 (blue) and B02 (red) for the beach nourishment test.

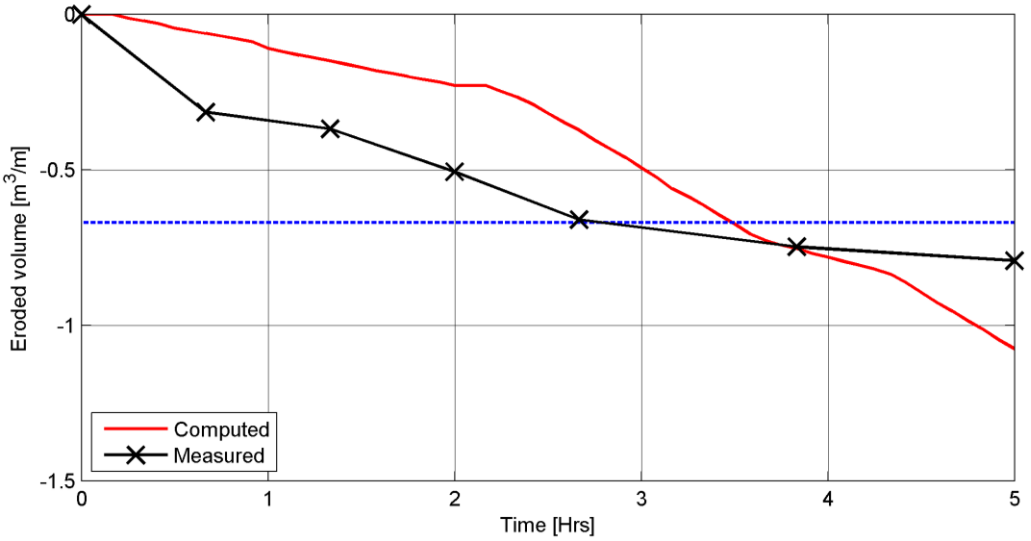

Figure 7.10 – Computed erosion of the beach nourishment (red) and measured erosion of the beach nourishment (black). The first two hours were run with accretive waves (Hs = 0.51 m & Tp = 7 s), the rest with erosive waves (Hs = 0.9 m & Tp = 5.34 s). The blue dotted line indicates the total volume of the beach nourishment.

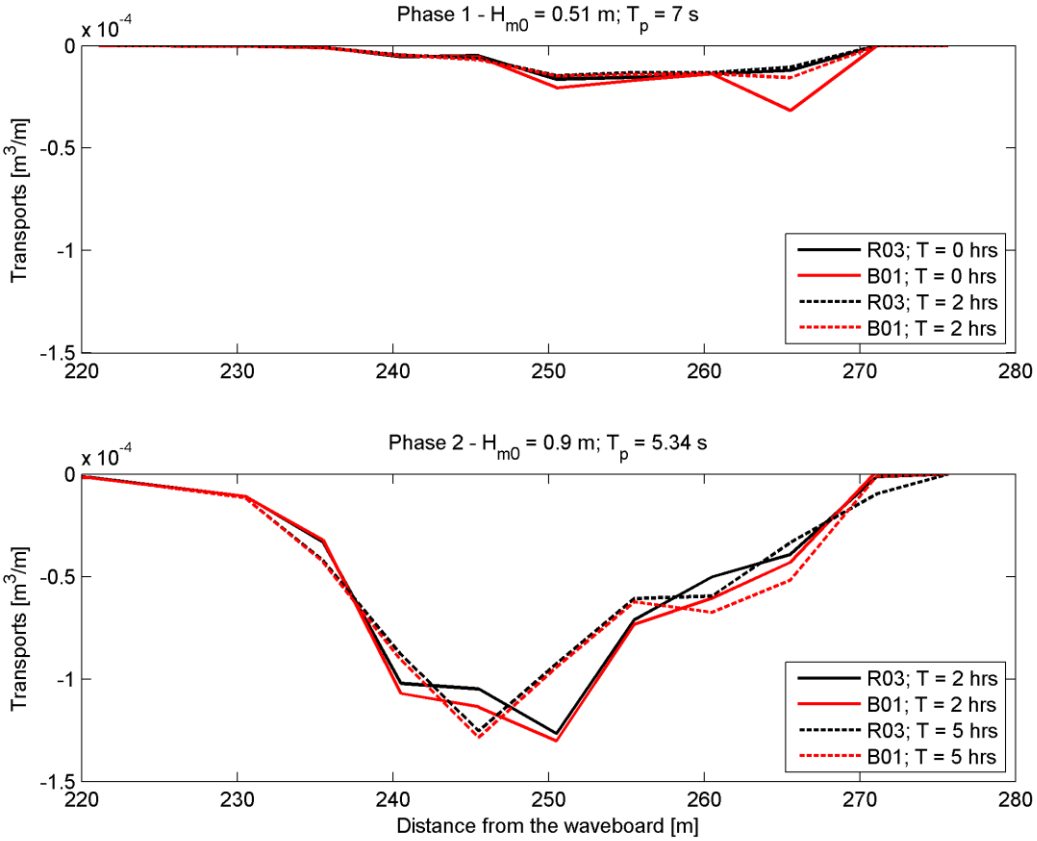

Figure 7.11 – Total transports for reference profile (black) and nourished profile (red) along the flume for phase 1 (upper panel) and phase 2 (lower panel) of the experiments. Transports at the beginning (solid line) and at the end (dashed line) of the simulation are computed.

7.2.2 Shoreface nourishments

In Figure 7.12 - Figure 7.15 the relative development of the different shoreface nourishment designs is shown. The figures show the difference between a computed profile with and without nourishment. A general trend observed is that in the upper-shoreface a positive relative depth-change is found, indicating reduces erosion (or increased deposition). For the high nourishment designs a strong positive relative depth change is found around x = 238 m, indicating that compared to the reference situation larger volumes of sand are deposited in this area. For both erosive and mildly accretive conditions a large part of the nourished sand is transported offshore and deposited around the bar area, creating a higher and wider breaker bar. For the low nourishment designs the positive relative depth change in the upper part of the profile is less strong than for the high nourishment designs. Based on Figure 7.14 and Figure 7.15 the nourishment is more or less stable; there is no strong offshore movement of sand around the nourishment.

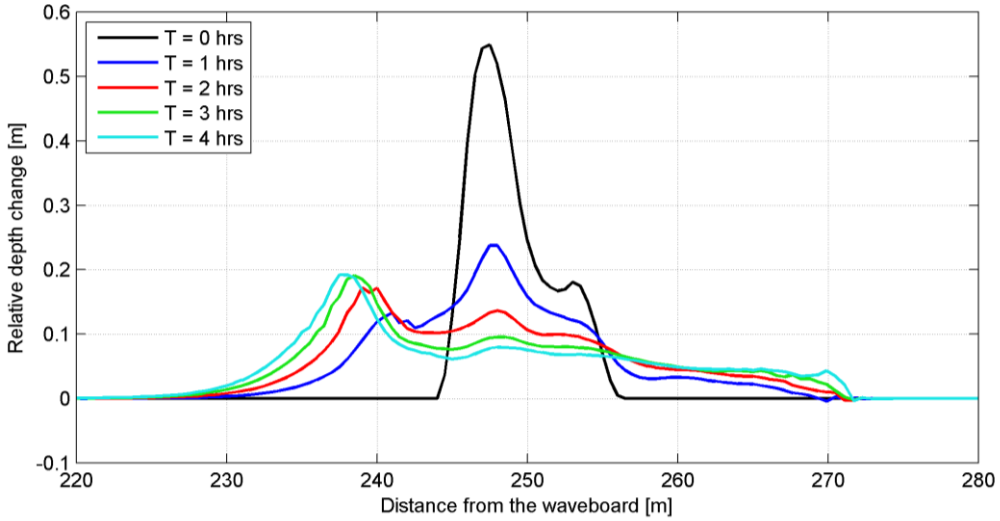

Figure 7.12 - Computed relative morphological development of simulation H01, high design, erosive wave conditions (Hs = 0.82 m & Tp = 5.2 s).

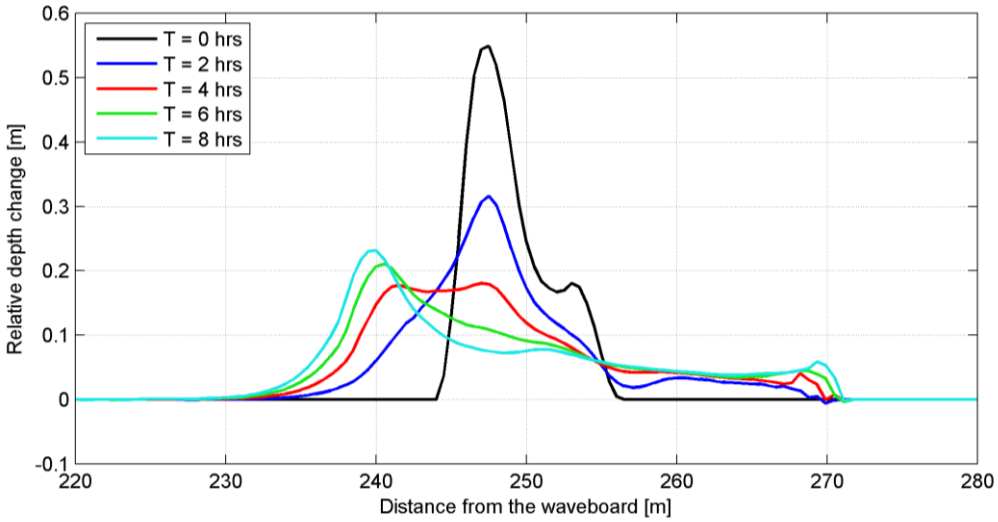

Figure 7.13 - Computed relative morphological development of simulation H02, high design, mildly accretive wave conditions (Hs = 0.62 m & Tp = 6.3 s)

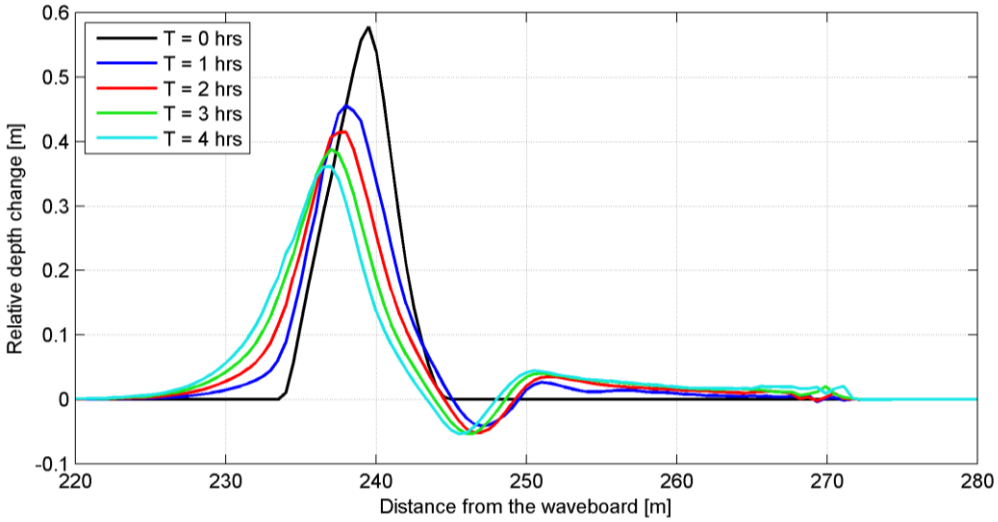

Figure 7.14 - Computed relative morphological development of simulation L01, low design, erosive wave conditions (Hs = 0.82 m & Tp = 5.2 s).

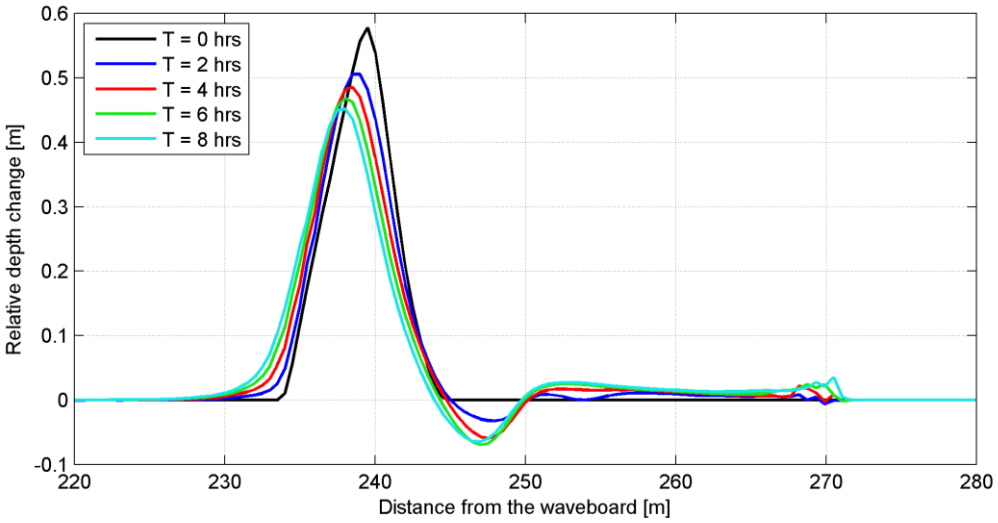

Figure 7.15 - Computed relative morphological development of simulation L02, low design, mildly accretive wave conditions (Hs = 0.62 m & Tp = 6.3 s).

Figure 7.16 shows the bar position and bar height for the reference situation and the nourished profiles. From this figure it is seen that the nourishment leads to an offshore movement of the bar, which is stronger for the low nourishment. This is not in accordance with the measurements, where a shoreward movement of the bar position was observed for both erosive and accretive waves. At the end of the simulations, the bar height for both erosive and mildly accretive waves converge to an equal (equilibrium) height, which is significantly larger than the bar height for the reference situation.

To further quantify the effect of the shoreface nourishments the erosion of the upper part of the profile is computed. The upper part of the profile is taken from x = 253.5 m to x = 280 m. Figure 7.17 shows the eroded volumes of the erosive and mildly accretive tests compared to the reference tests. Both the low and high designs have a positive effect on the erosion of the upper part of the profile. Smaller erosion is observed for the mildly-accretive wave condition.

For the high nourishment designs for both wave conditions a relative increase of sand volume in the upper part of the profile is approximately 30%. For the low nourishment design this is approximately 18% for both wave conditions. In accordance to the results of Walstra et al. (2011) it is observed that the high nourishment design leads to the largest reduction of erosion.

Different mechanisms play a role in the development of both shoreface nourishment designs. In Figure 7.18 the cross-shore wave height distributions are plotted for both designs relative to the reference profile. For the low nourishment there is a decrease of wave heights visible around the shoaling zone but in the upper part of the profile no decrease is observed. The low nourishment shows significantly less sheltering effect in the upper shoreface. The high nourishment design results in wave height decrease along the entire profile by acting as a submerged breakwater. The reduction of the wave climate leads to smaller offshore transports by the mean flow thus reducing the upper shoreface erosion. This is illustrated in Figure 7.19 where the mean total transports along the cross-shore profile are plotted. Increased transports are observed at the location of the nourishment for both the high and low design. In the upper shoreface, transports are indeed significantly less compared to the reference simulation. Over the complete cross-shore profile, transports are offshore directed. In section 7.3 the transports are investigated into more detail and it will be shown that in fact none of the nourished sands are transported onshore; all transport is offshore directed. The nourished sands do however feed the bars, leading to higher more offshore located bars. Therefore, the success of the nourishments is mainly based on their breaker berm function and not so much on their feeder berm function.

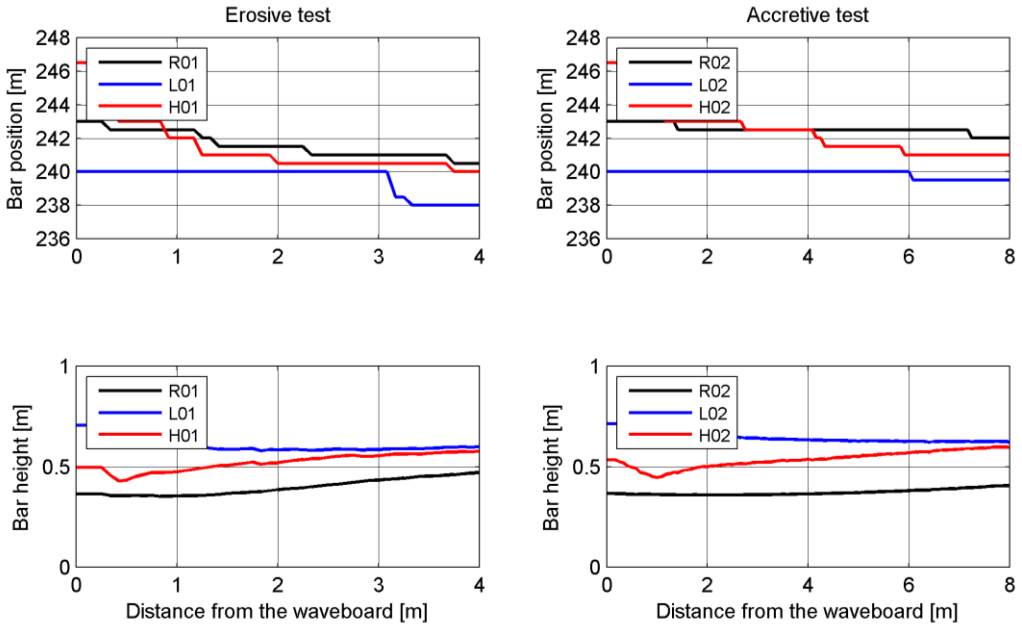

Figure 7.16 – Bar position (upper panels) and height (lower panels) for erosive (left panels) and mildly accretive (right panels) wave conditions.

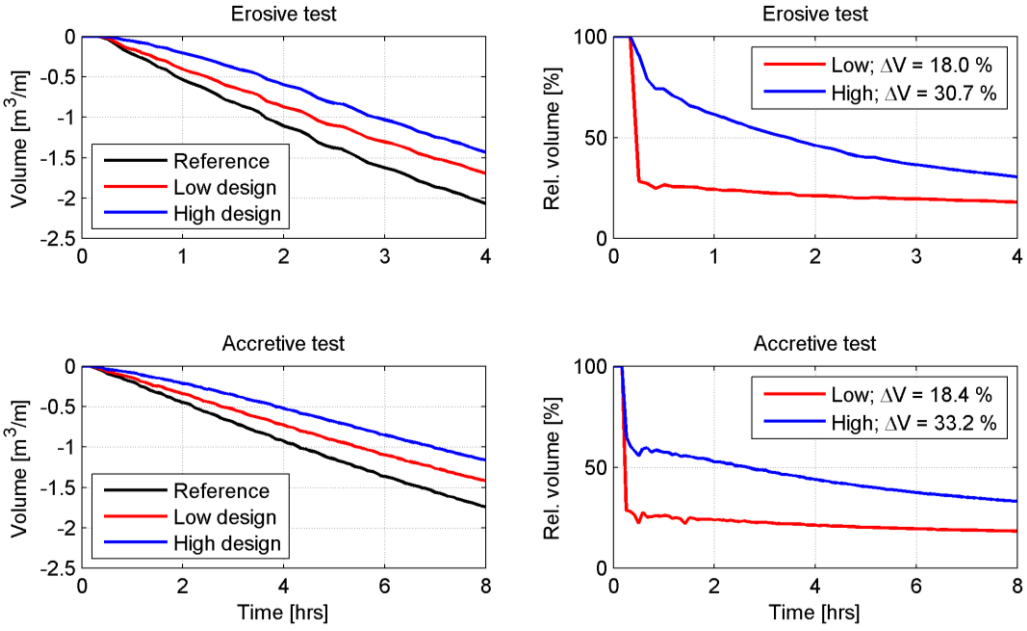

Figure 7.17 – Eroded volumes (right) of the upper part of the profile for the reference profile (black), the low nourishment design (red) and the high nourishment design (blue). Relative volume increase is plotted on the left side for the low (red) and high (blue) design.

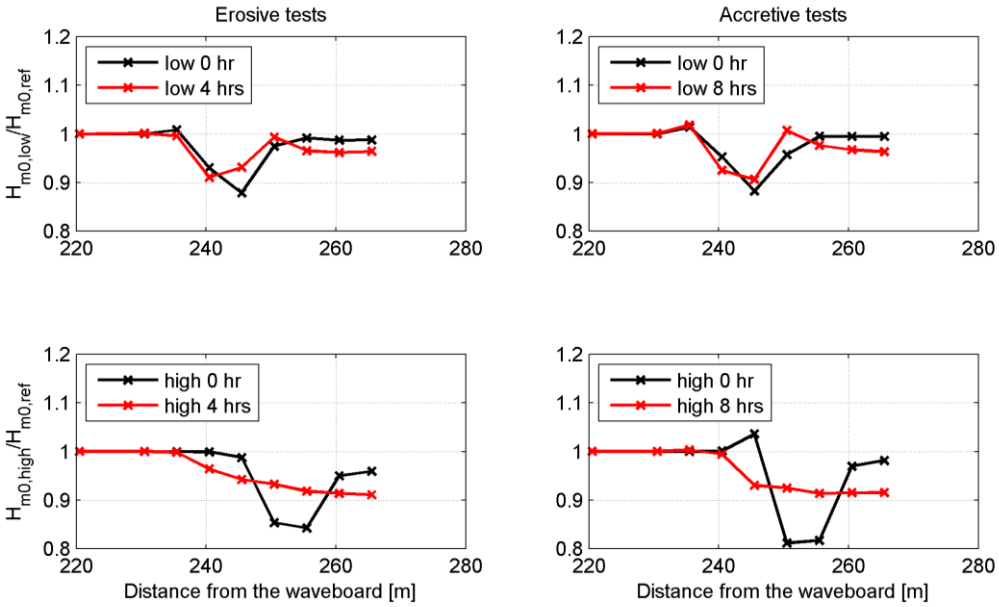

Figure 7.18 – Relative wave height distribution along the flume for both the low (upper panel) and high (lower panel) nourishment design initially (black) and in the final state (red). Erosive wave conditions are plotted at the left side, mildly accretive wave conditions are plotted at the right side.

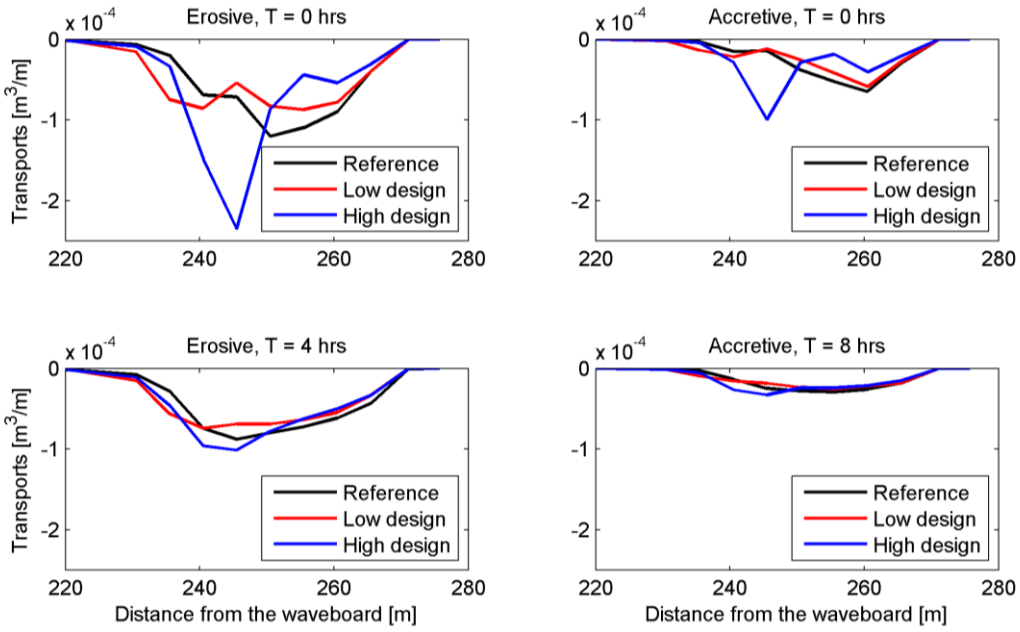

Figure 7.19 – Mean total transports for reference profile (black), low nourishment design (red) and high nourishment design (blue) for erosive (left) and accretive conditions (right) initially (upper panels) and final (lower panels).

7.2.3 Effect of nourishment with larger grain size

The effect of using a larger grain size for the fill material than the native beach is investigated in this section.

The figures showing morphological development for the simulations using a coarser grain are shown in appendix D.2, since the results are almost equal to the results shown in section 7.1.1 and section 7.1.2; apparently taking a coarser grain does not significantly influence the morphological development in this case. This is most likely related to the fact that the native sands are already relatively coarse (medium sands with a D_{50} of 300 µm). Looking at results of van Rijn et al. (2011) a similar trend is observed. In this study a beach was nourished using a grain diameter of 200 µm, 300 µm and 400 µm. While a significant difference between the erosion volumes using 200 µm and 300 µm was observed, the difference between 300 µm and 400 µm was very small.

In Figure 7.20 the beach nourishment lifetime is plotted, now including the line indicating the coarser nourishment. Up until the point that the nourishment is eroded away the lines are approximately the same. From the moment the beach nourishment is eroded away completely, there is significantly stronger erosion observed for simulation B02 compared to B01. The coarse sediments form a protective layer lower in the profile; to still fulfil the equilibrium concentration of the suspended sediment, more sediment is entrained at the location of the nourishment leading to enhanced erosion at this location compared to simulation B01. However, the protective armouring layer of coarser sediments eventually leads to a reduced erosion of the upper shoreface region as can be seen in Figure 7.21. In this figure the eroded volume of the upper shoreface, taken from x = 253 m to x = 265 m (excluding the nourishment), is depicted. For simulation B02 more sand stays in this zone compared to simulation B01, thus nourishing with a coarser grain leads to larger volumes of sand for a larger time in the upper part of the profile.

In section 7.2 the effect of the shoreface nourishments was discussed in terms of upper shoreface erosion. For the shoreface nourishments the erosion was shown in Figure 7.17; a similar figure is plotted for the shoreface nourishment simulations using a larger grain size for the nourished sands (Figure 7.22). Compared to Figure 7.17, the high nourishment design shows *less* reduction of erosion; the relative volumes are 29.0% for erosive conditions and 32.3% for accretive conditions compared to 30.7 and 33.2 % for the previous sections. This means that using a coarser grain for the nourishment does not yield less erosion of the upper shoreface.

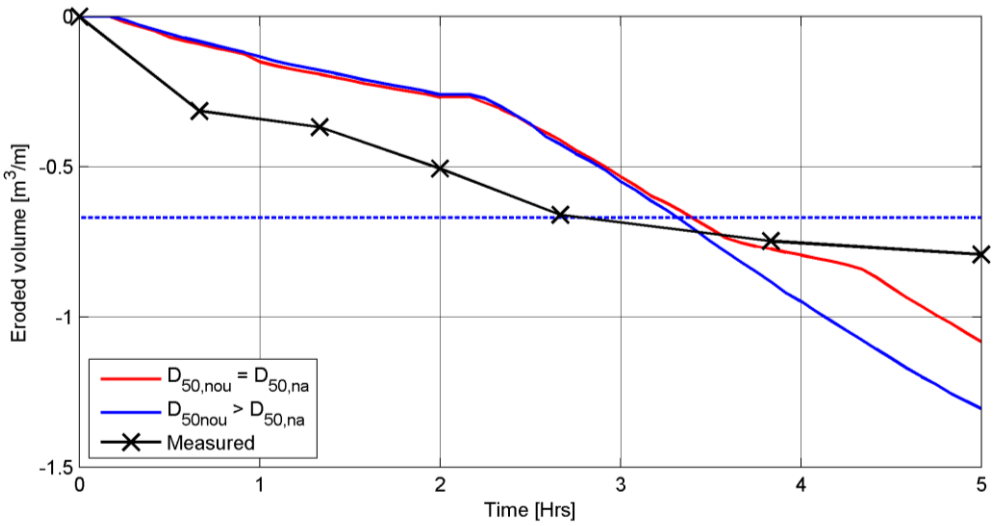

Figure 7.20 - Computed erosion of the beach nourishment (red), beach nourishment using a coarser grain size (blue) and measured erosion of the beach nourishment (black).

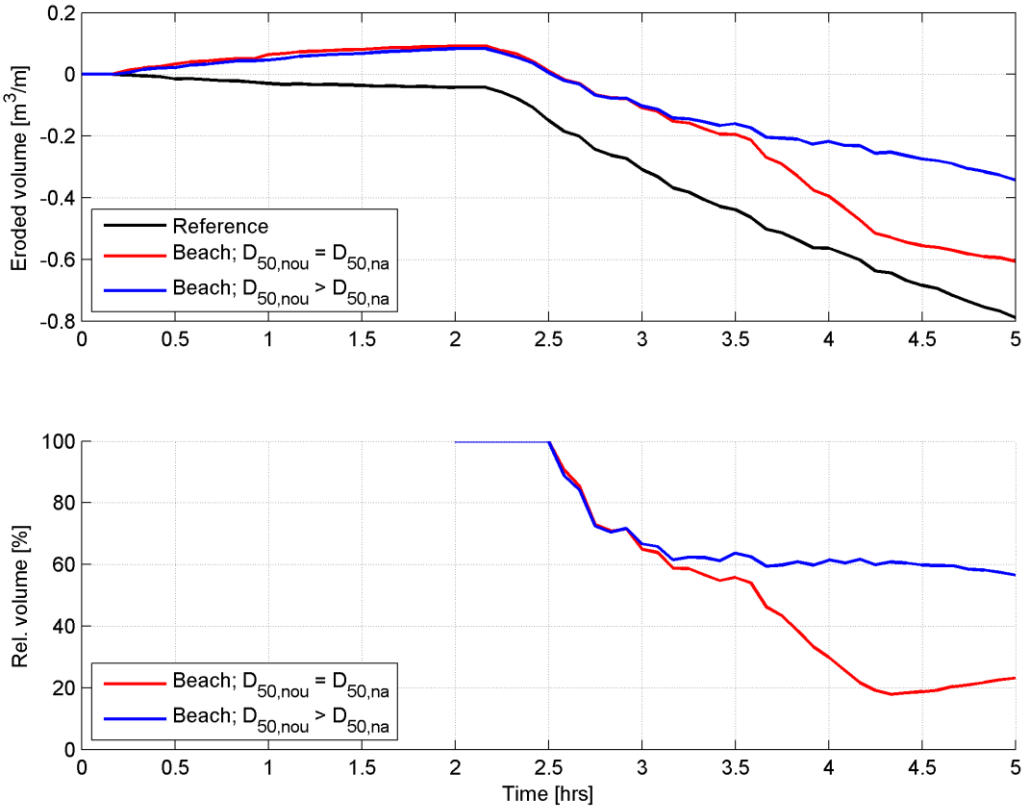

Figure 7.21 - Upper shoreface erosion for the reference (black) and nourished profiles. Red indicates simulation B01 and blue indicates simulation B02. Relative volume is plotted in the lower panel.

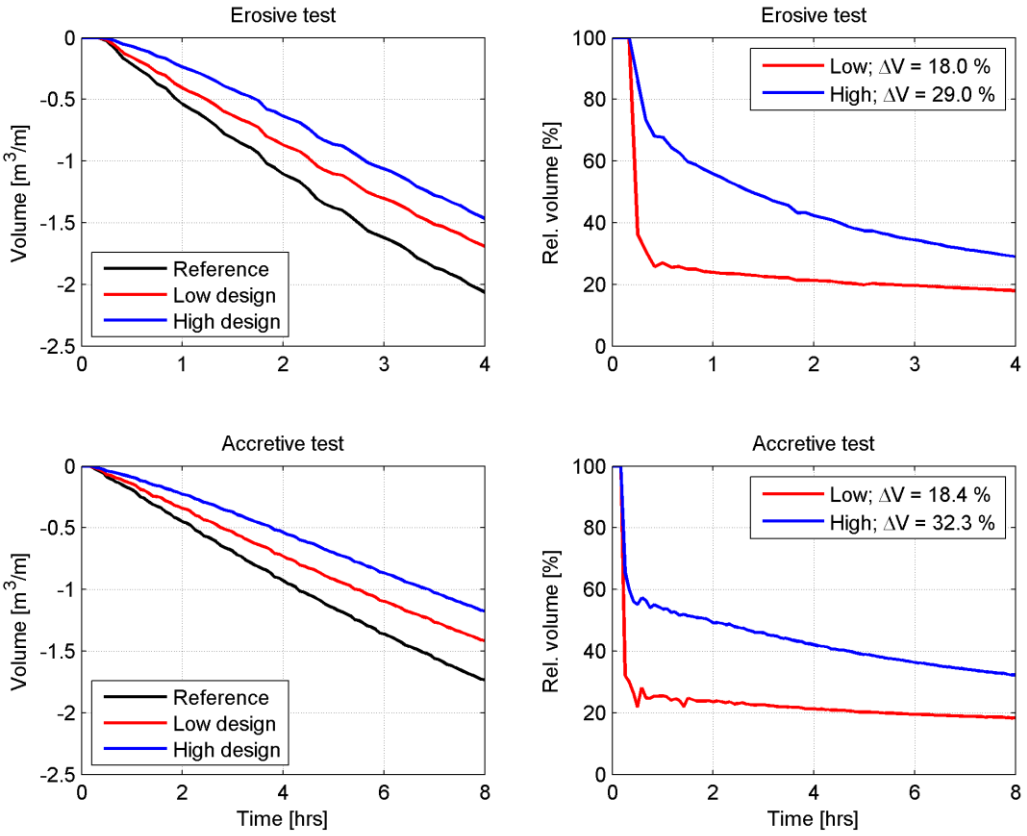

Figure 7.22 – Grain size of the nourished sand is larger than the grain size of the native sands. Eroded volumes (right) of the upper part of the profile for the reference profile (black), the low nourishment design (red) and the high nourishment design (blue). Relative volume increase is plotted on the left side for the low (red) and high (blue) design.

7.3 Sorting processes

In this section the role of grain sorting in combination with the development of the nourished beaches is analysed for nourishments using an equal and coarser grain size than the native beach.

7.3.1 Beach nourishment

For the beach nourishment the development of the sorting will be considered for phase 1 and phase 2 separately. Phase 1 is characterized by accretive waves (H_s = 0.51 m, T_p = 7 s) and phase 2 is characterized by erosive waves (H_s = 0.9 m, T_p = 5.34 s).

Figure 7.23 shows the results of phase 1 of simulation B01 (nourishment grain size equals the grain size of the native sand) and B02 (nourishment grain size is larger than the native grain size). For B01 the nourishment is slowly eroded away under the accretive waves. A very small coarsening is observed at x = 260 m to x = 265 m; the coarsest sediments of the nourishment are deposited at this location. The finer sediments are transported further offshore by the flow and deposited along the profile. The largest amount of fine sediments are deposited offshore of the bar crest, where a fining of the sediments is computed; there is a narrowing of the sediment curve as can be seen from the standard deviation.
For simulation B02 the nourishment is also slowly eroded away. A coarsening of the sediment is observed from x = 246 to x = 268 m. This is due to the coarse sediments from the nourishment which are deposited along the profile and the finer sediments which are transported further offshore. The fining is found at the same location as B01 in the profile with the same magnitude; the coarser grain size of the nourishment does not influence the offshore transport of the fine sediments. On top of the breaker bar, an increase in grain size is found, due to the location of the trough.
Figure 7.24 shows the result of phase 2 of simulation B01 and B02. For B01 a little extra coarsening compared to phase 1 occurs along the profile. Offshore of the bar crest (x = 235 m) fining of the sand is observed. The fining is found more offshore compared to phase 1 related to higher transport capacity of the waves. The coarser sediments are also transported more offshore than in phase 1. Between x = 230 m and x = 240 m the standard deviation increases significantly indicating a wider distribution, due to the settling of coarser sediments compared to phase 1. The offshore fining leads to a narrower sediment curve.
For simulation B02 between x = 265 and x = 270 fining is observed. This is attributed to the distribution of the coarse nourished sediments throughout the profile and the mixing with the original (native) sands of the beach. The strongest coarsening is found at x = 260 m, indicating the location of deposition of the coarsest sediments while the finer sediments are transported further offshore. A drop in standard deviation is observed at this location indicating a narrower sediment distribution, caused by the settling of only coarse sediments. The coarsening continues until x = 233 m, where fining of the sediment is observed.
More insightful for sorting effects are Figure 7.25 and Figure 7.26, where the vertical distribution of the grain size is depicted. Using a coarser grain size for the fill material in general shows a large effect on the sorting. The lifetime of the nourishment is not affected by the larger grain size (Figure 7.20), but the upper shoreface erosion of the profile is. The coarse sands are distributed along the profile, leading to a coarse layer on top of the original sands. This coarse layer further reduces upper shoreface erosion.

Based on the grain size and standard deviation of the sediment along the profile, it can be stated that suspension sorting plays a large role in the morphological development of the beach nourishment. Based on the wave energy, all or most sediments are entrained and transported offshore by the undertow, where the coarsest grains settle higher in the profile than the finer sediments, that settle around the bar area.

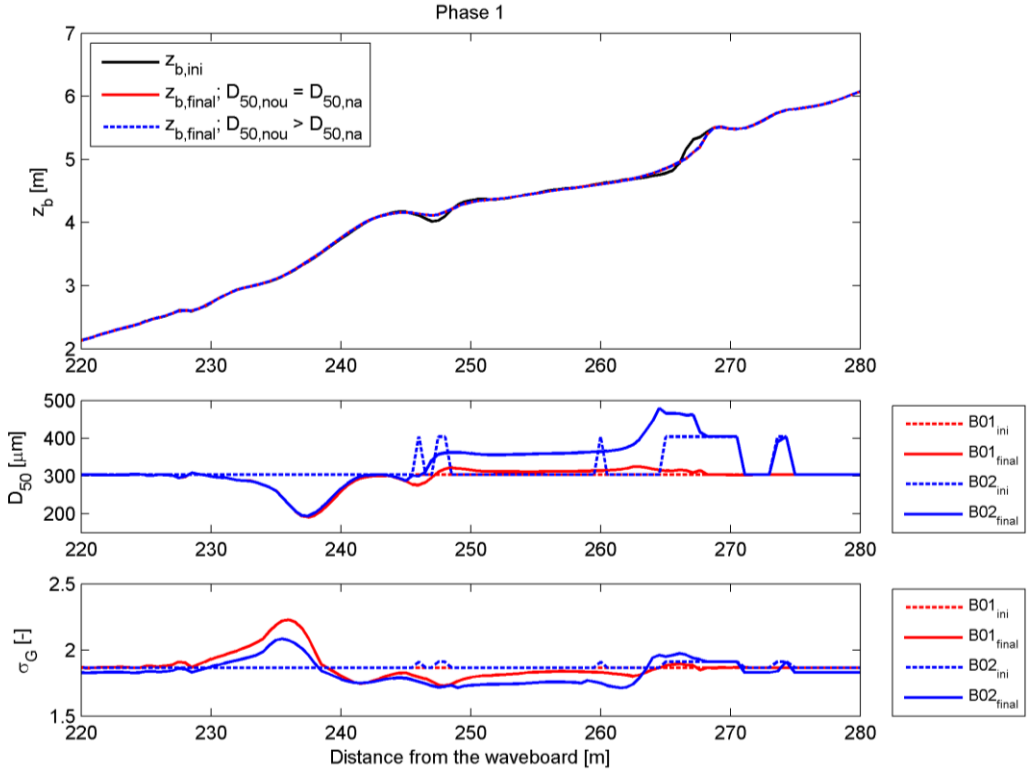

Figure 7.23 – Computed bottom profile (upper panel), grain diameter (middle panel) and standard deviation (lower panel) for phase 1 of simulations B01 (red) and B02 (blue).

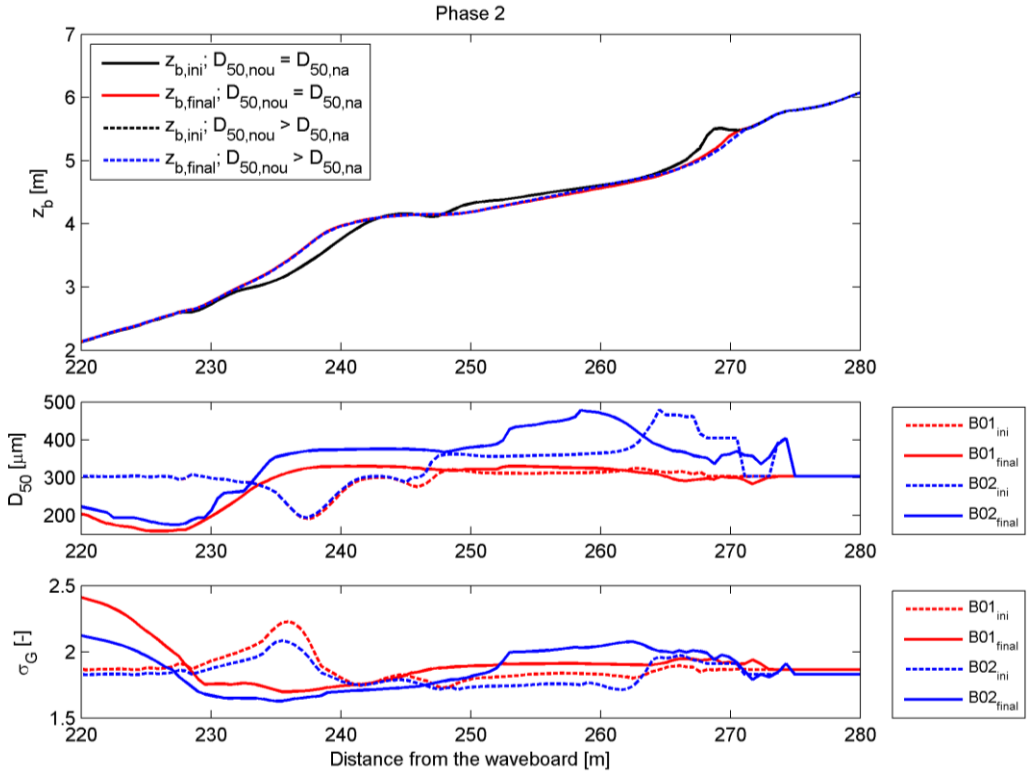

Figure 7.24 - Computed bottom profile (upper panel), grain diameter (middle panel) and standard deviation (lower panel) for phase 2 of simulations B01 (red) and B02 (blue).

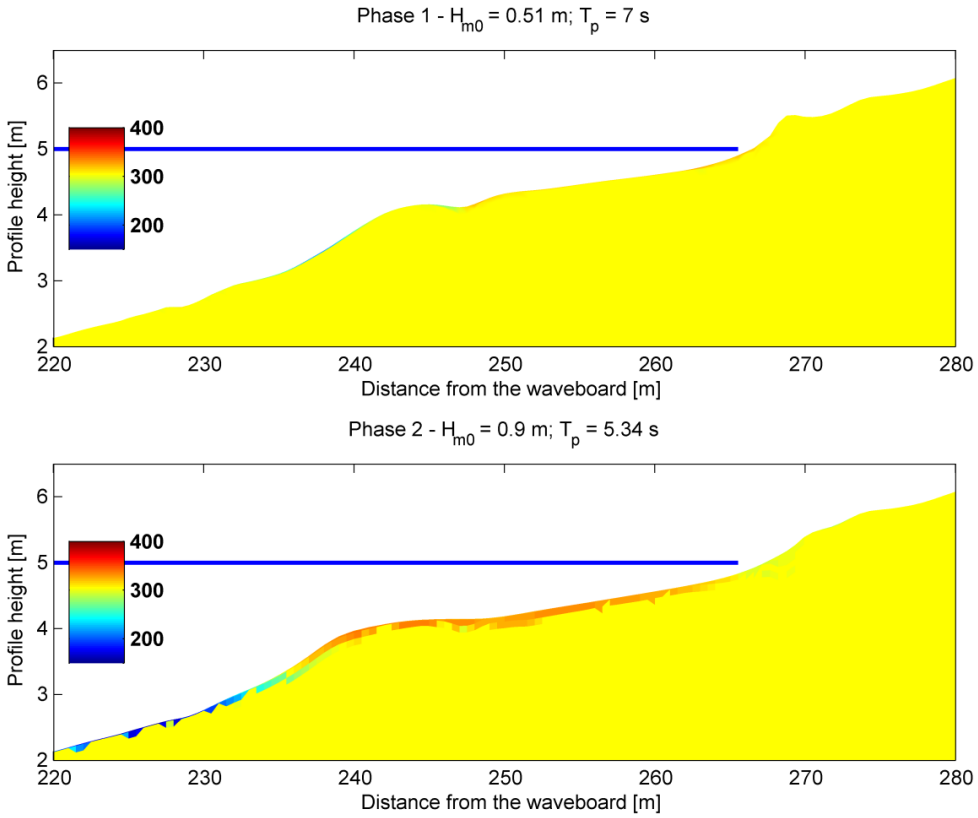

Figure 7.25 – Computed grain size along the profile for simulation B01

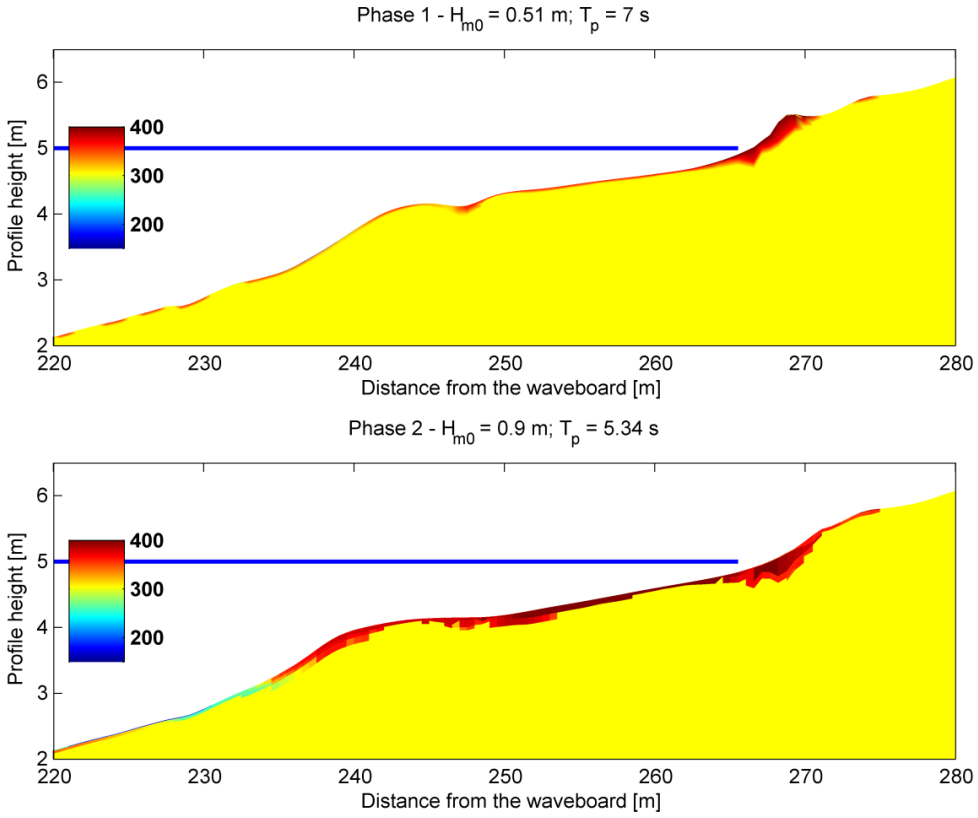

Figure 7.26 – Computed grain size along the profile for simulation B02

7.3.2 Shoreface nourishments

Figure 7.27 shows the results of simulation H01 and H03 (high nourishment, erosive waves). No differences are observed between the simulated profile of H01 and H03 thus indicating that there is no effect on the morphological development visible from the coarser grain size.
For simulation H01 a small fining is observed between x = 265 and x = 270 m. Coarsening of the sand is observed from x = 235 till x = 265 m followed by a fining offshore of the bar. The fining between x = 265m and x = 270 m combined with a coarsening around x = 270 m is linked to swash events. Sediments are transported onshore by the flow and deposited at the shore break; during a next event where the wave power is less, only the finer sediments are picked up and deposited a little more offshore causing the fining in that area.
The coarsening between x = 235 m and x = 265 m is explained by the erosion of the upper shoreface; the flow has enough transport capacity for the finer sediments and not enough for the coarser sediments that are deposited around x = 260. The coarsening further offshore is related to the development of the nourishment; on top of the nourishment the coarsening is smallest; breaking waves on top of the nourishment possess enough power to entrain most sediment which is transported offshore leading to coarsening at the top of the bar. The coarsening around x = 260 m is more likely caused by the erosion of sediment in the upper part of the profile; coarser sediments are deposited when the flow loses capacity.
For simulation H03 similar trends are observed; there is fining around x = 268 m, coarsening between x = 233 and x = 268 m and a strong fining offshore of x = 233 m. Besides, there is also a coarsening of the sediment is observed around x = 270 m. The coarsening is again related to swash like events, where the coarsest sediments are deposited around the shorebreak. Compare to simulation H01, extra coarsening is found in the nourishment area. This is related to the coarser sands used for the nourishment; part of the eroded sand in the upper part of the profile settles in this area, while part of the nourishment is eroded away, leading to a mixture of sediments. The coarsest sediments of the nourishment and the upper part of the profile settle around x = 245 m, indicated by the large grain size and the drop in standard deviation, interpreted as a narrowing of the sediment sample.
From x = 240 until x = 228 the standard deviation increases, indicating a wider distribution. The enriching of the sand here is caused by settling of not only coarse sediments but also finer sediments. The finest sediments are transported further and settle offshore from x = 233 m. A drop in standard deviation is found from x = 228 m, from that point on the finest sediments settle leading to a narrower distribution.

Figure 7.28 shows the result of simulation H02 and H04 (high nourishment, accretive waves). No differences are observed between the simulated profile of H02 and H04.
For simulation H02 a coarsening from x = 265 to x = 238 is observed, offshore from x = 238 m a strong fining is observed, and around x = 270 a very small coarsening is found.
For simulation H04 the same grain size distribution is found from x = 255 m to x = 270 m, offshore of x = 255 m the grain size is larger for case H04. This is caused by the larger grain size used for the nourishment. Since the waves are lower the flow has a smaller transport capacity, leading to the stronger increase of grain size around x = 240 m compared to the erosive wave conditions. Also the offshore fining takes place over a smaller distance.
So, comparing the results of simulation H02 and H04 to the results of simulations H01 and H03 the same observations apply but for the accretive condition the differences are smaller and more localized; for the erosive wave conditions a stronger spreading is found for the quantities. This further illustrates the strong dependency of waves on the sorting phenomena.

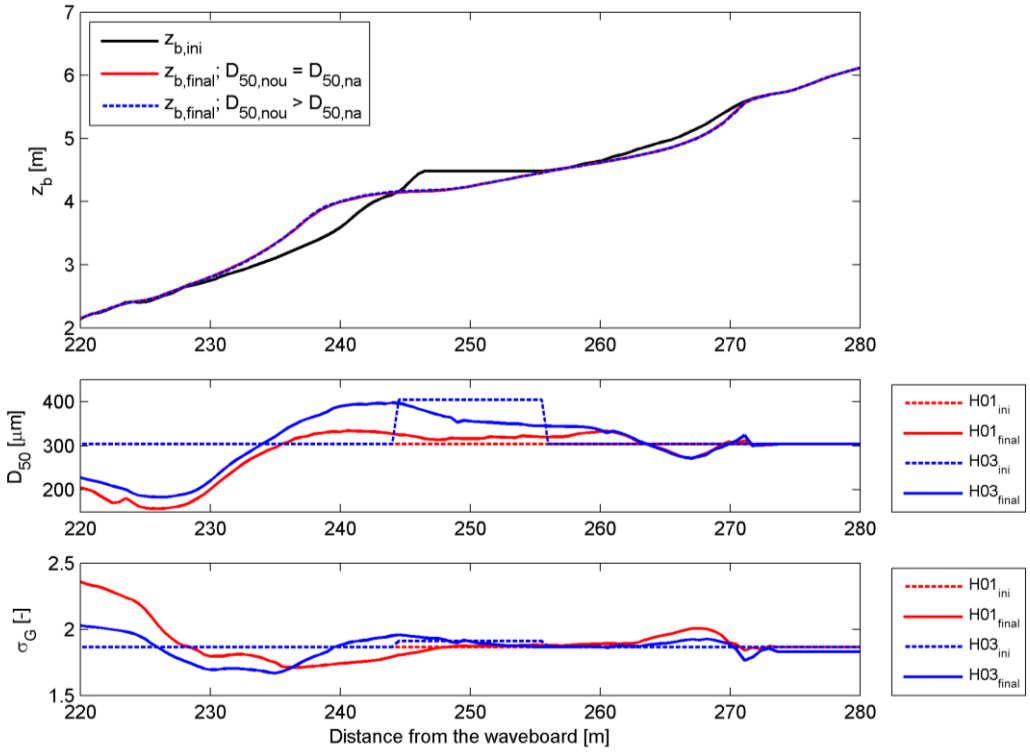

Figure 7.27 – Computed bottom profile (upper panel), grain diameter (middle panel) and standard deviation (lower panel) for simulations H01 (red) and H03 (blue) (High nourishment design, erosive waves).

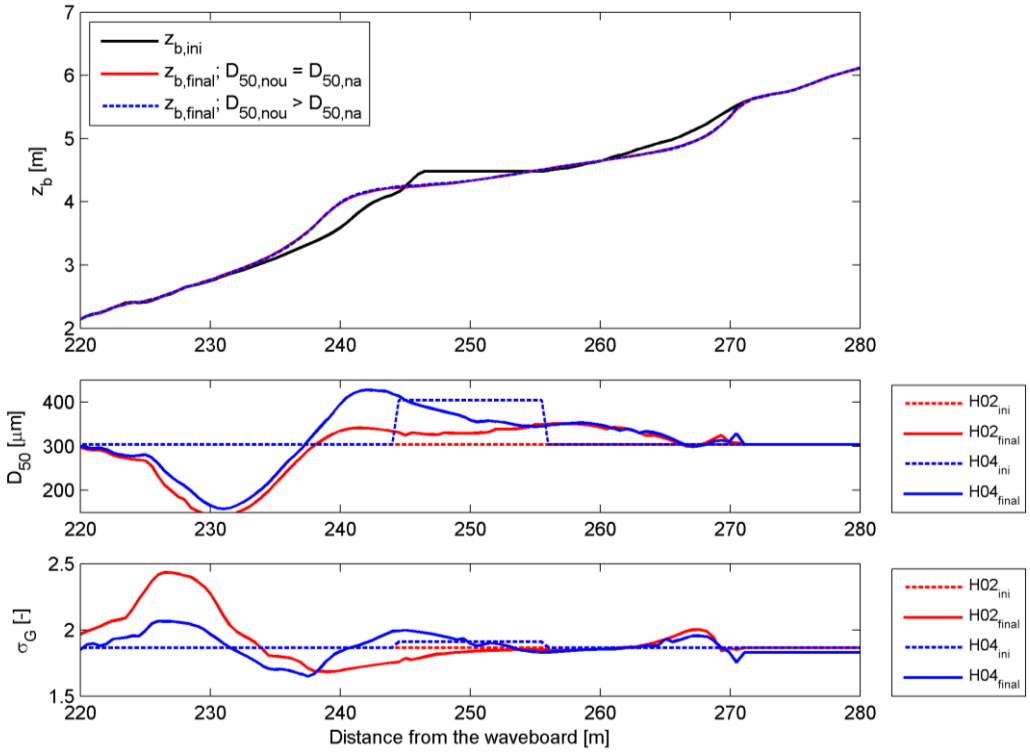

Figure 7.28 – Computed bottom profile (upper panel), grain diameter (middle panel) and standard deviation (lower panel) for simulations H02 (red) and H04 (blue) (High nourishment design, mildly accretive waves).

Figure 7.29 shows the result of simulation L01 and L03 (low nourishment, erosive waves). Again, no differences are observed between the simulated profile of L01 and L03 thus indicating there is no noticeable effect of the nourishment grain size.
For simulation L01 a drop in grain size is observed between x = 264 m and x = 270 m paired with a drop in standard deviation. Sediment is uniformly eroded away; finer sediments are deposited in this area transported from the nourishment. From x = 262 to x = 235 a constant increase in standard deviation is found. A steady widening of the sediment curve is observed in this area, due to deposits from the eroded sands of the upper shoreface along the profile. These deposits lead to the coarsening of the sediment in this area. Strong fining is observed offshore from x = 232 m. The decrease in standard deviation indicates narrowing of the sediment distribution due to the deposits of fine sediments.
For simulation L03 the grain size distribution and standard deviation of the sediment is similar to the results found for simulation L01. Using a coarser grain size for the nourishment does not influence the sorting according to the model computations. This will be elaborated further on in the text.

Figure 7.30 shows the result of simulation L02 and L04 (low nourishment, accretive waves). The same trends as observed for simulations L01 and L03 are observed here. The offshore fining is observed more onshore for both L02 and L04.

7.3.2.1 Transport analysis

Although for both nourishment designs a coarsening around the nourishment area is observed that is in accordance with observations mentioned in literature (see section 2.8.2) it seems that the choice of grain size plays a larger role for the high nourishment design than for the low nourishment design. To explain this, a closer look is taken to the transports of the nourished sands, and more particularly, to the location of the nourished sands in time.
In Figure 7.31 and Figure 7.32 the distribution of sediment mass along the flume for the nourished sands is shown. For simulation H03 (Figure 7.31) an offshore movement of nourished material for all fractions is observed, while for simulation L03 (Figure 7.32) only very small offshore movement is seen. The other simulations show similar patterns. So, for case H03 there is not only transport of the native sand located in the upper part of the profile, but there is also transport of the nourished sand. Around the nourishment area there is mixing of the native and nourished sands; the wave action is strong enough in this area to mobilize the nourished sand (further illustrated in Figure 7.33). For case L03 something different is observed; sand is mainly eroded in the upper part of the profile and settles along the flume, as seen by the slight increase in standard deviation. Sorting processes seem less strong here, much less mixing between the nourished sand and native sand is observed. The lower location of the nourishment leads to the waves being less capable of transporting the nourished sand, and mainly sand eroded from the upper part of the profile settles around this area. This is further illustrated in Figure 7.34.

This explanation holds also for the other simulations: sorting plays a larger role at the high nourishment designs, since it is more affected by waves. The low nourishment design seems more or less stable, and the sorting processes observed are linked to the eroded sand from the upper part of the profile.

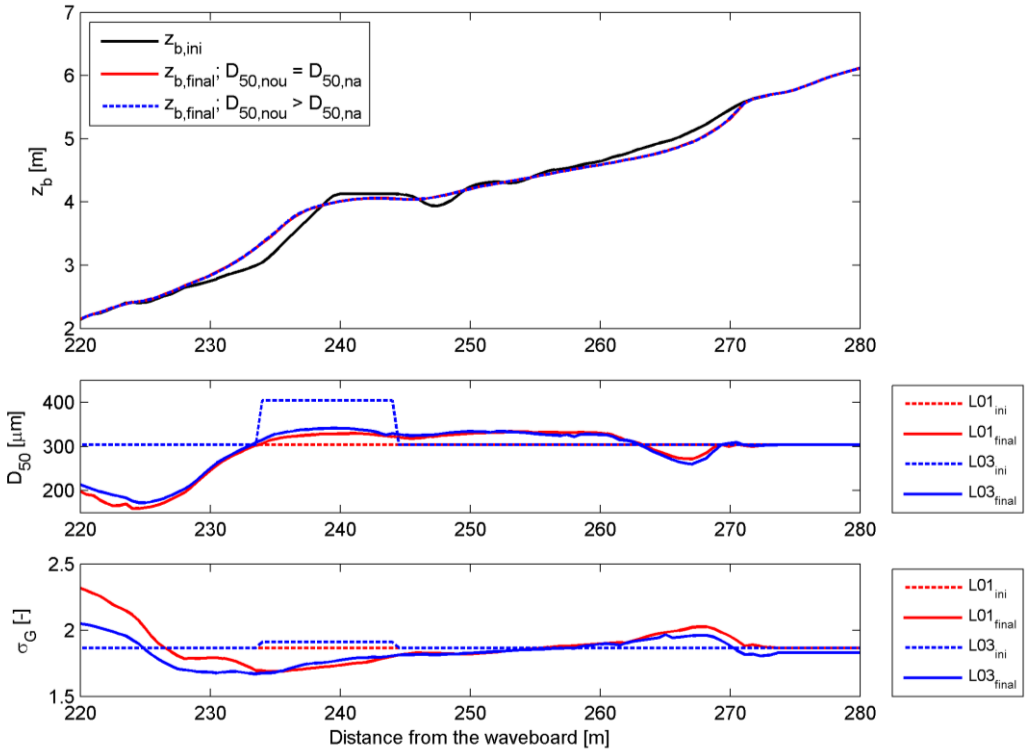

Figure 7.29 – Computed bottom profile (upper panel), grain diameter (middle panel) and standard deviation (lower panel) for simulations L01 (red) and L03 (blue) (Low nourishment design, erosive waves).

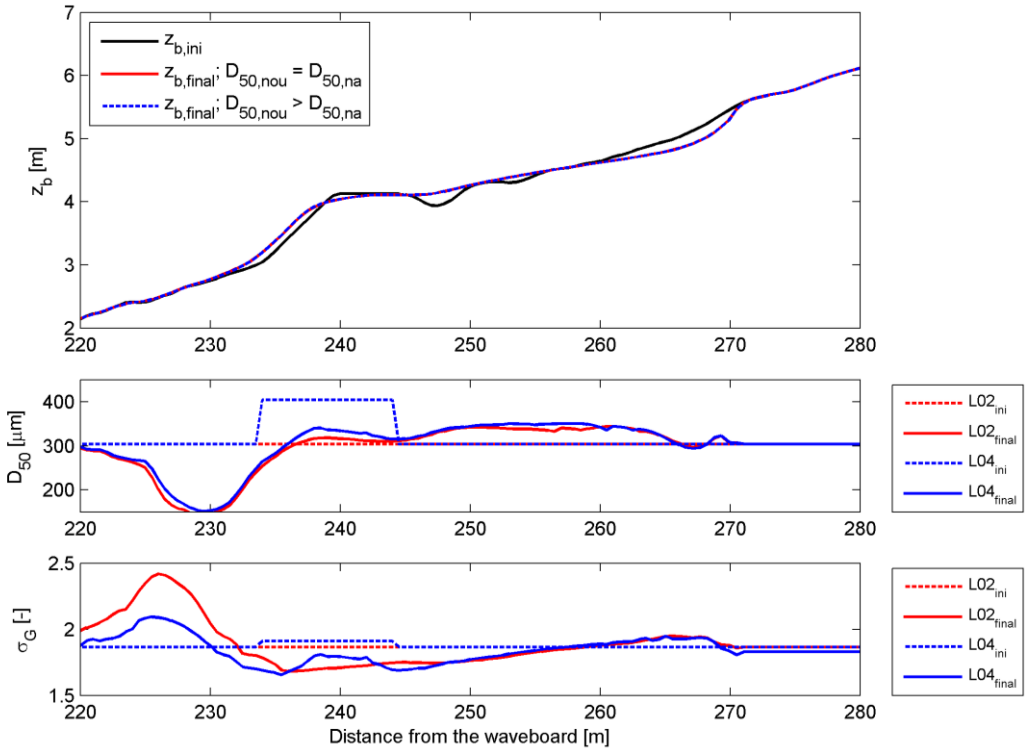

Figure 7.30 – Computed bottom profile (upper panel), grain diameter (middle panel) and standard deviation (lower panel) for simulations L02 (red) and L04 (blue) (Low nourishment, accretive waves).

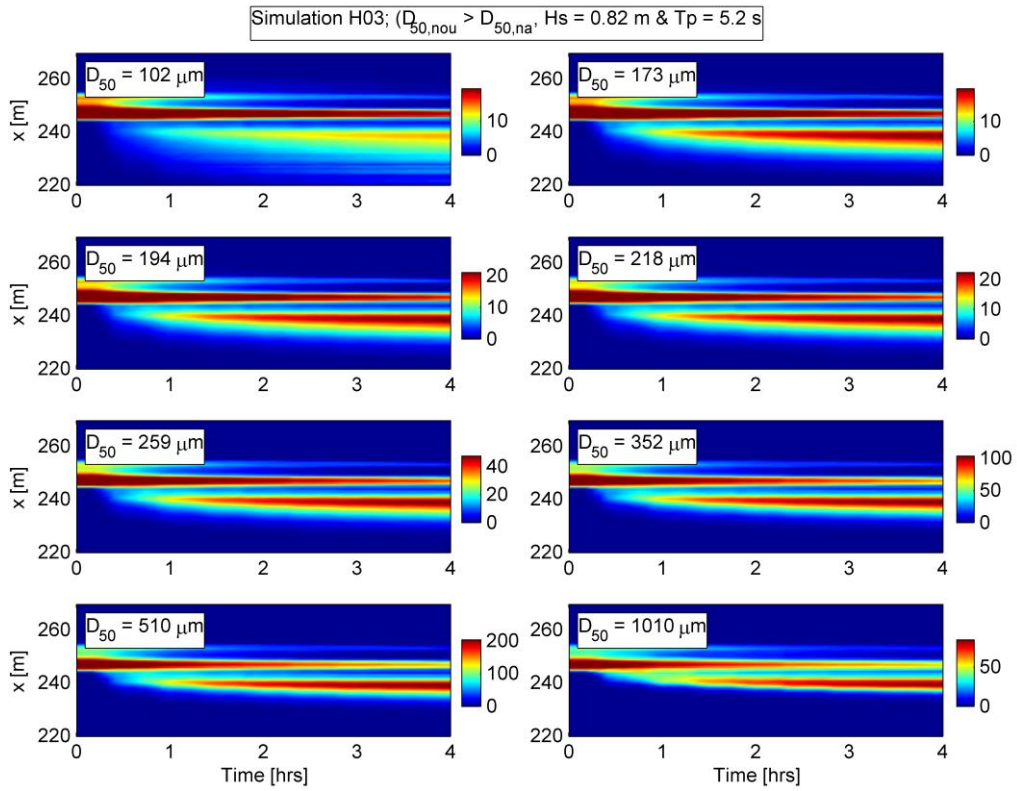

Figure 7.31 - Sediment mass in the flume in time for all 8 fractions of sand for simulation H03 (high design, erosive waves).

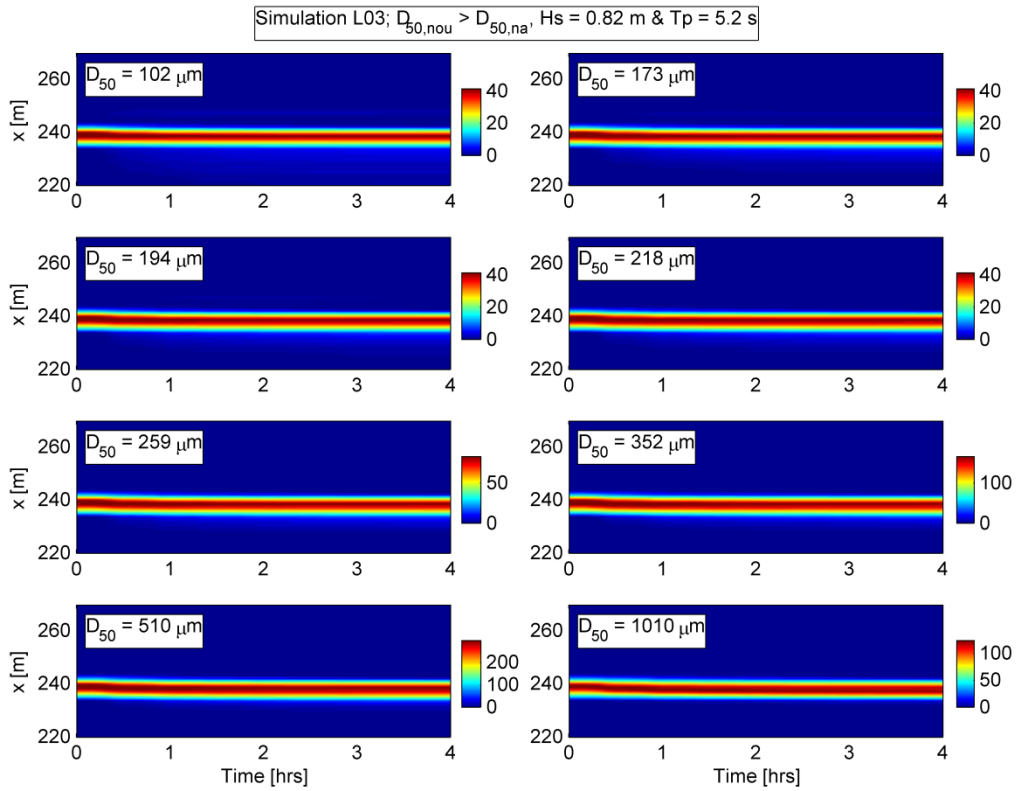

Figure 7.32 - Sediment mass in the flume in time for all 8 fractions of sand for simulation L03 (low design, erosive waves).

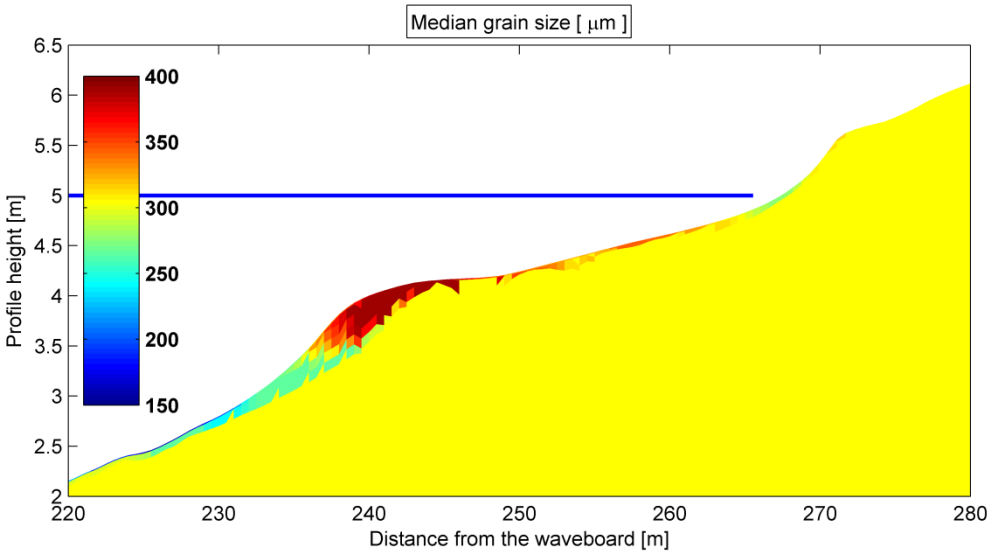

Figure 7.33 - Vertical grain size distribution for simulation H03 (high design, erosive waves).

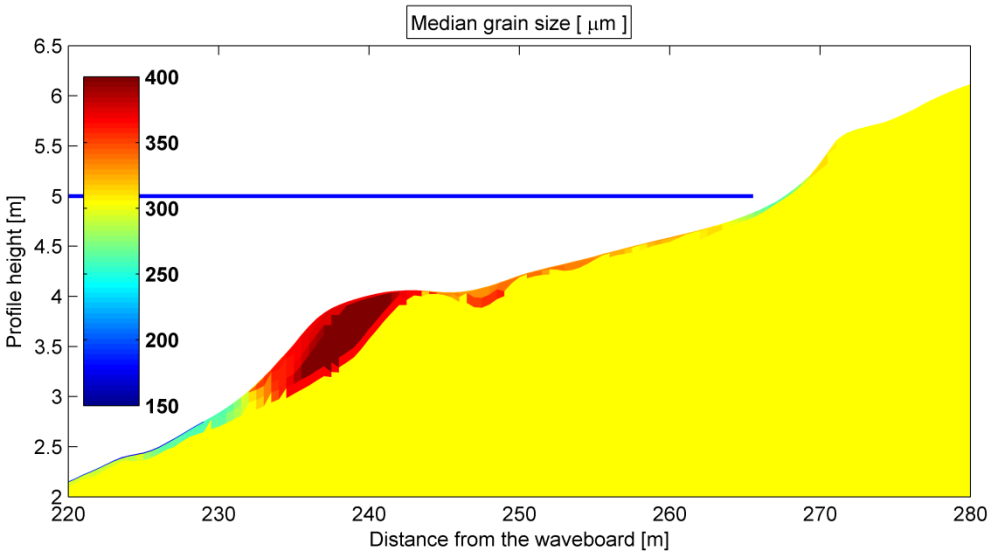

Figure 7.34 - Vertical grain size distribution for simulation L03 (low design, erosive waves).

Part IV – Conclusions and Recommendations

8 Conclusions

The main purpose of this study was to gain insight in grain sorting mechanisms which would contribute to a better understanding of sediment transport processes and morphological development of the nearshore area. This translated into the following research objective:

Setting-up and validation of a modelling approach to understand and assess the effect of grain sorting on the nearshore morphodynamics for both natural and nourished beaches.

This was accomplished by analysing data from physical experiments focussing on the morphological development of natural beaches and subsequently calibrating and validating a number of models using this data. After extensively analysing several different modelling approaches, one was chosen to investigate sorting processes for nourished beaches. The main conclusions of this study are presented in this chapter.

8.1 Physical experiment

Physical experiments carried out in the Hannover flume were in line with observations and findings from literature. Three test cases using different wave heights (erosive, mildly accretive and accretive waves) were chosen as representative for different wave conditions (section 3.1.3). Measurements showed that sorting processes are highly dependent on the wave forcing.

The profile development was related to the following parameters: median grain size, standard deviation and skewness of the sediment distribution (section 3.2).

During erosive wave conditions (representative of storm-like events) fining offshore of the breaker bar was observed. This was described by offshore sand samples skewed towards the fine tail of the sieve curve and a decrease in sorting. The decrease in sorting means that the sample became better graded and thus had a wider distribution. The offshore fining was explained considering the lower settling velocity and higher transport velocity of fine sediments, which therefore tend to settle further offshore than the coarser sediment. Moreover, large coarsening of the sediment is observed on top and offshore of the breaker bar. For less energetic wave conditions an increase of the grain size at the upper shoreface was observed. This is related to a reduced entrainment of coarser particles due to a reduction in wave power while the finer sediment is still transported by the flow. For accretive wave conditions (representative of mild wave conditions), finer sediment is transported onshore from the inner bar towards the beach. Accretion is found above the water line and some coarsening is observed at the water line.

8.2 Modelling approach

In this thesis a modelling study was carried out using the Delft3D modelling system. Two different wave modelling approaches were used, one accounting only for short-wave action and one where the effect of short-wave groupiness on (bound) long waves was taken into account. Besides the different wave modelling approaches, the way the sediment distribution was modelled was varied. On one side, the classical description of grain size was used, where the sediment is schematized by one single fraction and the bed is a uniform well-mixed bed; on the other side a schematization using multiple sediment fractions and a layered-bed stratigraphy to account for sorting processes was used.

This led to a total number of four modelling methodologies (see section 4.2). Their performance in simulating hydro-morphodynamics in a 2DV cross-shore model representing

the Hannover flume experiments was evaluated. Besides a qualitative validation based on the models capability to represent the physical processes in the nearshore area, the Brier Skill Score was used as an independent measure for the models performance in simulating morphology. Based on the modelling of the three representative cases (erosive, mildly accretive and accretive wave conditions) it is concluded that the inclusion of long waves into the model computations yields significant better results than a model approach that does not take this into account. This was mainly caused by the better predicted bar location; in the upper shoreface additional shear stresses are found due to the presence of the long wave motion, leading to higher sediment concentrations in the water column of this location. This eventually leads to larger transport rates, causing the deposits to be more offshore compared to the regular short-wave model.
Simulating with multiple sediment fractions and a layered bed-stratigraphy does show slight improvement compared to the single-fraction approach, but not as much as the improvement obtained by including long waves (section 5.4). This was mainly caused by a better prediction of upper-shoreface erosion. The erosion in the upper part of the profile was slightly reduced due to the presence of coarser fractions, thus leading to a higher skill score. The inclusion of multiple sediment fractions does not lead to a better representation of the bar. A smoothening of the bar was observed caused by the finer fractions being transported further offshore by the flow.

To summarize, the modelling approach including long waves and multiple sediment fractions and layered stratigraphy was able to represent the hydro-morphodynamics in the flume with excellent skill for storm-conditions, good skill for mildly accretive conditions and poor skill for accretive conditions. Furthermore, sorting processes were computed significantly better using the long wave approach compared to the regular short wave approach. Therefore, this approach is chosen as the best suitable to simulate hydro-morphodynamics and sorting processes in cross-shore direction.

8.3 Nourishment case study

Based on the results found with the Hannover Flume Model, the modelling approach that yielded the best results was chosen to investigate sorting processes at the morphological development of different nourishment designs. Two fundamentally different nourishment types were investigated: a beach nourishment and a shoreface nourishment. For the shoreface nourishment two designs were investigated: one located high in the profile (on top of the breaker bar) and one located low in the profile (seaward of the breaker bar) (see section 6.1).
Both shoreface nourishment designs and the beach nourishment design were compared to available data; the beach nourishment design was quantitatively validated with flume experiments of Vousdoukas et al. (2014) and the shoreface nourishments were validated qualitatively with an experimental study by Walstra et al. (2011). The model was able to simulate the development of the beach nourishment with a Brier Skill Score of ‘fair’ for accretive conditions and ‘good’ for erosive conditions. However, it was observed that for lower wave conditions the erosion rate of the nourishment was underestimated while for higher wave conditions the erosion rate was overestimated.
For the shoreface nourishment designs the model computations showed qualitatively a similar development of the profile as observed by Walstra et al. (2011). Accretive processes were not found in the model computations, but a clear difference in behaviour for erosive and mildly accretive waves was found (see section 7.1.2).

The functioning of the different nourishment designs was assessed. The beach nourishment is redistributed in the upper part of the profile, leading to a relative increase of sand volume in

the upper shoreface. The presence of the beach nourishment does not influence the bar dynamics in the lower part of the profile (section 7.2.1). The largest factor contributing to sorting for beach nourishments is different settling velocities for different sediment classes. Using a coarser grain size for the beach nourishment leads to a layer of coarser sediment redistributed on top of the upper profile, caused by settling of the coarser grains while the finer grains are transported further offshore. This may eventually lead to a reduction of the upper shoreface erosion by acting as an armouring layer (section 7.3.1).

The shoreface nourishments reduced erosion by reducing the wave height. Different from what is generally observed, no onshore movement of nourished sands was observed in the model computations, thus excluding the possibility that it acts as a feeder berm for the upper shoreface. The reduction of wave action in the upper part of the profile was highest for the nourishment design located high in the profile, while the lower shoreface nourishment reduced wave action more localized around the nourishment. Using a coarser grain size did not yield visible differences in the morphological development of the profile. However, this was mainly due to the fact that the sediment size used for the nourishment (400 µm) was rather similar to the native sand (300 µm).

For all shoreface nourishment designs a coarsening around the nourished area was observed. Due to reduced wave action the coarser fraction tends to settle in this area, while in the non-nourished case wave energy is sufficient to move part of the coarser fraction further offshore (section 7.3).

9 Limitations and Recommendations

In this study sorting phenomena during cross-shore development of natural and nourished beaches were investigated using a physical experiment and a numerical model. In this chapter a number of recommendations are presented, based on limitations from this present study. The recommendations are divided into three parts: recommendations on the physical experiments, recommendations on the modelling part of this thesis, some general recommendations for future research and practical implications of this work.

9.1 Physical experiments

In this study, data gathered in the context of the EU WISE project was made available. Moreover, recommendations on the setting-up of similar future experiments are given:

- During the experiments sediment samples were collected to investigate sorting processes. However, the location and number of samples taken was different in different tests. It is recommended to increase the number of samples taken, and to pre-determine the locations of sampling. It is also recommended to have additional samples taken further offshore to assess the length scale of the offshore fining trend. The volume of sand that is sampled is also a crucial parameter. Especially the thickness of the surface layer where the sediment is taken from largely influences the measured grain size distribution. Therefore, a pre-determined sand volume and thickness of the samples is required to obtain consistent measurements.

- Besides a higher spatial resolution in the sampling, a higher temporal resolution is also recommended; not only for the sediment samples but also for the morphological development. Each experiment (i.e. erosive & accretive) is characterized by a number of wave sequences. Bed profiling and sediment sampling is now performed after a certain number of wave sequences at the end of an experimental case. It is recommended to perform bed profiling and sampling during the test cases as well, thus at the end of each wave sequence. In this way also sorting processes and morphological development is monitored during the experiments.

- Sediment concentration data on vertical profiles in combination with velocity profiles should also be collected, as they can help in understanding the different mechanisms playing a role in morphological development (e.g. in case of different wave conditions).

9.2 Numerical modelling

A numerical model was used to investigate sorting processes for natural and nourished beaches. Although the model was able to capture most of the processes and observed phenomena a number of suggestions for future work is given.

- Although the model results have shown that simulating with multiple fractions can lead to coarsening of the top layer and thus a reduction of erosion, hiding and exposure is not computed explicitly in the transport formulation of Van Rijn (2007). It is expected that taking hiding and exposure into account will largely influence the sediment distribution in the cross-shore direction. When a coarser grain was used for the nourishment practically no differences in morphological development were found compared to the situation where the same material was use. In the change in grain size distribution however large differences were found. It is hypothesized that using a hiding and exposure formulation may show different trends.

- In this study it was shown that the inclusion of bound long waves in the Delft3D computation via the instationary roller model yields significantly better results for the morphological development of the profile. However, it was also observed that for lower waves, the shoaling was underestimated by the instationary roller module. The model without long waves shows a significantly better short wave height prediction for lower waves. This is likely related to the different wave dissipation formulae used for both the regular roller model and the instationary roller model (section 4.3). It is recommended to incorporate the dissipation formula of Baldock et al. (1998) also in the instationary roller model.

- The model was not able to reproduce the inner bar dynamics: no clear trough and secondary bar were computed by the model. It is hypothesized that this is related to a missing mechanism describing wave breaking generated turbulence in the Delft3D-code. In the trough area violent breaking waves (plunging) occur, leading to the large volumes of sand being eroded away in this part. Due to the trough formation, a slight decrease of flow velocity occurs here leading to the coarsening of sand in this area. Delft3D was not able to compute these inner-bar dynamics, leading to a wrong prediction of the sorting in this area. It is recommended to improve the modelling of wave-breaking phenomena around the bar area to capture sorting processes in this area as well.

- Delft3D showed difficulties in simulating accretive proceses. Bar behaviour is the result of a balance between offshore-directed current related suspended load and near-bed transport that can be either offshore or onshore directed. The onshore transport contributions are underestimated in Delft3D leading to difficulties in reproducing profile development especially for accretive wave conditions. This is crucial to be able to assess the morphological development under different wave conditions.

- The Delft3D model generally overestimates the beach erosion. Including long waves slightly improved the computation of the upper beach erosion, but still overestimation was observed. This is related to inaccuracies in the computed bed shear stress in the upper part of the profile and the absence of swash motion for the regular roller model. Including long waves implicitly implies including a swash motion. A different modelling approach, including explicit modelling of swash processes, might be required.

9.3 Future research

Using a 2DV-model and physical experiments, sorting phenomena were investigated. A new modelling approach was used in this study that showed promising results. However, a number of questions still remain unanswered which are worth investigating with this modelling approach:

- It is recommended to investigate sorting processes as a function of a larger number of parameters. In this study the only parameter varied was the wave condition, with Dean numbers ranging between 1 and 5. It is advised to investigate the long wave model and sorting phenomena for varying slopes and different sediment compositions (in terms of grain size and grading). This should also be done for the nourished beaches, in order to find general trends for different parameters.

- It is also recommended to investigate alongshore effects on sediment sorting patterns. It is advised to extend and test the modelling approach introduced in this thesis for full 3D situations, starting with highly schematized, simple benchmark cases, and then move on to field studies.

- The inclusion of long waves turned out to yield significant improvements in predicting the bar dynamics in this model. For engineering purposes it might be interesting to investigate if the effect of long waves on sediment transport can be parameterized and included in the regular short wave computation.

- Different options are available in Delft3D to describe the active layer thickness. Moreover, the number of fractions to describe the sieve curve is also a free parameter. Further investigation is recommended to assess the importance of these parameters.

9.4 Practical implications of this research

Several modelling approaches were tested against experimental data, and subsequently one modelling approach was applied to a case study where the morphological development of nourishments was simulated. Based on this study, some recommendations for a more practical approach are given:

- Based on this thesis, it is stated that for a correct representation of the morphology of natural beaches it is not necessary to take into account multiple sediment fractions (chapter 5). For nourished beaches, it is hypothesized that this is also the case, and that sediment variability between natural and nourished sand can be resolved by using two fractions: one for the natural sand, and one for the nourished sand. This notion still has to be investigated. For now it is stated that including multiple fractions into the computation is only necessary if the aim is to investigate sorting with the model. Another reason why one might be interested in using multiple sediment fractions is for keeping track of the sediments as shown in chapter 7.

- In chapter 5 and 7 it was shown that a modelling approach using long waves and multiple sediment fractions yields improved prediction of the morphodynamic evolution of natural and nourished beaches. Used correctly, it can yield more accurate predictions of nourishment lifetime and efficiency. It can also be used to further investigate how nourishments affect bar behaviour in the nearshore area.

- For policy makers the state of the coast is usually summarized by using coastal indicators. These are simple quantities like the beach width, dune foot position or coastline position. The model can be used to quantify the effect of nourishments on coastal indicators which may help in decision making regarding the placement of nourishments or nourishment strategy.

- It was shown in chapter 5 and 7 that the model is capable of (qualitatively) predicting sorting processes for natural and nourished beaches. Nourishing the beach has large effects on the biodiversity of the nearshore and beach area. Numerous species that are situated in the nearshore area may be affected in one or more ways by human alteration of the beach or surfzone. An accurate prediction of sorting processes may provide insight in effect of nourishments on species in the nourishment area. It can be used to determine a trade-off between nourishment life-time and ecological effects, or to determine how long it will take before the natural grain size of the region is restored.

References

Antia, E. E. (1993). Surficial grain-size statistical parameters of a North Sea shoreface-connected ridge : patterns and process implication. *Geo-Marine Letters*, *13*, 172–181.

Bagnold, R. A. (1954). Experiments on a Gravity-free Dispersion of Large Solid Spheres in a Newtonian Fluid Under Shear. *Proceedings of the Royal Society of London, Series A. Mathematical and Physical Sciences*, *225*(1160), 49–63.

Bagnold, R. A. (1963). Mechanics of Marine Sedimentation. *The Sea: Ideas and Observations*, *3*, 507–528.

Baldock, T. E., Holmes, P., Bunker, S., Van Weert, P. (1998). Cross-shore hydrodynamics within an unsaturated surf zone. *Coastal Engineering*, *34*, 173–196.

Baldock, T. E., Manoonvoravong, P., Pham, K. S. (2010). Sediment transport and beach morphodynamics induced by free long waves, bound long waves and wave groups. *Coastal Engineering*, *57*(10), 898–916. doi:10.1016/j.coastaleng.2010.05.006

Benedet, L., Finkl, C. W., Campbell, T., Klein, A. (2004). Predicting the effect of beach nourishment and cross-shore sediment variation on beach morphodynamic assessment. *Coastal Engineering*, *51*(8-9), 839–861. doi:10.1016/j.coastaleng.2004.07.012

Blott, S. J., Pye, K. (2001). GRADISTAT : a grain size distribution and statistics package for the analysis of unconsolidated sediments. *Earth Surface Processes and Landforms*, *26*, 1237–1248. doi:10.1002/esp.261

Bosboom, J., Stive, M. J. F. (2013). *Coastal Dynamics 1* (version 0.). VSSD.

Brière, C., Giardino, A., van der Werf, J. (2010). Morphological Modeling of Bar Dynamics With Delft3D: The Quest for Optimal Free Parameter Settings Using an Automatic Calibration Technique. *Coastal Engineering*, 1–12.

Brière, C., Walstra, D. J. R. (2006). *Modelling of Bar Dynamics*. Report Z4099, WL|Delft Hydraulics, The Netherlands.

Bruun, P. (1954). *Coast Erosion and the Development of Beach Profiles*. Techn. Mem. No. 44, Beach Erosion Board, U.S. Army Corps of Engineers.

Caceres, I. (n.d.). *Data Storage Report WISE Benchmark*.

Clifton, H. E. (1969). Beach lamination: nature and origin. *Marine Geology*, *7*, 553–559.

De Vriend, H. (1989). 2DH Modelling of Transient Sea Bed Evolutions. In *Coastal Engineering Proceedings* (p. 20).

Dean, R. G. (1977). Equillibrium Beach Profiles: Characteristics and Applications. *Journal of Coastal Research*, *7*(1), 53–84.

Dean, R. G. (1987). Coastal Sediment Processes: Toward Engineering Solutions. In *Coastal Sediments* (pp. 1–24).

Dean, R. G. (2002). *Beach Nourishment: Theory and Practice*. Volume 18. World Scientific.

Deigaard, R., Jakobsen, J. B., Fredsøe, J. (1999). Net sediment transport under wave groups and bound long waves. *Journal of Geophysical Research*, *104*(C6), 13559. doi:10.1029/1999JC900072

Dette, H. ., Larson, M., Murphy, J., Newe, J., Peters, K., Reniers, a, Steetzel, H. (2002). Application of prototype flume tests for beach nourishment assessment. *Coastal Engineering*, *47*(2), 137–177. doi:10.1016/S0378-3839(02)00124-2

Doering, J. C., Bowen, a. J. (1995). Parametrization of orbital velocity asymmetries of shoaling and breaking waves using bispectral analysis. *Coastal Engineering*, *26*(1-2), 15–33. doi:10.1016/0378-3839(95)00007-X

Eitner, V., Ragutzki, G. (1994). Effects of Artificial Beach Nourishment on Nearshore Sediment Distribution (Island of Norderney, Southern North Sea). *Journal of Coastal Research*, *10*(3), 637–650.

Folk, R. L. (1980). *Petrology of Sedimentary Rocks*. Austin, Texas 78703: Hemphill Publishing Company.

Folk, R. L., Ward, W. C. (1957). Brazos River Bar: A Study in the Significane of Grain Size Parameters. *Journal of Sedimentary Petrology*, *27*(1), 3–26.

Fredsøe, J., Deigaard, R. (1992). *Mechanics of Coastal Sediment Transport* (Volume 3.). World Scientific.

Gallagher, E. L., Elgar, S., Guza, R. T. (1998). Observations of sand bar evolution on a natural beach. *Journal of Geophysical Research*, *103*(C2), 3203–3215.

Giardino, A., Brière, C., van der Werf, J. (2011). *Morphological modelling of bar dynamics with Delft3D: The quest for optimal parameter settings*.

Grasso, F., Michallet, H., Barthélemy, E. (2011). Sediment Transport Associated with Morphological Beach Changes Forced by Irregular Asymmetric, Skewed Waves. *Journal of Geophysical Research*, *116*(C3), C03020. doi:10.1029/2010JC006550

Guillén, J., Hoekstra, P. (1996). The " equilibrium " distribution of grain size fractions and its implications for cross-shore sediment transport : a conceptual model. *Marine Geology*, *135*, 15–33.

Hamm, L., Capobianco, M., Dette, H. ., Lechuga, a, Spanhoff, R., Stive, M. J. . (2002). A summary of European experience with shore nourishment. *Coastal Engineering*, *47*(2), 237–264. doi:10.1016/S0378-3839(02)00127-8

Hoekstra, P., Houwman, K. T., Kroon, A., Ruessink, B. G., Roelvink, J. A., Spanhoff, R. (1996). Morphological development of the Terschelling shoreface nourishment in response to hydrodynamic and sediment transport processes. *Coastal Engineering*, 2897–2910.

Holthuijsen, L. (2007). *Waves in oceanic and coastal waters*.

Komar, P. D., Wang, C. (1984). Processes of Selective Grain Transport and the Formation of Placers on Beaches. *The Journal of Geology*, 637–655.

Lesser, G. R., Roelvink, J. A., van Kester, J. A. T. M., Stelling, G. S. (2004). Development and validation of a three-dimensional morphological model. *Coastal Engineering*, *51*(8-9), 883–915. doi:10.1016/j.coastaleng.2004.07.014

Lippmann, T. C., Holman, R. A. (1990). The Spatial and Temporal Variability of Sand Bar Morphology. *Journal of Geophysical Research*, *95*(C7), 575–590.

List, J. H. (1991). Wave groupiness variations in the nearshore. *Coastal Engineering*, *15*(5-6), 475–496. doi:10.1016/0378-3839(91)90024-B

Longuet-Higgins, M. S., Stewart, R. W. (1964). Radiation stresses in water waves; a physical discussion, with applications. *Deep-Sea Research*, *11*, 529–562.

Medina, R., Losada, M. A., Losada, I. J., Vidal, C. (1994). Temporal and spatial relationship between sediment grain size and beach profile. *Marine Geology*, *118*, 195–206.

Reniers, A. J. H. M., Gallagher, E. L., MacMahan, J. H., Brown, J. A., van Rooijen, A. A., van Thiel de Vries, J. S. M., van Prooijen, B. C. (2013). Observations and modeling of steep-beach grain-size variability. *Journal of Geophysical Research: Oceans*, *118*(2), 577–591. doi:10.1029/2012JC008073

Rocha, M. V. L., Michallet, H., Silva, P. A., Abreu, T., Barthélemy, E. (2013). Nonlinearities of Short and Long Waves Across the Shoaling, Surf and Swash Zones: Physical Model Results. In *Coastal Dynamics* (pp. 1329–1340).

Roelvink, J. A. (1993). Dissipation in Random Wave Groups Incident on a Beach. *Coastal Engineering*, *19*, 127–150.

Roelvink, J. A., Meijer, T. J. G. P., Houwman, K., Bakker, R., Spanhoff, R. (1995). Field Validation and Application of a Coastal Profile Model. In *Proceedings Coastal Dynamics Conference* (pp. 818–828).

Roelvink, J. A., Stive, M. J. . (1989). Bar-Generating Cross-Shore Flow Mechanisms on a Beach. *Journal of Geophysical Research*, *94*(C4), 4785–4800.

Ruessink, B. ., Walstra, D. J. ., Southgate, H. . (2003). Calibration and verification of a parametric wave model on barred beaches. *Coastal Engineering*, *48*(3), 139–149. doi:10.1016/S0378-3839(03)00023-1

Sirks, E. E. (2013). *Sediment Sorting at a Large Scale Nourishment*. Delft University of Technology.

Slingerland, R., Smith, N. D. (1986). Occurrence and Formation of Water-Laid Placers. *Annual Review of Earth and Planetary Sciences*, *14*, 113–147.

Smit, M. W. J., Reniers, A. J. H. M., Stive, M. J. F. (2010). What Determines Nearshore Bar Response? *Coastal Engineering*, *32*, 1–7.

Stauble, D. K. (2005). A Review of the Role of Grain Size in Beach Nourishment Projects.

Steidtmann, J. R. (1982). Size-Density Sorting of Sand-Size Spheres During Deposition from Bedload Transport and Implications Concerning Hydraulic Equivalence. *Sedimentology*, *29*, 877–883.

Svendsen, I. A. (1984). Mass Flux and Undertow in a Surfzone. *Coastal Engineering*, *8*, 347–365.

Tonnon, P. K., Hoyng, C. W., Van Rijn, L. C. (2009). Beach Profile Modeling At Different Scales. In *Coastal Dynamics*.

Van Bemmelen, C. E. (1988). *De korrelgrootte-samenstelling van het strandzand langs de Nederlandse Noordzee-kust*.

Van Duin, M. J. P., Wiersma, N. R., Walstra, D. J. R., van Rijn, L. C., Stive, M. J. F. (2004). Nourishing the shoreface: observations and hindcasting of the Egmond case, The Netherlands. *Coastal Engineering*, *51*(8-9), 813–837. doi:10.1016/j.coastaleng.2004.07.011

Van Rijn, L. C. (1998). The Effect of Sediment Composition on Cross-Shore Bed Profiles. In *Coastal Engineering* (pp. 2495–2508).

Van Rijn, L. C. (2007a). Unified View of Sediment Transport by Currents and Waves . I : Initiation of Motion , Bed Roughness , and Bed-Load Transport. *Journal of Hydraulic Engineering*, *133*(June), 649–667.

Van Rijn, L. C. (2007b). Unified View of Sediment Transport by Currents and Waves. II: Suspended Transport. *Journal of Hydraulic Engineering*, *133*(6), 668–689. doi:10.1061/(ASCE)0733-9429(2007)133:6(668)

Van Rijn, L. C. (2013). Basic Hydrodynamic Processes in the Coastal Zone.

Van Rijn, L. C., Roelvink, J. A., Horst, W. T. (2000). *Approximation formulae for sand transport by currents and waves and implementation in DELFT-MOR*. Tech. Rep. Z3054.40, WL|Delft Hydraulics, Delft, The Netherlands.

Van Rijn, L. C., Tonnon, P. K., Walstra, D. J. R. (2011). Numerical modelling of erosion and accretion of plane sloping beaches at different scales. *Coastal Engineering*, *58*(7), 637–655. doi:10.1016/j.coastaleng.2011.01.009

Van Rijn, L. C., Walstra, D. J. R., Grasmeijer, B., Sutherland, J., Pan, S., Sierra, J. P. (2003). The predictability of cross-shore bed evolution of sandy beaches at the time scale of storms and seasons using process-based Profile models. *Coastal Engineering*, *47*(3), 295–327. doi:10.1016/S0378-3839(02)00120-5

Van Rooijen, A. A. (2011). *Modelling of Sediment Transport in the Swas Zone*. Delft University of Technology.

Vousdoukas, M. I., Kirupakaramoorthy, T., Oumeraci, H., de la Torre, M., Wübbold, F., Wagner, B., Schimmels, S. (2014). The role of combined laser scanning and video techniques in monitoring wave-by-wave swash zone processes. *Coastal Engineering*, *83*, 150–165. doi:10.1016/j.coastaleng.2013.10.013

Walstra, D. J. R., Hoyng, C. W., Tonnon, P. K., van Rijn, L. C. (2011). Experimental study investigating various shoreface nourishment designs. In *32nd International Conference on Coastal Engineering, ICCE 2010, June 30 - July 5, Shanghai, China* (pp. 1–13).

Walstra, D. J. R., Van Rijn, L. C., Van Ormondt, M., Brière, C., Talmon, A. M. (2007). The Effects of Bed Slope and Wave Skewness on Sediment Transport and Morphology, 1–14.

Wang, P., Davis, R. A., Kraus, N. C. (1998). Cross-shore distribution of sediment textures under breaking waves. *Journal of Sedimentary Research*, *68*(3), 497–506.

Wright, L. D., Short, A. D. (1984). Morphodynamic Variability of Surf Zones and Beaches: a Synthesis. *Marine Geology*, *56*(1), 93–118.

Appendices

A Appendix to chapter 3 – Experiments

A summary of all the experiments performed by Michalis Vousdoukas in the GWK at Hannover is provided in Table A.1. In test case 3, 4 and 10 it was not possible to maintain a certain wave height, therefore leading to the classification 'varying'. Case 5 is named 'RESET', meaning that the profile was restored to a uniform 1/15 linear slope. The experiments that were used in this study (defined as 1, 2 and 3 in the main body) are case 1 (erosive), case 2 (mildly accretive) and case 3 (accretive).

Table A.1 - Overview of all the test cases in the GWK.

Test case	Test nature	H_s [m]	T_p [s]	Duration (h)
1	Erosive	0.9	5.1	4.75
2	Accretive	0.6	6.3	10
3	-	Varying	Varying	14.5
4	-	Varying	Varying	17.7
5	RESET	-	-	-
6	Erosive	0.9	5.1	4.75
7	Accretive	0.51	7.0	20.5
8	Erosive	1.0	5.0	7.25
9	Accretive	0.4	10.0	7.0
10	-	Varying	Varying	9.2
11	Erosive	1.0	5.0	7.25
12	Accretive	0.4	10.0	7.5
13	Accretive	0.3	10.0	7.0
14	Accretive	0.2	10.0	7.0
15	Erosive	1.0	5.0	5.85

B Appendix to chapter 4 – Model input

In this appendix the model input to set-up the Hannover Flume Model is treated. A summary of the settings is provided, and the input that must be provided for the wave models, sediment models and bed models are given.

B.1 Input for the Stationary Roller Model

To have the roller equations included in the FLOW-module, it has to be switched on by including a flag in the mdf-file:

Roller = #yes#

The boundary information for the SRM is found in the wavecon-file, which is stored in the working directory as <wavecon.*rid*>. Here *rid* stands for Run-ID, the name of the mdf-file. The structure of the wavecon-file is given in Table B.1.

Table B.1 – Structure of the wavecon-file.

*** ltdate**	**Hs**	**Tp**	**Dir (^{0})**	**ms**	**wl**	**windspeed**	**wind dir. (^{0})**
BL01							
3 8 * number of rows number of colums							
T_0	0.82	5.2	270	5.0	0.0	0.0	0.0
T_1	0.82	5.2	270	5.0	0.0	0.0	0.0
T_{end}	0.82	5.2	270	5.0	0.0	0.0	0.0

Note that in this table there are three rows specified, meaning 3 wave conditions. The user-specified (or computed by the WAVE-module) significant wave height can be time-varying, making this a quasi-stationary boundary-condition. In this study, only a significant wave height at T_0 and T_{end} is prescribed, which does not change over time thus making this a stationary boundary. The parameters that must be specified are:

Itdate [min]	Time point after reference date in minutes.
Hs [m]	Significant wave height, this value will be prescribed on the boundary, where it is used to calculate the wave energy. The roller model then calculates the energy propagation throughout the model domain.
Tp [s]	Peak period of the energy spectrum, this value will be prescribed on the boundary.
Dir [^{0}]	Mean wave direction according to Nautical convention (in degrees). For this model waves are travelling in one horizontal dimension: the x-direction.
ms [-]	Width of the energy distribution.
Water level [m]	The additional water level over the entire model domain.
Wind speed [m/s]	Wind velocity at 10 m elevation. Since an indoor wave-flume experiment is modelled, there is no wind in the model.
Wind direction [^{0}]	Wind direction at 10 m elevation. Since an indoor wave-flume experiment is modelled, there is no wind in the model.

B.2 Input for the InStationary Roller Model

To let the model run in Instationary mode, a wave spectrum to generate the boundary conditions with must be given in a file specified in the mdf-file through a keyword:

Filwcm = #wavcmp#

Here <wavcmp> may be any legitimate filename. In this file a number of spectral wave components is given that represent the wave spectrum. The structure of the <wavcmp>-file is shown in Table B.2.

Table B.2 – Input structure of <wavcmp>-file

Record	Record Description
1	Arbitrary number of description records starting with an asterisk (*). These lines will be ignored except for the line containing the version number, which should read "* version 1".
2	N_c
3	h
4	f_{split}
5 to 4+N_c	f_j $a_{bc,j}$ $\varphi_{bc,j}$ $\theta_{bc,j}$
5 + N_c	nmskf nmskl mmskf mmskl
6 + N_c	timtap [sec]

Entries 5 to 5+N_c consist of 4 columns. The parameters in this table are:

N_c	The number of spectral wave components specified in row 5 to 4+N_c.
h	The characteristic water depth in [m] at the open boundaries.
f_{split}	The splitting frequency in [Hz] between free long waves and short waves. Only the components which have a frequency lower than the splitting frequency will be prescribed at the boundary as free waves. The splitting frequency is computed by $f_p/2$, with f_p the peak frequency
f_j	Is the frequency of wave component j in [Hz]. Wave components should be specified in order of increasing wave frequency, i.e. $f_{j-1}<f_j$.
$a_{bc,j}$	The amplitude of the wave component j in [m].
$\varphi_{bc,j}$	The phase angle of the incoming wave component j in [deg].
$\theta_{bc,j}$	The direction of the incoming wave component j in [deg] in Cartesian convention, i.e. a direction of 90 degrees corresponds to a wave travelling to the north.
nmskf	The grid number in η direction below which the wave forces are gradually and artificially reduced to zero at the lower boundary. Value should be -1 for no reduction.
nmskl	The grid number in η direction above which the wave forces are gradually and artificially reduced to zero at the lower boundary. Value should be -1 for no reduction.
mmskf	The grid number in ξ direction below which the wave forces are gradually and artificially reduced to zero at the lower boundary. Value should be -1 for no reduction.
mmskl	The grid number in ξ direction above which the wave forces are gradually and artificially reduced to zero at the lower boundary. Value should be -1 for no reduction.

timtap — is the time in seconds that is used by the taper for the incoming signals. It is advised to define timtap at least several times as large as the period of a typical group in the signal.

In this study the values for nmskf, nmskl, mmskf, mmskl are set to -1.

The amplitude components in the <wavcmp>-file are determined from the energy spectrum. In the flume experiment waves are uni-directional, so there is no variation in $\theta_{bc,j}$. The phase angle of the j-th component is drawn from a uniform distribution on the interval [0, 2π]. To determine the amplitude components an equidistant grid with grid size Δf is used. The energy in one frequency bin can be approximated by:

$$\Delta f E\left(j\Delta f\right)=\frac{1}{2}a_j^2 \tag{1.1}$$

In this equation a_j is the amplitude of the j-th wave component. The energy spectrum E(f) is computed from the wave gauge data. If no wave gauge data is available, the theoretical energy spectrum can be computed. For the Hannover Flume experiment, the spectrum should represent a JONSWAP-spectrum with a gamma-value of 3.3. The spectrum is given by:

$$E\left(f\right)=A_0\nu^{-5}\exp\left(-\frac{5}{4}\nu^{-4}\right)\gamma_0^{\exp\left(-(\nu-1)^2/\left(2\sigma^2\right)\right)} \tag{1.2}$$

$$\nu=f/f_p \tag{1.3}$$

$$\sigma=\begin{cases}0.07, & \nu\le 1\\ 0.09, & \nu>1\end{cases} \tag{1.4}$$

In this equation γ_0 and f_p are assumed to be known constants, with f_p the peak frequency. The parameter A_0 is related to the significant wave height through:

$$H_{sig}^2=16\int_0^\infty E\left(f\right)df \tag{1.5}$$

Since A_0 is a constant, this equation is easily solved if the significant wave height is known. In [appendix] a comparison studies is performed where computations with input from a measured spectrum is compared with input from the theoretical spectrum.

B.3 Input for the single sediment fraction model

Input for the single sediment fraction model is given in Table B.3.

Table B.3 – Part of the input structure of the sediment input file used for single fractions

Input Record	Record Description
Input block sediment characteristics	
SedTyp	Must be 'sand', 'mud' or 'bedload'
RhoSol	Specific density
SedDia	Median sediment diameter (D50)
SedD10	10% passing percentage diameter
SedD90	90% passing percentage diameter
CDryB	Dry bed density
IniSedThick	Initial sediment layer thickness at bed, through a thickness file prescribing the layer thickness in meters.

B.4 Input for the multiple sediment fraction model

Input for the multiple sediment fraction model is given Table B.4

Table B.4 – Part of the input structure of the sediment input file used for multiple fractions

Input Record	Record Description
Input block sediment characteristics (repeated per sediment fraction)	
SedTyp	Must be 'sand', 'mud' or 'bedload'
RhoSol	Specific density
SedMinDia	Minimum sediment diameter of fraction
SedDia	Median sediment diameter (D50) of fraction
SedMaxDia	Maximum sediment diameter of fraction
CDryB	Dry bed density
SdBUni	Initial sediment availability at the bed, given as a total mass. Prescribed in a

The sediment can be divided in several ways; one way is shown in Figure 4.3. Three other ways were tested in this thesis.

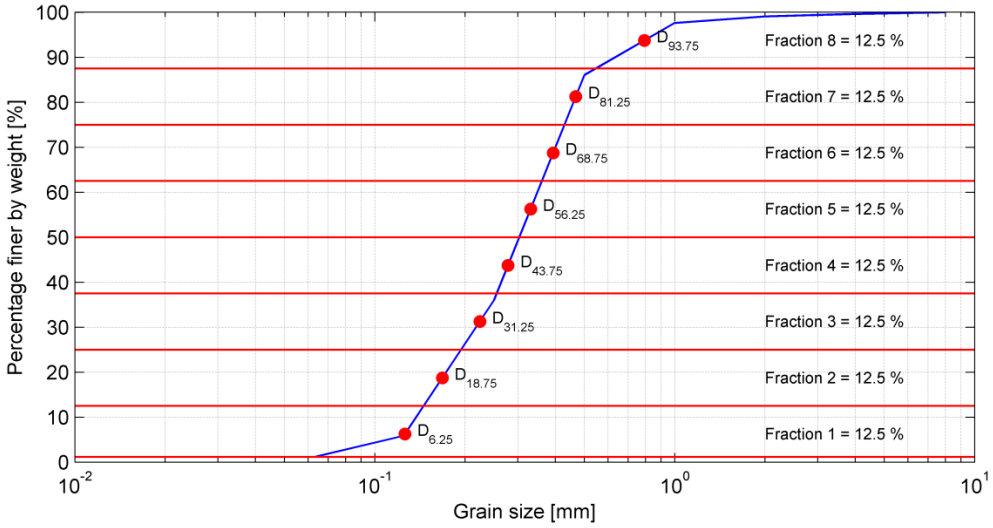

Figure B.1 - Original sample divided into eight equal fractions

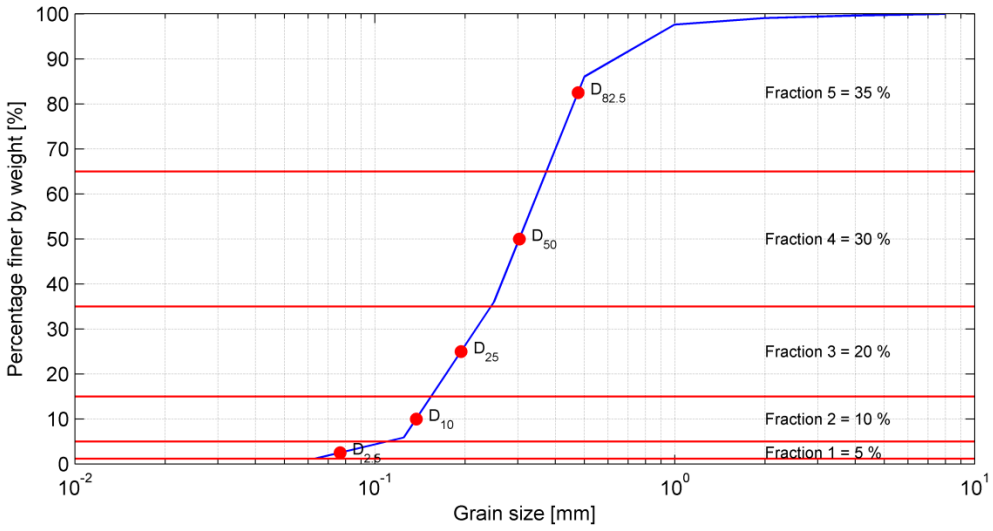

Figure B.2 - Original sample divided into five fractions, with emphasis on the fine tail.

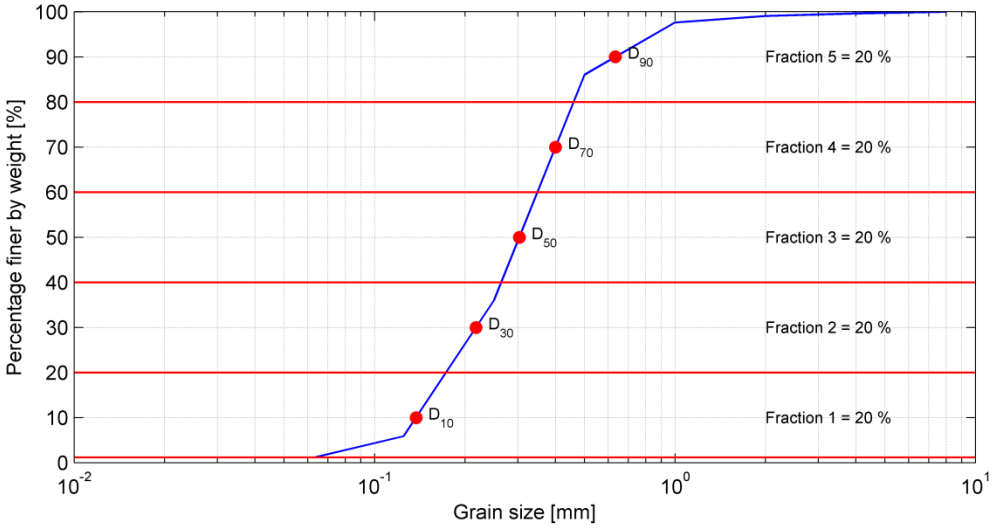

Figure B.3 - Original sample divided into five equal fractions.

B.5 Input for the layered bed-stratigraphy

In Table B.5 the input structure for specifying the layered bed-stratigraphy is given.

Table B.5 – Input structure of the Underlayer module

Input Record	Record Description
Underlayer input block	
IUnderlyr	Flag for underlayer concept
ExchLyr	
TTLForm	Transport layer thickness formulation
ThTrLyr	Transport layer thickness
MxNULyr	Number of underlayers
ThUnLyr	Thickness of each underlayer
UpdBaseLyr	Update the baselayer composition

The input structure for specifying an initially non-uniform bed is given in Table B.6.

Table B.6 – Input structure for an initial bed composition file.

Input Record	Record Description
Layer	
Type	Indicate type prescribed in layer (thickness, total mass, volume fraction, mass fraction)
Sedbed1 Sedbed2 . . . Sedbed*n*	Total sediment mass available in layer, prescribed through a <*.*sdb*>- file for spatial variation.
Repeat block as many times as desired for multiple layers	

C Appendix to chapter 5 – Model results HFM

This appendix is reserved for showing model results that are described in chapter 5 of the main body. The model results are put in the appendix to keep the main body as concise as possible.

C.1 Simulation results case 2

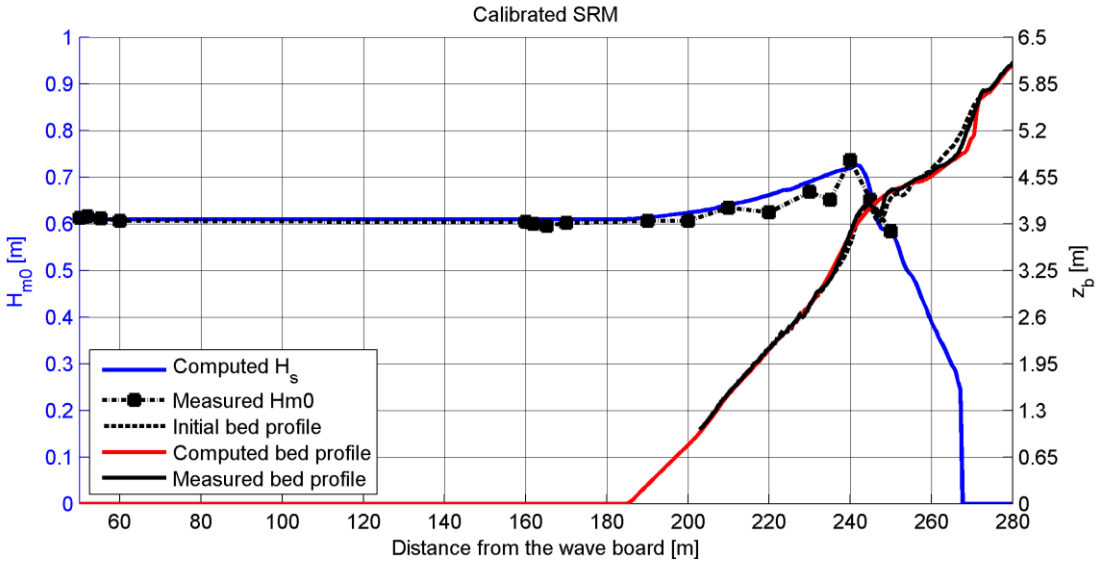

Figure C.1 - Simulation results for the Stationary Roller Model (single fraction)

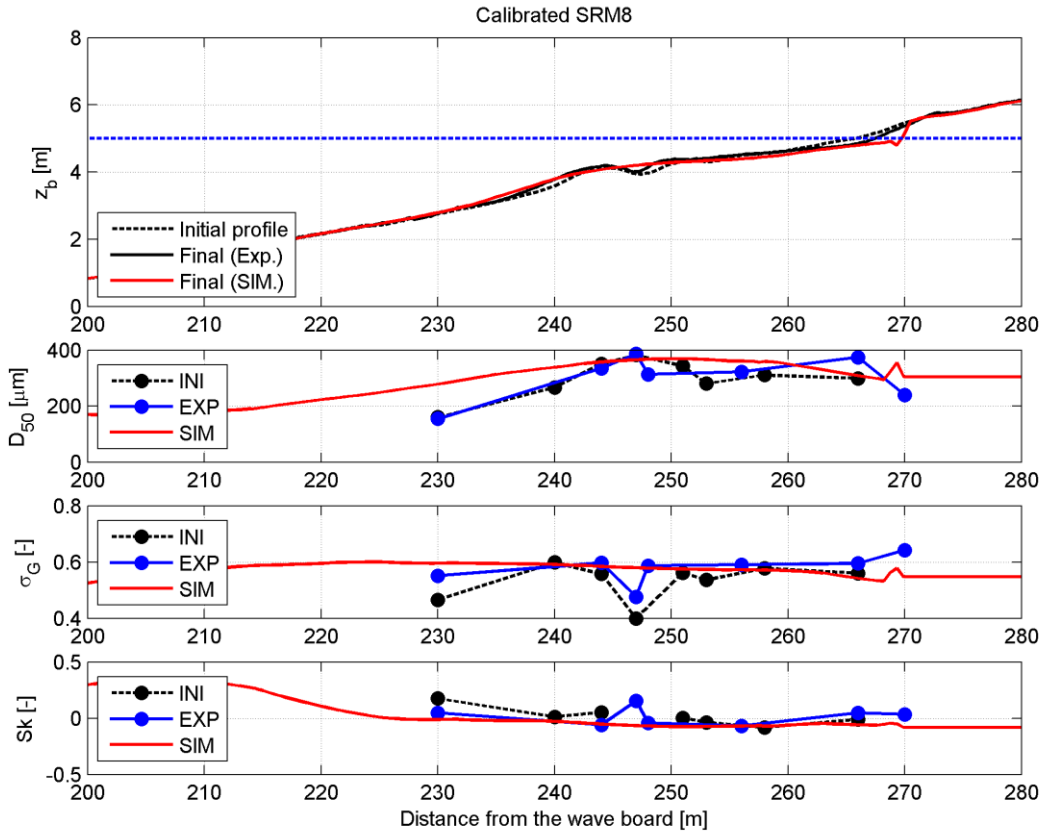

Figure C.2 - Simulation results of the Stationary Roller Model (multiple fractions)

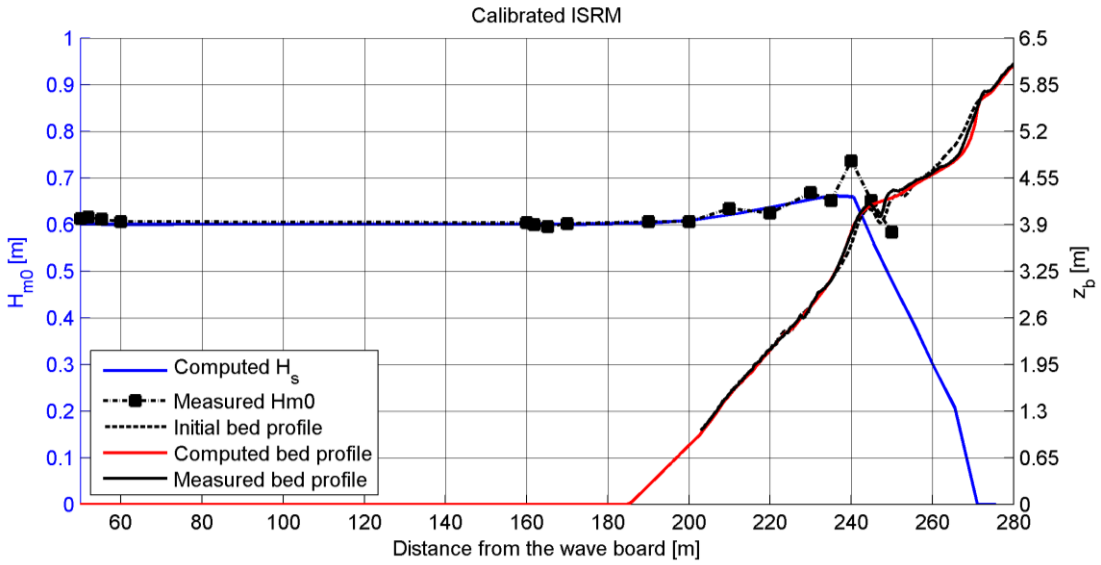

Figure C.3 - Simulation results of the InStationary Roller Model (single fraction).

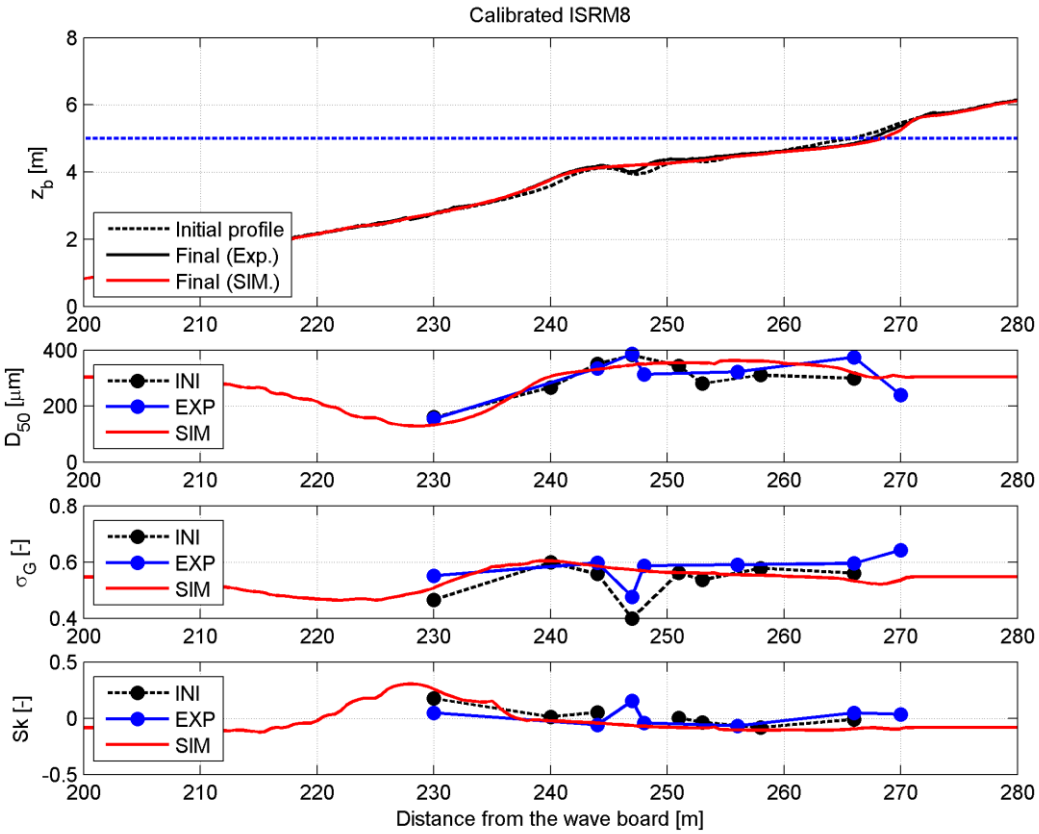

Figure C.4 - Simulations results of the InStationary Roller Model (multiple fractions)

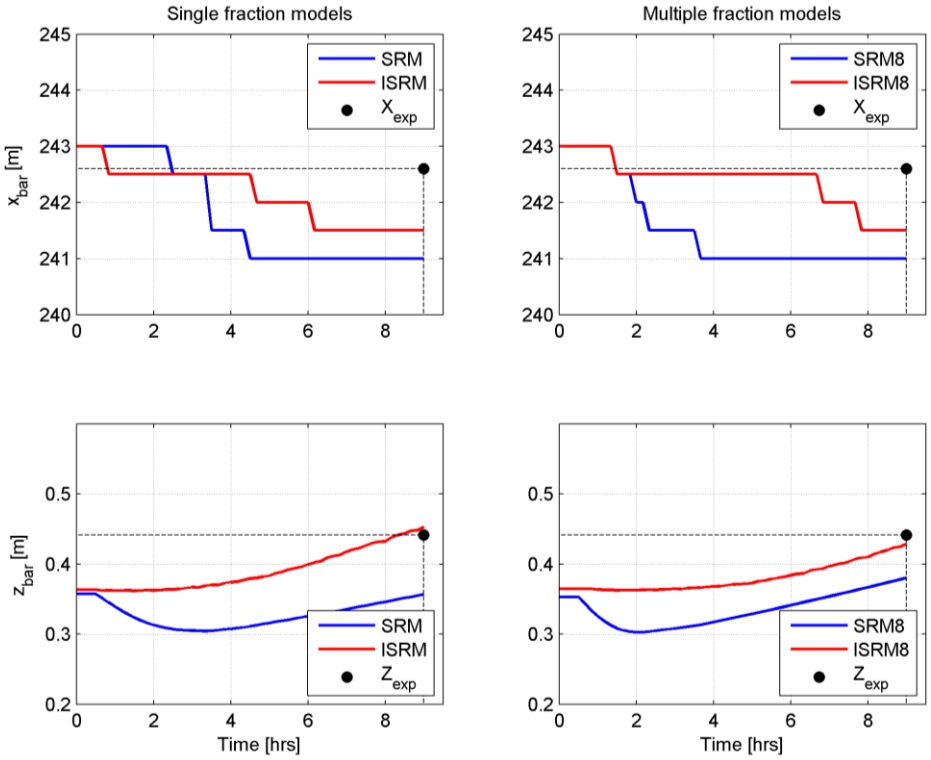

Figure C.5 - Bar position (upper panels) and bar height (lower panels) for the SRM (blue) and ISRM (red). Single fraction models are depicted in the left panels, multiple fraction models (SRM8 and ISRM8) are depicted in the right panels.

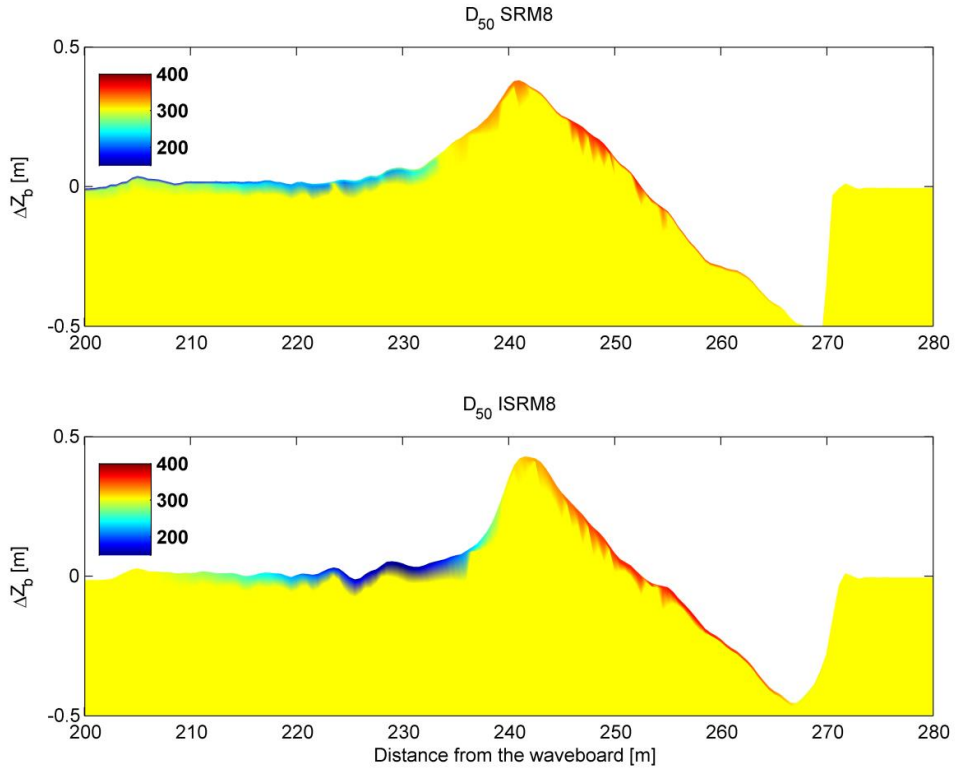

Figure C.6 - Vertical distribution of the median grain diameter for the SRM8 (upper panel) and ISRM8 (lower panel) along the flume against Δz

C.2 Simulation results case 3

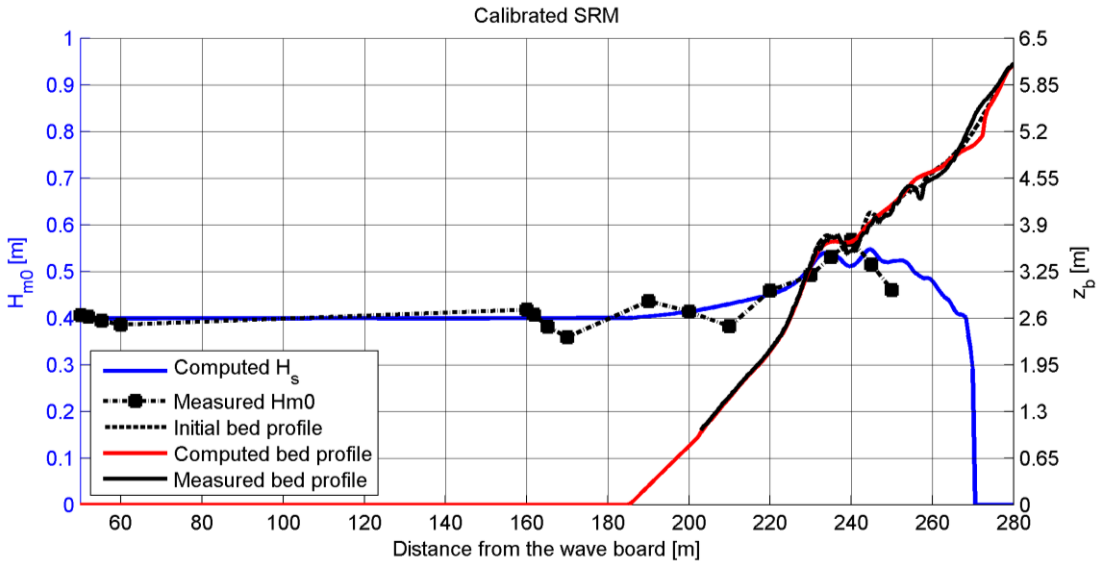

Figure C.7 - Simulation results for the Stationary Roller Model (single fraction)

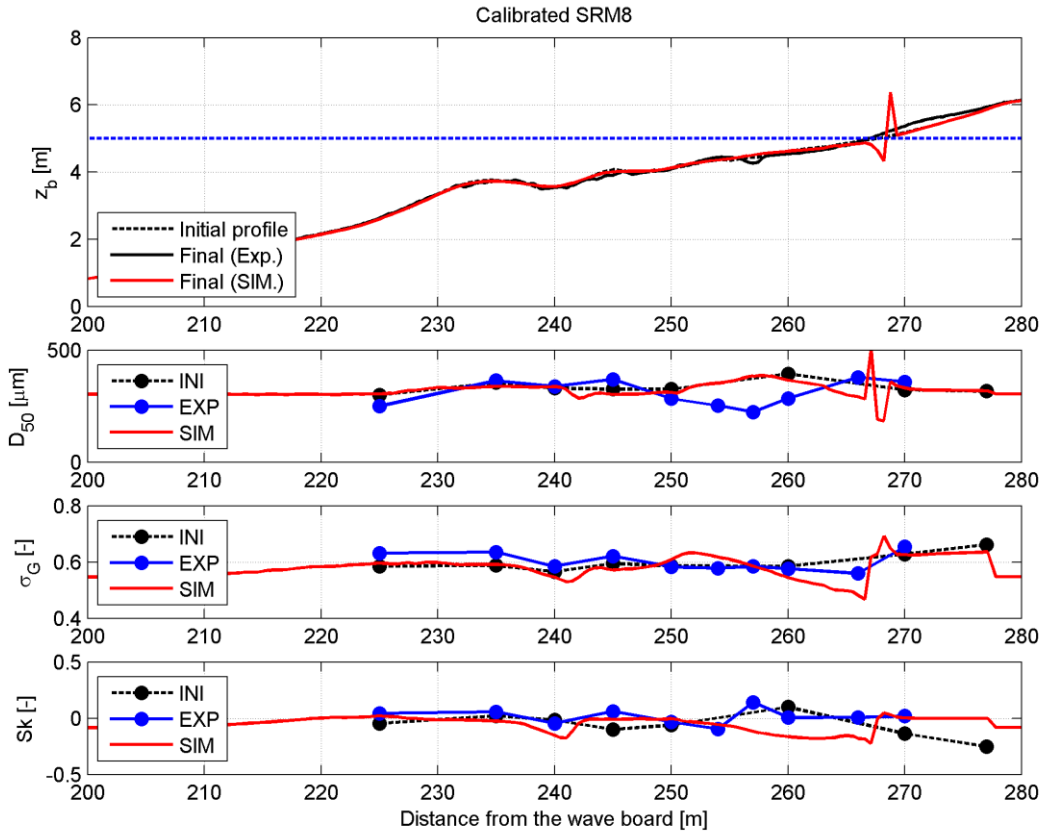

Figure C.8 - Simulation results for the Stationary Roller Model (multiple fractions)

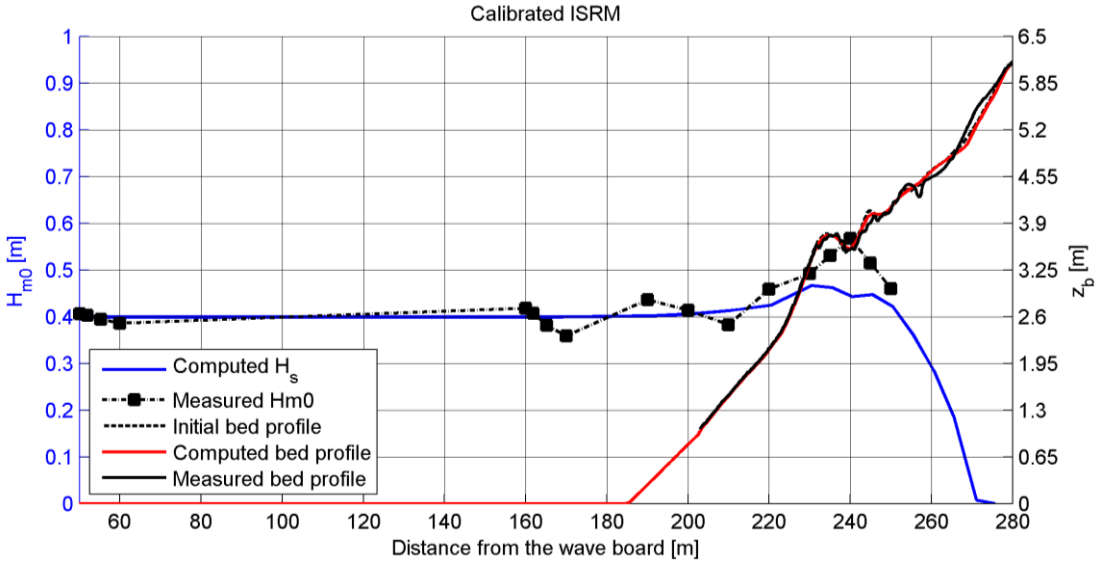

Figure C.9 - Simulation results of the InStationary Roller Model (single fraction).

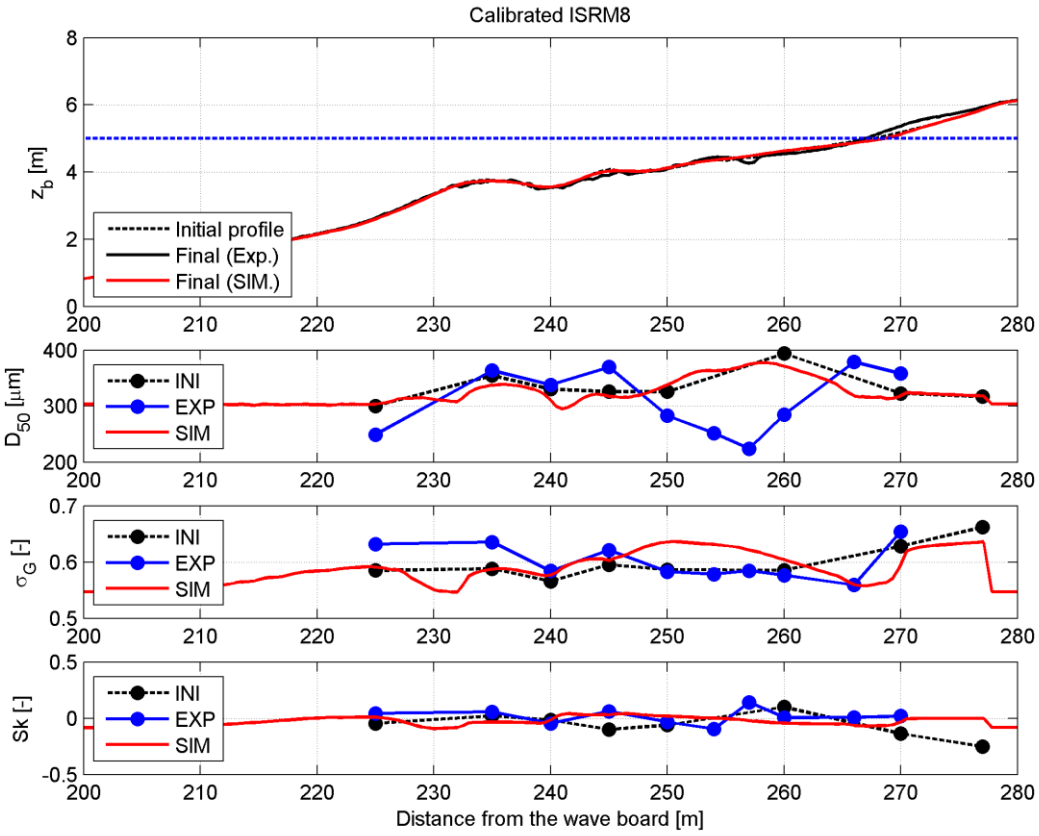

Figure C.10 - Simulation results of the InStationary Roller Model (multiple fractions).

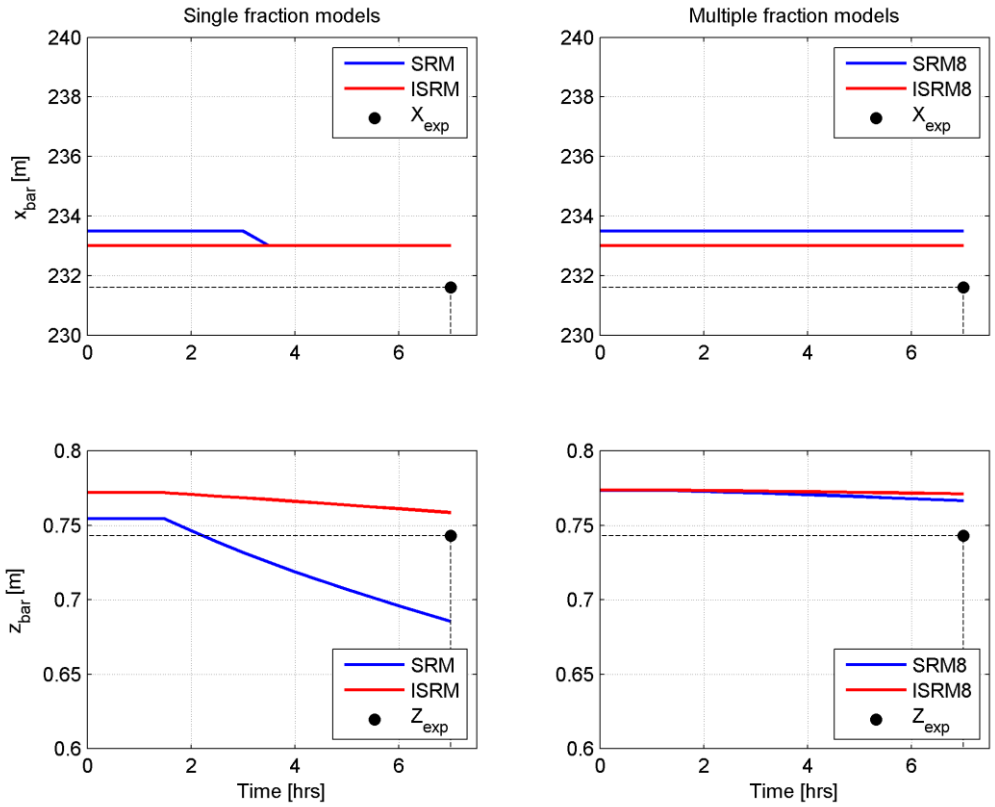

Figure C.11 - Bar position (upper panels) and bar height (lower panels) for the SRM (blue) and ISRM (red). Single fraction models are depicted in the left panels, multiple fraction models (SRM8 and ISRM8) are depicted in the right panels. The final measured values of bar position and bar height is denoted in the figure using a black dot.

D Appendix to chapter 7 – Case study results

Appendix B is reserved for the simulation results that are discussed in chapter 8. For the simulations mentioned in section 6.2 the following results are shown:

- Results from the study of Walstra et al. (2011)
- Time development of the profiles
- Relative development of the profiles
- Bar dynamics (position and height)

D.1 Results of Walstra et al. (2011)

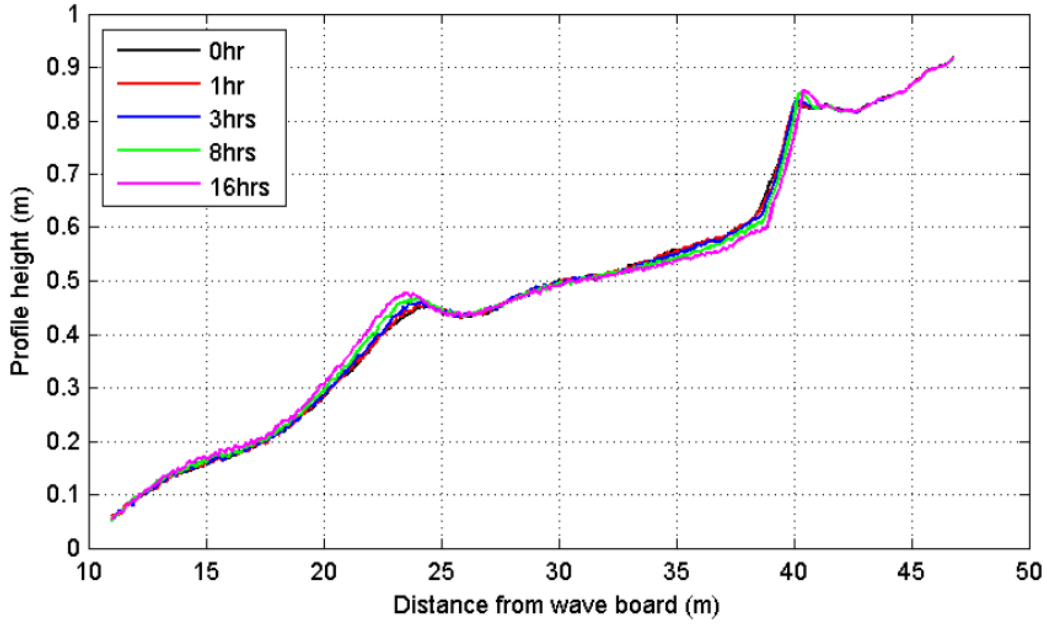

Figure D.1 - Observed profile development for the reference profile under erosive wave conditions

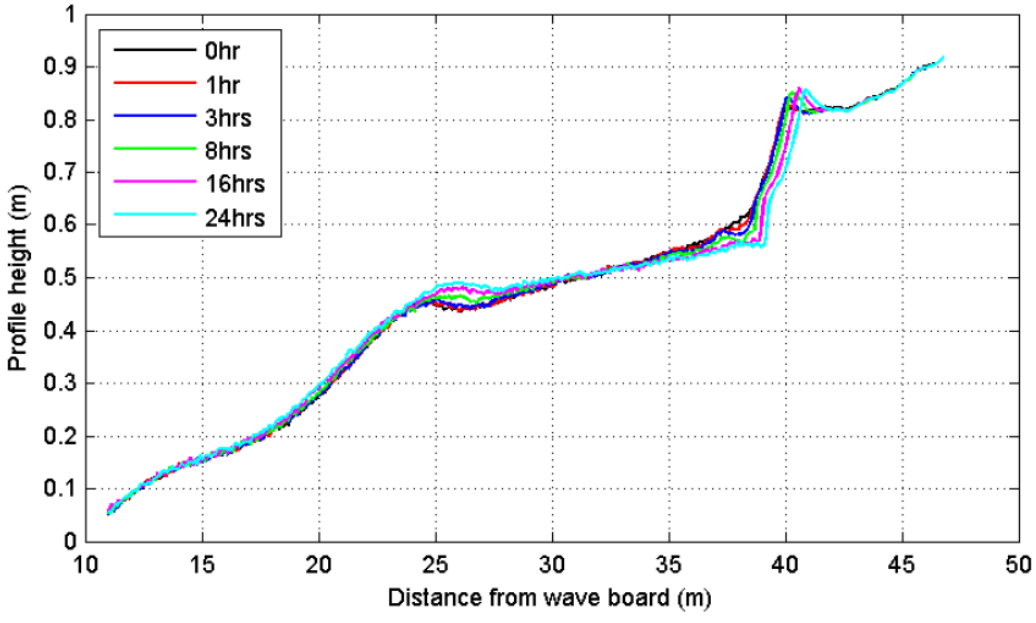

Figure D.2 - Observed profile development for the reference profile under accretive wave conditions

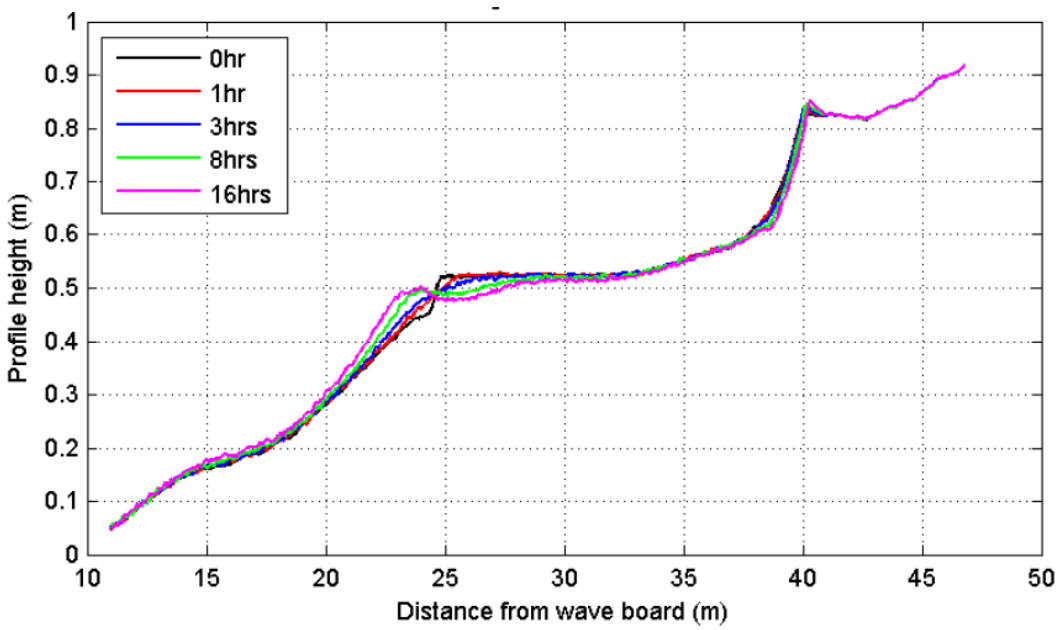

Figure D.3 - Observed profile development for the high nourishment design under erosive wave conditions

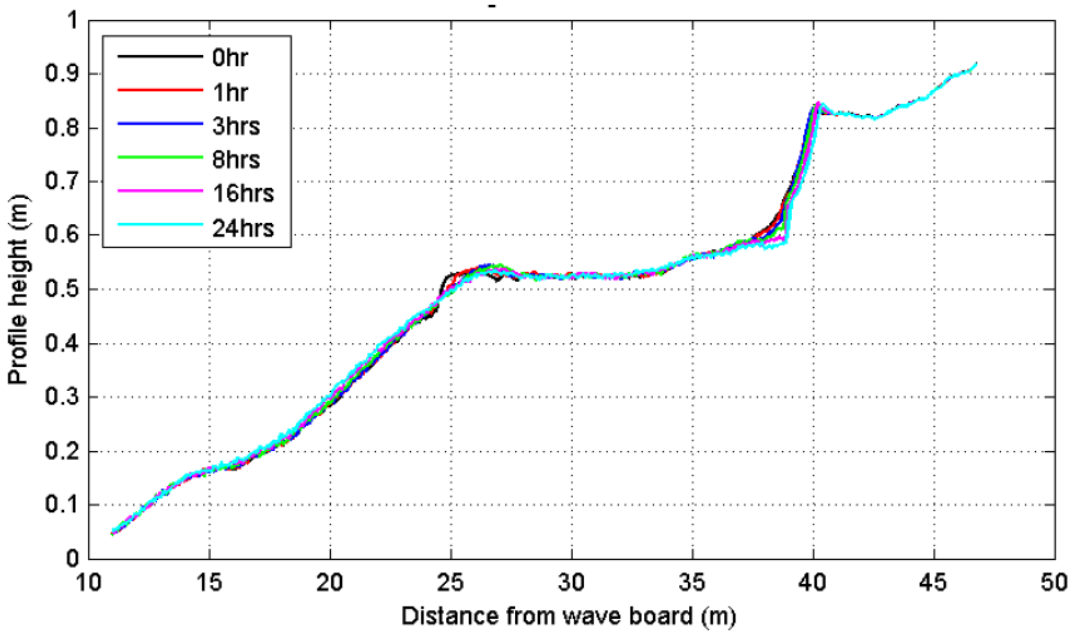

Figure D.4 - Observed profile development for the high nourishment design under accretive wave conditions

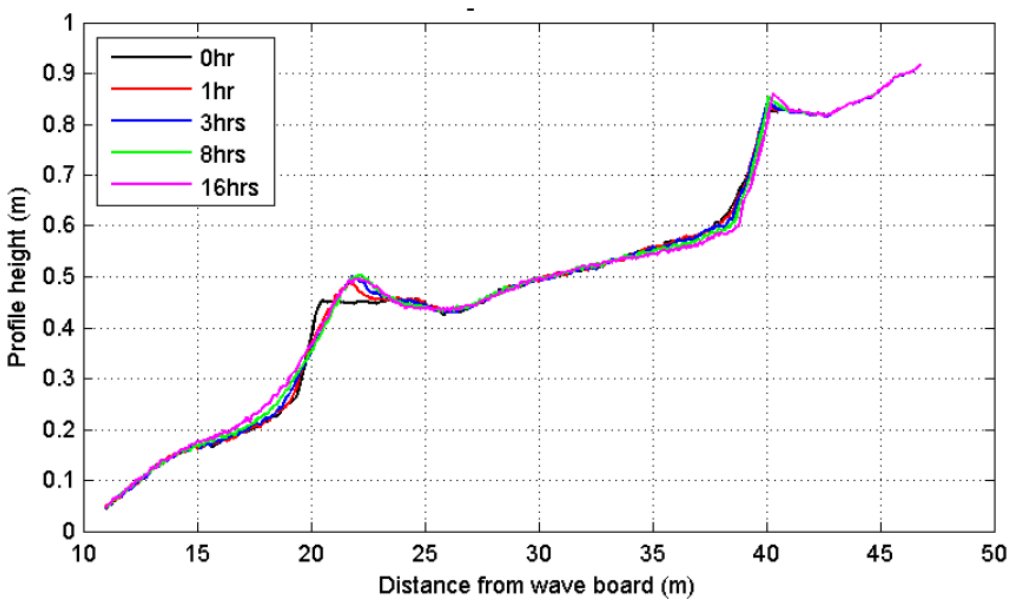

Figure D.5 - Observed profile development for the low nourishment design under erosive wave conditions

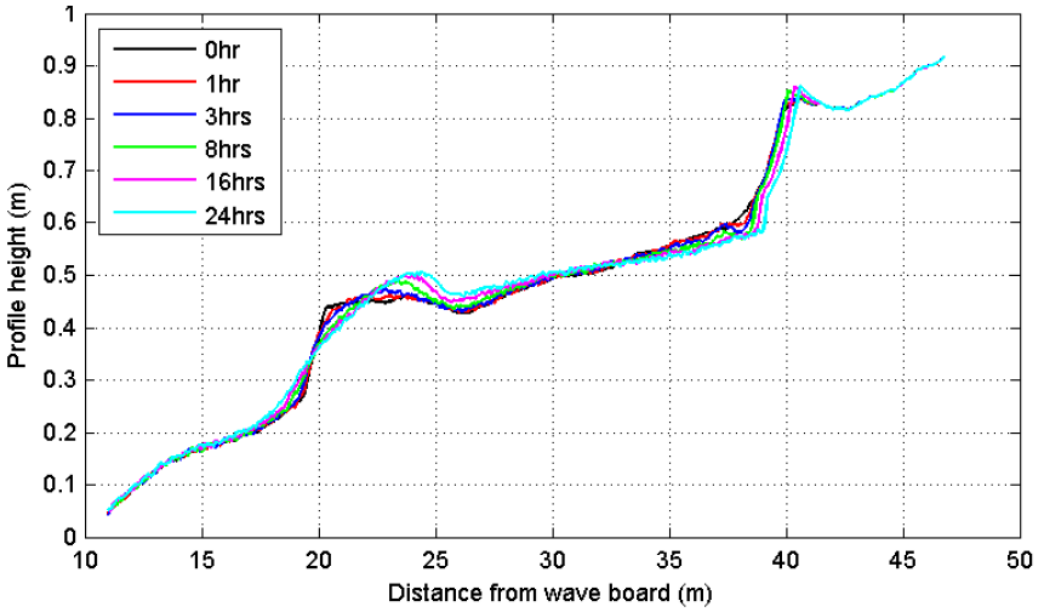

Figure D.6 - Observed profile development for the low nourishment design under accretive wave conditions.

D.2 Time development of the simulated profiles

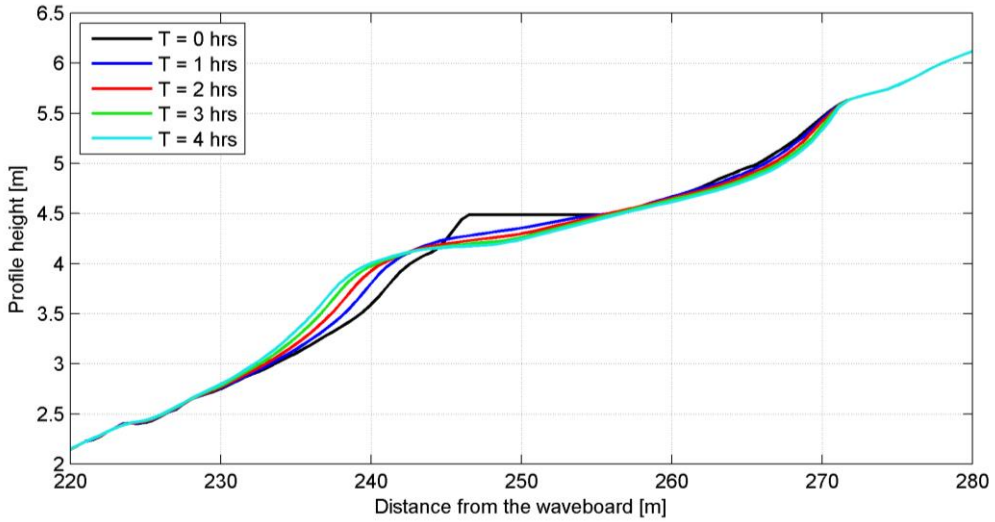

Figure D.7 - Computed morphological development of simulation H03

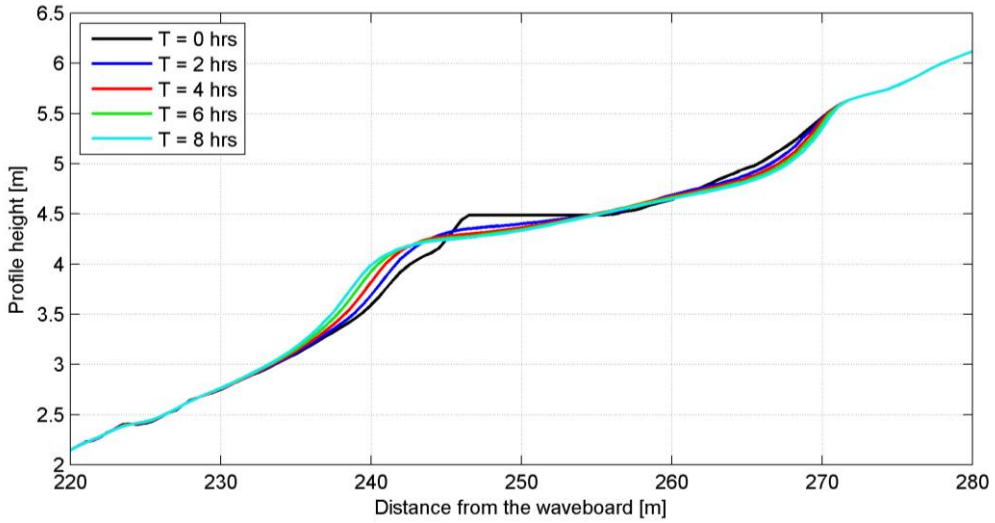

Figure D.8 - Computed morphological development of simulation H04

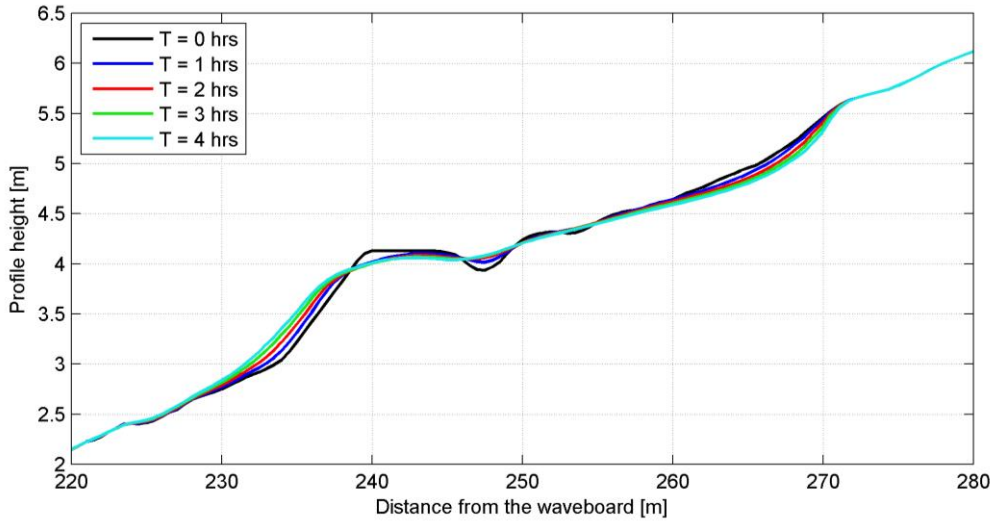

Figure D.9 - Computed morphological development of simulation L03

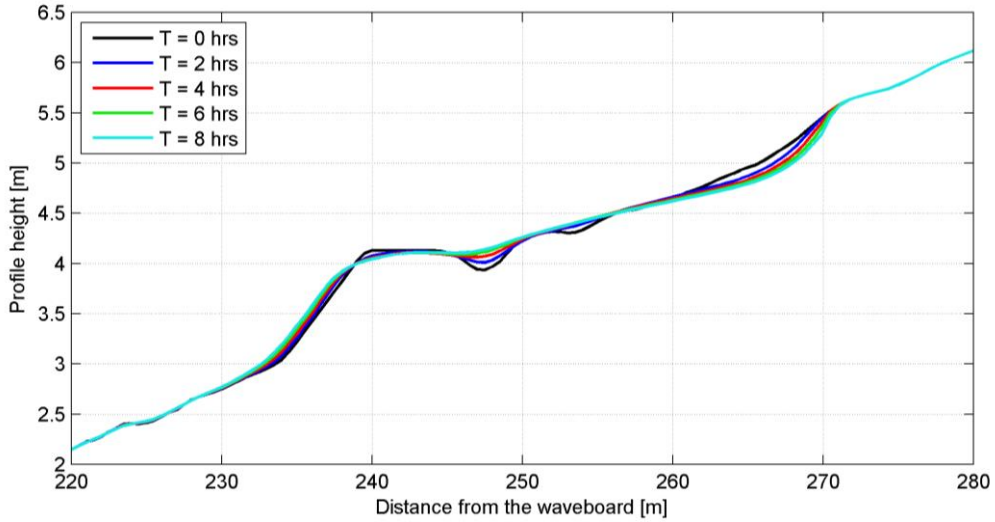

Figure D.10 - Computed morphological development of simulation L04

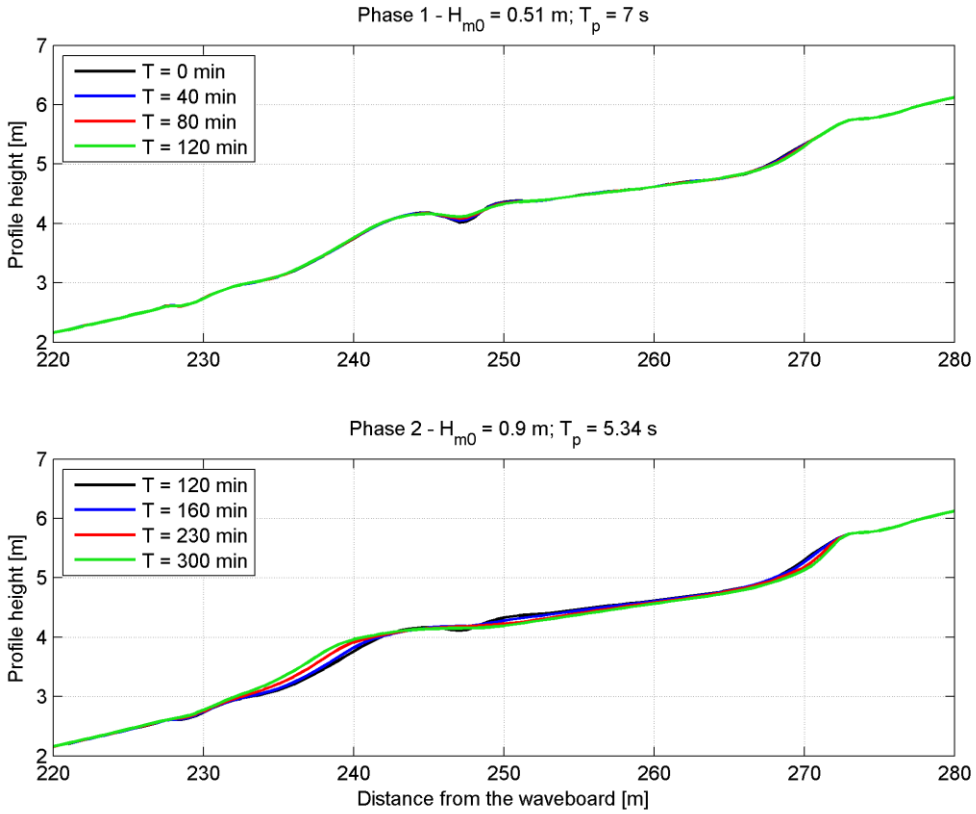

Figure D.11 - Computed morphological development of simulation R03

D.3 Relative development of the profiles

Relative development of the profiles is plotted in this section. The relative development is computed by subtracting the reference profile from the nourished profiles.

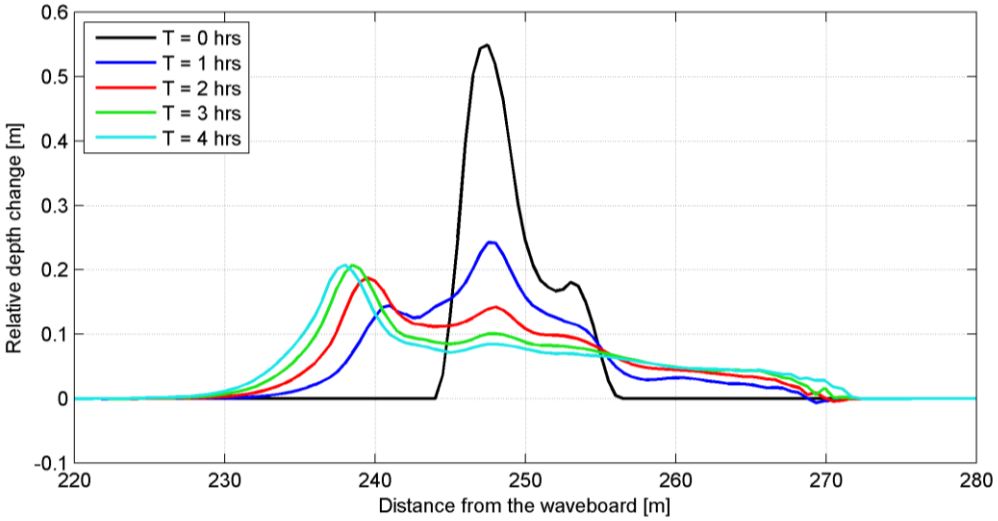

Figure D.12 - Computed relative morphological development of simulation H03

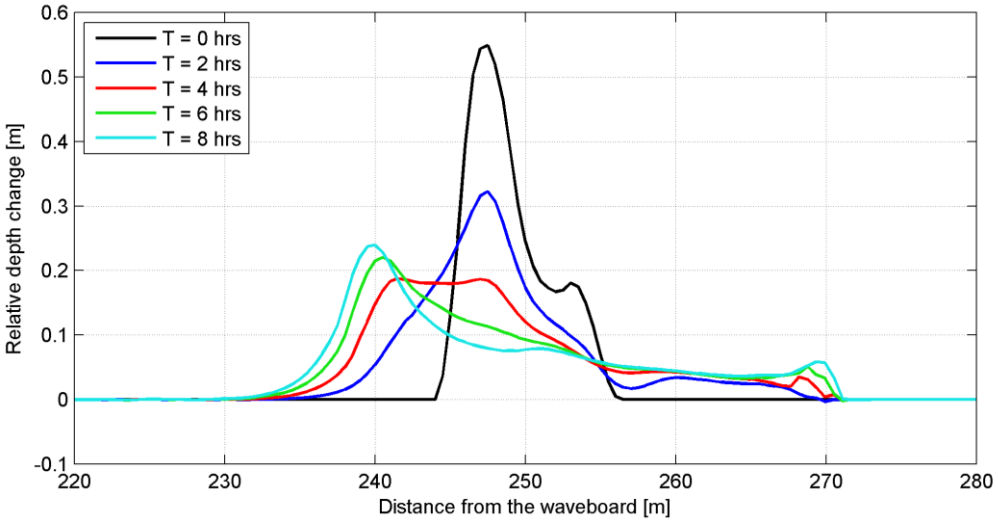

Figure D.13 - Computed relative morphological development of simulation H04

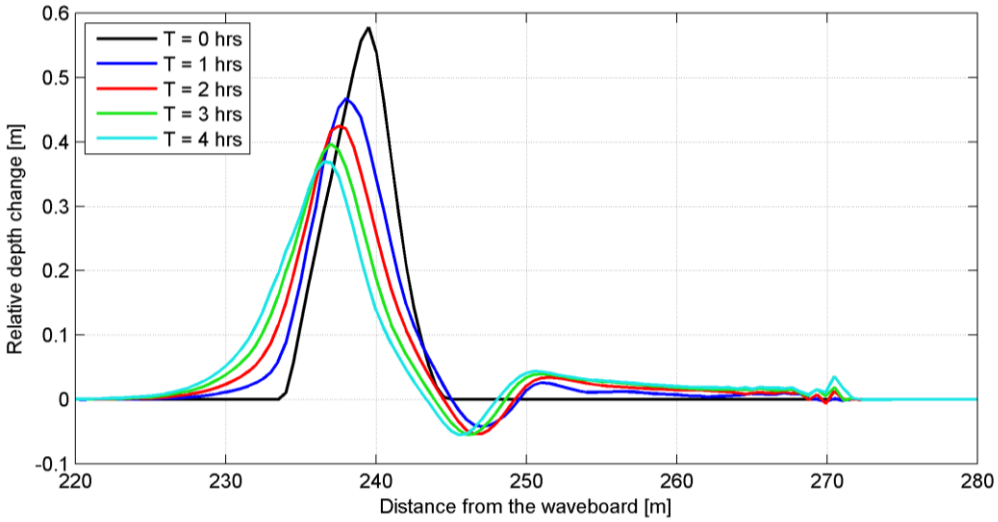

Figure D.14 - Computed relative morphological development of simulation L03

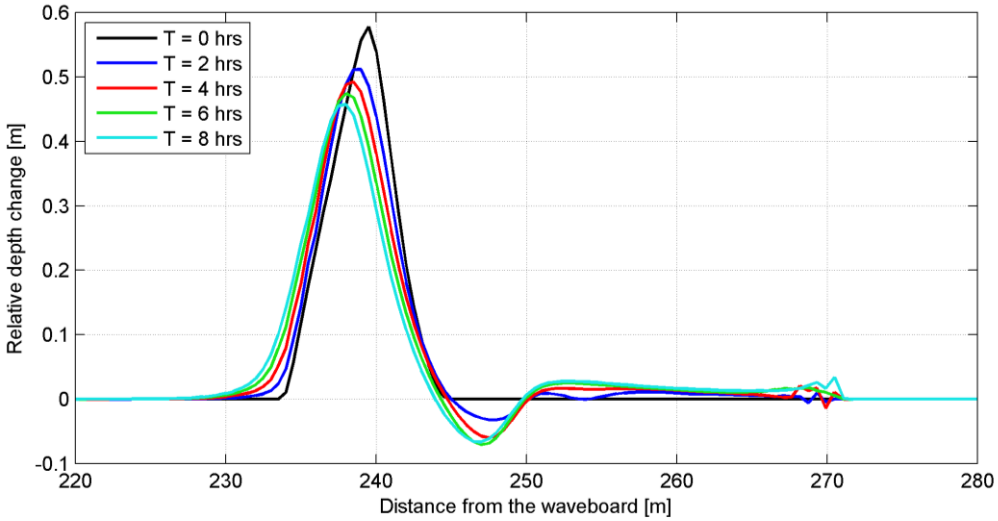

Figure D.15 - Computed relative morphological development of simulation L04

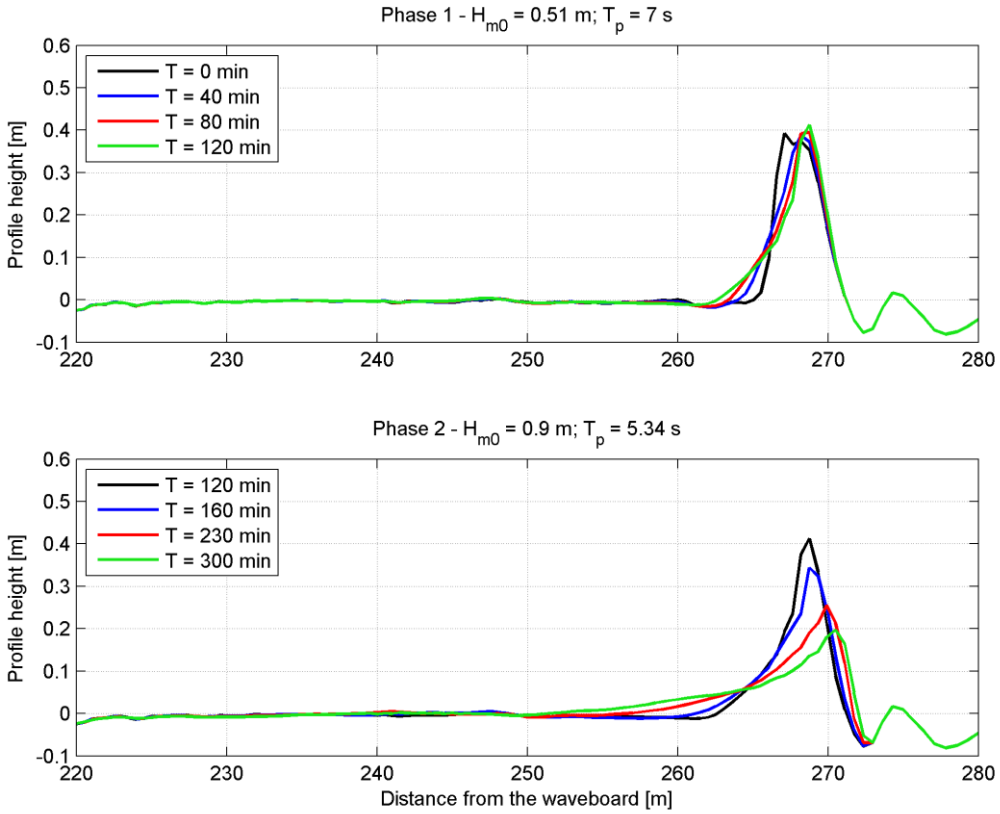

Figure D.16 - Computed relative morphological development of simulation B02

D.4 Bar dynamics

In this section figures showing bar position and height are given to assess the influence of the nourishment on the bar formation.

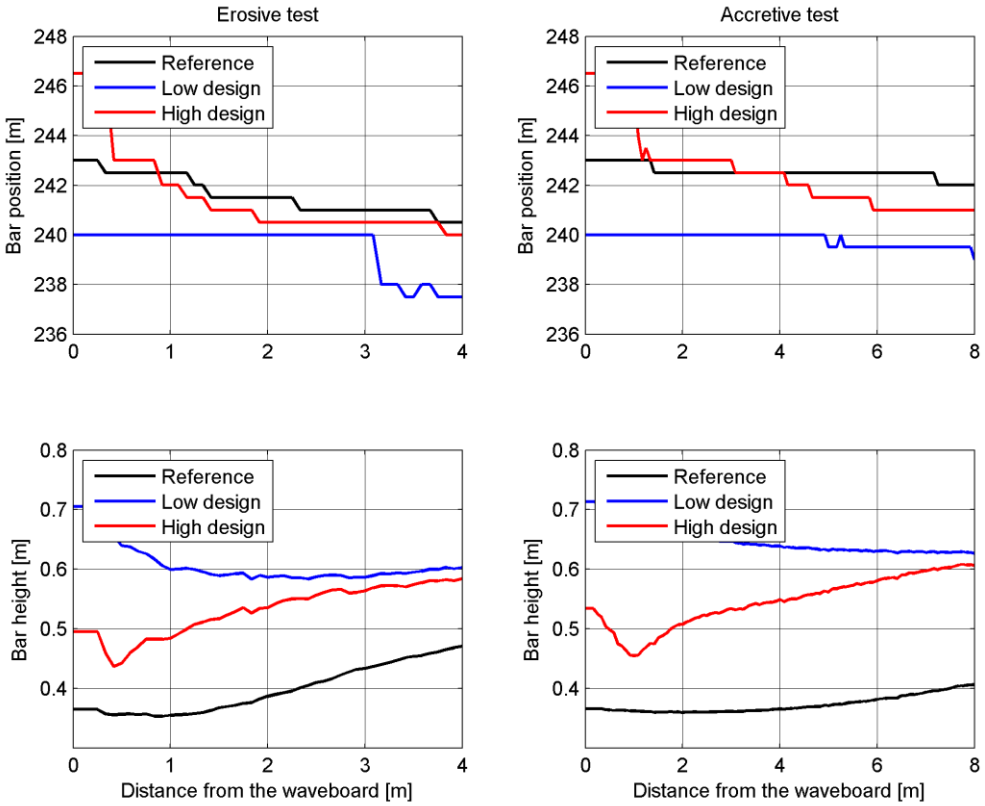

Figure D.17 - Computed bar position for reference simulations (black, R01 & R02), high design (red, H03 & H04) and low design (blue, L03 & L04) of the shoreface nourishments. Erosive (left) and accretive (right) conditions are shown. Upper panels are bar position, lower panels are bar height.

E Sensitivity analysis

In this appendix the sensitivity analysis is elaborated. The underlying principle of the measure used for sensitivity is elaborated, and the set-up of the analysis is discussed.

E.1 A measure on sensitivity

Define the parameter to be investigated β. We want to investigate the effect of an excitation Δβ from the original value on the solution of the simulation. Therefore we will use a relative deviation, given by (E.1):

$$\hat{\beta} = \left| \frac{\beta + \Delta\beta}{\beta} - 1 \right| \tag{E.1}$$

$\hat{\beta} =$ Relative deviation of the excitation compared to the original value of the parameter
$\beta =$ Original value of the investigated parameter
$\Delta\beta =$ Excitation of the original value of the investigated parameter

Now define the original solution of the simulation as f(β). We want to investigate the effect of the excitation Δβ on the original solution of the simulation, which we take as f(β+Δβ). Again, we will use a relative deviation; we take the solution compared to a reference situation, which is the initial condition, and compare this to the solution with the changed parameter relative to the reference situation. This is highlighted by (E.2):

$$\hat{f} = \left| \frac{f(\beta) - f_0}{f(\beta + \Delta\beta) - f_0} - 1 \right| \tag{E.2}$$

$\hat{f} =$ Relative deviation of the solution
$f(\beta) =$ The solution found with the original value of the parameter
$f(\beta + \Delta\beta) =$ The solution found with the deviated value of the parameter
$f_0 =$ Reference condition (Initial condition)

Now we define the sensitivity of a parameter as the relative deviation of the solution divided by the relative deviation of the investigated parameter. The parameter is classified as sensitive if a relative deviation of this parameter leads to an equally large or larger deviation of the solution from the initial condition or, according to equation (E.1), S>1.

$$S = \frac{\langle \hat{f} \rangle}{\hat{\beta}} = \frac{\left\langle \left| \frac{f(\beta) - f_0}{f(\beta + \Delta\beta) - f_0} - 1 \right| \right\rangle}{\left| \frac{\beta + \Delta\beta}{\beta} - 1 \right|} \tag{E.3}$$

In here, <..> denotes averaging over the full range of the solution.

If a range of parameters is used, the Sensitivity Index is taken as the weighted average of each S. With some rewriting, this leads to (E.4):

$$SI = \frac{\sum_{i=1}^{n} \left\langle \left| \frac{f(\beta_i) - f_0}{f(\beta_i + \Delta\beta_i) - f_0} - 1 \right| \right\rangle}{\sum_{i=1}^{n} \left| \frac{\beta_i + \Delta\beta_i}{\beta_i} - 1 \right|} \qquad \text{(E.4)}$$

E.2 Sensitivity of single fraction models

In Table E.1 the results of the sensitivity analysis for the single fraction models (SRM and ISRM) are summarized.

Table E.1- Sensitivity index for the free parameters of the single fraction models.

Parameter	SI	
	SRM	ISRM
β_{rol}	18.8[3]	77[4]
γ_w	10.2	8.8
f_{bed}	0.36	0.34
$f_{bed,w}$	0.26	0.14
f_{sus}	0.19	0.04
$f_{sus,w}$	1.3	1.37
α_{bs}	2.25[2]	0.40[2]

E.2.1 Stationary Roller Model

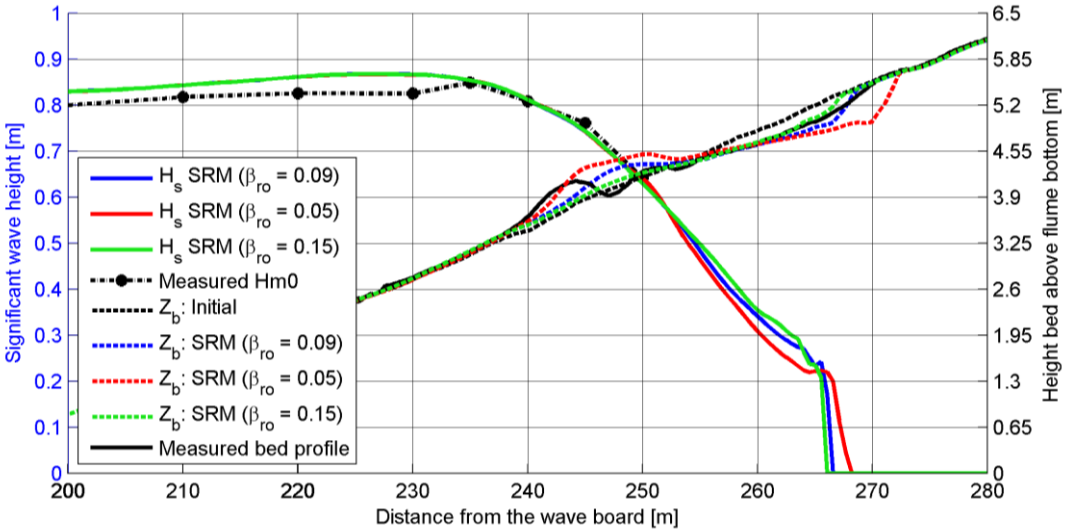

Figure E.1 - Sensitivity for the roller slope coefficient β_{rol}

[3] *Caused by large deviations in the swash zone*

[4] *Caused by instabilities in the model outcome for changed parameter*

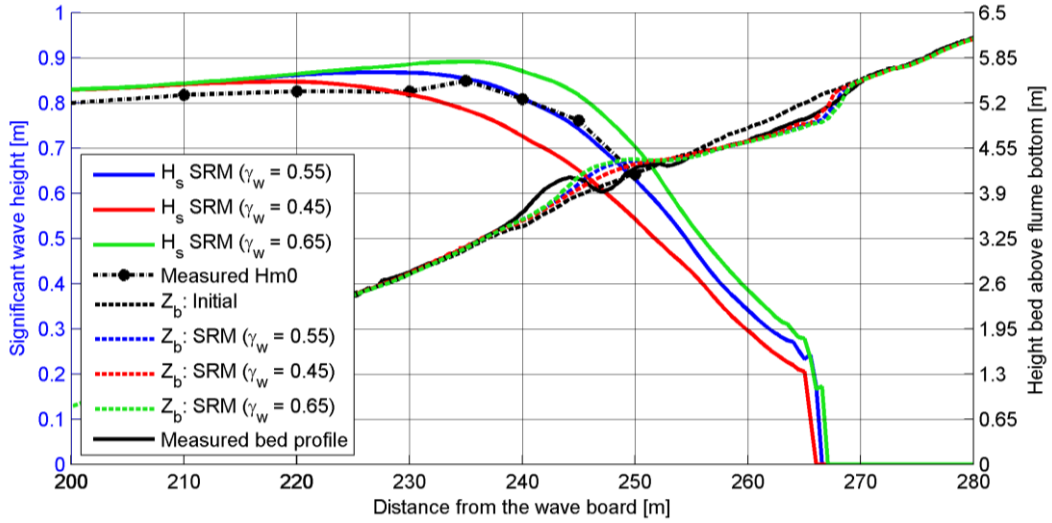

Figure E.2 - Sensitivity for the wave breaker parameter γ_w

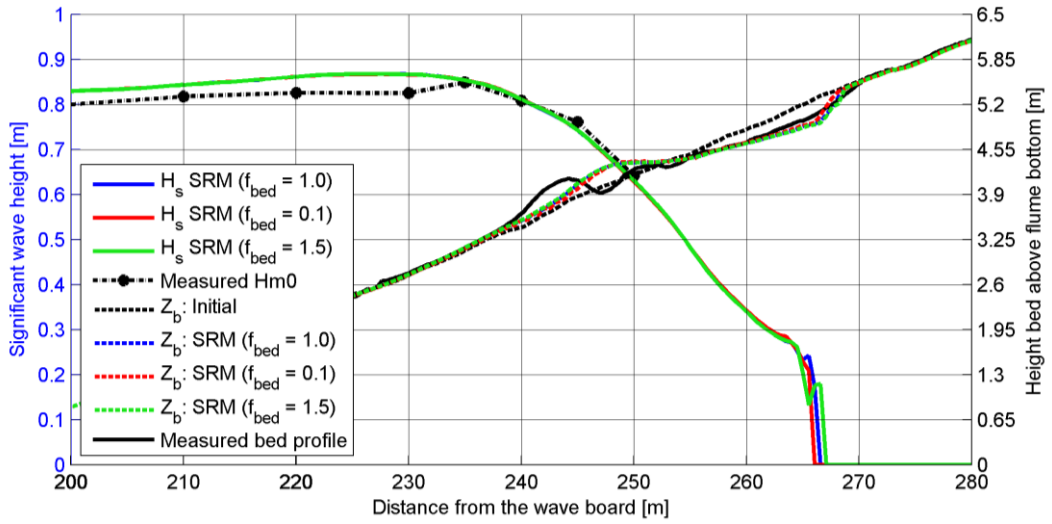

Figure E.3 - Sensitivity for the current related bed load scaling f_{bed}

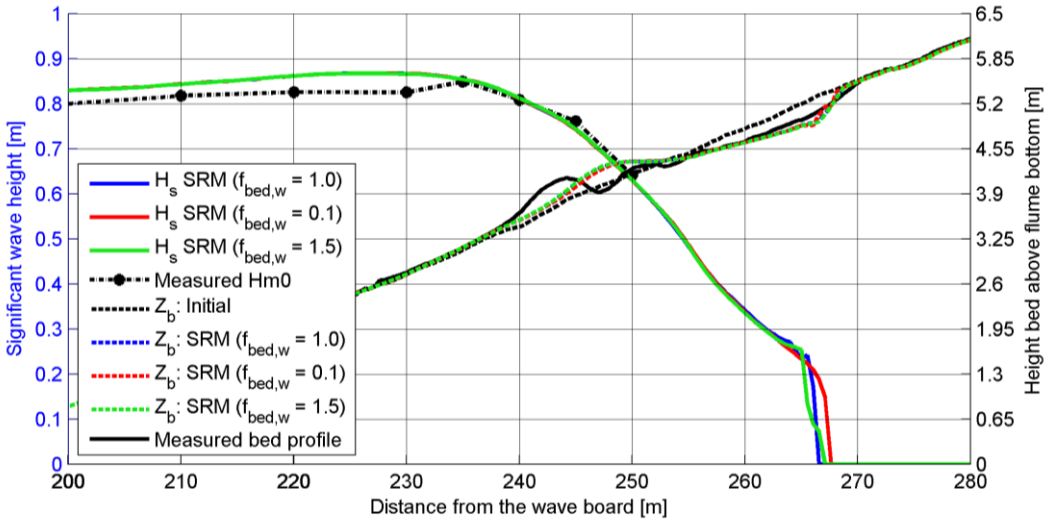

Figure E.4 - Sensitivity of the wave related bed load scaling factor $f_{bed,w}$

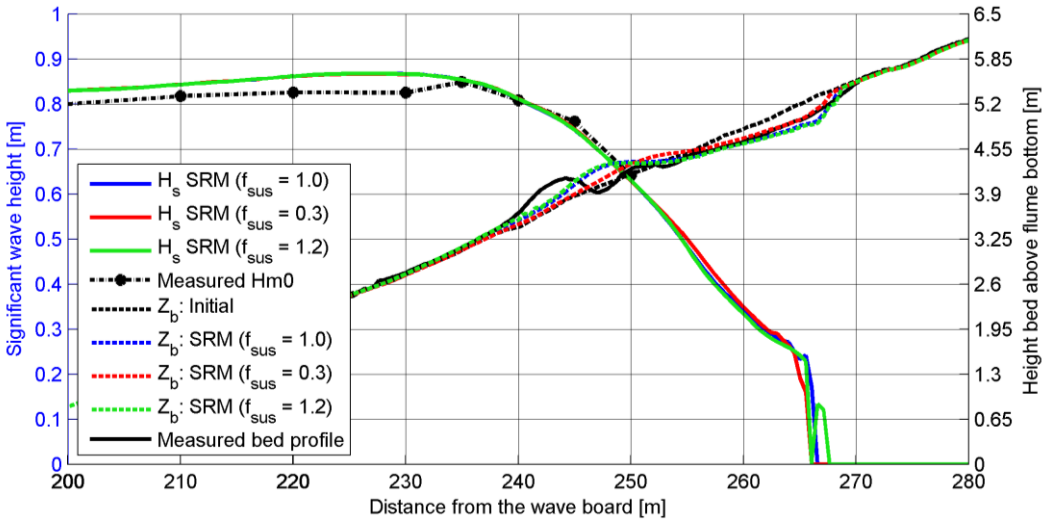

Figure E.5 - Sensitivity of the current related suspended load scaling factor f_{sus}

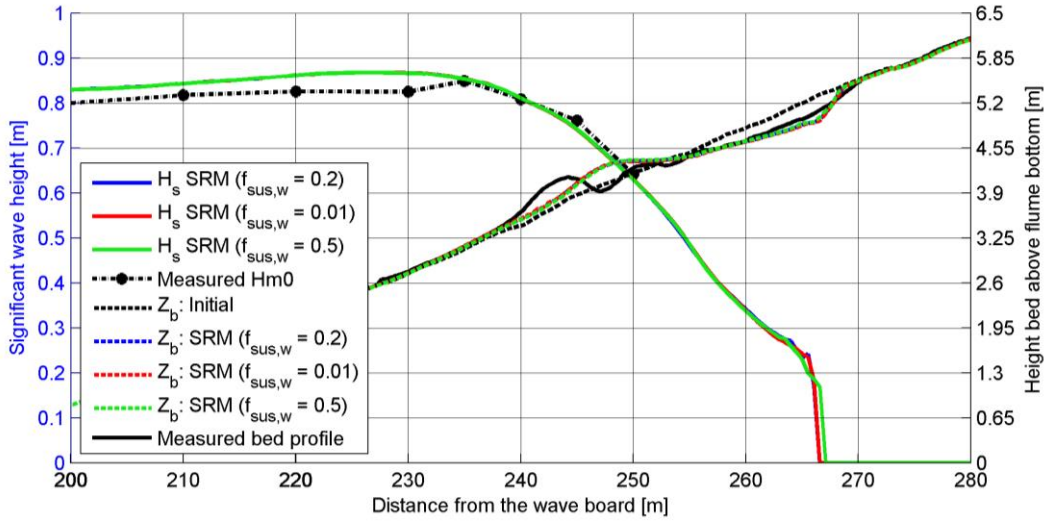

Figure E.6 - Sensitivity of the wave related suspended load scaling factor $f_{sus,w}$

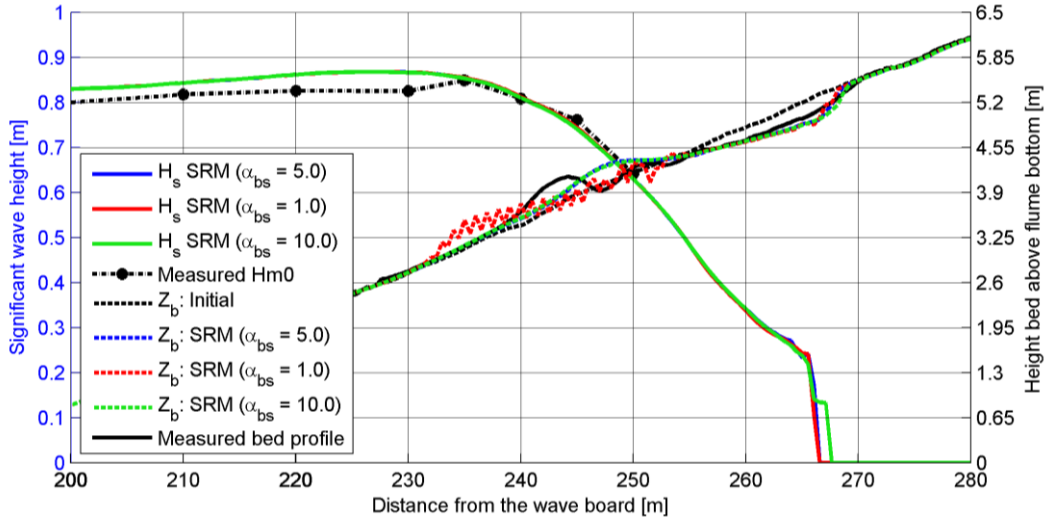

Figure E.7 - Sensitivity of the bed slope effect factor α_{bs}

E.2.2 InStationary Roller Model

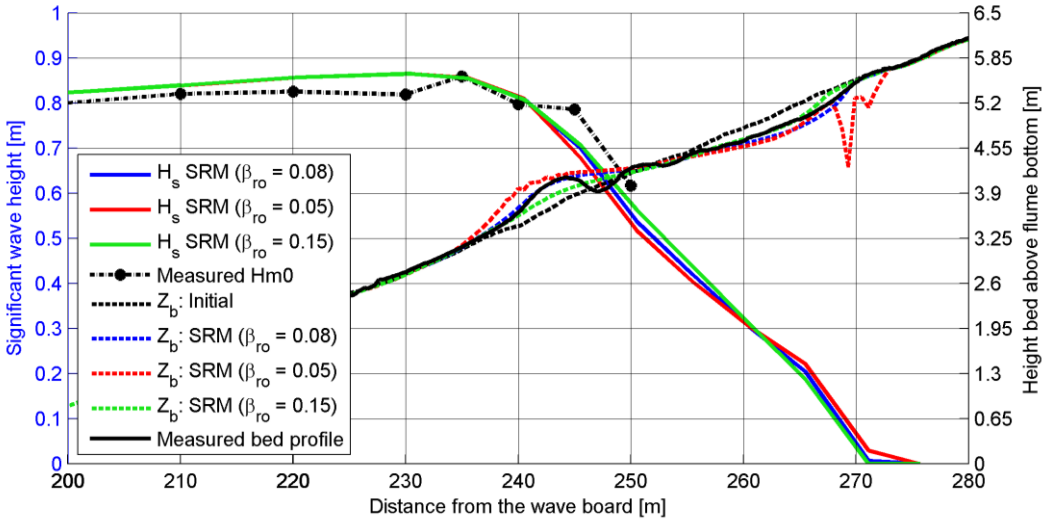

Figure E.8 - Sensitivity for the roller slope coefficient β_{rol}

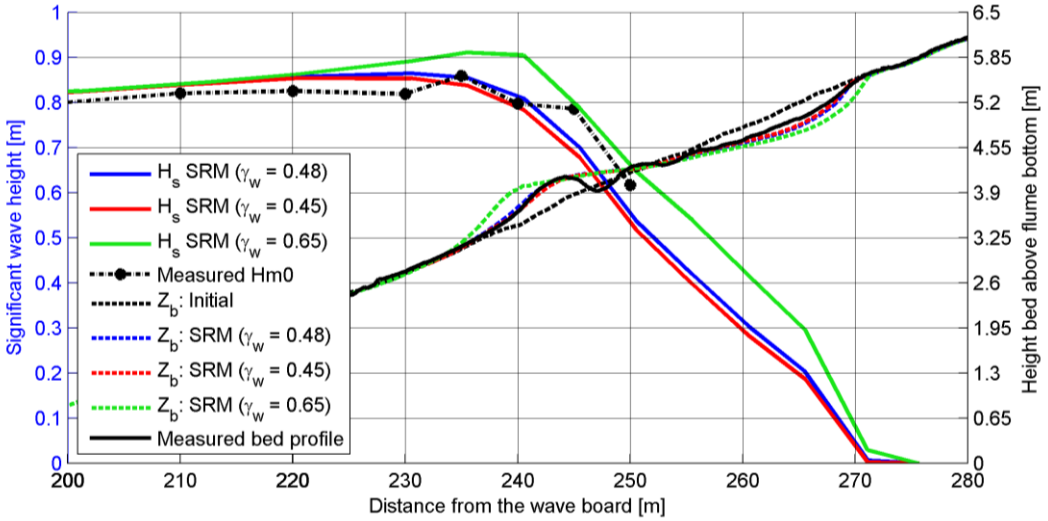

Figure E.9 - Sensitivity for the wave breaker parameter γ_w

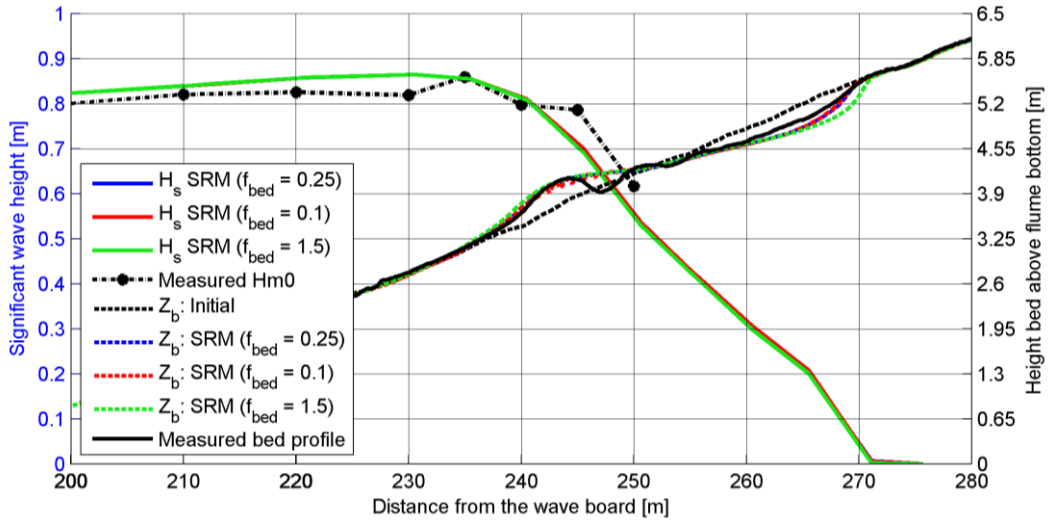

Figure E.10 - Sensitivity for the current related bed load scaling f_{bed}

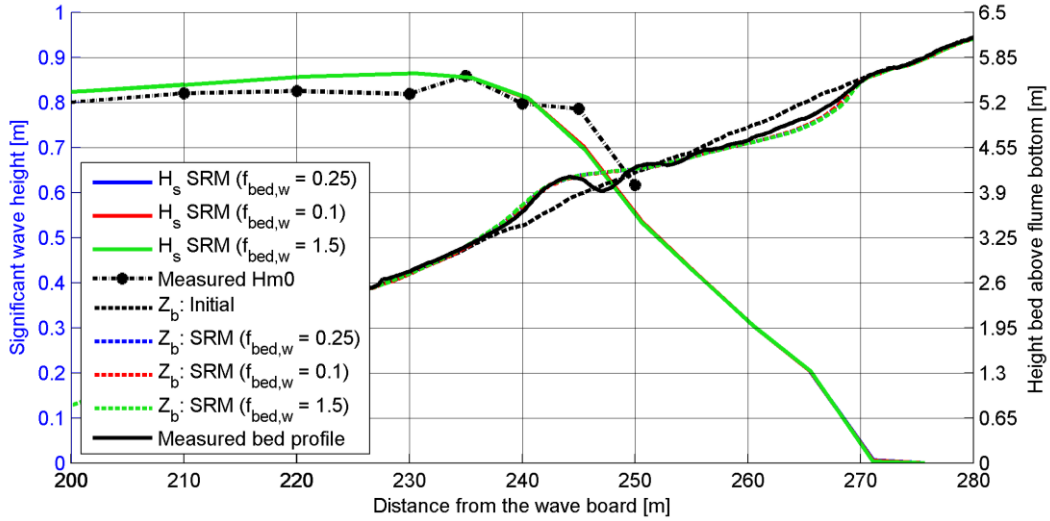

Figure E.11 - Sensitivity of the wave related bed load scaling factor $f_{bed,w}$

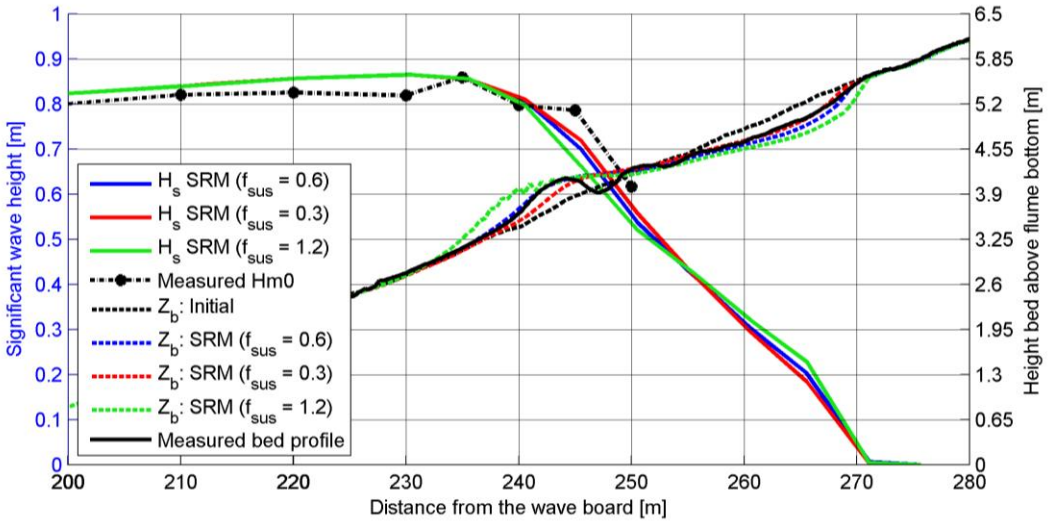

Figure E.12 - Sensitivity of the current related suspended load scaling factor f_{sus}

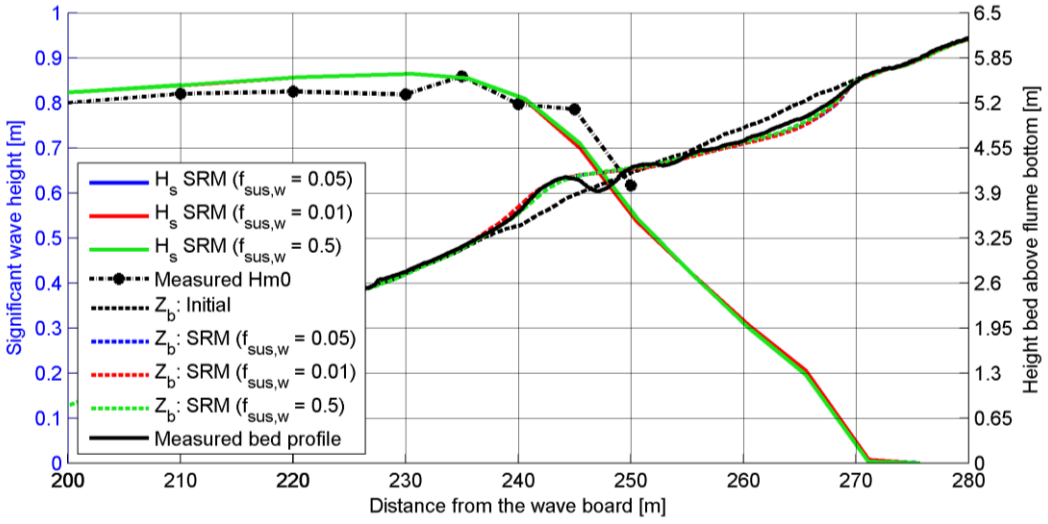

Figure E.13 - Sensitivity of the current related suspended load scaling factor $f_{sus,w}$

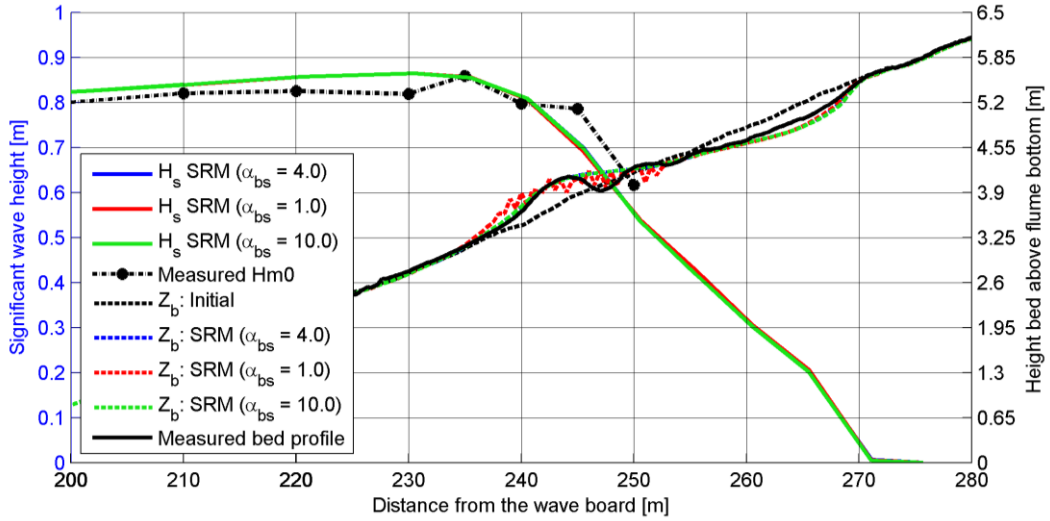

Figure E.14 - Sensitivity of the bed slope effect factor α_{bs}

F Re-calibration: Procedure & Results

In chapter 5 the results of the Hannover Flume Model were shown. The model was calibrated for erosive wave conditions (storm-conditions) and in those settings applied to other cases of the experiment with a milder wave condition. This proved to deliver accurate results, although for the ISRM the predicted wave height was too low in the shoaling zone. Based on the results of the sensitivity analysis, the model was re-calibrated for these lower wave conditions. To achieve the desired results, first the wave breaker parameter was re-calibrated, to get the correct wave heights. Then the results for the morphology are re-calibrated by scaling the transport components, in this case only the current related suspended load transport scaling factor. The results are shown in Figure F.1. Compared to Figure C.2, the upper-shoreface erosion is slightly larger for this case. However, qualitatively the results are the same. No improvement is obtained from the re-calibration, but the performance is not decreased either.

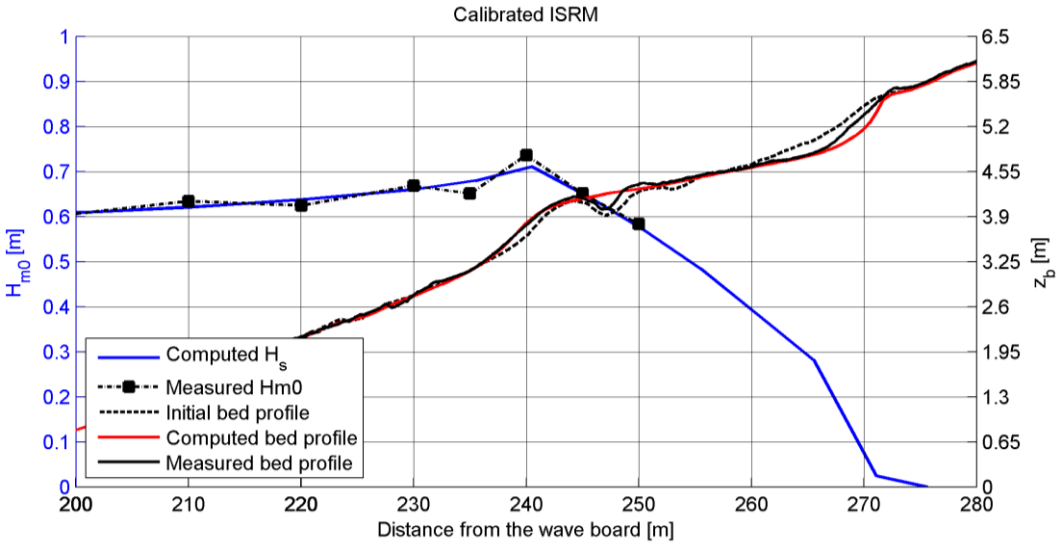

Figure F.1 - Re-calibrated model simulation results for the Hannover Flume Model using a milder wave condition.

G Computation of shear stresses

It was shown in section 5.2.3 that the suspended sediment concentration profile is crucial for determining transports and morphological change along the profile. The concentration profile is dependent on the near-bed boundary condition, which is a reference concentration calculated according to (Van Rijn, 2007b):

$$c_a = 0.015\rho_s \frac{D_{50} T_a^{1.5}}{a D_*^{0.3}} \tag{G.1}$$

c_a = reference concentration
ρ_s = Density of the sediment
T_a = Non-dimensional bed shear stress
a = Reference height a (usually taken as the top of the bed load layer)
D_* = Non-dimensional grain diameter

For all modeling situations in the flume, the parameter that induces the differences is the non-dimensional bed shear stress (T_a), which is defined as:

$$T_a = \frac{\tau_{b,cw} - \tau_{cr}}{\tau_{cr}} = \frac{\left(\mu_c \tau_{b,c} + \mu_w \tau_{b,w}\right) - \tau_{cr}}{\tau_{cr}} \tag{G.2}$$

$\tau_{b,cw}$ = Bed shear stress due to combined current-wave motion
μ_c = Current related efficiency factor
$\tau_{b,c}$ = Bed shear stress due to current
μ_w = Wave related efficiency factor
$\tau_{b,w}$ = Bed shear stress due to waves

The computation of the current related efficiency factor (μ_c), bed shear stress due to the current ($\tau_{b,c}$), the wave related efficiency factor (μ_w) and bed shear stress due to waves ($\tau_{b,w}$), is presented in this section.

G.1 Current related efficiency factor

The current related efficiency factor is defined as the grain related friction factor divided by the total current related friction factor:

$$\mu_c = \frac{f_c'}{f_c} \tag{G.3}$$

The grain related friction factor is given by:

$$f_c' = 0.24\left[{}^{10}\log\left(12\, h / D_{90}\right)\right]^{-2} \tag{G.4}$$

The total current related friction factor is given by:

$$f_c = 0.24\left[{}^{10}\log\left(12\,h/k_{s,c}\right)\right]^{-2} \tag{G.5}$$

In here, the current related roughness is given as:

$$k_{s,c} = \left[\left(k_{s,c,r}\right)^2 + \left(k_{s,c,mr}\right)^2 + \left(k_{s,c,d}\right)^2\right]^{0.5} \tag{G.6}$$

In this study the effective dune roughness ($k_{s,c,d}$) is assumed zero, leading to a total current related roughness that is only dependent on ripples ($k_{s,c,r}$) and megaripples ($k_{s,c,mr}$).

$$k_{s,c,r} = \alpha_r \begin{cases} 20D_{silt} & \text{if } D_{50} < D_{silt} \\ k^*_{s,r} & \text{otherwise} \end{cases} \tag{G.7}$$

$$k^*_{s,r} = \begin{cases} 150 f_{cs} D_{50} & \psi \le 50 \\ \left(182.5 - 0.65\psi\right) f_{cs} D_{50} & 50 < \psi \le 250 \\ 20 f_{cs} D_{50} & \psi > 250 \end{cases} \tag{G.8}$$

$$k_{s,c,\mathrm{mr}} = \alpha_{mr} \begin{cases} 20D_{silt} & \text{if } D_{50} < D_{silt} \\ k^*_{s,mr} & \text{otherwise} \end{cases} \tag{G.9}$$

$$k^*_{s,mr} = \begin{cases} 0.0002 f_{fs} \psi h & \psi \le 50 \\ \left(0.011 - 0.00002\psi\right) f_{fs} h & 50 \le \psi \le 550 \\ 0.02 & \psi > 550 \text{ and } D_{50} \ge 1.5 D_{sand} \\ 200 D_{50} & \psi > 550 \text{ and } D_{50} < 1.5 D_{sand} \end{cases} \tag{G.10}$$

$$f_{cs} = \left(\frac{0.25 * D_{gravel}}{D_{50}}\right)^{1.5} \tag{G.11}$$

$$f_{fs} = \frac{D_{50}}{1.5 D_{sand}} \tag{G.12}$$

$$D_{silt} = 32\ \mu m;\ D_{sand} = 62\ \mu m;\ D_{gravel} = 0.002\ m \tag{G.13}$$

$$\psi = \frac{U_{wc}^2}{\left[(s-1) g d_{50}\right]} = \frac{U_w^2 + u_c^2}{\left[(s-1) g d_{50}\right]} \tag{G.14}$$

In here, U_w is the near-bed peak orbital velocity and u_c is the depth-averaged current velocity

$f_c^{'}$ = Grain related efficiency factor [-]
f_c = Current related friction factor [-]
h = Total water depth [m]
$k_{s,c}$ = Current related roughness [m]
$k_{s,c,r}$ = Roughness height of the ripples [m]
$k_{s,c,mr}$ = Roughness height of megaripples [m]
$k_{s,c,d}$ = Roughness height of the dunes [m]
α_r = Scaling factor of O(1) for the ripples [-]
α_{mr} = Scaling factor of O(1) for the megaripples [-]
ψ = Mobility parameter [-]
U_{wc} = Combined wave and current velocity [m/s]
s = Relative density [-]

G.2 Wave related efficiency factor

The wave related efficiency factor is defined as:

$$\mu_w = \frac{0.7}{D_*}$$
$$\mu_{w,\min} = 0.14 \quad \text{for } D_* \geq 5 \qquad \text{(G.15)}$$
$$\mu_{w,\max} = 0.35 \quad \text{for } D_* \leq 5$$

G.3 Current related bed shear stress

The current related bed shear stress is given by:

$$\tau_{b,c} = 0.125 \cdot \rho_w f_c \bar{U} \qquad \text{(G.16)}$$

With f_c given by equation (G.5) and $\bar{U}$ the depth averaged current velocity.

G.4 Wave related bed shear stress

The wave related bed shear stress is given by:

$$\tau_{b,w} = 0.25 \cdot \rho_w f_w U_\delta^2 \qquad \text{(G.17)}$$

The wave related friction coefficient is given by:

$$f_w = \min\left(0.3;\ \exp\left[-6 + 5.2\left(A_w / k_{s,w,r}\right)^{-0.19}\right]\right) \qquad \text{(G.18)}$$

It is proposed by Van Rijn (2007a) that the physical wave related roughness of small-scale ripples is given by eq (G.7), thus:

$$k_{s,w,r} = k_{s,c,r} \qquad \text{(G.19)}$$

The peak orbital diameter is given by:

$$A_w = \frac{H_s}{2\sinh\left(\frac{2\pi h}{L}\right)} \tag{G.20}$$

In equation 1.17 the orbital velocity is defined as:

$$U_\delta = \left(0.5 \cdot u_{on}^3 + 0.5 \cdot u_{off}^3\right)^{1/3} \tag{G.21}$$

The onshore and offshore directed velocities are constructed in the following way:

$$u_{on} = u_{\max} \frac{0.5 + (r_{\max} - 0.5)\tanh(r_i - 0.5)}{r_{\max} - 0.5} \tag{G.22}$$

$$u_{off} = u_{\max} - u_{on} \tag{G.23}$$

$$r_{\max} = \max\left(0.62;\ \min\left(0.75;\ -2.5\frac{h}{L} + 0.85\right)\right) \tag{G.24}$$

$$r_i = \max\left(0.5;\ -5.25 - 6.1 \cdot \tanh(a_i)u_i - 1.76\right) \tag{G.25}$$

$$a_i = -0.0049\left(T_p\sqrt{g/h}\right)^2 - 0.069\left(T_p\sqrt{g/h}\right) + 0.2911 \tag{G.26}$$

$$u_i = \frac{u_{\max}}{\sqrt{gh}} \tag{G.27}$$

$$u_{\max} = 2\left(-0.4\,H_s/h\right)U_w \tag{G.28}$$

U_δ = Near-bed peak orbital velocity
$k_{s,w,r}$ = Wave related roughness of small-scale ripples [m]
A_w = Peak orbital diameter (particle excursion) [m]
H_s = Significant wave height [m]
L = Wave length
u_{on} = Onshore directed velocity [m/s]
u_{off} = Offshore directed velocity [m/s]
$r_{\max}$ = Maximum asymmetry proportionality [-]
r_i = Instantaneous asymmetry proportionality [-]
a_i = Instantaneous near-bed particle excursion [m]
u_i = Instantaneous near-bed orbital velocity [m/s]
$u_{\max}$ = Maximum orbital velocity [m/s]

H Modelling guidelines

In this section a concise overview of the steps taken to set up the model as used in this thesis is provided. Depending on whether it is desired to simulate sorting processes a multiple fraction approach should be implemented.

First step of setting up the model is creating the wave boundary. As mentioned in section 4.3, a wave component file must be prescribed at the boundary. The components can be constructed from a measured wave spectrum. If a measured spectrum is not available, a theoretical JONSWAP-spectrum can be constructed according to section B.2. The models sensitivity to either using a measured or a theoretical spectrum is shown in Figure H.1. The differences are small, thus indicating that the use of a measured or theoretical spectrum does not make a large difference.

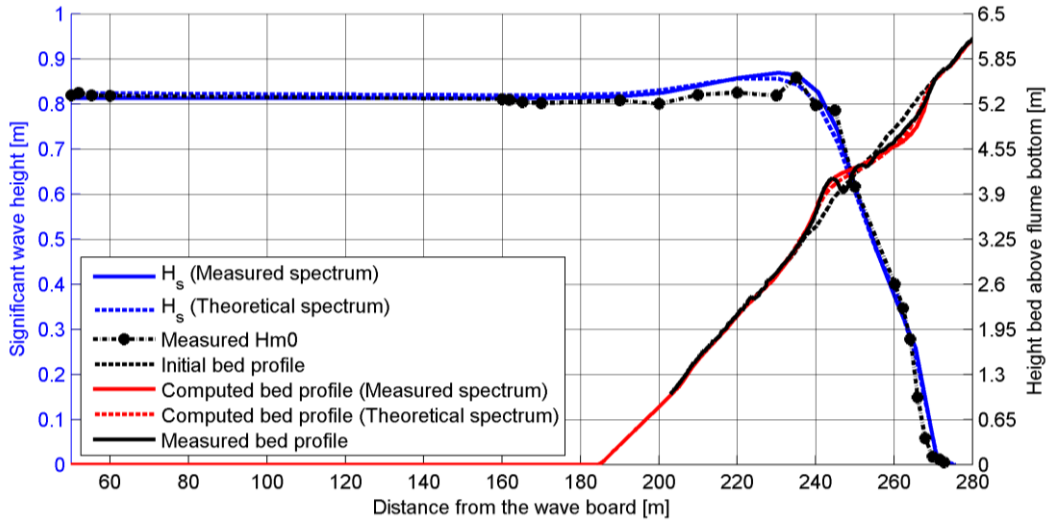

Figure H.1 - Sensitivity of the measured spectrum against the theoretical spectrum.

If it is desired to investigate sorting processes, a multiple fraction model must be set up. Depending on the width of the sediment sample, the number of fractions can be determined. It is advised to take more fractions in the finer tail of the sample, since there are more small grains than large grains in an equal volume of sand. It was shown in section 5.5 that the number of fractions (if taken enough) is not very sensitive, but the division is.

Depending on (knowledge of) the initial bed composition, a choice can be made to start from an initial uniform bottom composition of a non-uniform one. If it is chosen to start with an initially uniform well-mixed bed, keep in mind that the model may need some extra time to spin-up to a more natural bed composition. In some situations it is strictly necessary to start from a non-uniform bed composition. An initially non-uniform bed can be constructed by prescribing the sediment mass for each fraction per grid cell per vertical layer of the layered bed system.

Summarized, first the wave model is set up and if necessary then the layered bed model is set up, with optionally an initially non-uniform bed composition.